AD________________

Award Number: DAMD17-00-1-0455

TITLE: Scanning Microwave Induced Acoustic Tomography

PRINCIPAL INVESTIGATOR: Lihong Wang, Ph.D.

CONTRACTING ORGANIZATION: Texas Engineering Experiment Station
College Station, Texas 77843-3000

REPORT DATE: October 2004

TYPE OF REPORT: Final

PREPARED FOR: U.S. Army Medical Research and Materiel Command
Fort Detrick, Maryland 21702-5012

DISTRIBUTION STATEMENT: Approved for Public Release;
Distribution Unlimited

The views, opinions and/or findings contained in this report are those of the author(s) and should not be construed as an official Department of the Army position, policy or decision unless so designated by other documentation.

20050302 162

REPORT DOCUMENTATION PAGE

Form Approved
OMB No. 074-0188

Public reporting burden for this collection of information is estimated to average 1 hour per response, including the time for reviewing instructions, searching existing data sources, gathering and maintaining the data needed, and completing and reviewing this collection of information. Send comments regarding this burden estimate or any other aspect of this collection of information, including suggestions for reducing this burden to Washington Headquarters Services, Directorate for Information Operations and Reports, 1215 Jefferson Davis Highway, Suite 1204, Arlington, VA 22202-4302, and to the Office of Management and Budget, Paperwork Reduction Project (0704-0188), Washington, DC 20503

1. AGENCY USE ONLY *(Leave blank)*	**2. REPORT DATE** October 2004	**3. REPORT TYPE AND DATES COVERED** Final (1 Oct 2000 - 30 Sep 2004)

4. TITLE AND SUBTITLE
Scanning Microwave Induced Acoustic Tomography

5. FUNDING NUMBERS
DAMD17-00-1-0455

6. AUTHOR(S)
Lihong Wang, Ph.D.

7. PERFORMING ORGANIZATION NAME(S) AND ADDRESS(ES)
Texas Engineering Experiment Station
College Station, Texas 77843-3000

E-Mail: lwang@tamu.edu

8. PERFORMING ORGANIZATION REPORT NUMBER

9. SPONSORING / MONITORING AGENCY NAME(S) AND ADDRESS(ES)
U.S. Army Medical Research and Materiel Command
Fort Detrick, Maryland 21702-5012

10. SPONSORING / MONITORING AGENCY REPORT NUMBER

11. SUPPLEMENTARY NOTES

12a. DISTRIBUTION / AVAILABILITY STATEMENT
Approved for Public Release; Distribution Unlimited

12b. DISTRIBUTION CODE

13. ABSTRACT (Maximum 200 Words)

The combination of ultrasound and microwave has provided us a unique opportunity for early-cancer imaging with high resolution and high contrast. We have made significant technical progress in thermoacoustic imaging including data acquisition and imaging reconstruction. Specifically, our accomplishments include (1) an exact and an approximate time-domain reconstruction algorithm for thermoacoustic tomography in a spherical geometry was derived, (2) an exact frequency-domain reconstruction algorithm for thermoacoustic tomography in a planar geometry was derived, (3) an exact frequency-domain reconstruction algorithm for thermoacoustic tomography in a cylindrical geometry was derived, (4) high-resolution and high-contrast images were obtained, (5) further progress was made in the reconstruction algorithms, in the understanding of heterogeneity, and in extending the technology to other electromagnetic sources. We have imaged mastectomy specimens at M.D. Anderson Cancer Center in Houston.

14. SUBJECT TERMS
Detection, photoacoustic effect, microwave, ultrasonography

15. NUMBER OF PAGES
135

16. PRICE CODE

17. SECURITY CLASSIFICATION OF REPORT Unclassified	**18. SECURITY CLASSIFICATION OF THIS PAGE** Unclassified	**19. SECURITY CLASSIFICATION OF ABSTRACT** Unclassified	**20. LIMITATION OF ABSTRACT** Unlimited

Table of Contents

Cover 1
SF 298 2
Table of Contents 3
Introduction 4
Body 5
Key Research Accomplishments 16
Reportable Outcomes 17
Conclusions 21
Appendices (112 pages) 21

Introduction

A novel imaging technology, scanning microwave-induced-acoustic tomography, will be developed for breast imaging. X-ray mammography and ultrasonography are the current clinical tools for breast-cancer screening and detection. Mammography is the "gold standard", however, uses ionizing radiation and has difficulties imaging pre-menopausal breasts, which are radiographically dense. Ultrasonography is an adjunct tool to x-ray mammography and cannot detect many of the nonpalpable tumors. The cure rate of breast cancers is improved if they are detected early. To provide a new non-invasive, non-ionizing diagnostic tool for detection of early breast cancers, we will develop real-time microwave-induced-acoustic tomography for breast imaging. Microwave-induced-acoustic tomography is based on the photoacoustic effect, generation of acoustic wave by deposition of short-pulse electromagnetic energy safely into biological tissues. The microwave for this technology is short-pulsed, and its power is within the IEEE safety limits. The microwave-induced acoustic wave is then detected with an ultrasonic detector for imaging. The contrast between tumors and normal tissues in the microwave regime is significantly better than other imaging modalities. Cancerous breast tissues are found to be 2-5 times more strongly absorbing than surrounding normal breast tissues in the microwave, which has been attributed to an increase in bound water and sodium within malignant cells. However, pure-microwave imaging is fundamentally limited to poor resolution (on the order of 10 mm) because of the large wavelength of microwave. Ultrasonic imaging has good resolution (on the order of 1 mm) but has a poor contrast between tumors and normal tissues. Microwave-induced-acoustic tomography combines the contrast advantage of pure-microwave imaging and the resolution advantage of pure-ultrasonic imaging, therefore, has the potential for detection of early breast cancers and for assessing and monitoring treatments as well.

Body

In this section, we present our study of pulsed-microwave-induced thermoacoustic tomography in biological tissues. A short-pulsed microwave source was used to irradiate the tissue samples, and the thermoacoustic waves excited by thermoelastic expansion were then measured by a wide-band ultrasonic transducer along a circular path that encloses the sample under study. The acquired data were then used to reconstruct the microwave absorption distribution. Both an exact reconstruction solution and an approximate modified backprojection algorithm were derived. Experiments demonstrated that the images calculated by the backprojection method agreed with the original samples very well, and the spatial resolution in reconstruction was as good as 0.5 millimeters.

Introduction to thermoacoustic tomography

In thermoacoustic tomography, a short-pulsed microwave source is used to irradiate the tissue. Absorbed microwave energy causes thermoelastic expansion and radiates thermoacoustic waves from within the irradiate tissue. The relatively long wavelength of the microwave, e.g., ~3 cm at 3 GHz in tissues, serves to illuminate the tissue homogeneously. The microwave heating must be rapid to produce thermoacoustics waves; in other words, static temperature distribution or slow heating cannot produce thermoacoustic waves. A wide-band ultrasonic transducer can then be employed to acquire the thermoacoustic signals excited by thermoelastic expansion, which carries the microwave absorption property of the tissue. The ultrasonic transducer is very sensitive in detecting small vibrations from an object that are caused by weak energy absorption.

The key problem with this technique is how to determine the microwave absorption distribution from the measured data, i.e., how to map the inhomogeneity of the tissue. One approach is to use focused ultrasonic transducers to localize the thermoacoustic sources in linear or sector scans and then construct the images directly from the data as is often done in pulse-echo ultrasonography. An alternative method is to use wide-band unidirectional point detectors to acquire thermoacoustic data and then reconstruct the microwave absorption distribution. To date, we have not seen an exact inverse solution for this specific problem, although some researchers have arrived at approximate reconstruction algorithms, such as the weighted delay-and-sum method, the optimal statistical approach, and the Radon transform in far field approximation.

Based on spherical harmonic functions, we first deduced an exact solution of the problem in the three-dimensional case, which can be carried out in the frequency domain. We assume that the wide-band unidirectional ultrasonic transducer is set on a spherical surface, which encloses the sample under investigation. The data acquired from different directions are sufficient to allow us to reconstruct the microwave absorption distribution. In our case, the diameter of the sphere of detection is much larger than the ultrasonic wavelength. Next, an approximate algorithm is deduced, which is a modified backprojection of a quantity related with the thermoacoustic pressure. This approximate algorithm can be carried out in the time domain and is much faster than the exact solution. We have also tested a set of tissue samples. These experiments demonstrate that the images calculated by the modified backprojection method agree with the original samples very well. Moreover, the images have both the high contrast associated with pure-microwave imaging and the 0.5-millimeter spatial resolution associated with pure-ultrasound imaging.

Theory of thermoacoustic tomography

Fundamentals of thermoacoustics

Thermoacoustic theory has been discussed in many literature reviews such as. Here, we briefly review only the fundamental equations. If the microwave pumping pulse duration is much shorter than the thermal diffusion time, thermal diffusion can be neglected; consequently, the thermal equation becomes

$$\rho C_p \frac{\partial}{\partial t} T(\mathbf{r},t) = H(\mathbf{r},t), \tag{1}$$

where ρ is the density, C_p is the specific heat, $T(\mathbf{r},t)$ is the temperature rise due to the energy pumping pulse, and $H(\mathbf{r},t)$ is the heating function defined as the thermal energy per time and volume deposited by the energy source. We are interested in tissue with inhomogeneous microwave absorption but a homogeneous acoustic property. The two basic acoustic generation equations in a homogeneous medium are the linear inviscid force equation

$$\rho \frac{\partial^2}{\partial t^2} \mathbf{u}(\mathbf{r},t) = -\nabla p(\mathbf{r},t) \tag{2}$$

and the expansion equation

$$\nabla \cdot \mathbf{u}(\mathbf{r},t) = -\frac{p(\mathbf{r},t)}{\rho c^2} + \beta T(\mathbf{r},t) \tag{3}$$

where β is the isobaric volume expansion coefficient, c is the sound speed, $\mathbf{u}(\mathbf{r},t)$ is the acoustic displacement and $p(\mathbf{r},t)$ is the acoustic pressure.

Combining the above three equations, the pressure $p(\mathbf{r},t)$ produced by the heat source $H(\mathbf{r},t)$ obeys the following equation

$$\nabla^2 p(\mathbf{r},t) - \frac{1}{c^2}\frac{\partial^2}{\partial t^2} p(\mathbf{r},t) = -\frac{\beta}{C_p}\frac{\partial}{\partial t} H(\mathbf{r},t). \tag{4}$$

The above equation is a typical scalar Helmholtz equation. The solutions based on Green's function can be found in the literature of physics or mathematics. A general form can be expressed as

$$p(\mathbf{r},t) = \frac{\beta}{4\pi C_p} \iiint \frac{d^3 r'}{|\mathbf{r}-\mathbf{r}'|} \left.\frac{\partial H(\mathbf{r}',t')}{\partial t'}\right|_{t'=t-\frac{|\mathbf{r}-\mathbf{r}'|}{c}}. \tag{5}$$

The heating function can be written as the product of a spatial absorption function and a temporal illumination function:

$$H(\mathbf{r},t) = A(\mathbf{r}) I(t). \tag{6}$$

Thus, $p(\mathbf{r},t)$ can be expressed as

$$p(\mathbf{r},t) = \frac{\beta}{4\pi C_p} \iiint \frac{d^3 r'}{|\mathbf{r}-\mathbf{r}'|} A(\mathbf{r}') I'(t'). \tag{7}$$

Exact reconstruction theory

We first solve the problem where the pulse pumping is a Dirac delta function as

$$I(t) = I_0 \delta(t). \tag{8}$$

Suppose the detection point on the spherical surface $\mathbf{r} = \mathbf{r}_0$, which encloses the sample (**Fig. 1**). By dropping the primes, the pressure equation may be written as

$$p(\mathbf{r}_0, t) = \eta \iiint d^3 r A(\mathbf{r}) \frac{\delta'(t - \frac{|\mathbf{r}_0 - \mathbf{r}|}{c})}{4\pi |\mathbf{r}_0 - \mathbf{r}|}, \tag{9}$$

where $\eta = \frac{\beta I_0}{C_p}$. The inverse problem is to reconstruct the absorption distribution $A(\mathbf{r})$ from a set of data $p(\mathbf{r}_0, t)$ measured at position $\mathbf{r}_0$. Taking the Fourier transform on variable t of the above equation and denoting $k = \frac{\omega}{c}$, we get

$$\widetilde{p}(\mathbf{r}_0, \omega) = -i\omega\eta \iiint d^3 r A(\mathbf{r}) \frac{\exp(ik|\mathbf{r}_0 - \mathbf{r}|)}{4\pi |\mathbf{r}_0 - \mathbf{r}|}, \tag{10}$$

where following Fourier transform pair exists:

$$\widetilde{p}(\mathbf{r}_0, \omega) = \int_{-\infty}^{+\infty} p(\mathbf{r}_0, t) \exp(i\omega t) dt, \tag{11}$$

$$p(\mathbf{r}_0, t) = \frac{1}{2\pi} \int_{-\infty}^{+\infty} \widetilde{p}(\mathbf{r}_0, \omega) \exp(-i\omega t) d\omega. \tag{12}$$

The exact inverse solution to the pressure equation (Eq. 9) can be derived on the basis of the spherical harmonic function:

$$\boxed{A(\mathbf{r}) = \frac{1}{4\pi^2 \eta c} \iint_{\Omega_0} d\Omega_0 \int_{-\infty}^{+\infty} dk \widetilde{p}(\mathbf{r}_0, \omega) \sum_{m=0}^{\infty} \frac{(2m+1) j_m(kr)}{h_m^{(1)}(kr_0)} P_m(\mathbf{n} \cdot \mathbf{n}_0),} \tag{13}$$

where $\mathbf{n} = \mathbf{r}/r$, $\mathbf{n}_0 = \mathbf{r}_0 / r_0$, $j_l(\cdot)$ and $h_l^{(1)}(\cdot)$ are the spherical Bessel and Hankel functions, respectively; $P_l()$ represents Legendre polynomial. This inverse solution involves summation of a series and may take much time to compute. Therefore, it is desirable to further simplify the solution.

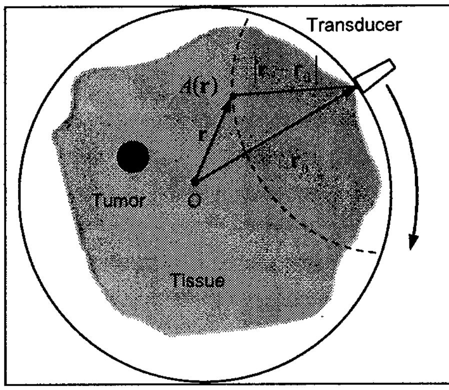

Fig. 1. Acoustic detection scheme. The ultrasonic transducer at position $\mathbf{r}_0$ records the thermoacoustic signals on a spherical surface with radius $|\mathbf{r} - \mathbf{r}_0|$.

Modified backprojection

In the experiments, the detection radius r_0 is much larger than the wavelengths of the thermoacoustic waves that are useful for imaging. Because the low-frequency components of the thermoacoustic signal do not significantly contribute to the spatial resolution, they can be removed by a filter. Therefore, we can assume $|k|r_0 >> 1$ and use the asymptotic form of the Hankel function to simplify the above exact inverse solution. The following two identities are involved:

$$\frac{\exp(-ik|\mathbf{r}_0 - \mathbf{r}|)}{4\pi|\mathbf{r}_0 - \mathbf{r}|} = \frac{-ik}{4\pi}\sum_{m=0}^{\infty}(2m+1)j_m(kr)h_m^{(2)}(kr_0)P_m(\mathbf{n}\cdot\mathbf{n}_0)\,; \tag{14}$$

When $|k|r_0 >> 1$,

$$h_m^{(1)}(kr_0) \approx \frac{1}{h_m^{(2)}(kr_0)}\left(\frac{1}{(kr_0)^2} + O\left(\frac{1}{(kr_0)^4}\right)\right), \tag{15}$$

where $h_l^{(2)}(\cdot)$ is the spherical Hankel function of the second kind. After some mathematical operations, the approximate inverse solution becomes

$$A(\mathbf{r}) = -\frac{r_0^2}{2\pi\eta c^3}\iint_{\Omega_0} d\Omega_0 \frac{1}{|\mathbf{r}_0 - \mathbf{r}|}\left.\frac{\partial p(\mathbf{r}_0, t)}{\partial t}\right|_{t=\frac{|\mathbf{r}_0 - \mathbf{r}|}{c}} \tag{16}$$

i.e.,

$$\boxed{A(\mathbf{r}) = -\frac{r_0^2}{2\pi\eta c^4}\iint_{\Omega_0} d\Omega_0 \frac{1}{t}\left.\frac{\partial p(\mathbf{r}_0, t)}{\partial t}\right|_{t=\frac{|\mathbf{r}_0 - \mathbf{r}|}{c}}\,.} \tag{17}$$

The above equation shows that the absorption distribution can be calculated by means of backprojection of the quantity $-\frac{1}{t}\left.\frac{\partial p(\mathbf{r}_0, t)}{\partial t}\right|_{t=\frac{|\mathbf{r}_0 - \mathbf{r}|}{c}}$ instead of the acoustic pressure itself. This approximate algorithm involves less computing time than the exact inverse solution.

For initial investigations, we reconstruct individual cross sections of samples. In these cases, the backprojection is carried out in a circle around the cross sections, and the approximate inverse solution can be simplified as

$$A(\mathbf{r}) = -\frac{r_0^2}{\pi\eta c^4}\int_{\varphi_0} d\varphi_0 \frac{1}{t}\left.\frac{\partial p(\mathbf{r}_0, t)}{\partial t}\right|_{t=\frac{|\mathbf{r}_0 - \mathbf{r}|}{c}}\,. \tag{18}$$

Experimental method of thermoacoustic tomography

Experimental setup

Fig. 2 shows the experimental setup. A plexiglass container is filled with mineral oil. A rotation stage and an unfocused ultrasonic transducer are immersed inside it in the same *x-y* plane. The slice sample can be put in the rotation stage horizontally. The transducer points horizontally to the rotation center and detects the acoustic signal from the sample. A step motor directly drives the rotation stage while the transducer is fixed. Obviously, this is equivalent to having a transducer rotationally scanning the sample. The transducer (V323, Panametrics) has a central frequency of 2.25 MHz and a diameter of 6 mm.

The microwave pulses are transmitted from a 3-GHz microwave generator with a energy of 10 mJ/pulse and a pulse width of 0.5 μs. A function generator (Protek, B-180) is used to trigger the microwave generator, control its pulse repetition frequency, and synchronize the oscilloscope sampling. Microwave energy is delivered to the sample from below by a rectangular waveguide with a cross section of 72 mm × 34 mm.

A personal computer is used to control the step motor in rotating the sample. The signal from the transducer is first amplified through a pulse amplifier, then recorded and averaged 200 times by an oscilloscope (TDS640A, Tektronix), and finally transferred to a personal computer for imaging.

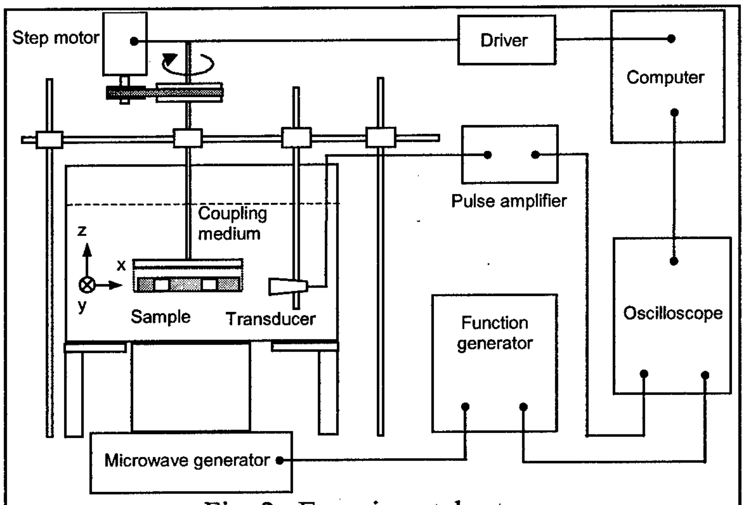

Fig. 2. Experimental setup.

Lastly, we want to point out that, in our experiments, the distance r_0 between the rotation center and the surface of the transducer is 4.3 cm. In the frequency domain (60 KHz–1.8 MHz), $|k|r_0 = 2\pi r_0 f / c$ with 1.5 mm/μs, we get $10 < |k|r_0 < 330$. Therefore, the required condition $|k|r_0 >> 1$ for the modified backprojection algorithm is satisfied.

Technical consideration

The ultrasonic transducer is not a real point detector. For simplicity, we can ignore its size if we put it far away from the sample. However, we still have to consider the impulse response $R(t)$ of the transducer and the pumping duration $I(t)$ of the microwave pulse. In general, the measured piezoelectric signal can be written as a convolution:

$$S(\mathbf{r}_0,t) = p(\mathbf{r}_0,t) * I(t) * R(t), \tag{19}$$

where $p(\mathbf{r}_0,t)$ is the thermoacoustic signal with delta-pulse microwave pumping. In the frequency domain, the above equation can be written as

$$S(\mathbf{r}_0,\omega) = p(\mathbf{r}_0,\omega) I(\omega) R(\omega), \tag{20}$$

where

$$I(\omega) = \int_{-\infty}^{+\infty} I(t)\exp(i\omega t)dt, \tag{21}$$

$$R(\omega) = \int_{-\infty}^{+\infty} R(t)\exp(i\omega t)dt. \tag{22}$$

Therefore, $\frac{\partial p(\mathbf{r}_0,t)}{\partial t}$ can be calculated by an inverse Fourier transformation,

$$\begin{aligned}\frac{\partial p(\mathbf{r}_0,t)}{\partial t} &= \mathrm{FFT}^{-1}\left\{\frac{-i\omega S(\mathbf{r}_0,\omega)}{I(\omega)R(\omega)}F(\omega)\right\} \\ &= \frac{1}{2\pi}\int_{-\infty}^{+\infty}\frac{-i\omega S(\mathbf{r}_0,\omega)}{I(\omega)R(\omega)}F(\omega)\exp(-i\omega t)dt\end{aligned}, \tag{23}$$

where $F(\omega)$ is a wide band-pass filter, which is used to eliminate the noise at high frequencies as well as the low frequency component to guarantee the condition $|k|r_0 >> 1$ for the modified backprojection.

In our experiments, $I(t)$ is approximately a rectangular function with duration $\tau = 0.5\ \mu\text{s}$. The ultrasonic transducer is of the videoscan type with a central frequency $f_0 = 2.25$ MHz. The generated thermoacoustic signal mainly exists in a frequency range below 1.8 MHz. Therefore, a band-pass filter $F(\omega)$ may be employed in data processing, which lets only the signal in the range between 60 KHz and 1.8 MHz pass through.

Results and discussion of thermoacoustic tomography

Image contrast

Image contrast is an important index for biological imaging. **Fig.** 3(a) shows a tested sample, which was photographed after the experiment. The sample was made according to the following procedure. First, we cut a thin piece of homogeneous pork fat tissue and shaped it arbitrarily to form a base. Its thickness is 5 mm and its maximum diameter is 4 cm. Then we used different screwdrivers to carefully make two pairs of holes that were approximately 4 mm and 6 mm in diameter, respectively. Finally, one big and one small hole on the left side was filled with pork muscle, while the big and small hole on the right side were filled with pork fat of the same type as that which made up the base.

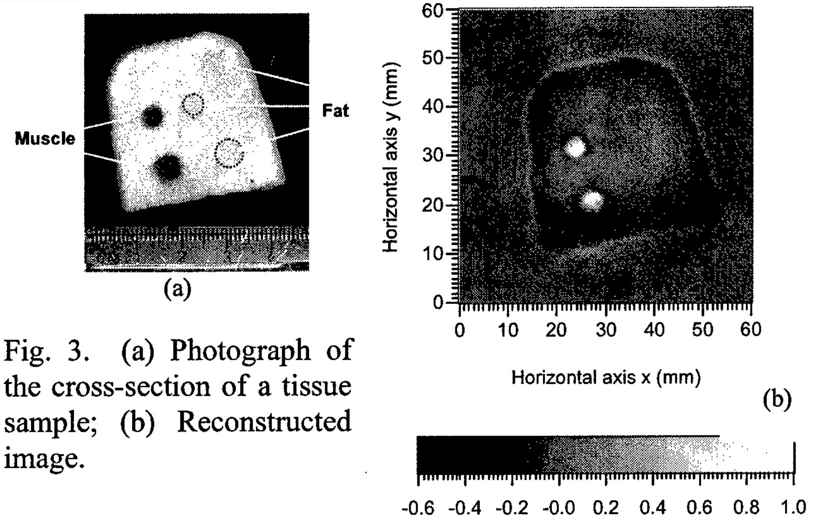

Fig. 3. (a) Photograph of the cross-section of a tissue sample; (b) Reconstructed image.

In the experiment, the transducer rotationally scanned the sample from 0 to 360 degrees with a step size of 2.25 degrees. We used the 160 series of data to calculate the image by our modified backprojection method.

The reconstructed image is shown in Fig. 3(b). The outline and size of the fat base as well as the sizes and locations of the two muscle pieces are in good agreement with the original sample in Fig. 3(a). The high contrast is due to the low microwave absorption capacity of fat and the high absorption capacity of muscle: at 3 GHz, the penetration depth for muscle and fat are 1.2 cm and 9 cm, respectively. The two pieces of fat are not visible in the image Fig. 3(b), which means the minute mechanical discontinuity between the boundaries of muscle and fat does not contribute much to the thermoacoustic signal. On the contrary, the discontinuity improves the strength of the echo sounds in pure-ultrasound imaging.

Spatial resolution

Spatial resolution is another important index for biological imaging. We used samples with a set of small thermoacoustic sources to test the resolution. One tested sample is shown in **Fig. 4**(a), which was also photographed after the experiment was completed.

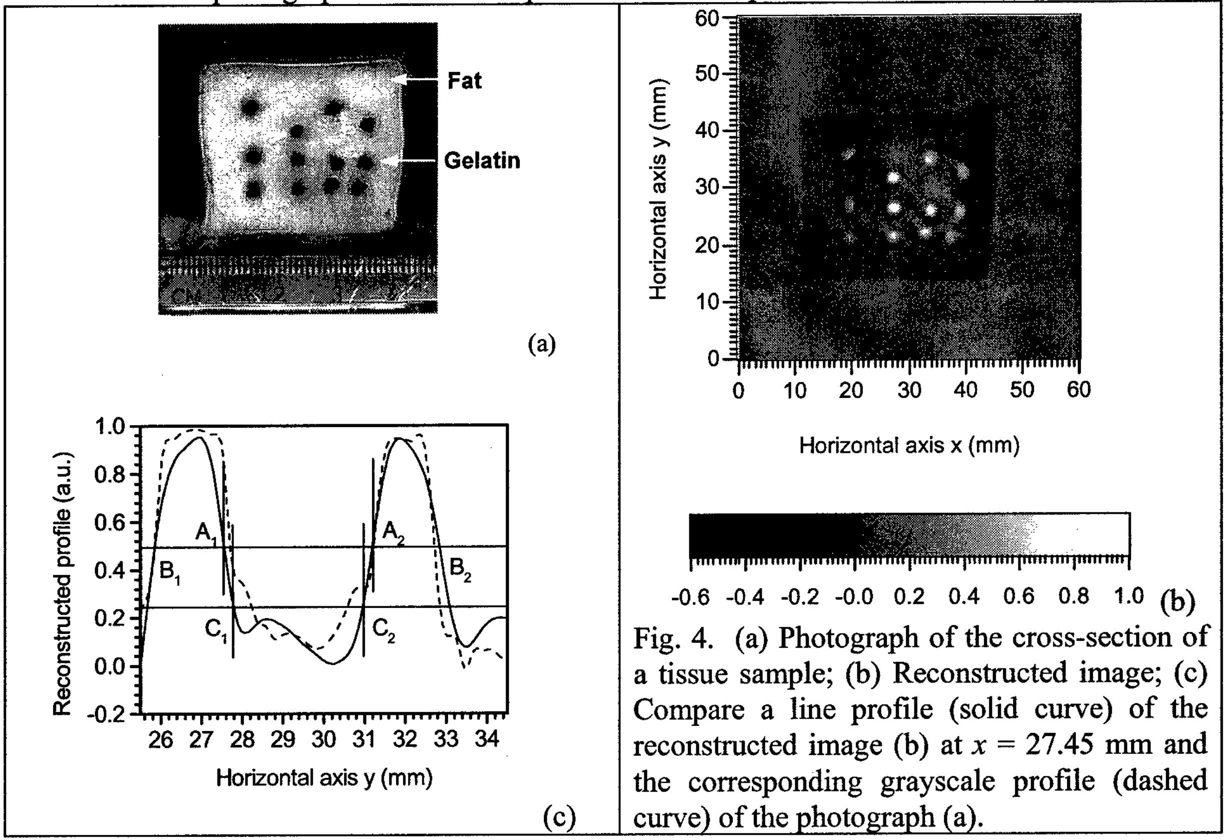

Fig. 4. (a) Photograph of the cross-section of a tissue sample; (b) Reconstructed image; (c) Compare a line profile (solid curve) of the reconstructed image (b) at x = 27.45 mm and the corresponding grayscale profile (dashed curve) of the photograph (a).

The sample was made according to the following procedure. First, we cut a thin piece of homogeneous pork fat tissue and made it into an arbitrary shape. Its thickness was 5 mm with a maximum diameter of 4 cm. Then we used a small screwdriver to carefully make a set of small holes about 2 mm in diameter. In the meantime, we prepared a hot solution with 5% gelatin, 0.8% salt and a drop of dark ink (to improve the photographic properties of the sample). Next, we used an injector to inject a drop of the gelatin solution into each small hole and subsequently blew out the air to make good coupling between the gelatin solution and the fat tissue. After being cooled in room temperature for about 15 minutes, the gelatin solution was solidified.

During the experiment, the transducer also rotationally scanned the sample from 0 to 360 degrees with a step size of 2.25 degrees.

The reconstructed image produced by our modified backprojection method is shown in Fig. 4(b), which agrees with the original sample very well. In particular, the relative locations and sizes of those small thermoacoustic sources are clearly resolved and perfectly match the original ones. Fig. 4(c) shows a reconstructed profile (solid curve) at position $x = 27.45$ mm of the image Fig. 4(b), which includes two gelatin sources with a distance of about 3 mm. Each gelatin source has a distinct profile in the image. The boundaries between them are clearly imaged. Moreover, the reconstructed profile is in good agreement with the original profile (dashed curve), which was a grayscale profile of the image Fig. 4(b). The half-amplitude line cuts across the reconstructed profile at points B_1, A_1, A_2 and B_2, respectively. The distances $|A_1B_1| = 1.72\,\text{mm}$ and $|A_2B_2| = 1.67\,\text{mm}$ in the image are close to the original values of about 1.80 mm and 1.60 mm, respectively, which were measured in the original objects. Therefore, the width of the profile at the half-amplitude closely measures its physical size.

We here define a resolving criterion for estimating spatial resolution. The quarter-amplitude line cuts across the profiles at points C_1 and C_2, respectively, as shown in Fig. 4(c). If the right source moves to the position of the left one, the reconstructed profile is equal to the spatial summation of the profiles of the two sources, because of the linear superposition property of acoustic waves. When point C_2 encounters C_1, the new amplitude at C_2 or C_1 reaches half amplitude, and the two sources can still be differentiated. If the right one moves more to the left, the new amplitude between their overlap regions goes up more than half amplitude. When we use a half-amplitude line to cut across the profiles, we get only two points on the far side of each profile, which means that these two sources can no longer be clearly distinguished. Further, when point A_1 touches A_2, these two sources join as an object.

Therefore, the minimum distance that can be differentiated is approximately equal to the summation of the horizontal distance between point A_1 and C_1 and the horizontal distance between point A_2 and C_2. We have checked additional pairs of sources resembling those in the image of Fig. 4(b), and found that this minimum distance is less than 0.5 mm. We can, therefore, claim the spatial resolution in our experiments reaches less than 0.5 mm, which agrees with the theoretical spatial resolution limit for 1.8 MHz signals whose half wavelength is ~0.5 mm with the sound speed of 1.5 mm/μs.

We further quantified the line-spread function (LSF) of the imaging system. A metal wire with a diameter of 0.2 mm was buried in pork fat and then imaged by our imaging system with a scan radius of 75 mm. The thermoacoustic image of the embedded wire is shown in **Fig. 5**(a). Fig. 5(b) shows the profile of the LSF across the wire, where the ringing is caused primarily by the limited bandwidth of the detected signals. The full width at half maximum (FWHM) of the LSF is 0.5 mm. In analogy to the Rayleigh criterion, an alternative definition of spatial resolution is the horizonal displacement between the maximum and the first minimum of the LSF, which is 0.55 mm [Fig. 5(b)]. The superposition of two LSFs that are 0.55 mm apart is shown in Fig. 7(c), in which two represented wires can be clearly distinguished. Because the wire has a 0.2-mm diameter, the actual resolution is as fine as 0.35 mm, which agrees with the theoretical limit for 2-MHz thermoacoustic signals whose half wavelength is 0.38 mm in soft biological tissues.

Of course, the detecting transducer has a finite physical size. If it is close to the thermoacoustic sources, it cannot be approximated as a point detector. Its size will blur the images and decrease the spatial resolution. Therefore, in experiments, the transducer must be placed some distance away from the tissue samples. In general, due to the finite size of the transducer, the farther away the transducer is from the detection center, the better the resolution at the expense of the signal.

Other factors limiting spatial resolution are the duration of the microwave pulse and the impulse response of the transducer. In general, using a shorter microwave pulse will produce more high-frequency components in the thermoacoustic signals. Selection of the duration of the pulse is dependent on the experimental conditions and measurement systems.

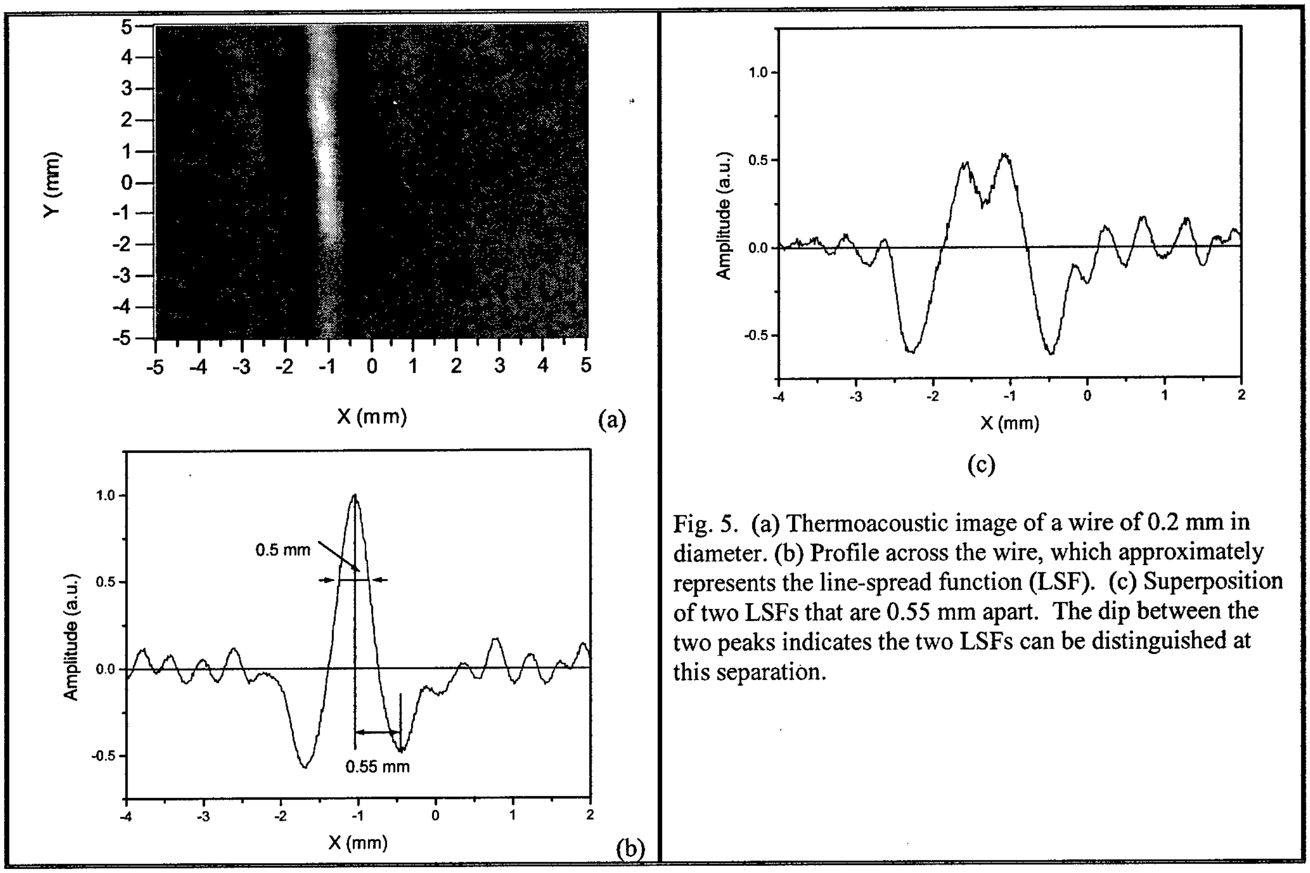

Fig. 5. (a) Thermoacoustic image of a wire of 0.2 mm in diameter. (b) Profile across the wire, which approximately represents the line-spread function (LSF). (c) Superposition of two LSFs that are 0.55 mm apart. The dip between the two peaks indicates the two LSFs can be distinguished at this separation.

Images of thick samples

The diagram and the photograph of a thick sample are shown in **Fig. 6**(a) and (b), respectively. The reconstructed image produced by our modified backprojection method is shown in Fig. 6(c), which agrees with the original sample very well. The relative locations and sizes of those thermoacoustic sources perfectly match the buried objects in the original sample.

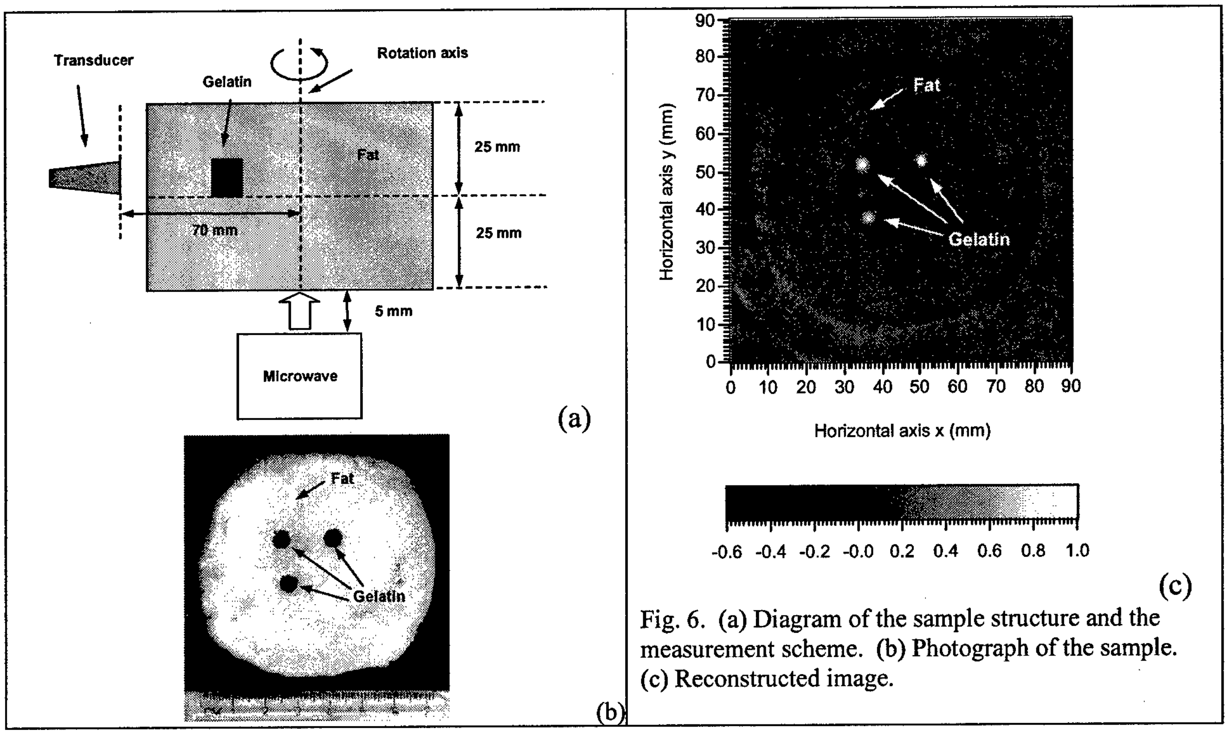

Fig. 6. (a) Diagram of the sample structure and the measurement scheme. (b) Photograph of the sample. (c) Reconstructed image.

Imaging of excised breast (mastectomy) tissues

Several excised breast (mastectomy) specimens were imaged at the University of Texas M.D. Anderson Cancer Center using our thermoacoustic imaging system. A mammogram obtained before the mastectomy surgery of the breast is shown in **Fig.** 7(a). After the surgery performed by Dr. Hunt, the excised specimen was placed in a plastic cylindrical container with a diameter of 10 cm; and it was then imaged by three imaging modalities. The nipple of the specimen faced the bottom of the container to simulate the proposed *in vivo* configuration. The thickness of the specimen in the container was ~6 cm. The container had minimal effect on the transmission of RF, ultrasound, and x-ray. Another radiograph of the specimen was taken from the top of the cylindrical container [Fig. 7(b)]. The contrast of the lesion in Fig. 10(b) was lower than that shown in Fig. 10(a) because the specimen was quite thick in the container. A conventional B-mode gray-scale sonogram of the specimen [Fig. 7(c)] was taken by Dr. Fornage using a real-time scanner (HDI 5000, Philips-ATL, Bothell, WA) equipped with a 5–12 MHz broadband linear array electronic transducer. The lesion was located ~2 cm above the bottom of the container. The specimen was also imaged in the slice 2 cm above the bottom of the container using our thermoacoustic imaging system [Fig. 7(d)]. A circular scan was carried out by a cylindrically focused ultrasound detector (2.25 MHz center frequency and 0.9 mm diameter) with a step size of 2-1/4 degrees. The scan radius was 7.5 cm. The reconstructed image was computed by the backprojection method. The tumor was marked by a red circle. After these imaging experiments, the specimen was rendered to the Department of Pathology for histopathological diagnosis. This lesion was diagnosed as invasive lobular carcinoma with a size of ~1.5 cm.

The yellow rectangle in Fig. 7(d) marks the wave-guide aperture. The wave-guide for this experiment was not large enough to cover the entire specimen. Since then, we have upgraded our system with a larger wave-guide to overcome this problem. More experiments on mastectomy specimens using the improved imaging system have yet to be done.

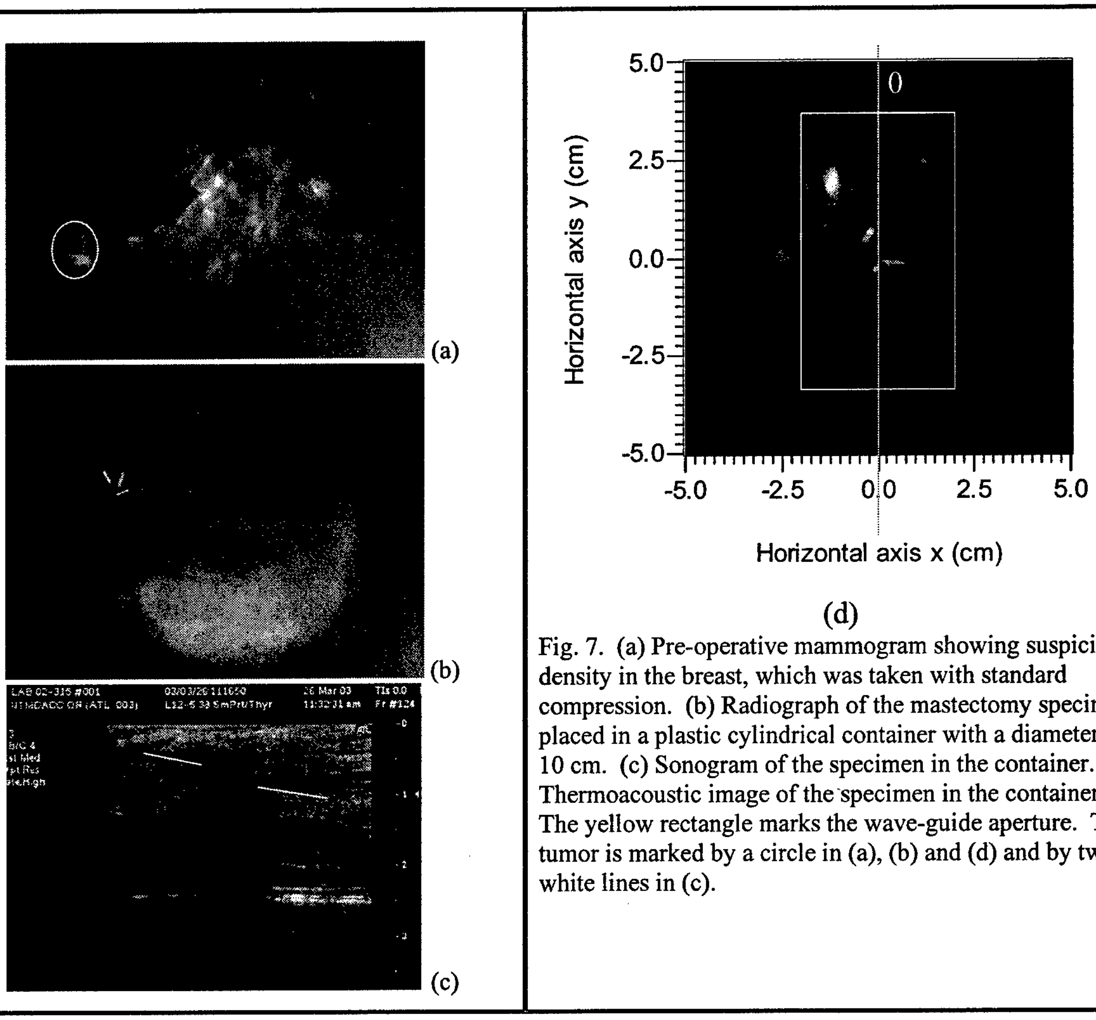

(d)

Fig. 7. (a) Pre-operative mammogram showing suspicious density in the breast, which was taken with standard compression. (b) Radiograph of the mastectomy specimen placed in a plastic cylindrical container with a diameter of 10 cm. (c) Sonogram of the specimen in the container. (d) Thermoacoustic image of the specimen in the container. The yellow rectangle marks the wave-guide aperture. The tumor is marked by a circle in (a), (b) and (d) and by two white lines in (c).

Statement of Work

Task 1: Setting up the scanning microwave-induced-acoustic tomography (SMIAT) instrument, Months 1–12:

a. Modify/connect the microwave generator and the ultrasonic scanner.
b. Image biological tissues in vitro with SMIAT.

Task 2. Extensive evaluation and optimization of the SMIAT setup, Months 13-36:

a. Simulate microwave-induced-acoustic signals to provide guidance on the experiments.

b. Optimize the ultrasonic and microwave parameters for good resolution and signal-to-noise ratio.
c. Quantify the maximum imaging depth with SMIAT.
d. Image biological tissues in vitro with SMIAT and quantify the imaging resolution.
e. Image biological tissues in vitro with SMIAT and ultrasonography and quantify the contrast improvement of SMIAT over ultrasonography.
f. Co-register the SMIAT images with the conventional ultrasonograms.

Both tasks have been successfully accomplished. We went beyond the original planned task by imaging mastectomy specimens at M.D. Anderson Cancer Center.

Key Research Accomplishments

We have accomplished the following during the past year:

- A reshaping filter was applied to the temporal piezoelectric signals from the transducer to increase the weight of the high-frequency components, which improved the lateral resolution, and to broaden the spectrum of the signal, which enhanced the axial resolution.
- Microwave-induced thermoacoustic tomography of inhomogeneous tissues was implemented using multi-sector scanning. We solved the problem of blind surfaces using this approach.
- We have applied the synthetic-aperture method to linear-scanning microwave-induced thermoacoustic tomography in biological tissues for the first time.
- A backprojection algorithm based on rigorous theory was derived and was used to reconstruct the cross-sectional image from the thermoacoustic measurements in a circular configuration. The results demonstrate the possibility of application in detecting small tumors buried in biological tissues using microwave absorption contrast and ultrasound spatial resolution.
- An exact and an approximate time-domain reconstruction algorithm for thermoacoustic tomography in a spherical geometry were derived and published.
- An exact frequency-domain reconstruction algorithm for thermoacoustic tomography in a planar geometry was derived and published.
- An exact frequency-domain reconstruction algorithm for thermoacoustic tomography in a cylindrical geometry was derived and published.
- High-resolution and high-contrast images were obtained and published.
- Further progress in the reconstruction algorithms was made and published.
- Better understanding of the mechanism of spatial resolution was achieved and published.
- Better understanding of the effect of heterogeneity on the images was achieved and published.
- Extension of the technology to other electromagnetic sources was achieved and published.
- Imaging of mastectomy specimens at M.D. Anderson Cancer Center in Houston was tested.

Reportable Outcomes

Peer-reviewed journal articles

1. Y. Xu and L.-H. Wang, "Signal processing in scanning thermoacoustic tomography in biological tissues," Medical Physics 28 (7), 1519–1524 (2001).

2. M. Xu, G. Ku, and L.-H. Wang, "Microwave-induced thermoacoustic tomography using multi-sector scanning," Medical Physics 28 (9), 1958–1963 (2001).

3. D. Feng, Y. Xu, G. Ku, and L.-H. Wang, "Microwave-induced thermoacoustic tomography: reconstruction by synthetic aperture," Medical Physics 28 (12), 2427–2431 (2001).

4. M. Xu and L.-H. Wang, "Time-domain reconstruction for thermoacoustic tomography in a spherical geometry," IEEE Transactions on Medical Imaging 21 (7), 814–822 (July 2002).

5. Y. Xu, D. Feng, and L.-H. Wang, "Exact frequency-domain reconstruction for thermoacoustic tomography—I: Planar geometry," IEEE Transactions on Medical Imaging 21 (7), 823–828 (July 2002).

6. Y. Xu, M. Xu, and L.-H. Wang, "Exact frequency-domain reconstruction for thermoacoustic tomography—II: Cylindrical geometry," IEEE Transactions on Medical Imaging 21 (7), 829–833 (July 2002).

7. M. Xu and L.-H. Wang, "Pulsed-microwave-induced thermoacoustic tomography: Filtered backprojection in a circular measurement configuration," Medical Physics 29 (8), 1661–1669 (August 2002).

8. X. Wang, Y. Xu, M. Xu, S. Yokoo, E. S. Fry, and L.-H. Wang "Photoacoustic tomography of biological tissues with high cross-section resolution: Reconstruction and experiment," Medical Physics 29 (12), 2799–2805 (December 2002).

9. M. Xu and L.-H. Wang, "Analytic explanation of spatial resolution related to bandwidth and detector aperture size in thermoacoustic or photoacoustic reconstruction," Physical Review E 67 (5), 056605, 1–15 (May 2003).

10. M. Xu, Y. Xu, and L.-H. Wang, "Time-domain reconstruction algorithms and numerical simulations for thermoacoustic tomography in various geometries," IEEE Transactions on Biomedical Engineering 50 (9): 1086–1099 (September 2003).

11. Y. Xu and L.-H. Wang, "Effects of acoustic heterogeneity on thermoacoustic tomography in the breast," IEEE Transactions on Ultrasonics Ferroelectrics and Frequency Control 50 (9), 1134–1146 (September 2003).

12. Y. Xu and L.-H. Wang, "Time reversal and its application to tomography with diffracting sources," Physical Review Letters 92 (3), 033902 (Jan. 23, 2004).

13. X. Wang, G. Ku, M. A. Wegiel, D. J. Bornhop, G. Stoica, and L.-H. Wang, "Noninvasive photoacoustic angiography of animal brains in vivo with NIR light and an optical contrast agent," Optics Letters 29 (7), 730–732 (Apr. 1, 2004).

14. Y. Xu, P. Kuchment, and L.-H. Wang, "Limited-view thermoacoustic tomography and reconstruction by truncated conjugate gradient," Medical Physics 31 (4), 724–733 (Apr. 2004).

Invited talks given by the PI

1. International Photonics Conference, Hsinchu, Taiwan.
2. Department of Bioengineering, University of Toledo, Toledo, Ohio.
3. Institute of Laser Life Science, South China Normal University, Guangzhou, China.
4. National Laboratory of Biomedical Photonics, Huazhong University of Science and Technology, Wuhan, China.
5. Department of Biomedical Engineering, Shanghai Jiaotong University, Shanghai, China.
6. School of Physical Sciences, University of Kent at Canterbury, UK.
7. Gordon Research Conference on Photoacoustic and Photothermal Phenomena, Oxford, UK.
8. Department of Medical Physics and Bioengineering, University College London, London, UK.
9. Department of Physics, University of Texas at San Antonio, Texas.
10. Saratov Fall Meeting 2001—Workshop on Optical Technologies in Biophysics & Medicine, Saratov, Russia.
11. Department of Physics, Texas A&M University, Texas.
12. Program of Bioengineering, University of Houston, Houston, Texas.
13. DOE/NIH Workshop on Applications of Thermography in Medical Diagnosis and Treatment, Bethesda, Maryland.

14. Lawrence Livermore National Laboratory, Livermore, California.

15. Laser Diagnostic Technologies, Inc., San Diego, California.

16. STARTech Early Ventures, Richardson, Texas.

17. Photonify Technologies Inc., Fremont, California.

18. Workshop on Microwave Photonics for Medical Imaging, International Microwave Symposium, Seattle, Washington.

19. Center for Industrial and Medical Ultrasound, University of Washington, Seattle, Washington.

20. Department of Chemistry, University of California, Davis, California.

21. International Quantum Electronics Conference (IQEC) and the Conference on Lasers, Applications, and Technologies (LAT), Presidium Building of the Russian Academy of Sciences (RAS), Moscow, Russia.

22. ESPCI, Paris, France.

23. Clinical Center, NIH, Bethesda, Maryland.

24. Dept. of Biological Engineering, Univ. of Missouri, Columbia, Missouri.

25. Dept. of Radiology, Univ. Chicago, Chicago, IL.

26. Dept. of Bioengineering, Univ. of Illinois at Chicago, Chicago, IL.

27. Annual Ultrasonic Transducer Conference, Univ. of Southern California, Los Angeles, CA.

28. 3rd Int'l Conf. on Photonics and Imaging in Biology and Medicine, Wuhan, China. Plenary.

29. 6th Int'l Conf. on Correlation Optics, Chernivtsi, Ukraine. Plenary.

30. Int'l Conf. on Adv. Laser Tech., Cranfield, UK. Plenary keynote. Expenses covered by host.

31. School of Electrical and Electronic Engineering, University of Nottingham, UK.

32. Institute of Cancer Research and Royal Marsden NHS Trust, Surrey, UK.

33. Saratov Fall Meeting on Optical Technologies in Biophysics & Medicine, Russia.

34. Frontiers in Optics, OSA Annual Meeting, Tucson, Arizona.

35. Dept. of Bioengineering, Rice Univ., Houston, Texas.

36. 146th Meeting of the Acoustical Society of America, Austin, Texas.

37. Conference on Lasers and Electro-Optics (CLEO), Taipei, Taiwan.

38. Departments of Nuclear Medicine and Experimental Diagnostic Imaging. Univ. of Texas M.D. Anderson Cancer Center, Houston, Texas.

39. University of Michigan, Ann Arbor, Michigan.

40. SPIE Int'l Symposium on Medical Imaging, San Diego, California.

41. NSF Center for Biophotonics Science and Technology sponsored Photonics-oriented Symposium, San Antonio, Texas.

42. Britton Chance's Laboratory, Univ. of Pennsylvania, Philadelphia, Pennsylvania.

43. Annual Ultrasonic Transducer Conference, NIH Resource on Medical Ultrasonic Transducer Technology, Univ. of Southern California, Los Angeles, California.

44. OSA Biomedical Optical Spectroscopy and Diagnostics and Advances in Optical Imaging and Photon Migration, Miami, Florida.

45. IEEE International Symposium on Biomedical Imaging, Washington, DC.

46. Grand Rounds, Dept. of Neurosurgery, University of California, San Francisco, California.

47. Boston Scientific Corp., Fremont, California.

48. Dept. of Physics, East Carolina University, Greenville, North Carolina.

49. Annual Meeting of the AIUM, Phoenix, Arizona.

50. IEEE EMBS Annual Conf., San Francisco, California.

51. Dept. of Biomedical Engineering, Washington University, St. Louis, Missouri.

52. Third Annual Meeting of The Society for Molecular Imaging, St. Louis, Missouri.

53. Saratov Fall Meeting on Optical Technologies in Biophysics & Medicine, Russia.

54. Optical Diagnostic Imaging from Bench to Bedside at the NIH, Bethesda, MD.

Degrees

1. D. Feng, Biomedical Eng., Texas A&M University (2001).
2. Y. Xu, Biomedical Eng., Texas A&M University (2003).
3. S. Jiao, Biomedical Eng., Texas A&M University (2003).
4. M. Xu, Biomedical Eng., Texas A&M University (2004).

Conclusions

The combination of ultrasound and microwave has provided us a unique opportunity for early-cancer imaging with high resolution and high contrast. We have made significant technical progress in thermoacoustic imaging including data acquisition and imaging reconstruction. Specifically, our accomplishments include (1) an exact and an approximate time-domain reconstruction algorithm for thermoacoustic tomography in a spherical geometry was derived and published, (2) an exact frequency-domain reconstruction algorithm for thermoacoustic tomography in a planar geometry was derived and published, (3) an exact frequency-domain reconstruction algorithm for thermoacoustic tomography in a cylindrical geometry was derived and published, and (4) high-resolution and high-contrast images were obtained and published. The reconstruction is an inverse source problem similar to that in PET (positron emission tomography); however, the reconstruction in PET is based on geometric optics whereas the reconstruction in thermoacoustic imaging is based on diffractive/wave optics. We have successfully imaged biological tissue with high resolution and high contrast. We have made further progress in the reconstruction algorithms (MP Aug. 2002 and IEEE-TBE 2003), in the mechanism of spatial resolution (PR 2003), in the understanding of heterogeneity (IEEE-UFFC 2003), and in extending the technology to other electromagnetic sources (MP Dec. 2002). We went beyond the original planned task by imaging mastectomy specimens at M.D. Anderson Cancer Center.

Appendices (112 pages)

1. [6 pages] Y. Xu and L.-H. Wang, "Signal processing in scanning thermoacoustic tomography in biological tissues," Medical Physics 28 (7), 1519–1524 (2001).
2. [6 pages] M. Xu, G. Ku, and L.-H. Wang, "Microwave-induced thermoacoustic tomography using multi-sector scanning," Medical Physics 28 (9), 1958–1963 (2001).
3. [5 pages] D. Feng, Y. Xu, G. Ku, and L.-H. Wang, "Microwave-induced thermoacoustic tomography: reconstruction by synthetic aperture," Medical Physics 28 (12), 2427–2431 (2001).

4. [9 pages] M. Xu and L.-H. Wang, "Time-domain reconstruction for thermoacoustic tomography in a spherical geometry," IEEE Transactions on Medical Imaging 21 (7), 814–822 (July 2002).

5. [6 pages] Y. Xu, D. Feng, and L.-H. Wang, "Exact frequency-domain reconstruction for thermoacoustic tomography—I: Planar geometry," IEEE Transactions on Medical Imaging 21 (7), 823–828 (July 2002).

6. [5 pages] Y. Xu, M. Xu, and L.-H. Wang, "Exact frequency-domain reconstruction for thermoacoustic tomography—II: Cylindrical geometry," IEEE Transactions on Medical Imaging 21 (7), 829–833 (July 2002).

7. [9 pages] M. Xu and L.-H. Wang, "Pulsed-microwave-induced thermoacoustic tomography: Filtered backprojection in a circular measurement configuration," Medical Physics 29 (8), 1661–1669 (August 2002).

8. [7 pages] X. Wang, Y. Xu, M. Xu, S. Yokoo, E. S. Fry, and L.-H. Wang "Photoacoustic tomography of biological tissues with high cross-section resolution: Reconstruction and experiment," Medical Physics 29 (12), 2799–2805 (December 2002).

9. [15 pages] M. Xu and L.-H. Wang, "Analytic explanation of spatial resolution related to bandwidth and detector aperture size in thermoacoustic or photoacoustic reconstruction," Physical Review E 67 (5), 056605, 1–15 (May 2003).

10. [14 pages] M. Xu, Y. Xu, and L.-H. Wang, "Time-domain reconstruction algorithms and numerical simulations for thermoacoustic tomography in various geometries," IEEE Transactions on Biomedical Engineering 50 (9): 1086–1099 (September 2003).

11. [13 pages] Y. Xu and L.-H. Wang, "Effects of acoustic heterogeneity on thermoacoustic tomography in the breast," IEEE Transactions on Ultrasonics Ferroelectrics and Frequency Control 50 (9), 1134–1146 (September 2003).

12. [4 pages] Y. Xu and L.-H. Wang, "Time reversal and its application to tomography with diffracting sources," Physical Review Letters 92 (3), 033902 (Jan. 23, 2004).

13. [3 pages] X. Wang, G. Ku, M. A. Wegiel, D. J. Bornhop, G. Stoica, and L.-H. Wang, "Non-invasive photoacoustic angiography of animal brains in vivo with NIR light and an optical contrast agent," Optics Letters 29 (7), 730–732 (Apr. 1, 2004).

14. [10 pages] Y. Xu, P. Kuchment, and L.-H. Wang, "Limited-view thermoacoustic tomography and reconstruction by truncated conjugate gradient," Medical Physics 31 (4), 724–733 (Apr. 2004).

Signal processing in scanning thermoacoustic tomography in biological tissues

Yuan Xu and Lihong V. Wang[a)]
Optical Imaging Laboratory, Biomedical Engineering Program, Texas A&M University, 3120 TAMU, College Station, Texas 77843-3120

(Received 12 December 2000; accepted for publication 27 March 2001)

Microwave-induced thermoacoustic tomography was explored to image biological tissues. Short microwave pulses irradiated tissues to generate acoustic waves by thermoelastic expansion. The microwave-induced thermoacoustic waves were detected with a focused ultrasonic transducer to obtain two-dimensional tomographic images of biological tissues. The dependence of the axial and the lateral resolutions on the spectra of the signals was studied. A reshaping filter was applied to the temporal piezoelectric signals from the transducer to increase the weight of the high-frequency components, which improved the lateral resolution, and to broaden the spectrum of the signal, which enhanced the axial resolution. A numerical simulation validated our signal-processing approach. © *2001 American Association of Physicists in Medicine.* [DOI: 10.1118/1.1380436]

Key words: microwave, ultrasonics, thermoacoustics, tomography, resolution, filter

I. INTRODUCTION

When electromagnetic radiation is absorbed in biological tissues, the heating and the subsequent expansion will cause emission of acoustic signals, which is called the thermoacoustic effect. In thermoacoustic tomography, the thermoacoustic signals from a tissue sample are collected to map the distribution of the radiative absorption within the sample. The radiative absorption is closely related to the physiological and pathological status of the tissue: for example, cancerous breast tissues are 2–5 times more strongly absorbing to microwaves than surrounding normal breast tissues, which has been attributed to an increase in bound water and sodium within malignant cells.[1–3]

Thermoacoustic tomography combines good imaging resolution with good imaging contrast. Purely microwave imaging has the advantage of good imaging contrast but suffers from poor spatial resolution due to the large wavelength of microwaves.[4–7] On the other hand, purely ultrasonic imaging has good spatial resolution but poor contrast. Thermoacoustic tomography can bridge the gap between them.

There are various types of thermoacoustic tomography, such as photoacoustic tomography and microwave-induced thermoacoustic tomography (MITT). In photoacoustic tomography,[8–11] due to the use of short laser pulses—several nanoseconds in pulse width—and the strong attenuation of the laser light by tissues, the frequency spectrum of the acoustic signal from the buried object of several micrometers in size is estimated to have significant components up to 75 MHz,[9] which makes its axial resolution as good as 10 μm. However, the maximum imaging depth in photoacoustic tomography is limited by the strong attenuation of the laser light and of the high-frequency acoustic waves. On the other hand, MITT can be used to image much deeper tissues due to the relatively low absorption of microwaves. The spectra of the acoustic signals in MITT are usually below 2 MHz, and the axial resolution is greater than 1 mm. Several investigators employed microwave-induced thermoacoustic waves in the 1980s for imaging of biological tissues; these early works, however, did not produce any tomographic or depth-resolved images.[12–14] Recent progress realized tomographic imaging of biological tissues based on microwave-induced thermoacoustic waves.[15–18]

We here present our studies on the signal-processing aspect of scanning MITT. Filtering has been applied to signal processing in photoacoustic tomography[11] and MITT;[15] however, it was used to eliminate the dc (direct current) offset and the effect of the response of the transducer on the piezoelectric signal, respectively. For the first time, we discuss in details how the spectra of signals influence the resolution of thermoacoustic tomography and how the resolution can be improved by signal processing. In our imaging approach, the lateral resolution was achieved by use of a focused ultrasonic transducer, whereas the axial resolution was obtained by measuring the temporal profiles of the acoustic signals. The dominance of the low-frequency (<0.5 MHz) components in the raw temporal signals limited the lateral resolution, and the narrow bandwidth of the signals restricted the axial resolution. Consequently, the image before signal processing had poor lateral resolution and many artifacts. We showed that a "simple" filtering method improved the lateral resolution to some extent but at the expense of the axial resolution. To overcome this problem, we proposed a new reshaping filter. It was applied to the temporal signals from the transducer to increase the weight of the high-frequency components, which improved the lateral resolution, and to broaden the spectrum of the signal, which enhanced the axial resolution. A numerical simulation validated our signal-processing approach.

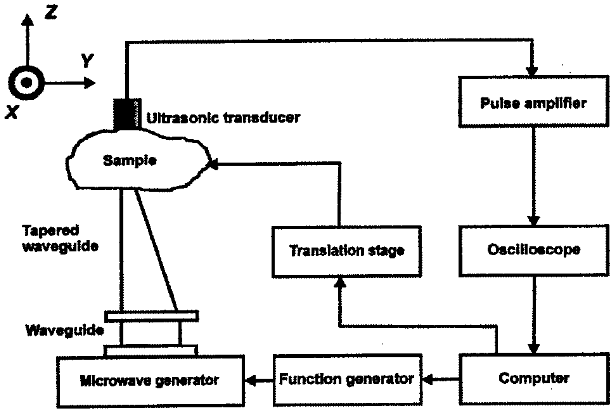

FIG. 1. Experimental setup for scanning MITT.

II. METHODS

A. Experimental setup

The experimental setup for this study is shown in Fig. 1. A Cartesian coordinate system was set up for reference: The x axis pointed outward perpendicularly to the drawing plane, the y axis pointed to the right in the drawing plane, and the z axis pointed upward along the acoustic axis. A 3 GHz microwave generator transmitted microwave pulses. The pulse width was modified from the original manufacturer's setting to 0.5 μs. A function generator was employed to trigger the microwave generator, to control its pulse repetition frequency, and to synchronize the sampling by the oscilloscope. Microwave energy was delivered by a tapered waveguide with a cross section that gradually narrowed from 72 mm $\times$34 mm to 72 mm$\times$5 mm. The object to be imaged was a slab of chicken muscle with a y-z cross section of 14 mm $\times$8 mm, and the slab was plunged into lard contained in a plexiglass tank. The tank was mounted on a two-dimensional (2D) x-y translation stage (MD2, Arrick Robotics), which was driven by two computer-controlled stepper motors. Lard and plexiglass were used for their low absorption to microwaves. Lard also provided good acoustic coupling to an ultrasonic transducer facing the microwave waveguide. The central frequency of the ultrasonic transducer (V314, Panametrics) was 1 MHz, the bandwidth was 0.6 MHz, the diameter of the active element was 1.9 cm, and the focal length was 2.5 cm. The transducer was connected to a low-noise pulse preamplifier. The amplified signal was averaged 100 times, recorded by an oscilloscope (TDS-640A, Tektronix), and then transferred to a personal computer.

In our scanning MITT, the ultrasonic transducer measured the time-of-arrival signals of the thermoacoustic waves. The distances between the thermoacoustic sources and the transducer were calculated by multiplying the time of arrival with the speed of sound in the medium. Therefore, a time-domain signal can be converted into a one-dimensional (1D) image along the acoustic axis (z axis), which is similar to an ultrasonic A-scan image. Scanning the sample along the x or the y axis and combining the multiple 1D images yielded a 2D cross-sectional image of the sample in the x-z or y-z plane, which is analogous to an ultrasonic B-scan image.

B. Signal processing

Two methods of signal processing in the frequency domain based on finite impulse response (FIR) filters were applied to the experimental data. The filtering is implemented by multiplying a properly selected real window function to the spectra of the signals, which introduces no phase distortion. In the first method, all the signals are processed with the same bandpass filter, which has a passband between 0.5 and 1.5 MHz with a transition bandwidth of ~0.5 MHz.

To overcome the difficulties of the first method, we proposed a reshaping method in the frequency domain. This method can make the bandwidth of the processed signal broader to enhance the axial resolution and weigh the high-frequency components more heavily to improve the lateral resolution. The essence of this method is to apply a reshaping filter to each temporal signal. The shape of the reshaping filter for the signal at any y position is chosen to be the inverse of the envelope of the original frequency spectrum, where the envelope of the spectrum is obtained by connecting the major local maxima. Without distorting the positions of the pulses in the temporal signal, this filter can achieve the widest possible bandwidth in the filtered signal and consequently the best axial resolution. Moreover, to filter out the very low-frequency disturbance—which is caused by the preamplifier—and the high-frequency noise beyond the cutoff frequency—where the signal-to-noise ratio is unity, a smoothing filter is applied to the signal. Unlike the reshaping filter, the smoothing filter is the same for the signals from all the scanned positions of the transducer. The final filter is the product of the above two filters in the frequency domain. To increase the contrast, the background value is subtracted from the spectrum before the final filter is applied. Lastly, to improve the lateral resolution, the final filter is scaled by a constant factor such that the spectral amplitudes of all the piezoelectric signals at a selected high frequency remain unchanged after filtering.

III. RESULTS AND DISCUSSION

An image of the chicken muscle is presented in Fig. 2(a). Each vertical line in this 2D image was obtained from a temporal piezoelectric signal of the ultrasonic transducer, and the sample was scanned horizontally along the y axis with a step size of 1 mm to acquire the multiple vertical lines. Figures 2(b) and 2(c) show the temporal wave forms and the corresponding frequency spectra, respectively, for y equal to 20 mm—where the transducer axis crossed the muscle—and equal to 2 mm—where the transducer axis did not cross the muscle. The buried muscle was clearly imaged as shown in Fig. 2(a): The white line at $z=17$ mm corresponds to the upper boundary between the lard and the muscle, and the dark line at $z=25.1$ mm to the lower one. The thickness of the muscle in the image is 8.1 mm and agrees with the actual one. But the lateral resolution is poor: The width of the muscle in the image appears to be 36 mm,

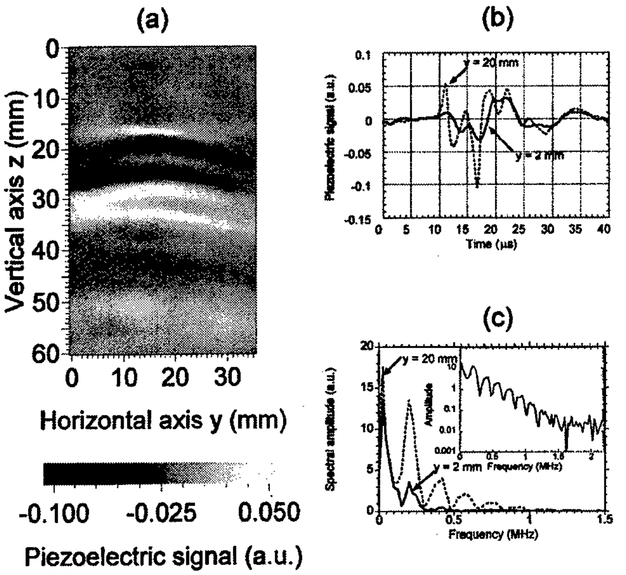

FIG. 2. (a) 2D image of the *y-z* cross section of the sample obtained by scanning MITT before data processing; (b) temporal microwave-induced thermoacoustic signals at different positions $y=20$ and 2 mm; (c) the main panel shows both of the corresponding spectra on a linear scale, and the inset shows the spectrum for $y=20$ mm on a logarithmic scale.

much greater than the actual 14 mm width. Furthermore, there appear many ghost objects between the two boundaries and below the lower boundary. Because the muscle and the lard are almost uniform, no heterogeneity in the image is expected from other than the boundaries.

To explain these problems, we resort to the relationship between the lateral resolution of the detecting ultrasonic transducer and the frequency spectrum of the received temporal wave form. The lateral resolution of the ultrasonic transducer is determined by its focal diameter, which is given by

$$d_f = \frac{1.02 \nu_a l_f}{d_a f_a}, \tag{1}$$

where ν_a is the speed of sound in the medium, l_f is the focal length of the transducer, d_a is the diameter of the active element in the transducer, and f_a is the acoustic frequency.

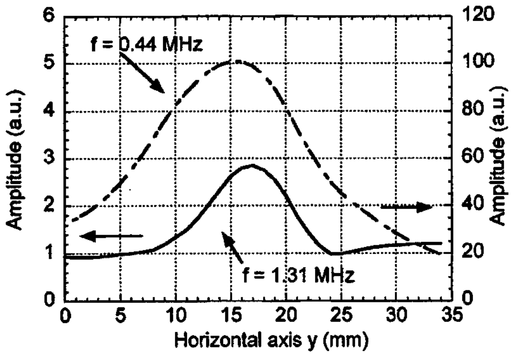

FIG. 3. The distributions of the signal components around $f=1.31$ and 0.44 MHz along the y axis.

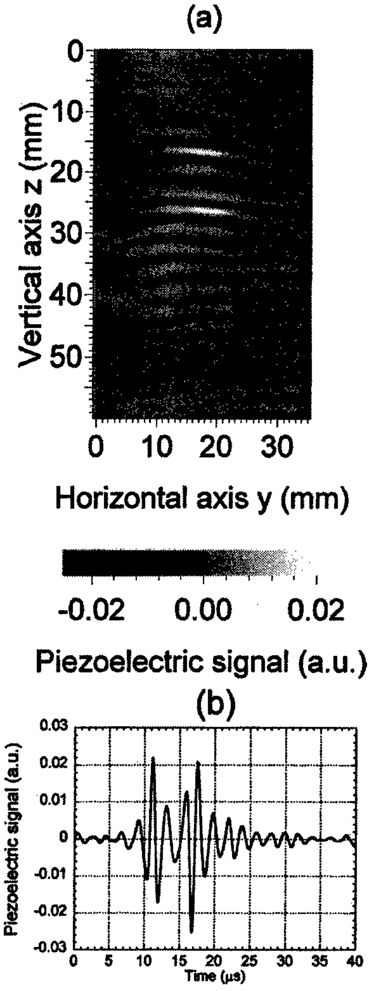

FIG. 4. (a) The 2D image after filtering the temporal signals with a standard bandpass filter; (b) the filtered temporal signal at $y=20$ mm.

Therefore, the lateral resolution is inversely proportional to the frequency of the acoustic signal or the piezoelectric signal. Because the dominant frequency components of the piezo-electrical signals are far below 1 MHz, as shown in Fig. 2(c), the lateral resolution is much worse than the focal diameter of the transducer, 2 mm, at its 1 MHz central frequency.

The dependence of the lateral resolution on the frequency spectra is illustrated more clearly in Fig. 3, which displays the 1D lateral images—along the y axis—corresponding to the 1.31 and 0.44 MHz components of the spectra, respectively. The 1.33 MHz image is sharper than the 0.44 MHz one, and therefore, has superior lateral resolution. Poor resolution that is caused by the dominating low-frequency components is also responsible for the ghost piezoelectric signals at $y=2$ mm, where the transducer axis does not cross the buried muscle and thus the received piezoelectric signals can be only wide-angle low-frequency signals. In comparison, the piezoelectric signal at $y=20$ mm—where the acoustic axis of the transducer crosses the muscle—is primarily from the transducer axis and hence has greater high-frequency

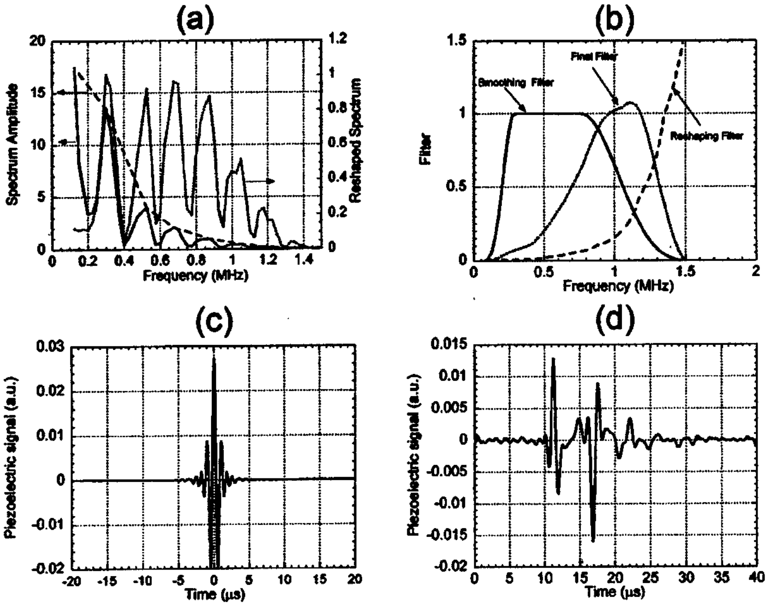

FIG. 5. (a) The envelope (dashed curve) of the spectrum (solid curve) of the temporal signal at $y = 20$ mm and the spectrum after the reshaping processing (dotted curve); (b) the reshaping filter—which is the inverse of the envelope, the smoothing filter—which is used to filter the high-frequency noise and the extremely low-frequency signal, and the final filter—which is the product of the reshaping filter and the smoothing filter; (c) the temporal wave form corresponding to the final filter; (d) the temporal wave form corresponding to the spectrum in Fig. 5(a) after the reshaping processing.

components than the piezoelectric signal at $y = 2$ mm, as shown in Fig. 2(c).

From the above discussion, it is clear that increasing the high-frequency components of the piezoelectric signals can improve the lateral resolution. The most natural solution is to apply a bandpass filter to cut off the low-frequency components. An example of such processing, in which the filter has a passband between 0.5 and 1.5 MHz with a transition bandwidth of ~0.5 MHz, is shown in Fig. 4(a). The lateral resolution is much improved but still unsatisfactory; however, the axial resolution seems worse, and some artifacts were generated, as shown in Fig. 4(b). The poor axial resolution is due to the decrease of bandwidth in the signal processing. As shown in the inset of Fig. 2(c), the spectral amplitude drops exponentially with the frequency; therefore, the filtered signal has a narrower bandwidth than the original one. A narrower bandwidth in the frequency domain results in a broader signal in the time domain thus poor axial resolution.

To overcome the difficulties of the simply filtering, we applied reshaping filters to the signals. The shape of the reshaping filter [Fig. 5(b)] for the signal at $y = 20$ mm is chosen to be the inverse of the envelope of the original frequency spectrum; where the envelope of the spectrum is obtained by connecting the major local maxima, as shown by the dashed curve in Fig. 5(a). Without distorting the positions of the pulses in the temporal signal, this filter can achieve the widest possible bandwidth in the filtered signal and consequently the best axial resolution. Moreover, to filter out the very low-frequency disturbance—which is caused by the preamplifier—and the high-frequency noise beyond the cutoff frequency—where the signal-to-noise ratio is unity, a smoothing filter is applied to the signal. Unlike the reshaping filter, the smoothing filter is the same for the signals from all the scanned positions of the transducer.

The final filter, which is the product of the above two filters in the frequency domain, is shown in Fig. 5(b); the final filter in the time domain is shown in Fig. 5(c). To increase the contrast, the background value—which is determined by the amplitude at both the ends of the solid curve in Fig. 3—is subtracted from the spectrum before applying the final filter. As we wish to obtain a lateral resolution approaching that at 1.31 MHz (Fig. 3), the final filter is scaled by a constant factor such that the spectral amplitude of the final filter at 1.31 MHz is set to unity; consequently, the spectral amplitudes of the piezoelectric signals for all piezoelectric signals remain unchanged at 1.31 MHz. The spectrum and the temporal wave form of the processed signal at $y = 20$ mm are displayed in Figs. 5(a) and 5(d). The axial resolution of the processed signal is much better than that of the unprocessed signal [Fig. 2(b)] because the processed spectrum is much broader than the unprocessed one [Fig. 2(c)]. The processed 2D image (Fig. 6) is also clearer than the original image. The ghost objects in the original images were removed, and the two boundaries became quite distinct from the background. The muscle along the y axis in the image is about 15 mm, which agrees well with the 14 mm actual size.

A numerical simulation was implemented to test our reshaping method. A simulated temporal waveform [Fig. 7(a)] includes three pulses at $t = 20$, 21, and 30 μs. The 20 and 30 μs pulses are determined by

$$s(t) = \exp\left(-\frac{(t-t_0)^2}{w^2}\right), \tag{2}$$

and the 21 μs pulse is determined by

$$s(t) = 1 \Bigg/ \left(1 + \frac{(t-t_0)^2}{w^2}\right), \tag{3}$$

where w is the pulse width and is set to 0.8 μs. The corresponding spectrum is shown in Fig. 7(b), which resembles the spectrum of the signal at $y = 20$ mm in our image. Be-

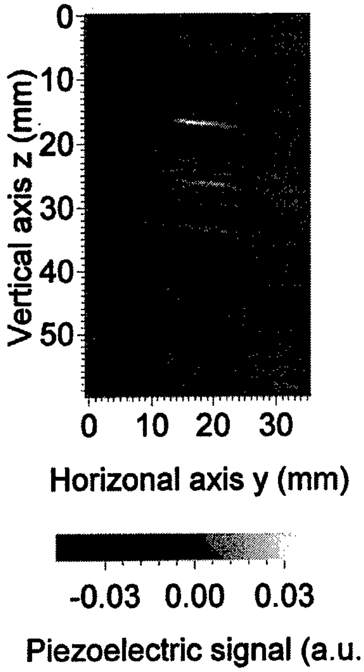

FIG. 6. The 2D image after applying the final filter to the temporal piezoelectric signals.

cause the 20 and 21 μs pulses are too close to each other, they merge into one pulse in the original constructed signal. In the signal processed by our method [Fig. 7(c)], the two pulses are separated distinctively, and all the pulses become sharper. The positioning errors of the restored peaks are within 10% of the pulse width. However, the signal-to-noise ratio (SNR) in Fig. 7(c) is lower than that in Fig. 7(a) as a result of the increased weighting of the noisy high-frequency components in the reshaping process. Nevertheless, the degradation of SNR in the processed signals has little influence on the image, as shown in Fig. 6. In contrast, the simple filtering did not produce as a good outcome [Fig. 7(d)].

Our reshaping method is especially efficient for signals that consist of multiple pulses of similar shapes, which is quite common in ultrasonic detection. Assuming a temporal signal comprises two identical pulses—for illustration purposes—at different times, its spectral amplitude can be written as

$$A(f)=s(f)|1+\exp(i2\pi f\Delta t)|=s(f)p(f), \tag{4}$$

where f is the frequency, $s(f)$ is the spectral amplitude of a single pulse, and Δt is the time interval between the two pulses. Because the oscillatory $p(f)$ has a flat envelope, the envelope of $A(f)$ approximately equals that of $s(f)$, which determines the shape of a single pulse. On the other hand, the features and the phase of the spectrum contain the positioning information of the pulses, which is the most important information in imaging. In our reshaping method, the signal is multiplied by the reciprocal of its own spectral envelope, resulting in a flat envelope in the processed spectrum; consequently, the pulses are narrowed in the time domain. As the reshaping filter is smooth, it does not alter the features and the phase of the spectrum; accordingly, the positions of the pulses in the time domain remain unchanged.

In general, applying the reshaping filter will sharpen the boundaries of signals, which can be illustrated with an ideal slab. The thermoacoustic wave from a slab irradiated by a sufficiently short microwave pulse can be represented by a square wave. It can be shown that filtering the square wave with the reshaping filter is equivalent to taking the first derivative of the wave in the time domain, which yields the two boundaries of the slab. The spectral amplitude of the square wave with a duration a is $|\sin(\pi af)/(\pi f)|$; thus its envelope is $1/(\pi f)$, and the reshaping filter is πf. Applying the reshaping filter to the square wave in the frequency domain is

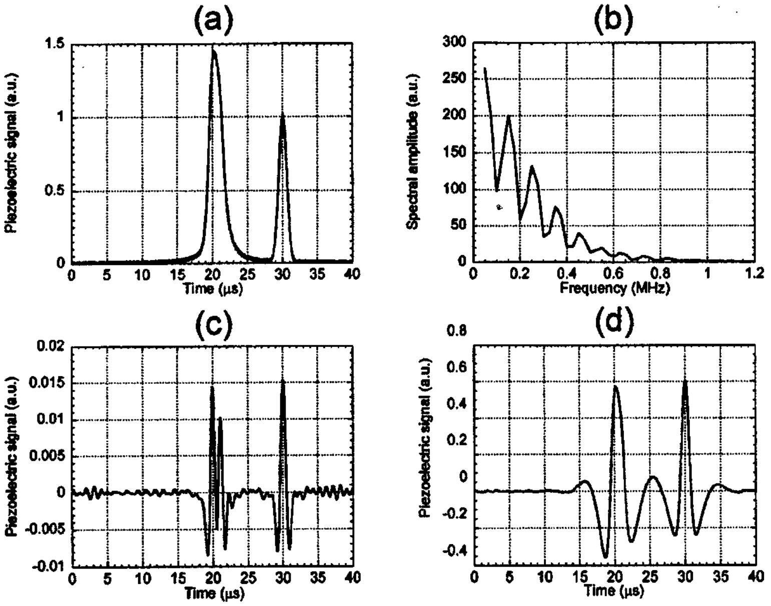

FIG. 7. (a) The simulated piezoelectric signal; (b) the corresponding spectrum; (c) the piezoelectric signal after reshaping the spectrum; (d) the piezoelectric signal after applying the smoothing filter as shown in Fig. 5(b).

equivalent, within a constant factor, to differentiating the signal in the time domain, which yields a positive delta function at the front boundary of the square wave and a negative one at the rear boundary.

Our study pointed out some potential approaches that can be used to improve the imaging resolution in our experiments. One approach is to improve the SNR of the signal so that the cutoff frequency is extended. Because only the spectral region with an SNR greater than unity provides useful information for our reshaping method, an increased cutoff frequency can broaden the usable spectrum and accordingly improve both the lateral and the axial resolutions. However, this advantage can only be realized when the spectrum is reshaped because the unprocessed high-frequency spectral amplitude is so small compared with the low-frequency one that it contributes little to improving the lateral and the axial resolutions, as shown in Fig. 2(c); after the reshaping, the weight of the high-frequency portion is increased greatly, resulting in an improved resolution. Another potential approach to improving the resolution is to shift the acoustic spectrum to a higher frequency by modulating the microwave source.

IV. CONCLUSIONS

Our studies showed that scanning MITT is a promising imaging tool for biological tissues. The boundaries of different tissue constituents can be imaged clearly and accurately with the assistance of image processing. By reshaping the spectra of the piezoelectric signals, the weight of the high-frequency components is increased greatly, resulting in much improved axial and lateral resolutions, both of which were 1 mm in our current experimental setup. The numerical simulation also verified our signal-processing method. Our spectral-reshaping method can also be applied to other ultrasonic signals comprising several pulses of similar shapes.

ACKNOWLEDGMENTS

We thank G. Ku for experimental assistance. This project was sponsored in part by the U.S. Army Medical Research and Materiel Command Grant No. DAMD17-00-1-0455, the National Institutes of Health Grants No. R01 CA71980 and No. R21 CA83760, the National Science Foundation Grant No. BES-9734491, and Texas Higher Education Coordinating Board Grant No. ARP 000512-0123-1999.

[a]Author to whom all correspondence should be addressed. Telephone: 979-847-9040; Fax: 979-845-4450; Electronic mail: LWang@tamu.edu; URL:http://oilab.tamu.edu

[1] W. Joines, R. Jirtle, M. Rafal, and D. Schaeffer, "Microwave power absorption differences between normal and malignant tissue," Int. J. Radiat. Oncol., Biol., Phys. **6**, 681–687 (1980).

[2] S. Chaudhary, R. Mishra, A. Swarup, and J. Thomas, "Dielectric properties of normal human breast tissues at radiowave and microwave frequencies," Indian J. Biochem. Biophys. **21**, 76–79 (1984).

[3] W. Joines, Y. Zhang, C. Li, and R. Jirtle, "The measured electrical properties of normal and malignant human tissues from 50–900 MHz," Med. Phys. **21**, 547–550 (1994).

[4] *Medical Applications of Microwave Imaging*, edited by L. E. Larsen and J. H. Jacobi (IEEE, Piscataway, NJ, 1986).

[5] S. Caorsi, A. Frattoni, G. L. Gragnani, E. Nortino, and M. Pastorino, "Numerical algorithm for dielectric-permittivity microwave imaging of inhomogeneous biological bodies," Med. Biol. Eng. Comput. **29**, NS37–NS44 (1991).

[6] M. S. Hawley, A. Broquetas, L. Jofre, J. C. Bolomey, and G. Gaboriaud, "Microwave imaging of tissue blood content changes," J. Biomed. Eng. **13**, 197–202 (1991).

[7] P. M. Meaney, K. D. Paulsen, and J. T. Chang, "Near-field microwave imaging of biologically-based materials using a monopole transceiver system," IEEE Trans. Microwave Theory Tech. **46**, 31–45 (1998).

[8] R. A. Kruger, P. Liu, Y. R. Fang, and C. R. Appledorn, "Photoacoustic ultrasound (PAUS)—reconstruction tomography," Med. Phys. **22**, 1605–1609 (1995).

[9] C. G. A. Hoelen, F. F. M. Demul, R. Pongers, and A. Dekker, "Three-dimensional photoacoustic imaging of blood vessels in tissue," Opt. Lett. **23**, 648–650 (1998).

[10] A. A. Karabutov, E. V. Savateeva, N. B. Podymova, and A. A. Oraevsky, "Backward mode detection of laser-induced wide-band ultrasonic transients with optoacoustic transducer," J. Appl. Phys. **87**, 2003–2014 (2000).

[11] C. G. A. Hoelen, R. Pongers, G. Hamhuis, F. F. M. Demul, and J. Greve, "Photoacoustic blood cell detection and imaging of blood vessels in phantom tissue," Proc. SPIE **3196**, 142–153 (1998).

[12] T. Bowen, L. Nasoni, A. E. Pifer, and G. H. Sembrosk, "Some experimental results on the thermoacoustic imaging of soft tissue-equivalent phantoms," Proc.-IEEE Ultrason. Symp. **2**, 823–827 (1981).

[13] R. G. Olsen and J. C. Lin, "Acoustic imaging of a model of a human hand using pulsed microwave irradiation," Bioelectromagnetics (N.Y.) **4**, 397–400 (1983).

[14] J. C. Lin and K. H. Chan, "Microwave thermoelastic tissue imaging—system design," IEEE Trans. Microwave Theory Tech. **32**, 854–860 (1984).

[15] R. A. Kruger, D. R. Reinecke, and G. A. Kruger, "Thermoacoustic computed tomography—technical considerations," Med. Phys. **26**, 1832–1837 (1999).

[16] L.-H. V. Wang, X. Zhao, H. Sun, and G. Ku, "Microwave-induced acoustic imaging of biological tissues," Rev. Sci. Instrum. **70**, 3744–3748 (1999).

[17] G. Ku and L.-H. V. Wang, "Scanning thermoacoustic tomography in biological tissue," Med. Phys. **27**, 1195–1202 (2000).

[18] G. Ku and L.-H. V. Wang, "Scanning microwave-induced thermoacoustic tomography: signal, resolution, and contrast," Med. Phys. **28**, 4–10 (2001).

Microwave-induced thermoacoustic tomography using multi-sector scanning

Minghua Xu, Geng Ku, and Lihong V. Wang[a)]
Optical Imaging Laboratory, Biomedical Engineering Program, Texas A&M University, 3120 TAMU, College Station, Texas 77843-3120

(Received 26 March 2001; accepted for publication 18 June 2001)

A study of microwave-induced thermoacoustic tomography of inhomogeneous tissues using multi-sector scanning is presented. A short-pulsed microwave beam is used to irradiate the tissue samples. The microwave absorption excites time-resolved acoustic waves by thermoelastic expansion. The amplitudes of the acoustic waves are strongly related to locally absorbed microwave-energy density. The acoustic waves may propagate in all spatial directions. A focused ultrasonic transducer is employed to acquire temporal acoustic signals from multiple directions. Each detected signal is converted into a one-dimensional (1D) image along the acoustic axis of the transducer. The cross-sectional images of the tissue samples are calculated by combining all of the 1D images acquired in the same planes. © *2001 American Association of Physicists in Medicine.*
[DOI: 10.1118/1.1395037]

Key words: microwave, thermoacoustics, tomography, imaging, sector, scan

I. INTRODUCTION

Microwave-induced thermoacoustic tomography of biological tissues has recently attracted considerable interest.[1–3] With this technique, a short-pulsed microwave beam is used to irradiate tissue samples. The tissue absorbs the microwave energy and excites thermoacoustic waves by thermoelastic expansion. The generated acoustic waves carry information about the microwave absorption properties of the sample. The different absorption properties among different types of tissue permit the construction of a distribution of microwave absorption in a homogeneous acoustic medium.

The microwave penetration depth in most soft tissues lies somewhere between that of the fat tissue, which lacks water and salt, and muscle tissue, which is abundant in water and salt.[2] Specifically, the penetration depths for fat and muscle tissue at 3-GHz microwave are 9 cm and 1.2 cm, respectively. The wide range of microwave absorption coefficients among various other tissues can lead to a high imaging contrast for biological tissues. However, it is difficult to achieve good spatial resolution using pure microwave imaging of biological tissues because of the long wavelength of microwaves, e.g., 3 cm at 3 GHz.[4,5] This problem can be overcome by the use of microwave-induced thermoacoustic waves. Because the velocity of acoustic waves in soft tissue is nearly 1.5 mm/μs, thermoacoustic signals at mega Hz can provide millimeter spatial resolution.

The intensities of the microwave-induced thermoacoustic signals are far lower than the ultrasonic pulses used in purely ultrasound imaging (ultrasonography). However, a unique advantage of thermoacoustic tomography is the detection of the inhomogeneous microwave absorption property of tissues when the acoustic property is homogeneous. Such a capability may lead to early detection of cancer.

Key problems in microwave-induced thermoacoustic tomography are the measurement of acoustic signals excited by microwave pulses and the construction of images from the acquired data. One approach is to use focused ultrasonic transducers to localize the thermoacoustic sources. The mature scanning techniques (linear and sector scans) in ultrasonography can be used to detect the thermoacoustic signals.[6] Each scan line may reflect the profile of the medium along the acoustic axis of the focused transducer. However, an acoustic source has a strong direction of radiation, especially if the surface is relatively smooth, from which the acoustic energy is mainly transmitted out in one direction. The higher the frequency of the acoustic wave is, the stronger the radiation direction is. The thermoacoustic signals caused by microwave pulses are composed of high-frequency components as well as low-frequency components, and the intensities of the high-frequency components are far less than the ultrasonic pulses used in ultrasonography. Only if its acoustic axis is nearly perpendicular to the surface of the acoustic source, can the focused transducer acquire enough high-frequency components for accurate spatial localizations of the thermoacoustic sources. Therefore, it is necessary, with this method, to scan the sample from all possible directions by a focused transducer. Since the thermoacoustic wave is weak, in order to get a good signal-and-noise ratio (SNR), we use a focused transducer with a big aperture area in our initial study, because the SNR is proportional to the square root of the aperture area.

Here we present our study on microwave-induced thermoacoustic tomography of inhomogeneous tissues by a two-dimensional (2D) full-directional scan—the combination of multiple-sector scans at various positions on a circle around the sample. Each detected time-resolved signal is converted into a one-dimensional image along the acoustic axis. The axial resolution is obtained by measuring the temporal profiles of the acoustic signals, and the lateral resolution is mainly determined by the focal diameter of the transducer.

The two-dimensional (2D) cross-sectional images are calculated from the data acquired in the same planes. Some images of biological-tissue samples are achieved experimentally. These images clearly reveal the boundaries of different tissues as well as their locations, which are in good agreement with the actual samples.

II. THEORY

A. Thermoacoustic wave

When the microwave pulse duration is very short, the thermal conduction time is far greater than the thermoacoustic transit time. In practice, the duration of the microwave pulse is less than 1 μs, which meets this criterion.[1] In this case, the heat diffusion's effect to the thermoacoustic wave in the tissue can be neglected. Consequently, the generation of thermoacoustic wave by deposition of microwave energy can be described by the following equation:[7]

$$\left(\nabla^2 - \frac{1}{c^2}\frac{\partial^2}{\partial t^2}\right)p(\mathbf{r},t) = -\frac{\beta}{C_p}\frac{\partial I(t)}{\partial t}A(\mathbf{r}), \tag{1}$$

where $p(\mathbf{r},t)$ is the thermoacoustic pressure at position $\mathbf{r}$ and time t, c is the speed of sound, β is the isobaric volume expansion coefficient, C_p is the heat capacity, $I(t)$ is the temporal profile of the microwave pulse, and $A(\mathbf{r})$ is the fractional energy-absorption per unit volume of soft tissue at position $\mathbf{r}$, which is proportional to the microwave absorption coefficient of the tissue at position $\mathbf{r}$.

Equation (1) shows that the amplitudes of the thermoacoustic waves are strongly related to locally absorbed microwave-energy density, i.e., the local microwave absorption coefficient or penetration depth. Considering a spherically symmetric deposition of microwave energy with radius R,

$$A(r) = A_0 U(-r+R), \tag{2}$$

where the step function

$$U(\xi) = \begin{cases} 1, & \xi \geq 0, \\ 0, & \xi < 0. \end{cases}$$

Assuming a delta pulse of the form $I(t) = I_0\delta(t)$, the thermoacoustic pressure at detection position r for $t>0$ is found from Eq. (1) to be[7]

$$p(r,t) = \frac{\beta I_0 c^2}{C_p}\frac{A_0}{2r}(r-ct)[U(-r+R+ct) + U(r+R-ct)]. \tag{3}$$

Moreover, the first derivative of the thermoacoustic pressure is written as

$$\frac{\partial p(r,t)}{\partial t} = -\frac{\beta I_0 c^3}{2rC_p}A_0 U(-|ct-r|+R). \tag{4}$$

Equation (4) indicates that the first derivative of the thermoacoustic pressure is a mapping of the spherically spatial energy deposition of Eq. (2). Therefore, we can use either the detected thermoacoustic pressure or its first derivative to construct the microwave absorption distribution and the latter is found to be better. In general, a large medium can be regarded as a set of small media or thermoacoustic sources, which have different microwave absorption coefficients. Through the following multi-sector scan method, each small thermoacoustic source can be localized.

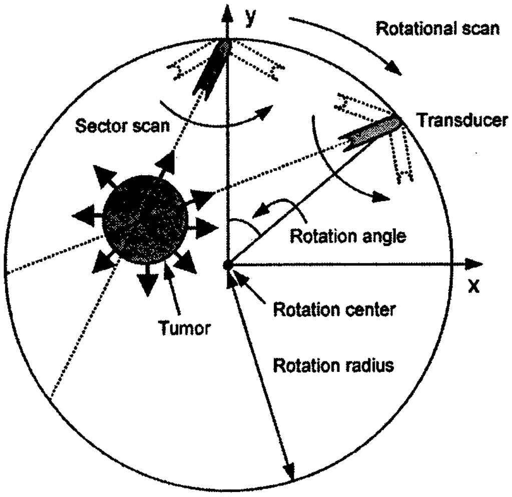

FIG. 1. A diagram of the multi-sector scan scheme.

B. Multi-sector scan

A diagram of the 2D multi-sector scanning scheme is shown in Fig. 1. A rectangular coordinate system (x,y) is set up for reference. Each sector-scan frame has a set of scan lines, which originate from the same location and radiate out in different directions as in ultrasonography. The origins of different frames are set on a circle around the sample so that the focused transducer may detect the signals from all directions in the same plane. For convenience, the center and radius of the circle are referred to as the rotation center and the rotation radius, respectively.

The microwave absorption and sample heating occur in a very short time, and the propagation velocity of the electromagnetic wave is far greater than that of an ultrasonic one. Therefore, it is reasonable to assume that the sample expansion resulting from the microwave pulses causes acoustic waves instantaneously. The distance between the thermoacoustic source and the transducer is simply calculated by multiplying the time of arrival by the velocity of the acoustic wave. Therefore, at each scan line, the thermoacoustic pressure along the acoustic axis induced by the microwave pulses can be obtained directly from the detected temporal signals.

All scan lines are used to construct a cross-sectional image by the method of linear interpolation. A sector frame can only detect part of the sound source. Figure 2(a) shows the same $x-y$ plane as in Fig. 1. The transducer is now set at the position of point O_1. A local polar coordinate system (d,α) is set up for the sector frame with the origin O_1, and its polar axis is through the rotation center point O. The angle θ between the polar axis and y axis is called the rotation angle.

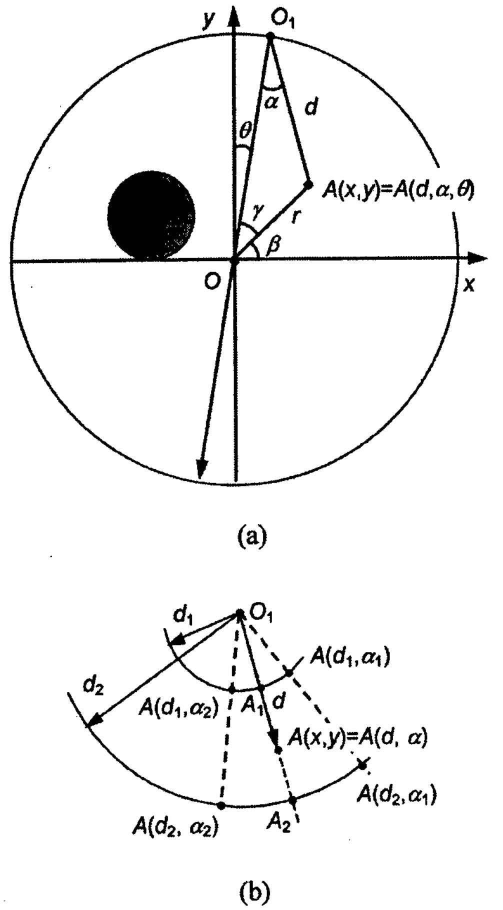

FIG. 2. (a) The rectangular coordinate system (x,y) and the local polar coordinate system (d,α,θ); (b) the diagram of the linear interpolation.

The rotation radius between point O and O_1 is R. The distance between the thermoacoustic source and the transducer is d. Therefore, at each scan line, the point $A(x,y)$ in the rectangular coordinate system can be denoted as $A(d,\alpha,\theta)$ in the local polar coordinate system with rotation angle θ. The relationship between (x,y) and (d,α,θ) is determined by the following equations:

$$\begin{aligned} d &= \sqrt{r^2+R^2-2rR\cos\gamma}, \\ \theta &= \arcsin(r\sin\gamma/d), \\ \beta &= \arctan(y/x), \\ \gamma &= \pi/2-\alpha-\beta, \\ r &= \sqrt{x^2+y^2}. \end{aligned} \tag{5}$$

In experiments, a series of discrete data are acquired in each local polar coordinate system. We use linear interpolations to project the data from each local polar coordinate system to the rectangular coordinate system. For simplicity, we neglect the symbol θ in the following description. As shown in Fig. 2(b), suppose that point (d,α) is among the measured data $A(d_1,\alpha_1)$, $A(d_2,\alpha_1)$, $A(d_1,\alpha_2)$, and $A(d_2,\alpha_2)$, i.e., $\alpha_1 \leqslant \alpha \leqslant \alpha_2$, $d_1 \leqslant d \leqslant d_2$, where $d_i\,(i=1,2)$ is the distance between the thermoacoustic source and the transducer and is calculated by multiplying the time of arrival $t_i\,(i=1,2)$ by the velocity of the acoustic wave c in the medium, i.e., $d_i = ct_i\,(i=1,2)$. Then $A(d,\alpha)$ can be calculated by

$$\begin{aligned} A(d,\alpha) &= \frac{d-d_1}{d_2-d_1}(A_2-A_1)+A_1, \\ A_1 &= A(d_1,\alpha_1)+\frac{A(d_1,\alpha_2)-A(d_1,\alpha_1)}{\alpha_2-\alpha_1}\times(\alpha-\alpha_1), \\ A_2 &= A(d_2,\alpha_1)+\frac{A(d_2,\alpha_2)-A(d_2,\alpha_1)}{\alpha_2-\alpha_1}(\alpha-\alpha_1). \end{aligned} \tag{6}$$

Function A could be the thermoacoustic pressure $p(t)$ or the derivative $dp(t)/dt$. The derivative is helpful for improving the sharpness of the boundaries between different tissues, which can be calculated through an inverse fast Fourier transformation (FFT) as

$$\frac{dp(t)}{dt} = \mathrm{FFT}^{-1}\{i\omega p(\omega)\}, \tag{7}$$

where $p(\omega)$ is the Fourier transformation of $p(t)$.

In this way, we can compute each image $A_\theta(x,y)$ from each sector frame $A(d,\alpha)$ at rotation angle θ. A full 2D cross-sectional image is obtained with the following summation:

$$A(x,y) = \sum_\theta A_\theta(x,y). \tag{8}$$

III. EXPERIMENTAL METHOD

We use a focused transducer to implement a multi-sector scan. Figure 3 shows the experimental setup. A plexiglass container is filled with mineral oil. A rotation stage and a focused transducer are immersed inside it in the same $x-y$ plane. The sample can be set in the rotation stage. The transducer is used to detect the thermoacoustic signal from the sample. The angle panel indicates the angle between the acoustic axis of the transducer and the rotation radius. We manually turn the transducer to point to one direction. A step motor directly drives the rotation stage while the transducer is fixed. Obviously, this is equivalent to a transducer that rotationally scans around the sample with a manual sector scan. The transducer (V314, Panametrics) has a central frequency of 1 MHz, a bandwidth of 0.6 MHz, a diameter of 1.9 cm, a focal length of 2.5 cm at 1 MHz, a 3-dB focal diameter of 2.1 mm, and a focal zone of 1.76 cm along the acoustic axis.

The microwave pulses transmitted from a 3-GHz microwave generator have a pulse energy of 10 mJ and a pulse width of 0.5 μs. A function generator (Protek, B-180) is used to trigger the microwave generator, control its pulse repetition frequency, and synchronize the oscilloscope sampling. Microwave energy is delivered to the sample by a rectangular wave guide with a cross section of 72 mm×34 mm.

A personal computer is used to control the step motor in rotating the sample. The signal from the transducer is first amplified through a pulse amplifier, then recorded and aver-

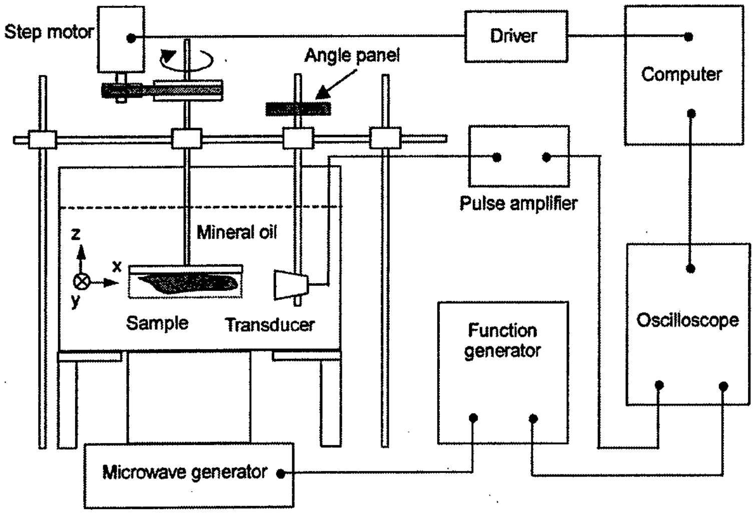
Step motor
Angle panel
Driver
Computer
Pulse amplifier
Mineral oil
z
x
y
Sample
Transducer
Function generator
Oscilloscope
Microwave generator

FIG. 3. Experimental setup.

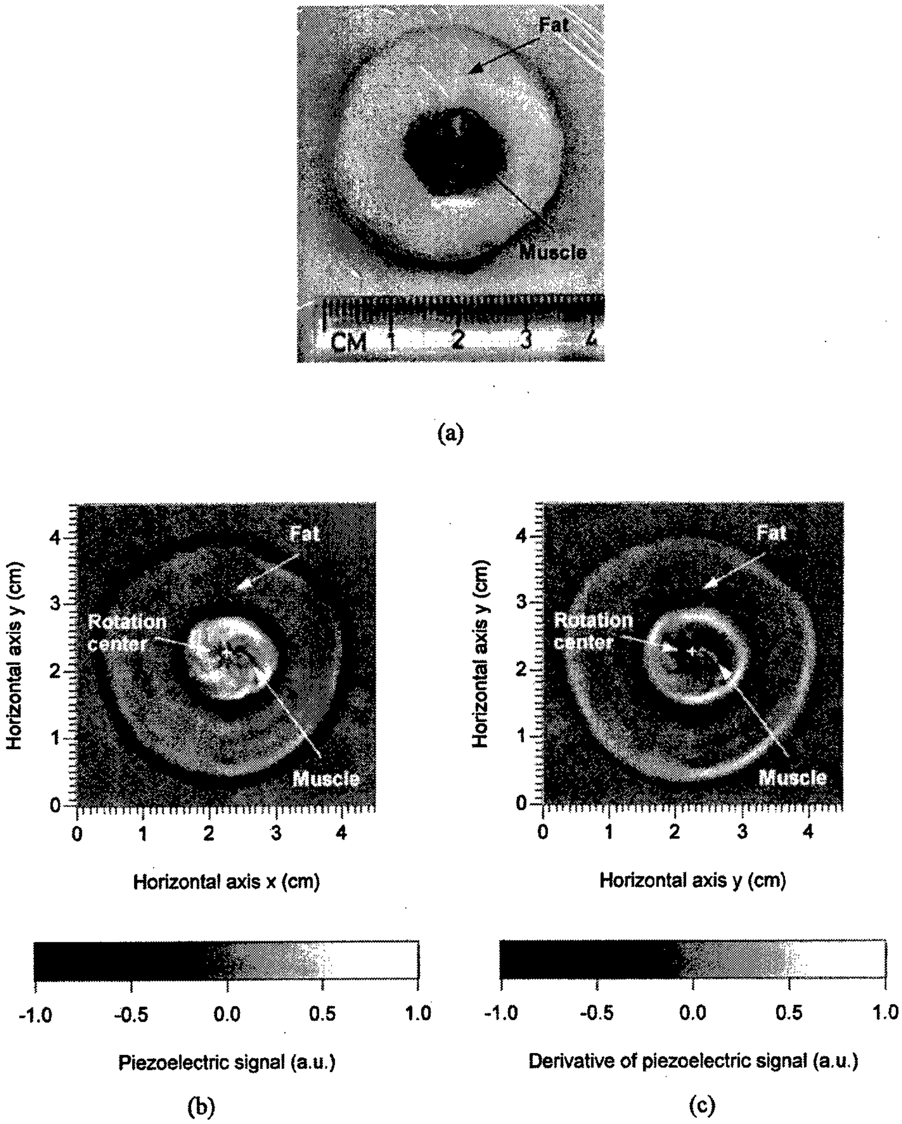
Fat
Muscle
CM 1 2 3 4
(a)
Fat
Rotation center
Muscle
Horizontal axis y (cm)
Horizontal axis x (cm)
0
1
2
3
4
-1.0
-0.5
0.0
0.5
1.0
Piezoelectric signal (a.u.)
(b)
Fat
Rotation center
Muscle
Horizontal axis y (cm)
Horizontal axis y (cm)
Derivative of piezoelectric signal (a.u.)
(c)

FIG. 4. (a) Cross section of a sample on the $x-y$ plane; 2D constructed images of the $x-y$ cross section of the sample (b) from the piezoelectric signals and (c) from the first derivative of the piezoelectric signals.

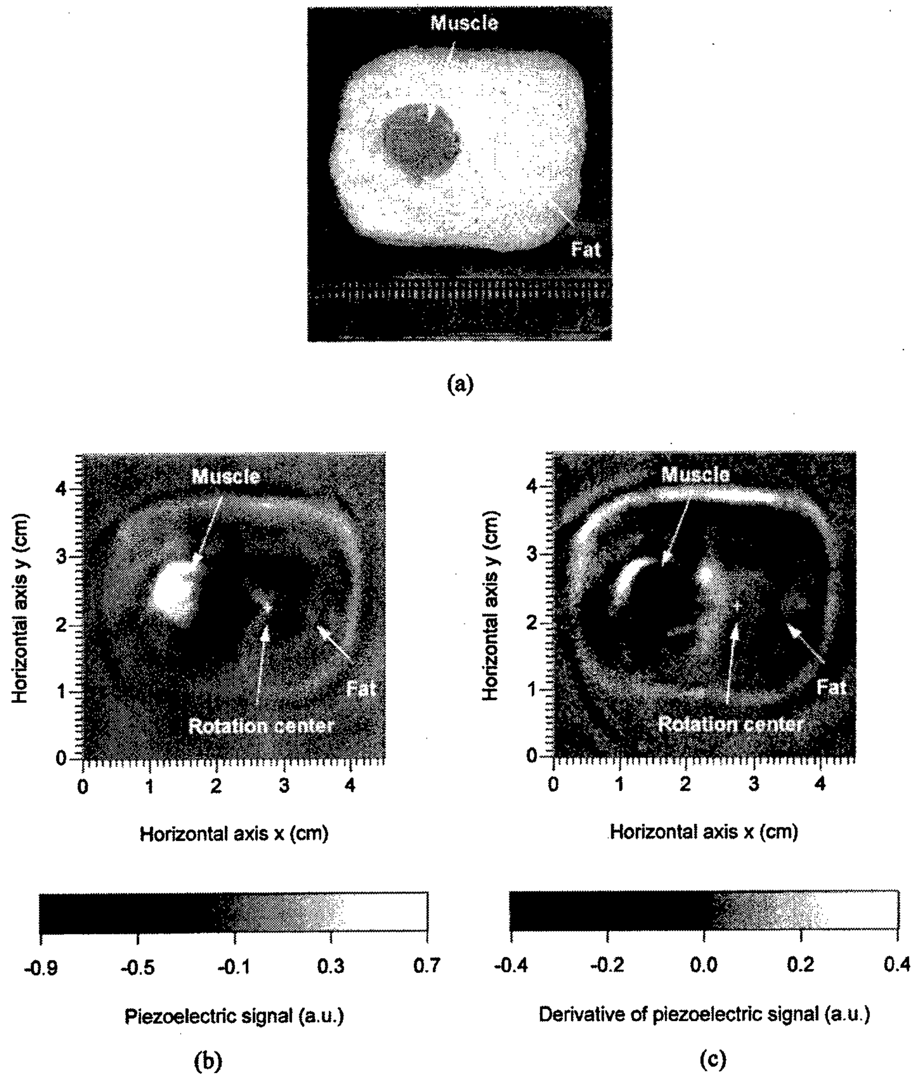

FIG. 5. (a) Cross section of a sample on the $x-y$ plane; 2D constructed images of the $x-y$ cross section of the sample (b) from the piezoelectric signals and (c) from the first derivative of the piezoelectric signals.

aged 100 times by an oscilloscope (TDS640A, Tektronix), and finally transferred to a personal computer for imaging.

IV. RESULTS AND DISCUSSION

The first sample we tested was a piece of muscle tissue—centered in a fat disc as shown in Fig. 4(a)—which was cut across and photographed after the experiment. Both the muscle and fat were cut from pork. The maximum diameter of the sample was 38 mm, and the thickness was 5 mm. The rotation center was set inside the muscle. The transducer rotationally scanned the sample (only in the rotation-radius directions) from 0 to 360 degrees with a step size of 2.25 degrees. We then used these 160 scan lines to calculate a 2D cross-sectional image with linear interpolations. Good agreement between the original profile in Fig. 4(a) and the constructed images in Figs. 4(b) and 4(c) was obtained, where Figs. 4(b) and 4(c) were computed from the measured piezoelectric signals and the first derivative of those, respectively. The boundaries between the fat and muscle or oil are clearly imaged. This is because when the rotation center is in the center of the sample, each scan line is nearly perpendicular to the boundaries of the muscle or fat, and the transducer can receive sufficient thermoacoustic signals from the radius directions alone for imaging.

The second sample had a structure as shown in Fig. 5(a), which was also cut across and photographed after the experiment. The fat was first cut from pork: the maximum diameter of the sample was 39 mm; and the thickness was 5 mm. Then we cut away a hole far away from its center and filled in a small piece of muscle, which was also cut from pork. The muscle size was about 10 mm in diameter and 5 mm in thickness. The rotation center was set outside the muscle. The rotation radius was 12.5 cm, which included the length of the transducer. The transducer rotationally scanned the sample from 0 to 360 degrees with a step size of 2.25 degrees, and at each stop a set of sector directions from -12 to 12 degrees with a step size of 2 degrees was scanned. Totally, 2080 scan lines were acquired to construct 2D cross-section images. Figure 5(b) was constructed directly from the piezoelectric signals, which was in good agreement with the original profile in Fig. 5(a). The boundaries between the fat and muscle or oil are clearly visible, except the rear boundary of the muscle. Figure 5(c) was constructed from the first derivatives of the piezoelectric signals, which agreed with the original profile of Fig. 5(a) very well. The boundary of the muscle was clearer than that in Fig. 5(b). In particular, the sizes and locations of the muscle and fat zones agreed with the original shapes. It indicates that the first derivative produces a better mapping of the microwave absorption distribution than the piezoelectric signal, i.e., the thermoacoustic pressure. Due to the high microwave absorption in muscle and the low absorption in fat, the muscle and fat can be differentiated by their "brightness" in the images.

In the above examples, the size deviations between the original objects and their constructed images are about 2 mm, which agree with the theoretical spatial resolution approximations as follows. The axial resolution along the acoustic axis is dependent on the width of the microwave pulse (0.5 μs) plus the width of the impulse response of the transducer (1.5 μs); therefore, it should be approximately 3 mm, because the velocity of the acoustic waves in the tissue is about 1.5 mm/μs. The lateral resolution is determined by the focal diameter of the focused transducer, ~2 mm for the 1 MHz transducer used in the above experiments. The use of shorter microwave pulses and narrower focal diameter ultrasonic transducers can improve the spatial resolution.[3]

V. CONCLUSION

Microwave-induced thermoacoustic tomography of inhomogeneous tissues by using multiple sector scans was studied. Cross-sectional images can be obtained by a few straightforward calculations from the temporal data acquired by a focused transducer rotationally sector scanning the samples. The experiments show that the constructed images are in good agreement with the original cross-section profiles of the samples, and the boundaries between different tissues are clearly imaged. Results indicate that this technique is a powerful imaging method with good spatial resolution that can be used for the investigation of inhomogeneous tissues. In the future, a circular array could be used to replace the single transducer, and some numerical compensation methods could be introduced to improve the spatial resolution further.

ACKNOWLEDGMENTS

This project was sponsored in part by the U.S. Army Medical Research and Materiel Command Grant No. DAMD17-00-1-0455, the National Institutes of Health Grant No. R01 CA71980, the National Science Foundation Grant No. BES-9734491, and Texas Higher Education Coordinating Board Grant No. ARP 000512-0123-1999.

[a] Author to whom all correspondence should be addressed. Electronic mail: lwang@tamu.edu; URL:http://oilab.tamu.edu

[1] R. A. Kruger, K. K. Kopecky, A. M. Aisen, D. R. Reinecke, G. A. Kruger, and W. L. Kiser, "Thermoacoustic CT with radio waves: A medical imaging paradigm," Radiology **211**, 275–278 (1999).

[2] G. Ku and L. V. Wang, "Scanning thermoacoustic tomography in biological tissues," Med. Phys. **27**, 1195–1202 (2000).

[3] G. Ku and L. V. Wang, "Scanning microwave-induced thermoacoustic tomography: Signal, resolution, and contrast," Med. Phys. **28**, 4–10 (2001).

[4] *Medical Applications of Microwave Imaging*, edited by L. E. Larsen and J. H. Jacobi (IEEE, Piscataway, NJ, 1986).

[5] P. M. Meaney, K. D. Paulsen, and J. T. Chang, "Near-field microwave imaging of biologically-based materials using a monopole transceiver system," IEEE Trans. Microwave Theory Tech. **46**, 31–45 (1998).

[6] P. N. T. Wells, "Ultrasonic imagining of the human body," Rep. Prog. Phys. **62**, 671–722 (1999).

[7] G. J. Diebold, T. Sun, and M. I. Khan, Photoacoustic waveforms generated by fluid bodies, in *Photoacoustic and Photothermal Phenomena III*, edited by D. Bicanic (Springer-Verlag, Berlin, Heidelberg, 1992), pp. 263–269.

Microwave-induced thermoacoustic tomography: Reconstruction by synthetic aperture

Dazi Feng, Yuan Xu, Geng Ku, and Lihong V. Wang[a)]
Optical Imaging Laboratory, Biomedical Engineering Program, Texas A&M University, 3120 TAMU, College Station, Texas 77843-3120

(Received 14 May 2001; accepted for publication 20 September 2001)

We have applied the synthetic-aperture method to linear-scanning microwave-induced thermoacoustic tomography in biological tissues. A nonfocused ultrasonic transducer was used to receive thermoacoustic signals, to which the delay-and-sum algorithm was applied for image reconstruction. We greatly improved the lateral resolution of images and acquired a clear view of the circular boundaries of buried cylindrical objects, which could not be obtained in conventional linear-scanning microwave-induced thermoacoustic tomography based on focused transducers. Two microwave sources, which had frequencies of 9 and 3 GHz, respectively, were used in the experiments for comparison. The 3 GHz system had a much larger imaging depth but a lower signal–noise ratio than the 9 GHz system in near-surface imaging. *© 2001 American Association of Physicists in Medicine.* [DOI: 10.1118/1.1418015]

Key words: thermoacoustics, tomography, synthetic aperture, microwave

I. INTRODUCTION

Microwave-induced thermoacoustic tomography is emerging as a nonionizing imaging modality. When electromagnetic radiation is irradiated upon biological tissues, the resulting heat-related expansion of the tissues produces acoustic waves. From the acoustic signals, we can reconstruct the distribution of electromagnetic absorption in soft tissues. The large differences in electromagnetic absorption in various tissues, which are associated with their physiological and pathological status, provide significant contrasts in imaging. For example, the absorption coefficient in cancerous breast tissue is two to five times greater than that in normal breast tissue, due to the increment of water and sodium bounded within malignant cells.[1–3] This large difference makes it promising to use microwave-induced thermoacoustic tomography to detect breast cancers.

Microwave-induced thermoacoustic tomography combines the advantages of both pure ultrasound and pure microwave imaging. Traditional imaging technology with pure ultrasound (ultrasonography) offers satisfactory spatial resolution but poor soft-tissue contrast, while pure microwave imaging provides good imaging contrast but barren spatial resolution.[4–7] Microwave-induced thermoacoustic tomography bridges the gap between them. By integrating ultrasound and microwave technology, microwave-induced thermoacoustic tomography has both satisfactory spatial resolution and good soft-tissue contrast.

In conventional linear-scanning microwave-induced thermoacoustic tomography (LMTT), a focused ultrasonic transducer is used to detect time-resolved acoustic signals. Since the focused transducer has a good response only along the transducer axis, each acoustic signal can be converted into a one-dimensional image. Linear scanning of the ultrasonic transducer yields multiple one-dimensional images, which can be combined to form a two-dimensional image of the sample.[8–10] In the two-dimensional images obtained with conventional LMTT, only boundaries that are nearly perpendicular to the axis of the ultrasonic transducer can be detected because most of the thermoacoustic waves travel in a small solid angle around the normals of boundaries; spherical or oblique boundaries of buried objects whose thermoacoustic waves have a large angle with the axis of the ultrasonic transducer cannot be imaged because the ultrasonic transducer receives little signal from these boundaries.

To overcome this deficiency of traditional LMTT, we have applied the synthetic-aperture method to LMTT. In this method, thermoacoustic signals were detected from multiple locations and the synthetic delay-and-sum algorithm was then used for the reconstruction of the images. The synthetic-aperture method has been applied in PAT previously;[11–14] and weights were assigned to the signals according to the sensor's directivity to improve the SNR at the expense of lateral resolution. In our experiment, the raw data were obtained by a 2.25 MHz nonfocused transducer instead of a focused one, as in traditional LMTT, and the synthetic-aperture reconstruction method based on the delay-and-sum algorithm was applied to reconstruct the images. By applying the synthetic-aperture method, we have improved the lateral resolution of the images and enhanced our ability to image spherical or oblique boundaries in the samples. Images acquired from two microwave sources with different frequencies were compared; the 3 GHz system has a much larger imaging depth but a lower SNR than the 9 GHz system in near-surface imaging.

II. METHODS

A. Reconstruction method

The image reconstruction method is illustrated in Fig. 1. For convenience, we converted both the signal-delay time

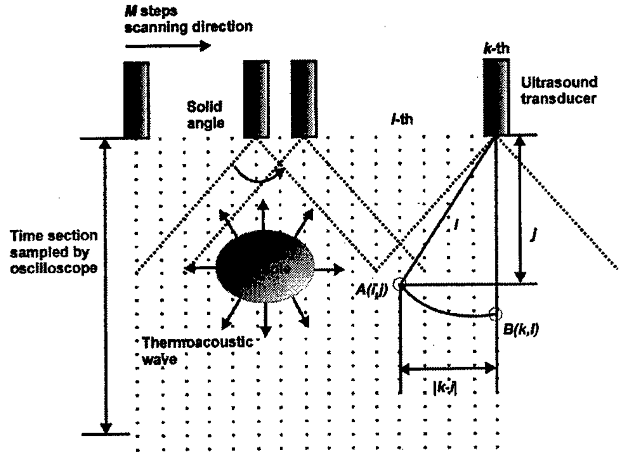

FIG. 1. Scanning and reconstruction method.

and the spatial distance into the number of pixels according to the speed of the acoustic wave traveling in the media. For the 50 MHz sampling rate, 1 μs$=50$ pixels$=1.5$ mm.

Because the transducer is nonfocused, it receives signals from a larger solid angle than does a focused counterpart. In the reconstruction, we evenly projected the signals to each point within the whole solid angle according to the time delay. The time delay corresponds to the distance from the transducer to the point to which we project the signal. This is the algorithm called "delay and sum." In other words, the signal intensity of each point $A(i,j)$ is the sum of the signals from the transducer at different positions delayed with the transit time from the transducer position to the point. So the signal intensity at any point, $A(i,j)$, can be expressed as

$$A(i,j)=\sum_{k=0}^{M} B(k,l),$$

where $B(k,l)$ is the signal intensity coming from the lth pixel point in the signals and from the kth transducer scanning position, M is the total number of steps that the transducer scanned, and l is the distance from the kth transducer scanning position to the point (i,j):

$$l=\sqrt{(k-i)^2+j^2}.$$

Let us consider a point (i_1,j_1) where there is a thermoacoustic source. During the data acquisition, all the detectors will receive signals from this particular point after time delays determined by the above equation. Conversely, in the reconstruction, all the detectors contribute signals to this particular point with the appropriate time delays. On the other hand, for a point (i_2,j_2) where there is no source, few detectors contribute signals to this point after time delays determined by the above equation. Consequently, the reconstructed intensity at point (i_1,j_1) will be much greater than that at point (i_2,j_2). In this reconstruction scheme, the detection can be artificially focused onto any specified point (i,j), which is the basic concept of synthetic aperture.

We attempted to add some corrections to the delay-and-sum algorithm but found them unnecessary. For example, we tried applying weights to the signals according to the transducer's directivity, as was done previously. It improved the SNR, but the lateral resolution deteriorated as a result. In our situation, we had already acquired a satisfactory SNR by averaging the thermoacoustic signals 100 to 200 times, indicating that the direct delay-and-sum algorithm works well in LMTT technology.

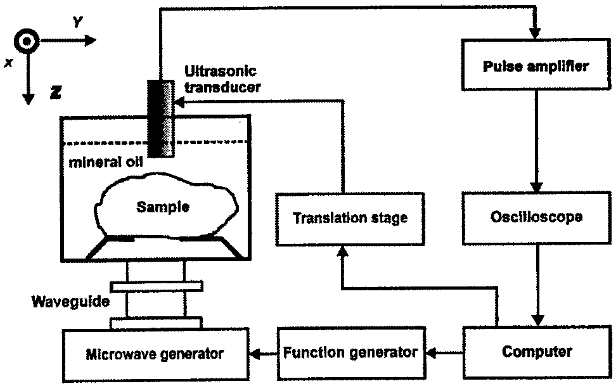

FIG. 2. Experimental setup.

B. Experimental setup

The experimental setup for this study is shown in Fig. 2. A Cartesian system was set up for reference. The z axis is along the ultrasonic axis pointing downward. The x axis is perpendicular to the drawing plane and pointed outward. The y axis is in the drawing plane and points to the right.

In the experimental setup, microwave pulses of 9 or 3 GHz, with a width of 0.5 μs were delivered into the samples. The sizes of the cross section of waveguides were 72 mm $\times 34$ mm in the 3 GHz system and 23 mm$\times$10 mm in the 9 GHz system. A function generator (DS345, Stanford Research System) was employed to trigger the microwave pulses and synchronize the sampling of an oscilloscope. A linear translation stage (MD2, Arrick Robotics), on which an ultrasonic transducer was mounted, was driven by a computer-controlled stepper motor. The transducer was scanned linearly. The nonfocused ultrasonic transducer (V323, Panametrics) mounted on the translation stage had a central frequency of 2.25 MHz and a 6 mm diam of an active element. A low-noise pulse preamplifier (500 PR, Panametrics) amplified the acoustic signals coming from the transducer. Then the amplified signals were collected and averaged by an oscilloscope (TDS-640A, Tektronix) and subsequently transferred to a personal computer. The acoustic waves from the sample were coupled to the ultrasonic transducer by mineral oil.

III. RESULTS AND DISCUSSION

In this section, we will present and discuss the images acquired from the 3 GHz microwave system and the 9 GHz microwave system, respectively. The first two sets of images were acquired from the 9 GHz system. In the first set of images, we imaged a semicylindrical fat sample with a

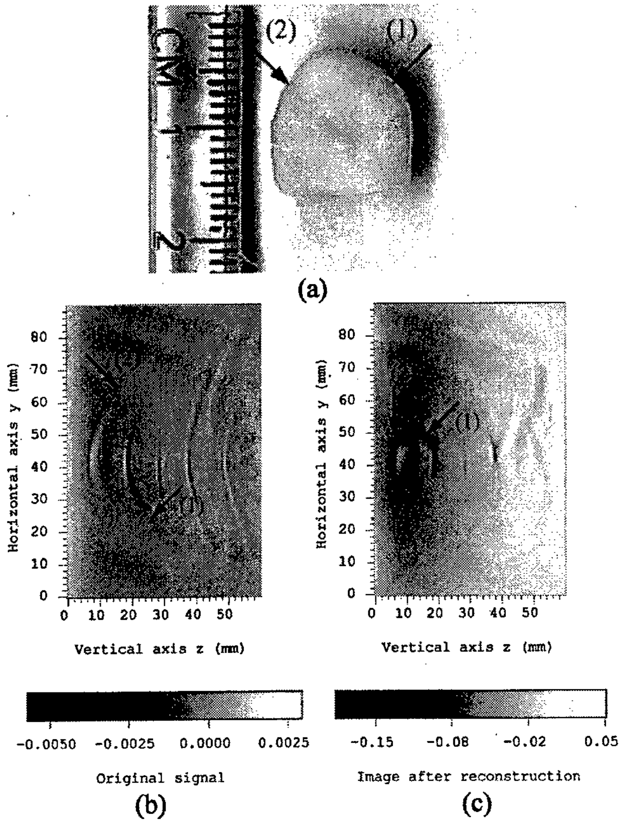

FIG. 3. (a) Cross-sectional picture of the sample with two curved boundaries marked with (1) and (2); (b) raw data of thermoacoustic signals acquired with the 9 GHz system, where the signals from the two curved boundaries are marked with (1) and (2), respectively; (c) image after the reconstruction, where the images of the two curved boundaries are marked with (1) and (2), respectively.

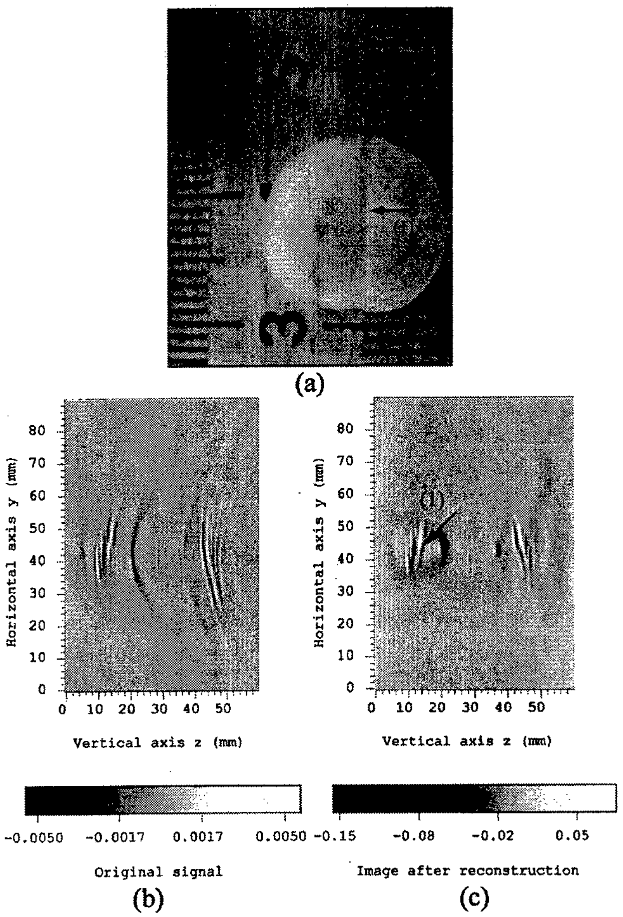

FIG. 4. (a) Cross-sectional picture of the sample, a pork fat cylinder with one layer of connective tissue (1) and discrete layers of muscle; (b) raw data of thermoacoustic signals acquired with the 9 GHz system; (c) Image after the reconstruction, where the images of the connective tissue layer is marked with (1).

simple structure to verify the synthetic-aperture method. In the second set of images, we imaged a small fat cylinder containing several detailed structures. The third set of images was acquired, using the 3 GHz system, from two muscle cylinders buried in an ellipse of pork fat. Comparing the last two sets of images demonstrates the effects of different object shapes and the different frequencies of the microwave sources.

A. Results

The sample in the first set of images is a semicylinder of pork fat immersed in mineral oil. Figure 3(a) shows a cross section of the semicylinder with two curved boundaries marked by (1) and (2). The transducer is on the left side of the picture, pointing to the sample and moving along the ruler. The original signals from the transducer are shown in Fig. 3(b). Because the thermoacoustic waves were propagating almost perpendicularly to the boundaries, the lateral signals (1) and (2) in Fig. 3(b) were from the corresponding curved boundaries (1) and (2) in Fig. 3(a). After reconstruction, the original signals (1) and (2) formed the curved boundaries (1) and (2) of the semicylinder in Fig. 3(c). The synthetic-aperture method was proved to be effective in imaging the curved boundaries. The flat boundary of the semicylinder is not visible in the image because this boundary was parallel to the axis of the transducer. The thermoacoustic waves from this flat boundary traveled perpendicularly to the axis of the transducer and never reached the transducer.

In the second set of images, Fig. 4(a) is the cross section of the sample, which was a pork fat cylinder with one layer of connective tissue (1) and several small pieces of muscle. The transducer was mounted on the left side of the picture, pointing to the sample and moving along the ruler. The images before and after reconstruction are shown in Fig. 4(b) and Fig. 4(c), respectively. The reconstructed image describes the structure of the sample very well. The connective tissue across the cylinder has been imaged clearly, as marked by (1) in Fig. 4(c). The muscles have been imaged as three slides parallel to each other because of the different distances between the muscles and the transducer. Because of the lateral convolution effect caused by the 6 mm diam of the transducer, the images of the muscles were stretched and overlapped along the y direction.

In the 9 GHz system, because of the small cross-sectional area in the 9 GHz waveguide, the microwaves were incident

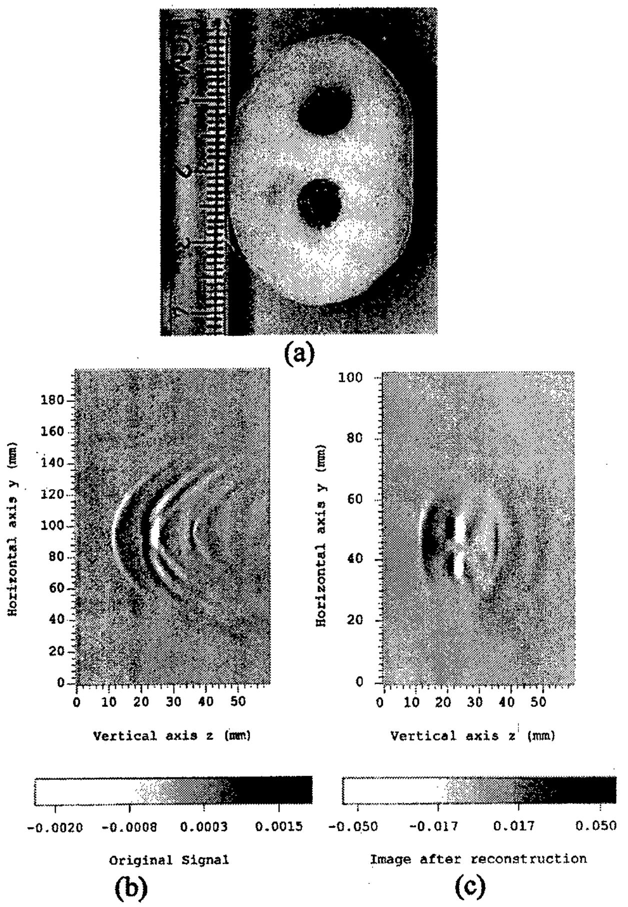

FIG. 5. (a) Cross-sectional picture of the sample, an ellipse of pork fat containing two muscle cylinders; (b) raw data of thermoacoustic signals acquired with the 3 GHz system; (c) image after the reconstruction.

upon the sample from the right to the left side along the transducer axis but in the opposite direction. In this case, the thermoacoustic waves emitted from the left curved edge were smaller than those emitted from the right curved edge. One reason is that the strong microwave absorption of the sample, especially the muscle layers in the sample in Fig. 4, decreased the intensity of the microwave field on the left side. The other reason is that the distribution of the microwave field, without considering sample absorption, also decreased with increasing distance from the sample to the outlet of the waveguide. Therefore, the left boundary of the sample in Fig. 4(c) is much weaker than the right one.

In the above two images acquired with the 9 GHz system, objects in the right part of the image produce a mirror image due to reflected thermoacoustic waves from the boundaries of the container. The reflected signals could be eliminated by time gating, but for comparison they were kept to maintain the same image scale as the images from the 3 GHz system.

The third set of images shown in Fig. 5 was gathered with the 3 GHz system. Shown in Fig. 5(a) is a cross section of the sample, which was an elliptic slab of pork fat with two muscle cylinders buried inside. With the sample being immersed in the mineral oil, the transducer pointed to the sample from the left side and moved along the ruler. In the 3 GHz system, the microwaves were incident upon the sample perpendicularly to the picture and pointed outward, which made the microwaves evenly distributed in the cross section of the sample. In the original signal data in Fig. 5(b), the signals from the muscle cylinder and the edge of the pork fat are spread into a hyperbola with similar shapes. The signals from the two muscle cylinders even cross each other in the center. After the reconstruction, the rebuilt image shown in Fig. 5(c) is in good agreement with the real sample shown in Fig. 5(a).

B. Discussion

From all of the images above, it is clear that the image resolution of curved boundaries of samples and of small cylinders is worse than that of horizontal boundaries, which emit thermoacoustic waves along the transducer axis. For example, the axial resolution of the slabs in Fig. 4(c) is much better than that of the two small cylinders in Fig. 5(c). The reason is that when the thermoacoustic wave does not come from the center of the transducer's receiving solid angle, it may reach different parts of the transducer surface at different times. In this case, the pulse signal is broadened and this broadening of the pulse is proportional to the dimensions of the transducer surface. If the thermoacoustic waves come from the center of the receiving solid angle of the transducer, the resolution is optimized. The propagating direction of most thermoacoustic waves from curved boundaries and small cylinders have large angles with the transducer axis. In other words, when the transducer detects these thermoacoustic waves, they are not from the center of the receiving solid angle. Therefore even after reconstruction, the axial resolution of the curved boundaries or small cylinders has been compromised. Also because of the 6 mm diam of the transducer, all of the images have been stretched along the y direction and the lateral resolution has deteriorated. Therefore, the diameter of the active element of the transducer is a key to both the axial and lateral resolutions. We can alleviate the effect of stretching and improve the axial resolution of the images by reducing the diameter of the transducer at the cost of losing the SNR.

Comparing the above images before and after reconstruction, the SNR has been greatly improved by the reconstruction. In the delay-and-sum algorithm, the signal intensity of every point is the sum of the signals from different positions that the transducer scanned. From the perspective of the SNR and randomization of the noise, summing up signals from k different positions has the equivalent effect of averaging the signal k times and will increase the SNR by $\sqrt{k}$ times. We can take advantage of this property to greatly reduce our average time in data acquisition and the dose of microwaves.

A comparison of the images in Fig. 4(c) and Fig. 5(c) shows that the 3 GHz system has a much larger image volume than the 9 GHz system due to the deeper penetration depth of the microwaves with a lower frequency and a larger cross section of the waveguide. For microwaves of 3 GHz, the penetration depths for muscle and fat are 1.2 and 9 cm, respectively, and for microwaves of 9 GHz, the penetration depths for muscle and fat are 0.27 and 2.6 cm. The depth we can image in the tissues is proportional to the penetration depth of the microwaves in the tissue. On the other hand, in near-surface imaging the 9 GHz setup has a better SNR than the 3 GHz system due to the larger attenuation of 9 GHz microwaves and the higher-power density of the microwave source.

In traditional LMTT, the ghost caused by the relatively small diameter of the focused transducer affects the lateral resolution. In synthetic aperture, the scanning nonfocused transducer can be artificially focused onto any specified point and the effect equals a focused transducer with a diameter of the scanning dimension. The large diameter, which is much larger than the diameter of the focused transducer used in conventional LMTT, greatly reduces the ghost and, therefore, improves the lateral resolution of the image.

In our study we point out that, compared with traditional LMTT, the synthetic-aperture method is effective for improving the lateral resolution of images and imaging the curved boundaries in samples. The resolution of the images can be further improved by reducing the diameter of the transducer or applying deconvolution with respect to the finite size of the transducer surface.

According to the IEEE standard, our case involves exposures under a controlled environment, which means the exposure is incurred by persons who are aware of the potential of exposure. For both the 3 and 9 GHz microwaves under a controlled environment, the upper limit of safe exposure is 10 $\mathrm{mW/cm^2}$. If it is used for partial body exposure, the upper limit is relaxed to 20 $\mathrm{mW/cm^2}$ for 3 GHz microwaves and 22.1 $\mathrm{mW/cm^2}$ for 9 GHz microwaves. The peak power of our 3 GHz microwave generator is 10 kW; the microwave pulse width is 0.5 μs; the pulse repetition rate is less than 40 Hz; and the outlet of the microwave generator is 72 mm $\times$34 mm. As a result, the power density of the 3 GHz microwave system is 8.2 $\mathrm{mW/cm^2}$. The peak power of our 9 GHz microwave generator is 25 kW; the microwave pulse width is 0.5 μs; the pulse repetition rate is about 2 Hz; and the outlet of the microwave generator is 23 mm$\times$10 mm. Consequently, the power density of the 9 GHz microwave system is 10.9 $\mathrm{mW/cm^2}$. Further, we assumed that the entire microwave has been coupled out of the waveguide without divergence. In practice, however, only part of the microwave is coupled out of the waveguide and diverged into a much larger area than the outlet of the waveguide. The power densities used in our experiments are below the limits of the IEEE standard and are safe to humans.

IV. CONCLUSIONS

The synthetic aperture, which has never been used in LMTT, is proved to be a powerful image reconstruction method. The reconstruction method based on the delay-and-sum algorithm has been verified to work well in LMTT because of its ability to image curved boundaries in samples, to improve the lateral resolution, and to reduce the noise of the system. The large diameter of the transducer causes resolution deterioration; the diameter can, however, be reduced to improve the resolution at the expense of the SNR. The comparison of the images shows that the 3 GHz system has a larger imaging volume but a poorer SNR than the 9 GHz system in near-surface imaging.

ACKNOWLEDGMENTS

This project was sponsored in part by the U.S. Army Medical Research and Material Command Grant No. DAMD17-00-1-0455, the National Institutes of Health Grants No. R01 CA71980 and No. R21 CA83760, the National Science Foundation Grant No. BES-9734491, and Texas Higher Education Coordinating Board Grant No. ARP 000512-0123-1999.

[a]Author to whom correspondence should be addressed. Telephone: 979-847-9040; fax: 979-845-4450; electronic mail: LWang@tamu.edu; URL: http://oilab.tamu.edu

[1] W. Joines, R. Jirtle, M. Rafal, and D. Schaeffer, "Microwave power absorption differences between normal and malignant tissue," Int. J. Radiat. Oncol., Biol., Phys. **6**, 681–687 (1980).

[2] S. Chaudhary, R. Mishra, A. Swarup, and J. Thomas, "Dielectric properties of normal human breast tissues at radiowave and microwave frequencies," Indian J. Biochem. Biophys. **21**, 76–79 (1984).

[3] W. Joines, Y. Zhang, C. Li, and R. Jirtle, "The measured electrical properties of normal and malignant human tissues from 50–900 MHz," Med. Phys. **21**, 547–550 (1994).

[4] L. E. Larsen and J. H. Jacobi, in *Medical Applications of Microwave Imaging* (IEEE, Piscataway, NJ, 1986).

[5] S. Caorsi, A. Frattoni, G. L. Gragnani, E. Nortino, and M. Pastorino, "Numerical algorithm for dielectric-permittivity microwave imaging of inhomogeneous biological bodies," Med. Biol. Eng. Comput. **29**, NS37–44 (1991).

[6] M. S. Hawley, A. Broquetas, L. Jofre, J. C. Bolomey, and G. Gaboriaud, "Microwave imaging of tissue blood content changes," J. Biomed. Eng. **13**, 197–202 (1991).

[7] P. M. Meaney, K. D. Paulsen, and J. T. Chang, "Near-field microwave imaging of biologically-based materials using a monopole transceiver system," IEEE Trans. Microwave Theory Tech. **46**, 31–45 (1998).

[8] L.-H. V. Wang, X. Zhao, H. Sun, and G. Ku, "Microwave-induced acoustic imaging of biological tissues," Rev. Sci. Instrum. **70**, 3744–3748 (1999).

[9] G. Ku and L.-H. V. Wang, "Scanning thermoacoustic tomography in biological tissue," Med. Phys. **27**, 1195–1202 (2000).

[10] G. Ku and L.-H. V. Wang, "Scanning microwave-induced thermoacoustic tomography: signal, resolution, and contrast," Med. Phys. **28**, 4–10 (2001).

[11] C. G. A. Hoelen, F. F. M. Demul, R. Pongers, and A. Dekker, "Three-dimensional photoacoustic imaging of blood vessels in tissue," Opt. Lett. **23**, 648–650 (1998).

[12] C. G. A. Hoelen, R. Pongers, G. Hamhuis, F. F. M. Demul, and J. Greve, "Photoacoustic blood cell detection and imaging of blood vessels in phantom tissue," SPIE **3196**, 142–153 (1998).

[13] A. A. Karabutov, E. V. Savateeva, N. B. Podymova, and A. A. Oraevsky, "Backward mode detection of laser-induced wide-band ultrasonic transients with optoacoustic transducer," J. Appl. Phys. **87**, 2003–2014 (2000).

[14] R. A. Kruger, P. Liu, Y. R. Fang, and C. R. Appledorn, "Photoacoustic ultrasound (PAUS)—Reconstruction tomography," Med. Phys. **22**, 1605–1609 (1995).

Time-Domain Reconstruction for Thermoacoustic Tomography in a Spherical Geometry

Minghua Xu and Lihong V. Wang*

Abstract—**Reconstruction-based microwave-induced thermoacoustic tomography in a spherical configuration is presented. Thermoacoustic waves from biological tissue samples excited by microwave pulses are measured by a wide-band unfocused ultrasonic transducer, which is set on a spherical surface enclosing the sample. Sufficient data are acquired from different directions to reconstruct the microwave absorption distribution. An exact reconstruction solution is derived and approximated to a modified backprojection algorithm. Experiments demonstrate that the reconstructed images agree well with the original samples. The spatial resolution of the system reaches 0.5 mm.**

Index Terms—**Microwave, reconstruction, thermoacoustic, tomography.**

I. INTRODUCTION

PULSED-MICROWAVE-INDUCED thermoacoustic tomography in biological tissues combines the advantages of pure microwave imaging [1]–[3] and pure ultrasound imaging [4], [5]. The wide range of microwave absorption coefficients found in different kinds of tissue leads to a high imaging contrast for biological tissues. However, it is difficult to achieve good spatial resolution in biological tissues using pure microwave imaging because of the long wavelength of microwaves. This problem can be overcome by the use of microwave-induced thermoacoustic waves. Because the velocity of acoustic waves in soft tissue is $\sim$1.5 mm/μs, thermoacoustic signals at megahertz can provide millimeter or better spatial resolution.

In thermoacoustic tomography, a short-pulsed microwave source is used to irradiate the tissue. The relatively long wavelength of the microwave, e.g., $\sim$3 cm at 3 GHz in tissues, serves to illuminate the tissue homogeneously. A wide-band ultrasonic transducer can then be employed to acquire the thermoacoustic signals excited by thermoelastic expansion, which carries the microwave absorption property of the tissue. The ultrasonic transducer is very sensitive in detecting small thermoacoustic vibrations from an object.

The key problem with this technique is how to determine the microwave absorption distribution from the measured data, i.e., how to map the inhomogeneity of the tissue. One approach is to use focused ultrasonic transducers to localize the thermoacoustic sources in linear or sector scans and then construct the images directly from the data as is often done in pulse-echo ultrasonography [6], [7]. An alternative method is to use wide-band point detectors to acquire thermoacoustic data and then reconstruct the microwave absorption distribution. To date, we have not seen an exact inverse solution for this specific problem, although some researchers have arrived at approximate reconstruction algorithms, such as the weighted delay-and-sum method [8], the optimal statistical approach [9], and other approach [10].

Based on spherical harmonic functions, in this paper we first deduce an exact solution to the problem in three-dimensional spherical geometry, which can be carried out in the frequency domain [11]–[14]. The exact reconstruction algorithms in planar and cylindrical geometries are reported in the companion papers [15], [16]. Spherical measurement geometry may be more suitable for investigation of external organs such as the breast. We assume that the wide-band unfocused ultrasonic transducer is set on a spherical surface, which encloses the sample under investigation. The data acquired from different directions are sufficient to allow us to reconstruct the microwave absorption distribution.

In many cases, the diameter of the sphere of detection is much larger than the ultrasonic wavelength. As a result, an approximate algorithm can be deduced, which is a modified backprojection of a quantity related to the thermoacoustic pressure. This approximate algorithm can be carried out in the time domain and is much faster than the exact solution. In our initial investigations, we have also tested tissue samples in a circular measurement configuration. These experiments demonstrate that the images calculated by the modified backprojection method agree well with the original samples. Moreover, the images have both the high contrast associated with pure microwave imaging and the 0.5-mm spatial resolution associated with pure ultrasonic imaging.

II. THEORY

A. Fundamental of Thermoacoustics

Thermoacoustic theory has been discussed in many literature reviews such as [13]. Here, we briefly review only the fundamental equations. If the microwave pumping pulse duration is

Manuscript received May 15, 2001; revised May 13, 2002. This work was supported in part by the U.S. Army under Medical Research and Material Command under Grant DAMD17-00-1-0455, in part by the National Institutes of Health (NIH) under Grant R01 CA71980, in part by the National Science Foundation (NSF) under Grant BES-9734491, and in part by the Texas Higher Education Coordinating Board under Grant ARP 000512-0123-1999. The Associate Editor responsible for coordinating the review of this paper and recommending its publication was G. Wang. *Asterisk indicates corresponding author.*

M. Xu is with the Optical Imaging Laboratory, Department of Biomedical Engineering, Texas A&M University, 3120 TAMU, College Station, TX 77843-3120 USA.

*L. V. Wang is with the Optical Imaging Laboratory, Department of Biomedical Engineering, Texas A&M University, College Station, TX 77843-3120 USA (e-mail: LWang@tamu.edu).

Publisher Item Identifier 10.1109/TMI.2002.801176.

0278-0062/02$17.00 © 2002 IEEE

much shorter than the thermal diffusion time, thermal diffusion can be neglected; consequently, the thermal equation becomes

$$\rho C_p \frac{\partial}{\partial t} T(\mathbf{r}, t) = H(\mathbf{r}, t) \tag{1}$$

where ρ is the density; C_p is the specific heat; $T(\mathbf{r}, t)$ is the temperature rise due to the energy pumping pulse; and $H(\mathbf{r}, t)$ is the heating function defined as the thermal energy per time and volume deposited by the energy source. We are initially interested in tissue with inhomogeneous microwave absorption but a relatively homogeneous acoustic property. The two basic acoustic generation equations in an acoustically homogeneous medium are the linear inviscid force equation

$$\rho \frac{\partial^2}{\partial t^2} \mathbf{u}(\mathbf{r}, t) = -\nabla p(\mathbf{r}, t) \tag{2}$$

and the expansion equation

$$\nabla \cdot \mathbf{u}(\mathbf{r}, t) = -\frac{p(\mathbf{r}, t)}{\rho c^2} + \beta T(\mathbf{r}, t) \tag{3}$$

where β is the isobaric volume expansion coefficient; c is the sound speed; $\mathbf{u}(\mathbf{r}, t)$ is the acoustic displacement; and $p(\mathbf{r}, t)$ is the acoustic pressure.

Combining (1)–(3), the pressure $p(\mathbf{r}, t)$ produced by the heat source $H(\mathbf{r}, t)$ obeys the following equation:

$$\nabla^2 p(\mathbf{r}, t) - \frac{1}{c^2}\frac{\partial^2}{\partial t^2} p(\mathbf{r}, t) = -\frac{\beta}{C_p}\frac{\partial}{\partial t} H(\mathbf{r}, t). \tag{4}$$

The solution based on Green's function can be found in the literature of physics or mathematics [12], [14]. A general form can be expressed as

$$p(\mathbf{r}, t) = \frac{\beta}{4\pi C_p} \iiint \frac{d^3 r'}{|\mathbf{r} - \mathbf{r}'|} \left.\frac{\partial H(\mathbf{r}', t')}{\partial t'}\right|_{t'=t-(|\mathbf{r}-\mathbf{r}'|/c)}. \tag{5}$$

The heating function can be written as the product of a spatial absorption function and a temporal illumination function

$$H(\mathbf{r}, t) = A(\mathbf{r}) I(t). \tag{6}$$

Thus, $p(\mathbf{r}, t)$can be expressed as

$$p(\mathbf{r}, t) = \frac{\beta}{4\pi C_p} \iiint \frac{d^3 r'}{|\mathbf{r} - \mathbf{r}'|} A(\mathbf{r}') I'(t') \tag{7}$$

where $I'(t') = dI(t')/dt'$.

B. Exact Reconstruction Theory

We first solve the problem where the pulse pumping is a Dirac delta function

$$I(t) = \delta(t). \tag{8}$$

Suppose the detection point on the spherical surface $\mathbf{r} = \mathbf{r}_0$, which encloses the sample (Fig. 1). By dropping the primes, (7) may be rewritten as

$$p(\mathbf{r}_0, t) = \eta \iiint d^3 r A(\mathbf{r}) \frac{\delta'\left(t - \frac{|\mathbf{r}_0 - \mathbf{r}|}{c}\right)}{4\pi |\mathbf{r}_0 - \mathbf{r}|} \tag{9}$$

where $\eta = \beta / C_p$. The inverse problem is to reconstruct the absorption distribution $A(\mathbf{r})$ from a set of data $p(\mathbf{r}_0, t)$ measured at positions $\mathbf{r}_0$. Taking the Fourier transform on variable t of (9), and denoting $k = \omega / c$, we get

$$\tilde{p}(\mathbf{r}_0, \omega) = -i\omega\eta \iiint d^3 r A(\mathbf{r}) \frac{\exp(ik|\mathbf{r}_0 - \mathbf{r}|)}{4\pi |\mathbf{r}_0 - \mathbf{r}|} \tag{10}$$

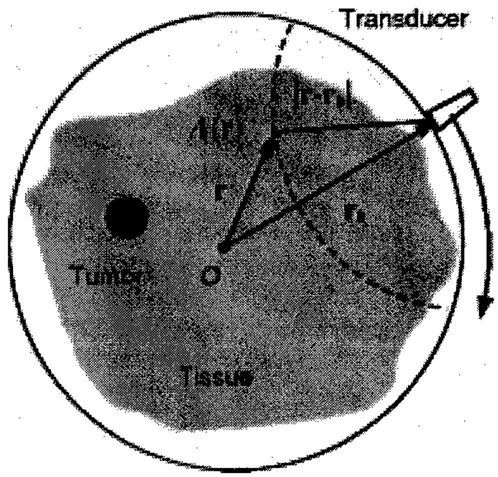

Fig. 1. Acoustic detection scheme. The ultrasonic transducer at position $\mathbf{r}_0$ records the thermoacoustic signals on a spherical surface with radius $|\mathbf{r} - \mathbf{r}_0|$.

where the following Fourier transform pair exists:

$$\tilde{p}(\mathbf{r}_0, \omega) = \int_{-\infty}^{+\infty} p(\mathbf{r}_0, t) \exp(i\omega t)\, dt, \tag{11a}$$

$$p(\mathbf{r}_0, t) = \frac{1}{2\pi} \int_{-\infty}^{+\infty} \tilde{p}(\mathbf{r}_0, \omega) \exp(-i\omega t)\, d\omega. \tag{11b}$$

We next derive the exact solution using the spherical harmonic function basis. In the derivation, we referred to the mathematical techniques for ultrasonic reflectivity imaging [11]. The mathematics utilized can also be found routinely in the mathematical literature, such as [12]. Here, we list the identities (12a)–(12f) used in the subsequent deduction:

1) The complete orthogonal integral of spherical harmonics $Y_l^m(\theta_0, \varphi_0)$

$$\iint_{\Omega_0} Y_l^m(\theta_0, \varphi_0) Y_k^{n^*}(\theta_0, \varphi_0)\, d\Omega_0 = \delta_{l,k}\delta_{m,n} \tag{12a}$$

where $d\Omega_0 = \sin\theta_0\, d\theta_0\, d\varphi_0$ and $*$ denotes the complex conjugate.

2) The Legendre polynomial

$$P_l(\mathbf{n} \cdot \mathbf{n}_0) = \frac{4\pi}{2l+1} \sum_{m=-l}^{+l} Y_l^m(\theta, \varphi) Y_l^{m^*}(\theta_0, \varphi_0) \tag{12b}$$

where the unit vectors $\mathbf{n}$ and $\mathbf{n}_0$ point in the directions (θ, φ) and (θ_0, φ_0), respectively.

3) The orthogonal integral of Legendre polynomials, derived from (12a) and (12b)

$$\iint_{\Omega_0} d\Omega_0 P_l(\mathbf{n} \cdot \mathbf{n}_0) P_m(\mathbf{n}' \cdot \mathbf{n}_0) = \frac{4\pi}{2l+1} \delta_{lm} P_l(\mathbf{n} \cdot \mathbf{n}') \tag{12c}$$

where the unit vector $\mathbf{n}' = \mathbf{r}'/r'$ points in the direction (θ', φ').

4) The expansion identity

$$\frac{\exp(ik|\mathbf{r}_0 - \mathbf{r}|)}{4\pi|\mathbf{r}_0 - \mathbf{r}|} = \frac{ik}{4\pi} \sum_{l=0}^{\infty} (2l+1) j_l(kr) h_l^{(1)}(kr_0) P_l(\mathbf{n} \cdot \mathbf{n}_0), \quad (k > 0) \tag{12d}$$

where $\mathbf{n} = \mathbf{r}/r$, $\mathbf{n}_0 = \mathbf{r}_0/r_0$, $j_l(\cdot)$ and $h_l^{(1)}(\cdot)$ are the spherical Bessel and Hankel functions, respectively.

5) The complete orthogonal integral of Bessel functions

$$\int_0^{+\infty} dk k^2 j_m(kr) j_m(kr') = \frac{\pi}{2r^2}\delta(r-r'). \tag{12e}$$

6) The summation identity of Legendre polynomials

$$\sum_{m=0}^{\infty}(2m+1)P_m(\mathbf{n}\cdot\mathbf{n}') = \frac{4\pi\delta(\theta-\theta')\delta(\varphi-\varphi')}{\sin\theta}. \tag{12f}$$

First, substituting (12d) into (10), we obtain

$$\tilde{p}(\mathbf{r}_0, \omega) = \frac{\omega k\eta}{4\pi}\iiint d^3r A(\mathbf{r})\sum_{l=0}^{\infty}(2l+1)j_l(kr) \cdot h_l^{(1)}(kr_0)P_l(\mathbf{n}\cdot\mathbf{n}_0). \tag{13}$$

Then, multiplying both sides of (13) by $P_m(\mathbf{n}'\cdot\mathbf{n}_0)$, and integrating with respect to $\mathbf{n}_0$ over the surface of the sphere, and considering the identity (12c), we obtain

$$\begin{aligned}
&\iint_{\Omega_0} d\Omega_0\tilde{p}(\mathbf{r}_0, \omega)P_m(\mathbf{n}'\cdot\mathbf{n}_0)\\
&\quad= \frac{\omega k\eta}{4\pi}\iiint d^3r A(\mathbf{r})\sum_{l=0}^{\infty}(2l+1)j_l(kr)h_l^{(1)}(kr_0)\\
&\qquad\cdot\iint_{\Omega_0} d\Omega_0 P_l(\mathbf{n}\cdot\mathbf{n}_0)P_m(\mathbf{n}'\cdot\mathbf{n}_0)\\
&\quad= \frac{\omega k\eta}{4\pi}\iiint d^3r A(\mathbf{r})\sum_{l=0}^{\infty}(2l+1)j_l(kr)h_l^{(1)}(kr_0)\frac{4\pi}{2l+1}\\
&\qquad\cdot\delta_{lm}P_l(\mathbf{n}\cdot\mathbf{n}')\\
&\quad= k^2\eta c\iiint d^3r A(\mathbf{r})j_m(kr)h_m^{(1)}(kr_0)P_m(\mathbf{n}\cdot\mathbf{n}')
\end{aligned}$$

i.e.,

$$\iint_{\Omega_0} d\Omega_0\tilde{p}(\mathbf{r}_0, \omega)P_m(\mathbf{n}'\cdot\mathbf{n}_0)\frac{1}{h_m^{(1)}(kr_0)} = k^2\eta c\iiint d^3r A(\mathbf{r})j_m(kr)P_m(\mathbf{n}\cdot\mathbf{n}'). \tag{14}$$

Further, multiplying both sides of (14) by $j_m(kr')$, integrating them with respect to k from zero to $+\infty$, and then multiplying both sides of (14) again by $(2m+1)$ and summing m from zero to ∞, and considering the identity (12e) and (12f), we get

$$\begin{aligned}
&\iint_{\Omega_0} d\Omega_0\int_0^{+\infty} dk\tilde{p}(\mathbf{r}_0, \omega)\sum_{m=0}^{\infty}\frac{(2m+1)j_m(kr')}{h_m^{(1)}(kr_0)}P_m(\mathbf{n}'\cdot\mathbf{n}_0)\\
&\quad= \eta c\iiint d^3r A(\mathbf{r})\sum_{m=0}^{\infty}(2m+1)P_m(\mathbf{n}\cdot\mathbf{n}')\int_0^{+\infty} dk k^2\\
&\qquad\cdot j_m(kr')j_m(kr)\\
&\quad= \eta c\iiint d^3r A(\mathbf{r})\frac{4\pi\delta(\theta-\theta')\delta(\varphi-\varphi')}{\sin\theta}\frac{\pi}{2r^2}\delta(r-r')\\
&\quad= 2\pi^2\eta c A(\mathbf{r}').
\end{aligned}$$

Finally, dropping the primes, we can rewrite the equation as

$$A(\mathbf{r}) = \frac{1}{2\pi^2\eta c}\iint_{\Omega_0} d\Omega_0\int_0^{+\infty} dk\tilde{p}(\mathbf{r}_0, \omega) \cdot\sum_{m=0}^{\infty}\frac{(2m+1)j_m(kr)}{h_m^{(1)}(kr_0)}P_m(\mathbf{n}\cdot\mathbf{n}_0). \tag{15}$$

This is the exact inverse solution of (9). It involves summation of a series and may take much time to compute. Therefore, it is desirable to further simplify the solution.

C. Modified Backprojection

In experiments, the detection radius r_0 is usually much larger than the wavelengths of the thermoacoustic waves that are useful for imaging. Because the low-frequency component of the thermoacoustic signal does not significantly contribute to the spatial resolution, it can be removed by a filter. Therefore, we can assume $|k|r_0 \gg 1$ and use the asymptotic form of the Hankel function to simplify (15). The following two identities are involved [12]:

1) The expansion identity similar to (12d)

$$\frac{\exp(-ik|\mathbf{r}_0-\mathbf{r}|)}{4\pi|\mathbf{r}_0-\mathbf{r}|} = \frac{-ik}{4\pi}\sum_{m=0}^{\infty}(2m+1)j_m(kr) \cdot h_m^{(2)}(kr_0)P_m(\mathbf{n}\cdot\mathbf{n}_0), \qquad (k>0). \tag{16a}$$

2) The approximation when $|k|r_0 \gg 1$

$$h_m^{(1)}(kr_0) \approx \frac{1}{h_m^{(2)}(kr_0)}\left(\frac{1}{(kr_0)^2}+O\left(\frac{1}{(kr_0)^4}\right)\right) \tag{16b}$$

where $h_l^{(2)}(\cdot)$ is the spherical Hankel function of the second kind.

Substituting (16b) into (15), we get

$$A(\mathbf{r}) \approx \frac{1}{2\pi^2\eta c}\iint_{\Omega_0} d\Omega_0\int_0^{+\infty} dk\tilde{p}(\mathbf{r}_0, \omega)k^2r_0^2\sum_{m=0}^{\infty}(2m+1) \cdot j_m(kr)h_m^{(2)}(kr_0)P_m(\mathbf{n}\cdot\mathbf{n}_0). \tag{17}$$

Considering the form of (16a), the above equation can be rewritten as

$$\begin{aligned}
A(\mathbf{r}) &= \frac{r_0^2}{2\pi^2\eta c}\iint_{\Omega_0} d\Omega_0\int_0^{+\infty} dk\tilde{p}(\mathbf{r}_0, \omega)(ik)\\
&\quad\cdot\frac{\exp(-ik|\mathbf{r}_0-\mathbf{r}|)}{|\mathbf{r}_0-\mathbf{r}|}\\
&= -\frac{r_0^2}{\pi\eta c^3}\iint_{\Omega_0} d\Omega_0\frac{1}{2\pi}\int_0^{+\infty} d\omega\tilde{p}(\mathbf{r}_0, \omega)(-i\omega)\\
&\quad\cdot\frac{\exp\left(-i\omega\frac{|\mathbf{r}_0-\mathbf{r}|}{c}\right)}{|\mathbf{r}_0-\mathbf{r}|}.
\end{aligned}$$

Because $p(\mathbf{r}, t)$ is a real function, $p^*(\mathbf{r}, \omega) = p(\mathbf{r}, -\omega)$. Taking the summation of the above equation with its complex conjugate and then dividing it by two, we get

$$\begin{aligned}
A(\mathbf{r}) &= \frac{r_0^2}{4\pi^2\eta c}\iint_{\Omega_0} d\Omega_0\int_{-\infty}^{+\infty} dk\tilde{p}(\mathbf{r}_0, \omega)(ik)\\
&\quad\cdot\frac{\exp(-ik|\mathbf{r}_0-\mathbf{r}|)}{|\mathbf{r}_0-\mathbf{r}|}\\
&= -\frac{r_0^2}{2\pi\eta c^3}\iint_{\Omega_0} d\Omega_0\frac{1}{2\pi}\int_{-\infty}^{+\infty} d\omega\tilde{p}(\mathbf{r}_0, \omega)(-i\omega)\\
&\quad\cdot\frac{\exp\left(-i\omega\frac{|\mathbf{r}_0-\mathbf{r}|}{c}\right)}{|\mathbf{r}_0-\mathbf{r}|}.
\end{aligned}$$

Recalling the inverse Fourier transform (11b), we get

$$A(\mathbf{r}) = -\frac{r_0^2}{2\pi\eta c^3}\iint_{\Omega_0} d\Omega_0\,\frac{1}{|\mathbf{r}_0-\mathbf{r}|}\,\frac{\partial p(\mathbf{r}_0,t)}{\partial t}\bigg|_{t=|\mathbf{r}_0-\mathbf{r}|/c} \tag{18}$$

i.e.,

$$A(\mathbf{r}) = -\frac{r_0^2}{2\pi\eta c^4}\iint_{\Omega_0} d\Omega_0\,\frac{1}{t}\,\frac{\partial p(\mathbf{r}_0,t)}{\partial t}\bigg|_{t=|\mathbf{r}_0-\mathbf{r}|/c}. \tag{19}$$

Equation (19) shows that the absorption distribution can be calculated in the time domain by the means of backprojection and coherent summation over spherical surfaces of the quantity $-(1/t)(\partial p(\mathbf{r}_0,t)/\partial t)$ instead of the acoustic pressure itself. This approximate algorithm requires less computing time than the exact solution (15).

For initial investigations, we measure the samples in a circular configuration. In these cases, the backprojection is carried out in a circle around the slices, and (19) can be simplified to

$$A(\mathbf{r}) = -\frac{r_0^2}{2\pi\eta c^4}\int_{\varphi_0} d\varphi_0\,\frac{1}{t}\,\frac{\partial p(\mathbf{r}_0,t)}{\partial t}\bigg|_{t=|\mathbf{r}_0-\mathbf{r}|/c}. \tag{20}$$

III. EXPERIMENTAL METHOD

A. Diagram of Setup

Fig. 2 shows the experimental setup for the circular measurement configuration, which is modified from our previous paper [7]. For the convenience of the reader, the system is briefly described here. The unfocused transducer (V323, Panametrics) has a central frequency of 2.25 MHz and a diameter of 6 mm. It is fixed and it points horizontally to the center of the rotation stage, which is used to hold the samples. For good coupling of acoustic waves, both the transducer and the sample are immersed in mineral oil in a container.

The microwave pulses are transmitted from a 3-GHz microwave generator with a pulse energy of 10 mJ and a width of 0.5 μs, and then delivered to the sample from the bottom by a rectangular waveguide with a cross section of 72 mm × 34 mm. A function generator (Protek, B-180) is used to trigger the microwave generator, control its pulse repetition frequency, and synchronize the oscilloscope sampling. The signal from the transducer is first amplified through a pulse amplifier, then recorded and averaged 200 times by an oscilloscope (TDS640A, Tektronix). A personal conputer is used to control the step motor for rotating the sample and transferring the data.

Last, we want to point out that, in our experiments, the smallest distance r_0 between the rotation center and the surface of the transducer is 4.3 cm. In the frequency domain (100 KHz- 1.8 MHz), $|k|r_0 = 2\pi r_0 f/c$ with 1.5 mm/μs, we get $18 < |k|r_0 < 330$. Therefore, the required condition $|k|r_0 \gg 1$ for the modified backprojection algorithm is satisfied.

B. Technical Consideration

During measurement, we find that the piezoelectric signal $S_0(\mathbf{r}_0, t)$ detected by the transducer includes the thermal acoustic signal $S(\mathbf{r}_0, t)$ as well as some noise. The noise comes from two contributors. One is the background random noise of the measurement system, which can be suppressed by averaging the measured data. The other part, $S_{mp}(t)$, results from the microwave pumping via electromagnetic induction.

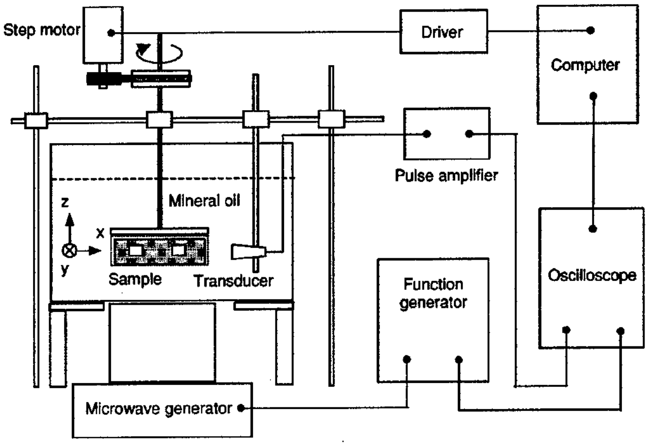

Fig. 2. The experimental setup.

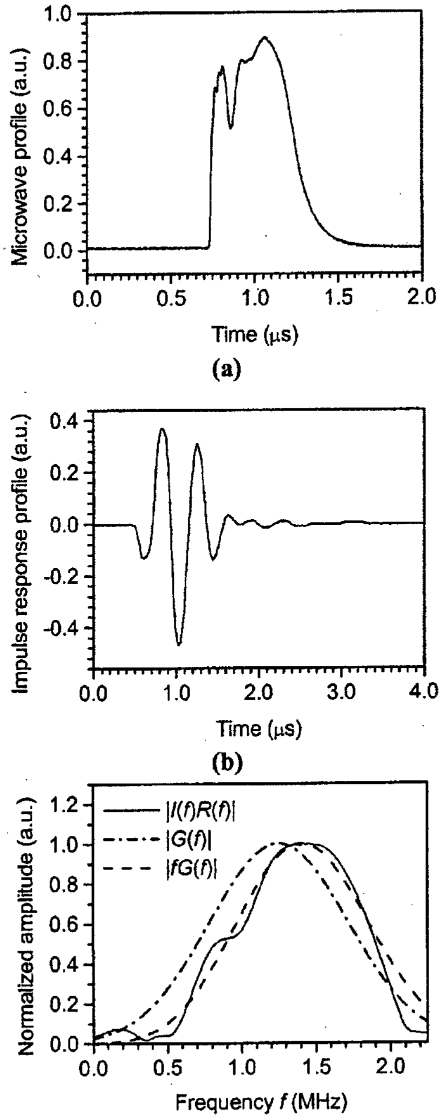

(a)

(b)

(c)

Fig. 3. (a) The temporal profile of the microwave pulse; (b) the temporal profile of the impulse response of the transducer; (c) compare the normalized amplitudes of the spectrum $I(f)R(f)$, $G(f)$ and $fG(f)$.

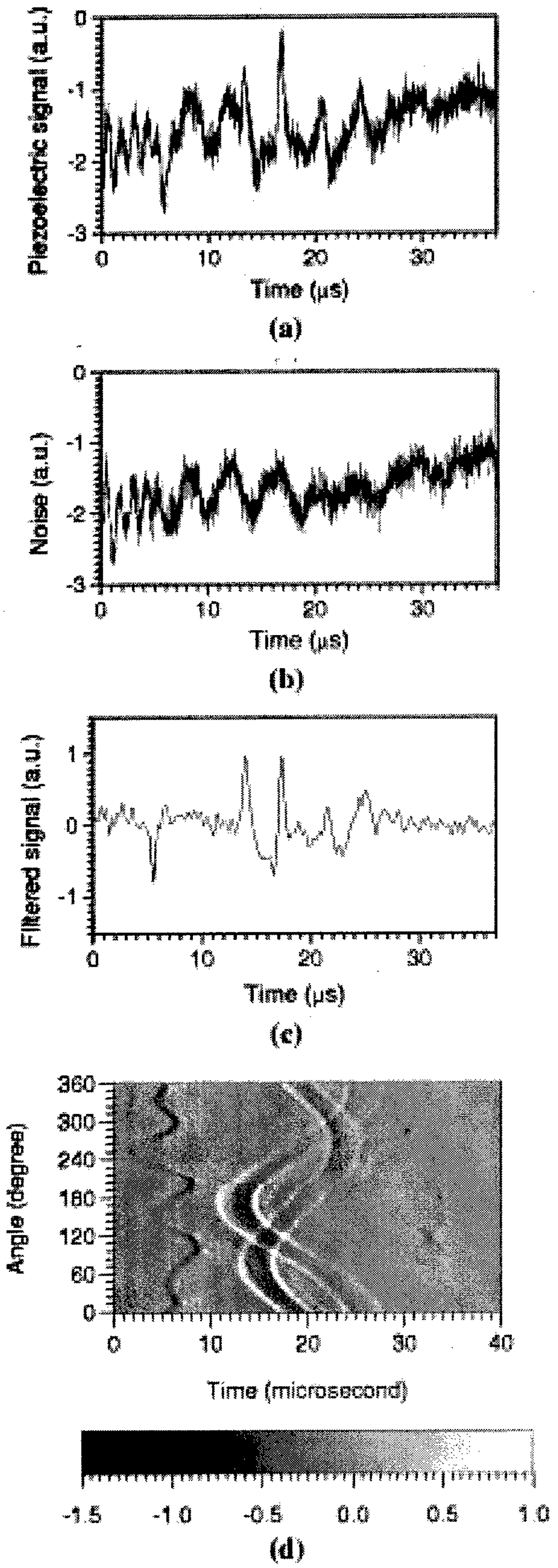

Fig. 4. (a) An example of temporal piezoelectric signal; (b) an example of temporal noise; (c) an example of filtered signal; and (d) an example of filtered thermoacoustic signals detected at different angular positions from 0° to 360°.

The pumping component of the noise can be measured without a sample, and can be subtracted from the measured data

$$S(\mathbf{r}_0, t) \approx S_0(\mathbf{r}_0, t) - S_{mp}(t). \tag{21}$$

In fact, the transducer is not a real point detector. For simplicity, we can ignore its size if we put it far away from the sample. However, we still have to consider the impulse response $R(t)$ of the transducer and the pumping duration $I(t)$ of the microwave pulse. In general, the measured thermoacoustic signal can be written as a convolution

$$S(\mathbf{r}_0, t) = p(\mathbf{r}_0, t) * I(t) * R(t) \tag{22}$$

where $p(\mathbf{r}_0, t)$ is the thermoacoustic signal with delta-pulse microwave pumping. In the frequency domain, (22) can be written as

$$S(\mathbf{r}_0, \omega) = p(\mathbf{r}_0, \omega) I(\omega) R(\omega) \tag{23}$$

where

$$I(\omega) = \int_{-\infty}^{+\infty} I(t) \exp(i\omega t)\, dt, \tag{24a}$$

$$R(\omega) = \int_{-\infty}^{+\infty} R(t) \exp(i\omega t)\, dt. \tag{24b}$$

Because of the presence of noise and the finite bandwidth of $I(\omega)$ and $R(\omega)$, an appropriate deconvolution algorithm should be used to calculate $p(\mathbf{r}_0, \omega)$. In the reconstruction, only the high-frequency component of the thermoacoustic signal is required. Therefore, we compute $p(\mathbf{r}_0, \omega)G(\omega)$ instead, where $G(\omega)$ is a high-frequency bandpass filter such as a Gaussian filter

$$G(\omega) = \exp\left[-\alpha\left(\frac{\omega}{\omega_0} - 1\right)^2\right]$$

and α and ω_0 are two parameters of the filter, $\omega = 2\pi f$ and $\omega_0 = 2\pi f_0$.

In our experiments, $I(t)$ is approximately a rectangular function with duration $\tau = 0.5$ μs and its temporal profile is shown in Fig. 3(a). Its spectrum $I(\omega)$ covers the range from 0 to 2 MHz. The transducer that we used is of the videoscan type with a central frequency of $f_0 = 2.25$ MHz, and the temporal profile of the impulse response is shown in Fig. 3(b). It is observed that the generated thermoacoustic signal under microwave pumping with duration $\tau = 0.5$ μs exists primarily in a frequency range below 1.8 MHz. We chose the parameters $\alpha = 3.6$ and $f_0 = 1.25$ MHz in the Gaussian filter

$$G(f) = \exp\left[-\alpha\left(\frac{f}{f_0} - 1\right)^2\right]$$

to eliminate the noise at high as well as low frequencies. The spectrum $G(f)$ is shown as the dash-dot line in Fig. 3(c). We compared the normalized spectrum $I(f)R(f)$ [solid line in Fig. 3(c)] with $fG(f)$ [dash line in Fig. 3(c)], and found $|fG(f)| \approx |I(f)R(f)|$ when $f < 2$ MHz. Of course, this approximated equality is a special case for our measurement system only. Therefore, the filtered $\partial p(\mathbf{r}_0, t)/\partial t$ can be simply calculated by an inverse fast Fourier transform (IFFT)

$$\frac{\partial p(\mathbf{r}_0, t)}{\partial t} \approx \mathrm{IFFT}\left\{S(\mathbf{r}_0, \omega)F(\omega)\right\} \tag{25}$$

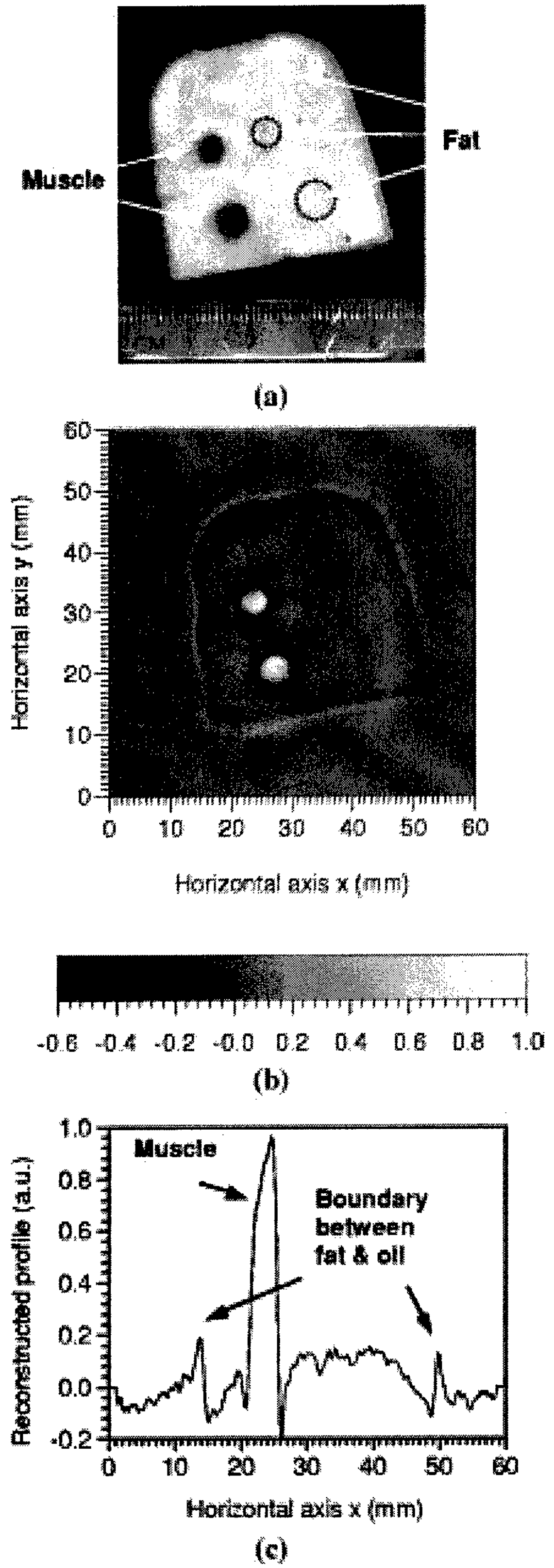

Fig. 5. (a) Cross section of a tissue sample; (b) reconstructed image; and (c) a line profile of the reconstructed image at $y = 31.5$ mm.

where $F(\omega)$ is a wide bandpass filter, which is used to further eliminate noise at high and low frequencies in order to guarantee the condition $|k|r_0 \gg 1$ for the modified backprojection. A simple filter is

$$F(f) = \begin{cases} 1, & 0.1\,\text{MHz} < f < 1.8\,\text{MHz} \\ 0, & \text{otherwise.} \end{cases} \tag{26}$$

IV. RESULTS AND DISCUSSION

Finally, we use the above modified backprojection algorithm and the experimental method to investigate some tissue samples.

A. Experimental Data Preprocessing

The measured piezoelectric data include the useful thermoacoustic signal as well as some noise data as illustrated by the following example. Fig. 4(a) is a typical measured temporal piezoelectric signal, which is from the sample shown in Fig. 5(a). One portion of the noise resulting from the microwave pumping looks like the curve in Fig. 4(b), which is acquired at the same sampling rate and the same delay time with the transducer in the same position as the curve in Fig. 4(a). Because the slice is very thin, the thermoacoustic signal is not much higher than the noise resulting from the microwave pumping. Next, we subtract the noise from the raw thermoacoustic signal and use a wide bandpass filter to eliminate some of the useless low-frequency and high-frequency components. This processed data is shown in Fig. 4(c); it is much cleaner than the raw data in Fig. 4(a). The filtered thermoacoustic signals detected at different angular positions from 0° to 360° are shown in Fig. 4(d).

B. Image Contrast

Image contrast is an important index for biological imaging. Fig. 5(a) shows a tested sample, which was photographed after the experiment. The sample was made according to the following procedure. First, we cut a thin piece of homogeneous pork fat tissue and shaped it arbitrarily to form a base. Its thickness is 5 mm and its maximum diameter is 4 cm. Then we used different screwdrivers to carefully make two pairs of holes that were approximately 4 and 6 mm in diameter, respectively. Finally, one big and one small hole on the left side were filled with pork muscle, while the two holes on the right side were filled with pork fat of the same type as that which made up the base.

In the experiment, the transducer rotationally scanned the sample from 0° to 360° with a step size of 2.25°. The detection radius r_0 was 4.3 mm. We used the 160 series of data as shown in Fig. 4(d) to calculate the image by our modified backprojection method.

The reconstructed image is shown in Fig. 5(b). The outline and size of the fat base as well as the sizes and locations of the two muscle pieces are in good agreement with the original sample in Fig. 5(a). Fig. 5(c) shows a line profile for the small piece of muscle in the image. It indicates that the contrast between the fat and the muscle is very high. This high contrast is due to the low microwave absorption capacity of fat and the high absorption capacity of muscle: at 3 GHz, the penetration depth for muscle and fat are 1.2 and 9 cm, respectively. However, the two pieces of fat are not visible in the image [Fig. 5(b)], which means the minute mechanical discontinuity between the boundaries of muscle and fat does not contribute much to the thermoacoustic signal. On the contrary, discontinuity improves the strength of the echo sounds in pure ultrasound imaging.

C. Spatial Resolution

Spatial resolution is another important index for biological imaging. We used samples with a set of small thermoacoustic sources to test the resolution. One tested sample is shown in Fig. 6(a), which was also photographed after the experiment was completed.

The sample was made according to the following procedure. First, we cut a thin piece of homogeneous pork fat tissue and made it into an arbitrary shape. Its thickness was 5 mm with a maximum diameter of 4 cm. Then we used a small screwdriver to carefully make a set of small holes about 2 mm in diameter. In the meantime, we prepared a hot solution with 5% gelatin, 0.8% salt, and a drop of dark ink (to improve the photographic properties of the sample). Next, we used an injector to inject a drop of the gelatin solution into each small hole and subsequently blew out the air to make good coupling between the gelatin solution and the fat tissue. After being cooled in room temperature for about 15 min, the gelatin solution was solidified. During the experiment, the transducer also rotationally scanned the sample from 0° to 360° with a step size of 2.25°. The detection radius r_0 was 4.3 mm.

The reconstructed image produced by our modified backprojection method is shown in Fig. 6(b); it also agrees with the original sample well. In particular, the relative locations and sizes of those small thermoacoustic sources are clearly resolved and perfectly match the original ones. Fig. 6(c) shows a reconstructed profile (solid curve) at position $x = 27.45$ mm of the image Fig. 6(b), which includes two gelatin sources with a distance of about 3 mm. Each gelatin source has a distinct profile in the image. The boundaries between them are clearly imaged. Moreover, the reconstructed profile is in good agreement with the original profile (dashed curve), which was a grayscale profile of the image Fig. 6(b). The half-amplitude line cuts across the reconstructed profile at points B_1, A_1, A_2, and B_2, respectively. The distances $|A_1B_1| = 1.72$ mm and $|A_2B_2| = 1.67$ mm in the image are close to the original values of about 1.80 and 1.60 mm, respectively, which were measured in the original objects. Therefore, the width of the profile at the half-amplitude closely measures its physical size.

We here define a resolving criterion to estimate the spatial resolution. The quarter-amplitude line cuts across the profiles at points C_1 and C_2, respectively, as shown in Fig. 6(c). If the right source moves to the position of the left one, the reconstructed profile is equal to the spatial summation of the profiles of the two sources, because of the linear superposition property of acoustic waves. When point C_2 encounters C_1, the new amplitude at C_2 or C_1 would reach the half amplitude, and the two sources could still be differentiated. If the right one moves more to the left, the new amplitude between their overlap regions would elevate to more than the half amplitude. When we use a half-amplitude line to cut across the profiles, we get only two points on the far side of each profile, which means that these two sources can no longer be clearly distinguished. Further, when point A_1 touches A_2, these two sources join as a single object in the image.

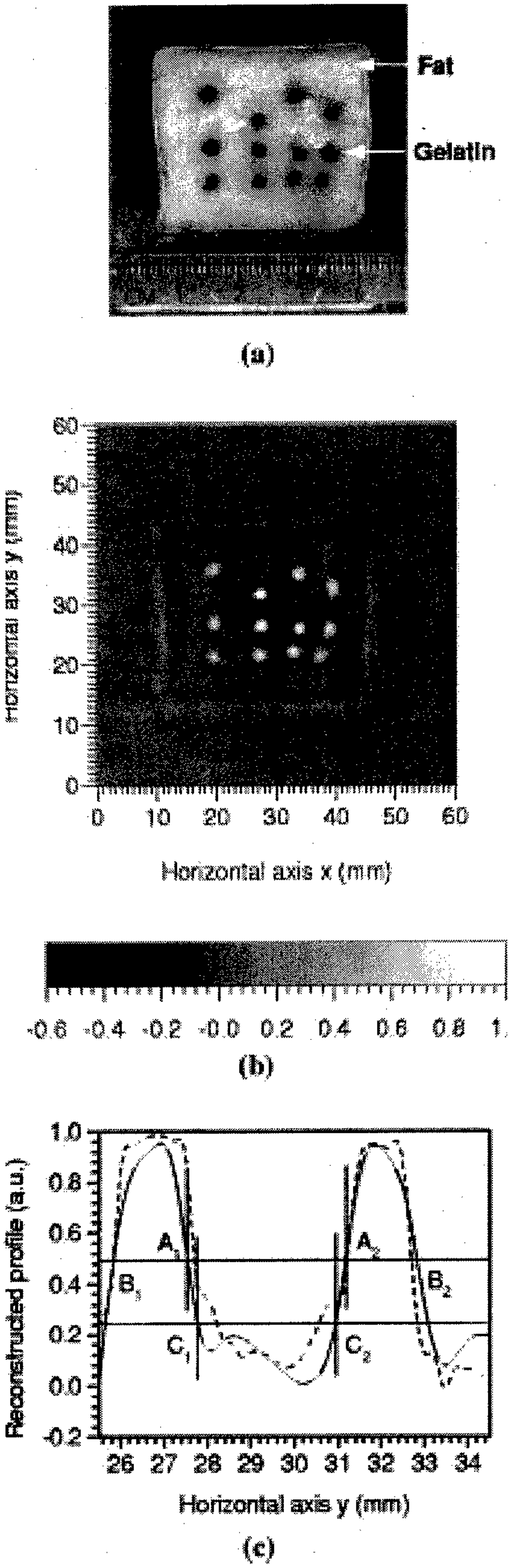

Fig. 6. (a) Cross section of a tissue sample; (b) reconstructed image; and (c) comparison between a line profile (solid curve) of the reconstructed image (b) at $x = 27.45$ mm and the corresponding grayscale profile (dashed curve) of the original image (a).

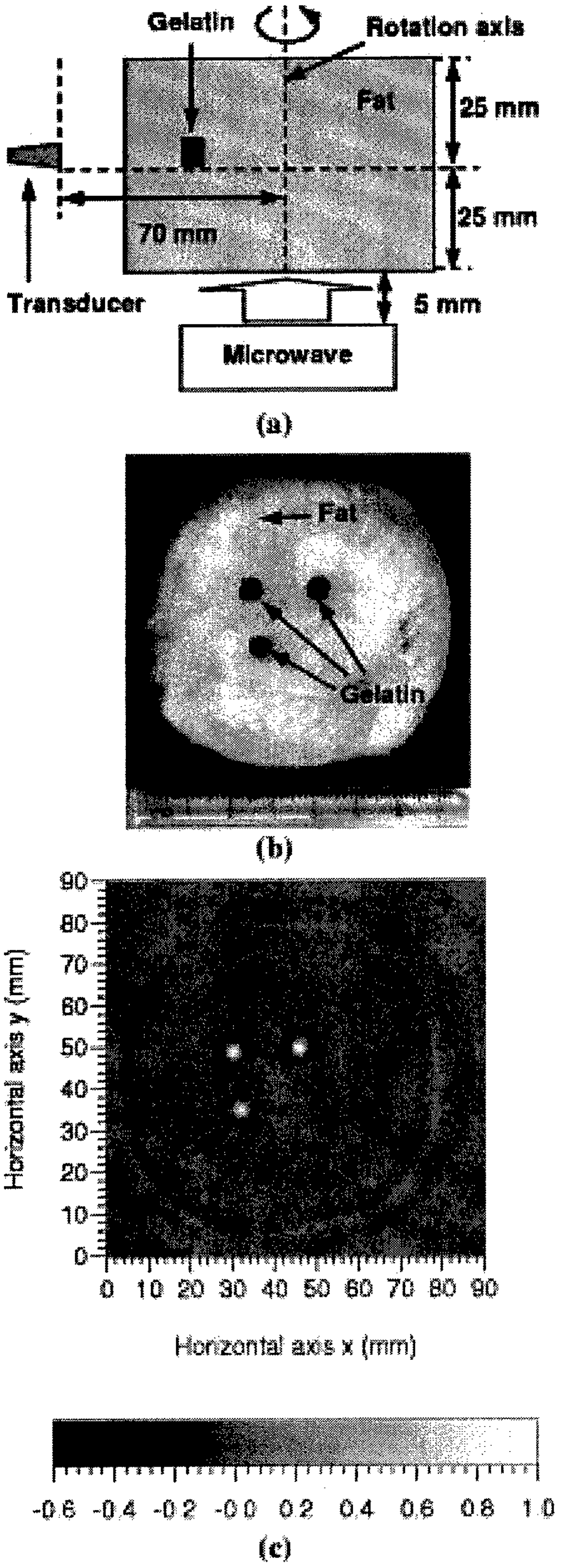

Fig. 7. (a) Diagram of the sample structure and the measurement; (b) cross section of the tissue sample; and (c) reconstructed image.

Therefore, the minimum distance that can be differentiated is approximately equal to the summation of the horizontal distance between point A_1 and C_1 and the horizontal distance between point A_2 and C_2. We have checked additional pairs of sources resembling those in the image of Fig. 6(b), and found that this minimum distance is less than 0.5 mm. We can, therefore, claim that the spatial resolution in our system reaches less than 0.5 mm, which agrees with the theoretical spatial resolution limit for 1.8-MHz signals whose half wavelength is ~0.5 mm with the sound speed of 1.5 mm/μs.

Of course, the detecting transducer has a finite physical size. If it is close to the thermoacoustic sources, it cannot be approximated as a point detector. Its size will blur the images and decrease the spatial resolution. Therefore, in experiments, the transducer must be placed some distance away from the tissue samples. In general, due to the finite size of the transducer, the farther away the transducer is from the detection center, the better the resolution at the expense of the signal strength.

Other limiting factors of spatial resolution include the duration of the microwave pulse and the impulse response of the transducer. In general, using a shorter microwave pulse will produce more high-frequency components in the thermoacoustic signals. The disadvantages resulting from employing a shorter pulse, however, are insufficient energy delivery and a decrease in the signal-to-noise ratio. Selection of the duration of the pulse is dependent on the experimental conditions and measurement systems. In biological tissues, microwaves at 300 MHz~3 GHz with 0.1~1 μs pulse width are often adopted. Therefore, the high-frequency of the thermoacoustic signals reaches several MHz. Such a wide-band transducer for measuring acoustic waves at ~MHz is widely available.

D. Thick Sample

The advantage of using microwave is its long penetration depth in soft tissue. A microwave can reach a tumor buried inside tissue and heat it to generate thermoacoustic waves. One tested sample is shown in Fig. 7(a). The experiment was conducted according to a procedure similar to the one above. Three small absorbers were buried inside a big fat base. The big pork fat tissue had a maximum diameter of 7 cm. Screwdrivers were used to carefully make three holes about 5 mm in diameter with a depth of 2.5 cm. Next, an injector was used to inject a drop of the same gelatin solution as above into each small hole, and, subsequently, air was blown out to improve the coupling between the gelatin solution and the fat tissue. These gelatin sources were about 5 mm in diameter. After being cooled at room temperature for about 15 min, the gelatin solutions solidified. The photograph of the sample at this stage is shown in Fig. 7(b). Finally, the holes were filled with fat, and the gelatin sources were buried in the fat tissue.

During the experiment, a microwave was transmitted out to the sample from below. The transducer rotationally scanned the sample, including the gelatin sources, from 0° to 360° in a plane as Fig. 7(a) shows. The distance between the transducer and the rotation center was 7 cm. The reconstructed image produced by our modified backprojection method, which agrees well with the original sample, is shown in Fig. 7(c).

The above experiments verified the principle of the modified backprojection algorithm, which implies back projection and coherent summation over spherical surfaces. In particular, a set of circular measurement data would be sufficient to yield a satisfactory cross-sectional image for a sample with only small absorption sources in the same horizontal plane and a lower absorption background. Of course, for a complicated sample, data from only a circular measurement would be insufficient for 3-D reconstruction unless cylindrical focusing is employed. This limited view problem will be addressed in our future work.

Finally, we must point out that an inhomogeneous acoustic property, such as the speed of sound variation, might result in reconstruction errors. Fortunately, the speed of sound in most soft tissue is relatively constant at ~ 1.5 mm/μs. The above experiments demonstrated that the small speed variations between fat and muscle or gelatin did not result in significant reconstruction artifacts. The reason is that thermoacoustic waves are produced internally by microwave absorption and are propagated one-way to the detectors. Thus, a small speed variation does not affect the travel time of the sound very much in a finite-length path, for example, 10 cm, which is comparable to a typical breast diameter. Therefore, in thermoacoustic tomography, satisfactory contrast and resolution are obtainable even in tissue with a small degree of acoustic inhomogeneity.

V. CONCLUSION

Pulsed-microwave-induced thermoacoustic tomography of inhomogeneous tissues has been studied. Both an exact inverse solution and a modified backprojection algorithm have been derived, which are based on the data acquired by wide-band point detectors on a spherical surface that encloses the sample under study. A set of experiments on tissue samples has been investigated under a circular measurement configuration. The reconstructed images calculated by the modified backprojection method agree well with the original ones. Results indicate that this technique using reconstruction theory is a powerful imaging method that results in good contrast and good spatial resolution (0.5 mm), which can be used for the investigation of tissues with inhomogeneous microwave absorptions.

REFERENCES

[1] L. E. Larsen and J. H. Jacobi, *Medical Applications of Microwave Imaging*. Piscataway, NJ: IEEE Press, 1986.

[2] K. D. Paulsen and P. M. Meaney, "Nonactive antenna compensation for fixed-array microwave imaging Part I: Model development," *IEEE Trans. Med. Imag.*, vol. 18, pp. 496–507, June 1999.

[3] P. M. Meaney, K. D. Paulsen, J. T. Chang, M. W. Fanning, and A. Hartov, "Nonactive antenna compensation for fixed-array microwave imaging: Part II Imaging results," *IEEE Trans. Med. Imag.*, vol. 18, pp. 508–518, June 1999.

[4] F. W. Kremkau, *Diagnostic Ultrasound: Principles and Instruments*. Philadelphia, PA: W. B. Saunders, 1993.

[5] E. Steen and B. Olstad, "Volume rendering of 3D medical ultrasound data using direct feature mapping," *IEEE Trans. Med. Imag.*, vol. 13, pp. 517–525, June 1994.

[6] G. Ku and L. V. Wang, "Scanning microwave-induced thermoacoustic tomography: Signal, resolution, and contrast," *Med. Phys.*, vol. 28, pp. 4–10, 2001.

[7] M. H. Xu, G. Ku, and L. V. Wang, "Microwave-induced thermoacoustic tomography using multi-sector scanning," *Med. Phys.*, vol. 28, pp. 1958–1963, 2001.

[8] C. G. A. Hoelen and F. F. M. de Mul, "Image reconstruction for photoacoustic scanning of tissue structures," *Appl. Opt.*, vol. 39, no. 31, pp. 5872–5883, Nov. 2000.

[9] Y. V. Zhulina, "Optimal statistical approach to optoacoustic image reconstruction," *Appl. Opt.*, vol. 39, no. 32, pp. 5971–5977, Nov. 2000.

[10] R. A. Kruger, D. R. Reinecke, and G. A. Kruger, "Thermoacoustic computed tomography-technical considerations," *Med. Phys.*, vol. 26, no. 9, pp. 1832–1837, 1999.

[11] S. J. Norton and M. Linzer, "Ultrasonic reflectivity imaging in three dimensions: Exact inverse scattering solutions for plane, cylindrical, and spherical apertures," *IEEE Trans. Biomed. Eng.*, vol. BME-28, pp. 202–220, 1981.

[12] G. B. Arfken and H. J. Weber, *Mathematical Methods for Physicists*. San Diego, CA: Academic, 1995.

[13] A. C. Tam, "Application of photoacoustic sensing techniques," *Rev. Mod. Phys.*, vol. 58, pp. 381–431, 1986.

[14] P. M. Morse and H. Feshbach, *Methods of Theoretical Physics*. New York: McGraw-Hill, 1953.

[15] Y. Xu, D. Feng, and L. V. Wang, "Exact frequency-domain reconstruction for thermoacoustic tomography: I. Planar geometry," *IEEE Trans. Med. Imag.*, vol. 21, pp. 823–828, July 2002.

[16] Y. Xu, M. H. Xu, and L. V. Wang, "Exact frequency-domain reconstruction for thermoacoustic tomography: II. Cylindrical geometry," *IEEE Trans.. Med. Imag.*, vol. 21, pp. 829–833, July 2002.

IEEE TRANSACTIONS ON MEDICAL IMAGING, VOL. 21, NO. 7, JULY 2002

Exact Frequency-Domain Reconstruction for Thermoacoustic Tomography—I: Planar Geometry

Yuan Xu, Dazi Feng, and Lihong V. Wang*

***Abstract*—We report an exact and fast Fourier-domain reconstruction algorithm for thermoacoustic tomography in a planar configuration assuming thermal confinement and constant acoustic speed. The effects of the finite size of the detector and the finite length of the excitation pulse are explicitly included in the reconstruction algorithm. The algorithm is numerically and experimentally verified. We also demonstrate that the blurring caused by the finite size of the detector surface is the primary limiting factor on the resolution and that it can be compensated for by deconvolution.**

***Index Terms*—Fourier-domain reconstruction, planar, thermoacoustic tomography.**

I. INTRODUCTION

USING thermoacoustic tomography (TAT) to image biological tissues has two primary advantages. The first is the high spatial resolution comparable with pure ultrasound imaging. The second advantage results from the large contrast in microwave absorption that exists between cancerous tissue and the normal tissue [1]–[7]. Reviews of TAT and related works [8]–[17] can be found in [11] and [18].

Various reconstruction algorithms for TAT [8], [9], [16], [18], [19] have been reported. Under the approximation that the distance between the detector and the absorbing object is much larger than the dimension of the absorbing object, a three-dimensional (3-D) Radon transform was applied to reconstruct the object in TAT [8]. However, the fact that this approximation may not always hold in real-world situations limits the application of this method. Further, the spatial resolutions of the imaging system using this reconstruction method are limited by blurs [20] caused by the finite size of the transducer surface, the finite width of the stimulating pulse, and the finite bandwidth of the transducers and amplifiers. Among these effects, the blur from the size of the transducer surface is expected to be the largest contributor to the total blur. The analysis of error is limited in numerical simulations, and, hence, no analytical form was available prior to this work. A time-domain beam-forming technique was applied in one study to image reconstruction for the photoacoustic scanning of tissue structures [9]. A weighted delay-and-sum algorithm was used to account for the near-field effect and to reduce noise. This algorithm is an approximate one, and its lateral resolution is limited by the size of the detector surface. The above reconstructions were implemented in the time domain and consequently are time-consuming, especially in 3-D tomography. TAT was also obtained in a way similar to that used in conventional B-scan ultrasonic imaging, but it had difficulty detecting the boundaries of objects that are oblique to the transducer axis [16]. Exact reconstructions have been implemented for TAT in spherical and cylindrical configurations in the companion papers [18], [19].

Next, we present our studies on an exact and fast reconstruction algorithm using a Fourier transform for TAT in a planar configuration. The reconstruction of an image by Fourier transform has been used in X-ray computed tomography [21], ultrasonic reflectivity imaging [22]–[24], and diffraction tomography [25] successfully. The computation complexity is reduced greatly due to the efficiency of the Fourier transform. We developed image reconstruction by Fourier transform for planar TAT and obtained an exact reconstruction algorithm for the first time. Furthermore, some limitations from experiments, such as the effects of the finite size of the detectors and the finite length of the excitation pulse, are included explicitly in the reconstruction algorithm. The reconstruction algorithm is verified by both numerically simulated and experimental results. Our simulations also demonstrate that the blur due to the finite size of the detector surface, which is a key limiting factor on the resolution of images [9], [20], can be alleviated by deconvolution with respect to the size of the detector surface. Other effects that may cause blurring of images can be treated in a similar way. In our initial experiments, an image in good agreement with the real objects was reconstructed and the deconvolution improved the resolution of the imaging system.

II. METHODS

A. Image Reconstruction

Assume that the detector scans within the plane $z = 0$ and that the object is distributed only in the half space $z' > 0$. In order to obtain a spatial resolution of about 1 mm, the microwave pulse should be set to less than ~1 μs because the speed of sound in soft biological tissue is ~1.5 mm/μs. For these parameters, the diffusion term in the heat conduction equation is about six orders of magnitude less than the term of the

---

Manuscript received May 15, 2001; revised May 13, 2002. This work was supported in part by the U.S. Army Medical Research and Material Command under Grant DAMD17-00-1-0455, in part by the National Institutes of Health (NIH) under Grant R01 CA71980 and Grant R21 CA83760, in part by the National Science Foundation (NSF) under Grant BES-9734491, and in part by the Texas Higher Education Coordinating Board under Grant ARP 000512-0123-1999. The Associate Editor responsible for coordinating the review of this paper and recommending its publication was G. Wang. *Asterisk indicates corresponding author.*

Y. Xu and D. Feng are with the Optical Imaging Laboratory, Department of Biomedical Engineering, Texas A&M University, College Station, TX 77843-3120 USA.

*L. V. Wang is with the Optical Imaging Laboratory, Department of Biomedical Engineering, Texas A&M University, 3120 TAMU, College Station, TX 77843-3120 USA (e-mail: LWang@tamu.edu).

Publisher Item Identifier 10.1109/TMI.2002.801172.

0278-0062/02$17.00 © 2002 IEEE

first-derivative of the temperature [26]. Therefore, heat conduction can be ignored. This is known as the assumption of thermal confinement. In this case, the acoustic wave $p(\mathbf{r}, \overline{t})$ is related to microwave absorption $H(\mathbf{r}, \overline{t})$ by the following wave equation [26]:

$$\frac{\partial^2 p(\mathbf{r}, \overline{t})}{\partial \overline{t}^2} - \nabla^2 p(\mathbf{r}, \overline{t}) = \frac{\beta v_s}{C} \frac{\partial H(\mathbf{r}, \overline{t})}{\partial \overline{t}} \tag{1}$$

where $\overline{t} = t v_s$, v_s is the acoustic speed, C is the specific heat, and β is the coefficient of volume thermal expansion. In (1), the acoustic speed is assumed constant, which will be further addressed in the discussion section. Equation (1) can be rewritten in terms of $H(\mathbf{r}', \overline{t})$:

$$p(\mathbf{r}, \overline{t}) = \frac{\beta v_s}{4\pi C} \iiint \frac{\partial H(\mathbf{r}', t')}{\partial t'} \frac{d\mathbf{r}'}{|\mathbf{r} - \mathbf{r}'|} \tag{2}$$

where $t' = \overline{t} - |\mathbf{r} - \mathbf{r}'|$. The source term $H(\mathbf{r}', \overline{t})$ can further be written as the product of a purely spatial and a purely temporal component, i.e.,

$$H(\mathbf{r}', \overline{t}) = I_0 \varphi(\mathbf{r}') \eta(\overline{t}) \tag{3}$$

where I_0 is a scaling factor proportional to the incident radiation intensity, $\varphi(\mathbf{r}')$ describes the microwave absorption properties of the medium at $\mathbf{r}'$. $\eta(\overline{t})$ describes the shape of the irradiating pulse and is a nonnegative function whose integration over time equals the pulse energy. Substituting (3) into (2) results in

$$p(\mathbf{r}, \overline{t}) = \frac{I_0 \beta v_s}{4\pi C} \iiint \varphi(\mathbf{r}') \frac{d\eta(t')}{dt'} \frac{d\mathbf{r}'}{|\mathbf{r} - \mathbf{r}'|}. \tag{4}$$

We proceed by transforming the time-dependent wave equation into the temporal-frequency domain. Denoting the Fourier transforms of p and η by $\overline{p}$ and $\overline{\eta}$, we have

$$p(\mathbf{r}, \overline{t}) = \int_{-\infty}^{\infty} \overline{p}(\mathbf{r}, k) \exp(ik\overline{t})\, dk \tag{5}$$

$$\eta(\overline{t}) = \int_{-\infty}^{\infty} \overline{\eta}(k) \exp(ik\overline{t})\, dk. \tag{6}$$

Substituting (5)and (6) into (4) results in

$$\overline{p}(\mathbf{r}, k) = \frac{i\beta v_s I_0 k \overline{\eta}(k)}{4\pi C} \iiint \varphi(\mathbf{r}') \frac{\exp(-ik|\mathbf{r} - \mathbf{r}'|)}{|\mathbf{r} - \mathbf{r}'|}\, d\mathbf{r}'. \tag{7}$$

If the acoustic signals are collected along a line or in a plane, for example at $z = 0$, following the line of Nortan and Linzer in [22], it can be shown that for the case $|k| > \rho$ and $z' > 0$

$$\overline{P}(u, v, k) = \frac{\beta v_s I_0 k \eta(k) \operatorname{sgn}(k)}{2C\sqrt{k^2 - \rho^2}} \cdot \int_0^{\infty} \Phi(v, v, z') \exp\left(-iz' \operatorname{sgn}(k) \sqrt{k^2 - \rho^2}\right) dz' \tag{8}$$

where $\rho^2 = u^2 + v^2$, $\operatorname{sgn}(k)$ is the signum function

$$\overline{P}(u, v, k) = \frac{1}{(2\pi)^2} \iint \overline{p}(x, y, 0, k) \cdot \exp(-i(ux + vy))\, dx\, dy \tag{9}$$

and

$$\Phi(u, v, z') = \frac{1}{(2\pi)^2} \iint \varphi(\mathbf{r}') \cdot \exp(-i(ux' + vy'))\, dx'\, dy'. \tag{10}$$

Equation (8) can further be simplified to

$$\overline{P}(u, v, k) = \frac{\pi \beta v_s I_0 k \overline{\eta}(k) \operatorname{sgn}(k) \Phi_1\left(u, v, \operatorname{sgn}(k)\sqrt{k^2 - \rho^2}\right)}{C\sqrt{k^2 - \rho^2}} \tag{11}$$

where

$$\Phi_1(u, v, w) = \frac{1}{2\pi} \int_{-\infty}^{\infty} \Phi(u, v, z') \exp(-iwz')\, dz'. \tag{12}$$

The lower limit of the above integration is changed from 0 to $-\infty$ because $\Phi(u, v, z') = 0$ when $z' < 0$. Equation (11) gives an exact mapping relation between the spectrum of the collected signals and the spectrum of the distribution of microwave energy deposition and is the essence of our reconstruction method. However, (11) stands only if the acoustic detector is a point detector. In practice, the detector is of finite size, whose surface shape can be described by $R(x, y)$. The signal from the detector $p_d(x, y, t)$ can be expressed as an integral of the acoustic wave $p(\mathbf{r}, t)$ over the detector surface

$$p_d(x, y, t) = \iint_s p(x', y', t) R(x' - x, y' - y)\, dx'\, dy'. \tag{13}$$

After transforming (13) into the temporal- and spatial-frequency domain, we have

$$\overline{P}_d(u, v, k) = 4\pi^2 \overline{P}(u, v, k) \overline{R}(-u, -v) \tag{14}$$

where $\overline{P}_d(u, v, k)$ is the temporal and spatial Fourier transform of $p_d(x, y, t)$, and $\overline{R}(u, v)$ is the spatial Fourier transform of $R(x, y)$. Substituting (14) into (11) results in

$$\overline{P}_d(u, v, k) = \frac{4\pi^3 \beta v_s I_0 k \overline{\eta}(k) \operatorname{sgn}(k) \overline{R}(-u, -v) \Phi_1\left(u, v, \operatorname{sgn}(k)\sqrt{k^2 - \rho^2}\right)}{C\sqrt{k^2 - \rho^2}}. \tag{15}$$

Mapping the (u, v, k) space into the (u, v, w) space by the relation

$$w = \operatorname{sgn}(k)\sqrt{k^2 - \rho^2} \tag{16}$$

yields an explicit expression for Φ_1

$$\Phi_1(u, v, w) = \frac{Cw\overline{P}_d\left(u, v, \operatorname{sgn}(w)\sqrt{w^2 + \rho^2}\right)}{4\pi^3 \beta v_s I_0 \operatorname{sgn}(w) \sqrt{w^2 + \rho^2}\, \overline{\eta}\left(\operatorname{sgn}(w)\sqrt{w^2 + \rho^2}\right) \overline{R}(-u, -v)}. \tag{17}$$

At last, the distribution of the microwave energy deposition can be reconstructed from Φ_1 by 3-D inverse Fourier transform. Equation (17) gives an exact reconstruction algorithm for planar

TAT for the first time. Furthermore, the effects of the finite size of the detectors and the finite length of the excitation pulse are included explicitly. From (17), it can be inferred that the reconstructed image spectrum $\Phi_d(u, v, w)$ from the experimental data without the consideration of these two effects, as was presented by previous researchers [9], [20], is related to the actual image spectrum $\Phi_1(u, v, w)$ by

$$\Phi_d(u, v, w) = 4\pi^2\overline{\eta}\left(\mathrm{sgn}(w)\sqrt{w^2+\rho^2}\right)\overline{R}(-u, -v)\Phi_1(u, v, w). \quad (18)$$

Both of the effects result in multiplications of a function to the actual image spectrum in the frequency domain. They are equivalent to convolutions in the spatial domain, which blur the reconstructed image. However, given the pulse shape and the surface configuration of the detector surface, the two effects can be reduced by deconvolution.

To summarize, the reconstruction procedure consists of the following steps.

1) The signal from the detector $p_d(x, y, \overline{t})$ is Fourier transformed with respect to $\overline{t}$ to yield $\overline{p}_d(x, y, k)$. Deconvolution with respect to the finite pulse length can be implemented immediately after the Fourier transform.
2) $\overline{p}_d(x, y, k)$ is Fourier transformed with respect to x and y, yielding $\overline{P}_d(u, v, k)$.
3) According to (16) and (17), $\overline{P}_d(u, v, k)$ is mapped to $\Phi_d(u, v, w)$.
4) $\Phi_d(u, v, w)$ is deconvoluted with respect to the finite size of the detector, giving $\Phi_1(u, v, w)$.
5) $\Phi_1(u, v, w)$ is inversely Fourier transformed with respect to u, v, w to yield $\varphi(x', y', z')$.

The order of steps 4) and 5) can be exchanged so that more stable deconvolution algorithms can be applied. In numerical calculations, $\overline{P}_d(u, v, k)$ is obtained only at discrete points; hence the mapping from $\overline{P}_d(u, v, k)$ to $\Phi_d(u, v, w)$ needs interpolation, which can be a major source of distortion.

B. System Setting

The experimental setup was reported in [27] and, for convenience, is only briefly described here (Fig. 1). The x axis points perpendicularly to the drawing plane; the y axis points to the right in the plane; and the z axis points downward along the acoustic axis. Microwave pulses are transmitted by a 9-GHz microwave generator. The pulse width is 0.5 μs. The object to be imaged is a cylinder of pork fat containing a thin layer of connective tissue and six yellow microstructures. The diameter of the cylinder fat is 14 mm and the length in the x direction 30 mm. The cylinder was immersed in mineral oil in a plexiglass tank. The central frequency of the ultrasonic transducer (Panametrics) is 2.25 MHz; the bandwidth 1.8 MHz; and the diameter of the active element 6 mm. More details about the system can be found in [27].

III. RESULTS AND DISCUSSION

Our method was applied to reconstructing images from both the simulated and the experimental data in a two-dimensional (2-D) case, where the imaged objects were uniform along the x axis. Because the blur due to the finite size of the detector surface is a limiting factor on the resolution of images, we demonstrated how deconvolution with respect to the detector surface can deblur the images. We chose the 2-D case here because both the computational and experimental complexity can be reduced more in the 2-D case than in the 3-D one. Nevertheless, the extension of the conclusions of the 2-D case to the 3-D one is straightforward.

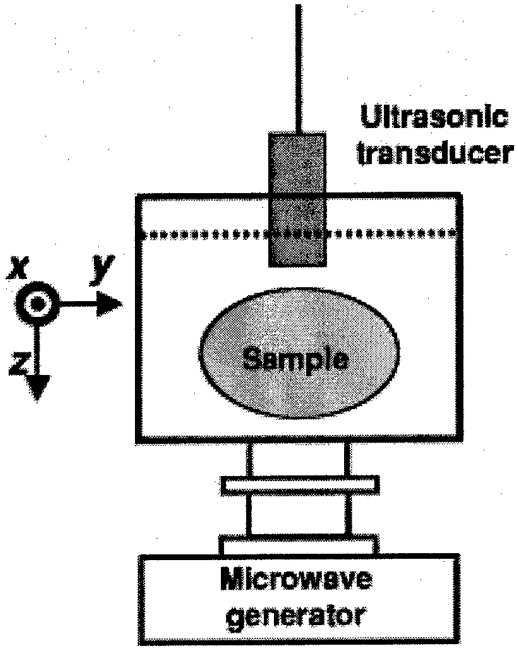

Fig. 1. Experimental setup for TAT.

A. Simulation

The thermoacoustic imaging of two cylinders was numerically simulated. Cylinders were chosen because the analytical expression for their thermoacoustic signal is available [28]. In the simulations, the temporal-frequency range was from near 0 to 1.5 MHz, which was in accordance with the experimental one and with our previous experiments [11]. Two simulations were run. The first one was to test our reconstruction algorithm under an ideal experimental condition, which is noiseless and does not consider any experimental limitations on the detectors. In the second case, the effect of the finite size of the detectors on the imaging was studied while noise was also added. Deconvolution with respect to the finite size of the detector surface was applied to improve the lateral resolution of the blurred image. Since energy deposition is a positive value, only the positive components of the reconstructed image were retained, and the others were set to zero.

In step 3) of the reconstruction, which is the mapping from $\overline{P}_d(u, v, k)$ to $\Phi_d(u, v, w)$, linear interpolation was applied. By adopting the zero-padding technique [25] for the time-domain data, one can increase the sampling density in the k-space and, consequently, obtain a better performance of the interpolation in the k-space. In the reconstruction from the simulation data and experimental data, we appended to the end of the data the same number of zeros as in the original collected data, so that

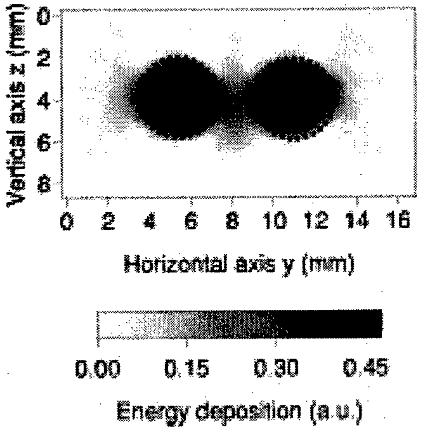

Fig. 2. The reconstructed image of the cross-section of two cylinders with a radius of 2 mm and the centers separated by 5.5 mm under ideal experimental conditions.

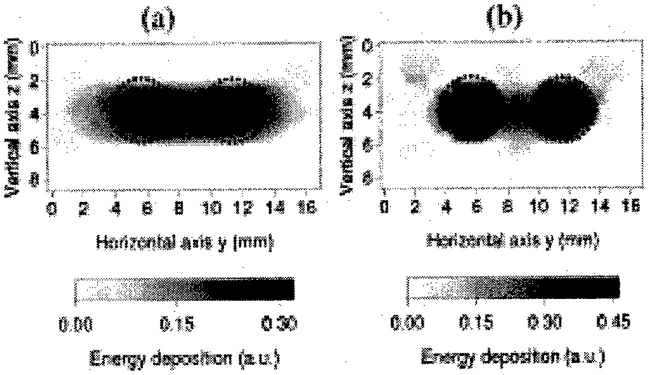

Fig. 3. The reconstructed images for the same two cylinders as in Fig. 2 from noisy data (a) before and (b) after the deconvolution with respect to the detector surface.

the sampling density in the k-space was doubled. By utilizing the Wiener filtering method [29], deconvolution with respect to the finite pulse length was implemented immediately after the Fourier transform with respect to time in step 1). As the deconvolution with respect to the finite size of the detector surface is much more unstable than the deconvolution with respect to the finite pulse length, we have tried two methods of deconvolution: the Wiener filtering method and the piecewise polynomial truncated singular value decomposition (PP-TSVD) [30] method. The first method can be implemented in the spatial-frequency domain and is more computationally efficient than the second, but the performance of the second method is much better, as it can restore sharp boundaries blurred by the convolution while avoiding the appearance of artificial oscillations in an unstable deconvolution. Therefore, we adopted the PP-TSVD method to process the images. Since the models in our simulation and experiment were uniform along the x axis, one-dimension deconvolution was applied.

Fig. 2 shows the reconstructed image from the simulated data under the ideal experimental condition, where the radius of the two cylinders was 2 mm; the distance between the centers of the cylinders was 5.5 mm; the centers of the cylinders were positioned in the plane of $z = 10$ mm; the scanning range of the detector along the y axis was 90 mm with a step size of 0.5 mm; and the thermoacoustic signals were sampled for 40 μs at a sampling rate of 50 MHz. The reconstructed image is in good agreement with the real objects, whose outlines are plotted as dotted circles in Fig. 2. The dimension of the cylinders is 3.75 mm along the z direction and 4.7 mm along the y direction. The cylinder is a little deformed laterally, which is due to the finite scanning range of the detector.

Fig. 3 shows the images before and after deconvolution with respect to the finite size of the detector surface in a case similar to our experimental conditions. The noise was added to the thermoacoustic signals, and the signal-to-noise ratio (SNR) was 50; the diameter of the detector was 6 mm. All of the other parameters were the same as those in the first case. The image before deconvolution is shown in Fig. 3(a). The dimension of the images of the objects is 3.5 mm along the y axis, which agrees well with the real one, 4 mm. However, along the z axis, the images of the two cylinders were blurred and consequently merged into one, which is predicted by our analysis of the effect of the finite size of the detector. The image shows no clear boundaries of the objects along the y axis. After deconvolution, the lateral boundaries of the objects become very clear and the width of the objects in Fig. 3(b) is 4.1 mm, which is quite close to reality. Furthermore, the two objects can be distinguished clearly. After comparing Fig. 3(a) with (b), it seems that the ghost images become slightly more obvious, which is a disadvantage of deconvolution. Nevertheless, it is obvious that deconvolution with respect to the finite size of the detector surface can improve the lateral resolution greatly.

In Figs. 2 and 3, there are some ghost images. In principle, our reconstruction method is exact under the assumption of thermal confinement and constant acoustic speed. However, several factors may introduce distortions. First, as mentioned at the end of part Section II-A, the mapping from $\overline{P}_d(u, v, k)$ to $\Phi_d(u, v, w)$ needs interpolation, which is a major source of distortion. This distortion can be reduced by increasing sampling time or applying a better interpolation algorithm in the mapping. Second, in experiments, the detector cannot be scanned over the whole plane. Nevertheless, Fig. 2 shows that collecting data within a finite area of the collection plane can produce images of sufficient definition to determine the configuration and position of the objects.

B. *Experimental Result*

Fig. 4 shows the experimental result. The images before and after deconvolution with respect to the finite size of the detector surface are shown in Fig. 4(a) and (b), respectively. Fig. 4(c) is the cross section of the biological tissue, which was a cylinder with a radius of about 14 mm and 3 cm long. It consisted of two parts of fat separated by a very thin layer of connective tissue, which is labeled as (7) in the middle of the sample. There were some yellow microstructures among the fat, labeled from (1)–(6), respectively. Fig. 4(a) is the image reconstructed from the experimental data before deconvolution. The connective tissue between the two parts of fat and the yellow microstructures are imaged clearly. The dimension of the image is 16.4 mm along the z direction and 19.2 mm along the y direction. However, it is obvious that the image before deconvolution is blurred along the y axis, which makes

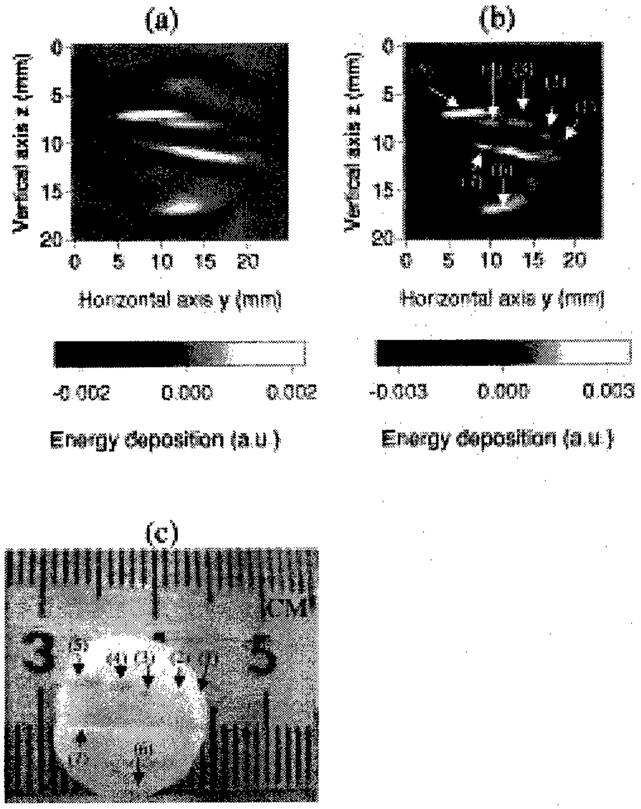

Fig. 4. The reconstructed images from the experimental data (a) before and (b) after the deconvolution with respect to the detector surface; (c) the cross section of a cylinder of fat sample containing six yellow microstructures labeled from (1)–(6) and a layer of connective tissue in the middle labeled as (7).

the lateral boundaries unclear and the yellow microstructures (1) and (2), (3) and (4) merge into one object, respectively. The lateral resolution of the image needs to be improved. Consequently, deconvolution with respect to the finite size of the detector surface was applied to Fig. 4(a), and the result is shown in Fig. 4(b). The lateral resolution of the image after deconvolution is much improved. The merged objects can be distinguished clearly, and the lateral boundaries of the cylinder become much clearer. The dimension of the image is 16.4 mm along the z direction and 16.7 mm along the y direction.

C. Discussion

There are several advantages of our reconstruction method. The first one is that it is an exact reconstruction algorithm. Unlike other reconstruction methods for TAT that are approximate ones, our reconstruction method provides a solid base for analyzing and improving the quality of reconstructed images. Furthermore, the exact reconstruction method has a broader application than the approximate ones. For example, in both our simulation and experiment, the closest distance between the objects and the detectors was only about 1 cm; this is possible because in principle there is no limitation on the detector–object distance in our method. In other words, the detector can be placed very close to the object to ensure a better SNR. The second advantage of our method is that it can explicitly include the effect of many limitations from the experiment, such as the finite size of detector surface, the microwave pulse length, and the finite frequency response range of the detector. Actually, these analyses are also valid for other approximate reconstruction methods as long as the other reconstruction methods are able to produce images approximating the real objects. Consequently, our analysis of the blur caused by the various experimental limitations can also be very useful for eliminating the limitations in other reconstruction methods. Lastly, since the reconstruction in our method is implemented in the frequency domain, the efficiency of computation is much better than the algorithm implemented in the time domain due to the use of the efficient Fourier transformation in our method. This is especially important for real-time 3-D imaging.

From the above images, it can be seen that there is no speckle in the reconstructed image. Speckles are an important factor limiting the quality of pure ultrasonic imaging. In our technology, the detected signals are directly from the primary acoustic waves rather than reflective or scattered waves. Further, the temporal frequency of the acoustic signals lies in a range from 0 to 1.5 MHz, which is only weakly scattered in the tissues. The above two factors guarantee that there is no obvious speckle in our experimental images. However, the issue of image speckle in more realistic medical imaging applications of our algorithm is a topic for future consideration.

The formulas in this paper are for TAT in planar geometry only. However, for cylindrical geometry [19], we can predict that the lateral resolution of images can also be improved by deconvolution with respect to the detector surface, where the deconvolution is carried out in a cylindrical surface instead of a plane. For spherical geometry [18], similar work can be conducted as well.

For many medical imaging applications, the acoustic speed may not be constant. For example, the acoustic speed inside the female breast may typically exhibit a 10% variation; however, our simulation, to be reported elsewhere, showed that the image distortion is relatively small.

IV. CONCLUSION

We developed a Fourier-domain reconstruction for TAT and obtained an exact and fast reconstruction algorithm. The effects of the finite size of the detectors and the finite length of the excitation pulse were included explicitly in the reconstruction algorithm. The reconstruction algorithm was verified by both numerical simulations and experimental results. Our simulations demonstrated that the blurring caused by the finite size of the detector surface, which is a key limiting factor on the resolution of images, can be alleviated by deconvolution with respect to the detector surface. Other effects that may cause the blur of the images can be treated in a similar way. In the initial experiment, an image in good agreement with the real objects was reconstructed and the deconvolution improved the resolution of the imaging system. The method can also be extended to other configurations of data collection.

REFERENCES

[1] W. Joines, R. Jirtle, M. Rafal, and D. Schaeffer, "Microwave power absorption differences between normal and malignant tissue," *Radiation Oncol. Biol. Phys.*, vol. 6, pp. 681–687, 1980.

[2] S. Chaudhary, R. Mishra, A. Swarup, and J. Thomas, "Dielectric properties of normal human breast tissues at radiowave and microwave frequencies," *Indian J. Biochem. Biophys.*, vol. 21, pp. 76–79, 1984.

[3] W. Joines, Y. Zhang, C. Li, and R. Jirtle, "The measured electrical properties of normal and malignant human tissues from 50–900 MHz," *Med. Phys.*, vol. 21, pp. 547–550, 1994.

[4] L. E. Larsen and J. H. Jacobi, Eds., *Medical Applications of Microwave Imaging*. Piscataway, NJ: IEEE Press, 1986.

[5] S. Caorsi, A. Frattoni, G. L. Gragnani, E. Nortino, and M. Pastorino, "Numerical algorithm for dielectric-permittivity microwave imaging of inhomogeneous biological bodies," *Med. Biol. Eng. Comput.*, vol. NS-29, pp. 37–44, 1991.

[6] M. S. Hawley, A. Broquetas, L. Jofre, J. C. Bolomey, and G. Gaboriaud, "Microwave imaging of tissue blood content changes," *J. Biomed. Eng.*, vol. 13, pp. 197–202, 1991.

[7] P. M. Meaney, K. D. Paulsen, and J. T. Chang, "Near-field microwave imaging of biologically-based materials using a monopole transceiver system," *IEEE Trans. Microwave Theory Tech.*, vol. 46, pp. 31–45, Jan 1998.

[8] R. A. Kruger, P. Liu, Y. R. Fang, and C. R. Appledorn, "Photoacoustic ultrasound (PAUS)—Reconstruction tomography," *Med. Phys.*, vol. 22, pp. 1605–1609, 1995.

[9] C. G. A. Hoelen, F. F. M. Demul, R. Pongers, and A. Dekker, "Three-dimensional photoacoustic imaging of blood vessels in tissue," *Opt. Lett.*, vol. 23, pp. 648–650, 1998.

[10] A. A. Karabutov, E. V. Savateeva, N. B. Podymova, and A. A. Oraevsky, "Backward mode detection of laser-induced wide-band ultrasonic transients with optoacoustic transducer," *J. Appl. Phys.*, vol. 87, pp. 2003–2014, 2000.

[11] Y. Xu and L.-H. V. Wang, "Signal processing in scanning thermoacoustic tomography in biological tissues," *Med. Phys.*, vol. 28, pp. 1519–1524, 2001.

[12] T. Bowen, L. Nasoni, A. E. Pifer, and G. H. Sembrosk, "Some experimental results on the thermoacoustic imaging of soft tissue-equivalent phantoms," in *Proc. IEEE Ultrasonics Symp.*, vol. 2, 1981, pp. 823–827.

[13] J. C. Lin and K. H. Chan, "Microwave thermoelastic tissue imaging—System design," *IEEE Trans. Microwave Theory Tech.*, vol. MTT-32, pp. 854–860, 1984.

[14] R. A. Kruger, D. R. Reinecke, and G. A. Kruger, "—Thermoacoustic computed tomographyTechnical considerations," *Med. Phys.*, vol. 26, pp. 1832–1837, 1999.

[15] L.-H. V. Wang, X. Zhao, H. Sun, and G. Ku, "Microwave-induced acoustic imaging of biological tissues," *Rev. Sci. Instrum.*, vol. 70, pp. 3744–3748, 1999.

[16] G. Ku and L.-H. V. Wang, "Scanning thermoacoustic tomography in biological tissue," *Med. Phys.*, vol. 27, pp. 1195–1202, 2000.

[17] ——, "Scanning microwave-induced thermoacoustic tomography: Signal, resolution, and contrast," *Med. Phys.*, vol. 28, pp. 4–10, 2001.

[18] M. Xu and L.-H. V. Wang, "Time-domain reconstruction for thermoacoustic tomography in a spherical geometry," *IEEE Trans. Med. Imag.*, vol. 21, pp. 814–822, July 2002.

[19] Y. Xu, M. Xu, and L.-H. V. Wang, "Exact frequency-domain reconstruction for thermoacoustic tomography—II: Cylindrical geometry," *IEEE Trans. Med. Imag.*, vol. 21, pp. 829–833, July 2002.

[20] W. J. Kiser, Jr. and R. A. Kruger, "Thermoacoustic computed tomography-limits to spatial resolution," *SPIE*, vol. 3659, pp. 895–905, 1999.

[21] H. Stark, J. W. Woods, I. Paul, and R. Hingoram, "Direct Fourier reconstruction in computer tomography," *IEEE Trans. Acoust. Speech Signal Processing*, vol. ASSP-29, pp. 237–245, 1981.

[22] S. J. Nortan and M. Linzer, "Ultrasonic reflectivity imaging in three dimensions: Exact inverse scattering solution for plane, cylindrical and spherical aperture," *IEEE Trans. Biomed. Eng.*, vol. BME-28, pp. 202–220, Feb. 1981.

[23] K. Nagai, "A new synthetic-aperture focusing method for ultrasonic b-scan imaging by the Fourier transform," *IEEE Trans. Sonics Ultrason.*, vol. SU-32, pp. 531–536, 1985.

[24] J. Lu, "Experimental study of high frame rate imaging with limited diffraction beams," *IEEE Trans. Ultrason. Ferroel. Frequency Control*, vol. 45, pp. 84–97, Jan. 1998.

[25] S. X. Pan and A. C. Kak, "A computational study of reconstruction algorithms for diffraction tomography: Interpolation versus filtered backprojection," *IEEE Trans. Acoust. Speech Signal Processing*, vol. ASSP-31, pp. 1262–1275, 1983.

[26] V. E. Gusev and A. A. Karabutov, *Laser Optoacoustics*. New York: Amer. Inst. Phys., 1993.

[27] D. Feng, Y. Xu, G. Ku, and L.-H. V. Wang, "Microwave-induced thermoacoustic tomography: Reconstruction by synthetic aperture," *Med. Phys.*, vol. 28, pp. 2427–2431, 2001.

[28] G. J. Diebold, M. I. Khan, and S. M. Park, "Photoacoustic signatures of particulate matter: Optical production of acoustic monopole radiation," *Science*, vol. 250, pp. 101–104, 1990.

[29] A. K. Jain, *Fundamentals of Digital Image Processing*. Englewood Cliffs, NJ: Prentice Hall, 1989.

[30] P. C. Hansen and K. Mosegaard, "Piecewise polynomial solutions without *priori* breakpoints," *Num. Lin. Alg. Applicat.*, vol. 3, pp. 513–524, 1996.

Appendix 6

IEEE TRANSACTIONS ON MEDICAL IMAGING, VOL. 21, NO. 7, JULY 2002

Exact Frequency-Domain Reconstruction for Thermoacoustic Tomography—II: Cylindrical Geometry

Yuan Xu, Minghua Xu, and Lihong V. Wang*

***Abstract*—Microwave-induced thermoacoustic tomography (TAT) in a cylindrical configuration is developed to image biological tissue. Thermoacoustic signals are acquired by scanning a flat ultrasonic transducer. Using a new expansion of a spherical wave in cylindrical coordinates, we apply the Fourier and Hankel transforms to TAT and obtain an exact frequency-domain reconstruction method. The effect of discrete spatial sampling on image quality is analyzed. An aliasing-proof reconstruction method is proposed. Numerical and experimental results are included.**

***Index Terms*—Cylindrical, frequency-domain reconstruction, thermoacoustic tomography.**

I. INTRODUCTION

THERMOACOUSTIC tomography (TAT) combines the strength of traditional microwave imaging and ultrasound imaging [1]–[14]. Reviews on TAT and related techniques can be found in [11], [12], [14]. Recently, we derived exact reconstruction algorithms for TAT in both planar and spherical configurations; these are reported in the companion papers [11], [12]. We recognize, however, that in some applications such as the imaging of the limbs, a cylindrical scanning surface may be more appropriate. In this paper, using a new expansion formula in cylindrical coordinates, we derive a frequency-domain reconstruction algorithm [15]–[19] and report our numerical and experimental results in two-dimensional (2-D) cases.

II. METHODS

We assume that the detector scans on a cylindrical surface with a radius of ρ, which encircles all microwave absorbing objects. In our paper, a coordinate with a prime refers to the position in an imaged object, while a coordinate without a prime refers to that of a detector. In the case of thermal confinement, the temporal spectrum of acoustic field $\overline{p}(\mathbf{r}, k)$ is related to the microwave absorption distribution $\varphi(\mathbf{r}')$ by the following equation [11]:

$$\overline{p}(\mathbf{r}, k) = \frac{i\beta v_s I_0 k \overline{\eta}(k)}{4\pi C} \iiint \varphi(\mathbf{r}') \frac{\exp(-ik|\mathbf{r}-\mathbf{r}'|)}{|\mathbf{r}-\mathbf{r}'|}\, d\mathbf{r}' \qquad (1)$$

where the symbols are defined as in [11]. Cylindrical coordinates are used in the following derivation, where z is shown in [12, Fig. 2], and ρ, ϕ are the polar coordinates within the x–y plane. Following the derivation of the series expansion of $1/|\mathbf{r}-\mathbf{r}'|$ [20], we obtained the following new identity for a series expansion of a spherical wave in a cylindrical coordinate system (see the Appendix for the derivation):

$$\begin{aligned}\frac{\exp(-ik|\mathbf{r}-\mathbf{r}'|)}{4\pi|\mathbf{r}-\mathbf{r}'|} &= \frac{-i}{8\pi}\int_{-\infty}^{\infty} dk_z \exp[-ik_z(z'-z)] \\ &\quad \cdot \sum_{m=-\infty}^{\infty} A(m, \mu\rho', \mu\rho)\exp[-im(\phi'-\phi)] \qquad (2)\end{aligned}$$

where $\mu = \operatorname{sgn}(k)\sqrt{|k^2 - k_z^2|}$; sgn( ) is the signum function; and A is the function defined as

$$A(m, \mu\rho', \mu\rho) = \begin{cases} J_m(\mu\rho')H_m^2(\mu\rho), & \text{if } |k| \geq |k_z| \\ \dfrac{2i}{\pi} I_m(|\mu|\rho')K_m(|\mu|\rho), & \text{if } |k| < |k_z| \end{cases}$$

where J_m, H_m^2, I_m, and K_m are the mth-order Bessel, second-kind Hankel, and modified Bessel functions, respectively. It has been assumed in the above two equations that $\rho > \rho'$. Substituting (2) into (1) results in

$$\begin{aligned}\overline{p}(\mathbf{r}, k) &= \frac{\beta v_s I_0 k \overline{\eta}(k)\operatorname{sgn}(k)}{8\pi C}\iiint d\mathbf{r}'\varphi(\mathbf{r}') \\ &\quad \cdot \int_{-\infty}^{\infty} dk_z \exp[-ik_z(z'-z)] \\ &\quad \cdot \sum_{m=-\infty}^{\infty} A(m, \mu\rho', \mu\rho)\exp[-im(\phi'-\phi)]. \qquad (3)\end{aligned}$$

The $|k| \geq |k_z|$ part of the integration with respect to k_z represents the contribution from the propagation wave, while the $|k| < |k_z|$ part represents the evanescent wave. As the evanescent wave decays rapidly at a distance several wavelengths from

---

Manuscript received July 30, 2001 revised May 13, 2002. This work was supported in part by the U.S. Army Medical Research and Material Command under Grant DAMD17-00-1-0455, in part by the National Institutes of Health (NIH) under Grant R01 CA71980 and Grant R21 CA83760, in part by the National Science Foundation (NSF) under Grant BES-9734491, and in part by the Texas Higher Education Coordinating Board under Grant ARP 000512-0123-1999. The Associate Editor responsible for coordinating the review of this paper and recommending its publication was G. Wang. *Asterisk indicates corresponding author.*

Y. Xu and M. Xu are with the Optical Imaging Laboratory, Department of Biomedical Engineering, Texas A&M University, College Station, TX 77843-3120 USA.

*L. Wang is with the Optical Imaging Laboratory, Department of Biomedical Engineering, Texas A&M University, 3120 TAMU, College Station, TX 77843-3120 USA (e-mail: LWang@tamu.edu).

Publisher Item Identifier 10.1109/TMI.2002.801171.

0278-0062/02$17.00 © 2002 IEEE

the source, it is not suitable for thermoacoustic imaging. For the case of $|k| \geq |k_z|$, after Fourier transforming both sides of the above equation with respect to ϕ and z, we have

$$\overline{p}_1(m, k_z, k) = \frac{\beta v_s I_0 k \overline{\eta}(k) H_m^2(\mu\rho)}{8\pi C} \cdot \int_0^\infty d\rho' \rho' \varphi_1(m, k_z, \rho') J_m(\mu\rho') \quad (4)$$

where $\overline{p}_1(m, k_z, k)$ and $\varphi_1(m, k_z, \rho')$ are the Fourier transforms of $\overline{p}(\mathbf{r}, k)$ and $\varphi(\mathbf{r}')$, respectively. Noticing that the right side of (4) is actually a Hankel transform, an inverse Hankel transform gives

$$\varphi_1(m, k_z, \rho') = \frac{8\pi C}{\beta v_s I_0} \int_0^\infty d\mu \, \frac{\mu \overline{p}_1(m, k_z, k) J_m(\mu\rho')}{k \overline{\eta}(k) H_m^2(\mu\rho)}, \quad |k| \geq |k_z|.$$

Applying a variable change of the integral variable from μ to k to the above equation results in

$$\varphi_1(m, k_z, \rho') = \frac{8\pi C}{\beta v_s I_0} \int_{k_z}^\infty dk \, \frac{\overline{p}_1(m, k_z, k) J_m(\mu\rho')}{\overline{\eta}(k) H_m^2(\mu\rho)}, \quad |k| \geq |k_z|. \quad (5)$$

At last, $\varphi_1(m, k_z, \rho')$ is inversely Fourier transformed with respect to m and k_z to yield $\varphi(\phi', z', \rho')$. Equation (5) gives an exact mapping relation between the spectrum of the collected signals and the spectrum of the distribution of microwave energy deposition and is the essence of our reconstruction method.

An exact reconstruction method for ultrasonic reflectivity imaging with a cylindrical scanning surface was given in [16]. However, our results are much simpler and more stable. In their equation A24, $J_m(\mu r_0)$, where r_0 is the radius of the scanning cylindrical surface, appeared in the denominator and can be zero for some values of μ; consequently, this term can cause instability. In our (5), $H_m^2(\mu\rho)$ appeared in the denominator, which cannot be zero for a finite μ.

To summarize, the reconstruction procedure consists of the following steps.

1) The signal from the detector $p(\phi, z, \overline{t})$ is Fourier transformed with respect to $\overline{t}$ to yield $\overline{p}(\phi, z, k)$. Deconvolution with respect to the finite pulse length can be implemented immediately after the Fourier transform.
2) $\overline{p}(\phi, z, k)$ is Fourier transformed with respect to z and ϕ, giving $\overline{p}_1(m, k_z, k)$.
3) According to (5), $\overline{p}_1(m, k_z, k)$ is mapped to $\varphi_1(m, k_z, \rho')$.
4) $\varphi_1(m, k_z, \rho')$ is inversely Fourier transformed with respect to m, k_z to yield $\varphi(\phi', z', \rho')$.

III. RESULTS AND DISCUSSION

To test our method, images from both numerically simulated and experimental data were reconstructed in a 2-D case. We chose the 2-D case rather than the three-dimensional (3-D) case to reduce the computational and experimental complexity. For the 2-D case, the reconstruction equation can be derived from (4) by replacing all k_z with zero. The extension of the conclusions of the 2-D case to a 3-D one is straightforward.

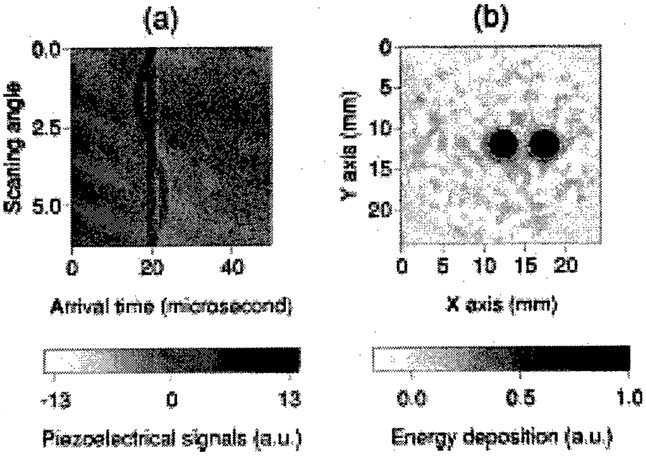

Fig. 1. The images (a) before and (b) after the reconstruction from the simulated data of two cylinders.

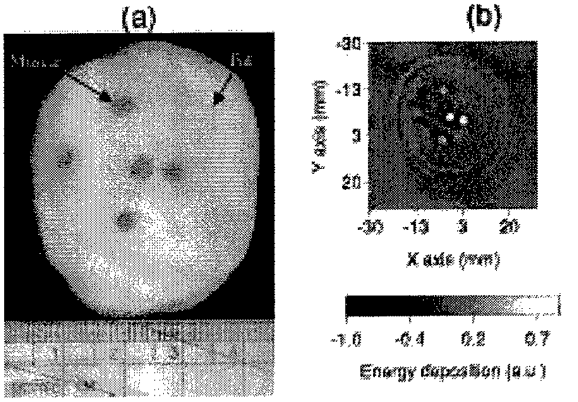

Fig. 2. (a) The cross section of a fat sample containing 5 pieces of muscle cylinders. (b) The reconstructed image from the experimental data.

A. Numerical Simulation

The thermoacoustic imaging of two cylinders was numerically simulated, where the radius of each cylinder was 2 mm; the distance between the centers of the cylinders was 5 mm; and the center of one of the cylinders was positioned at the origin of the circle of detection. Cylinders were chosen because the analytical expression for their thermoacoustic signal is available [21]. In the simulations, the temporal-frequency range was from about 0 to 2 MHz, which was close to our experimental situation [14]. For the noiseless simulated data, the reconstruction is almost perfect. Therefore, we show only the results from noisy data. Fig. 1 shows the images before and after the reconstruction from the simulated data with introduced additive noise. The units for the signals and energy deposition in Figs. 1 and 2 are relative ones. Calibration of our system is needed to obtain an absolute measurement. The radius of the circle of detection was 30 mm; the angular scanning range was 2π with 256 steps; and the thermoacoustic signals were sampled for 50 μs at a sampling rate of 4 MHz. The signal-noise-ratio (SNR) of the raw data shown in Fig. 1(a) was 1. The reconstructed image shown in Fig. 1(b) is in good agreement with the real objects, whose outlines are plotted as dotted circles in Fig. 1(b). The dimensions of the reconstructed cylinders are 4 mm along both the x and the y directions. The SNR of the reconstructed image is about 8, which is improved greatly compared with that of the raw data.

B. Experiment Results

The experimental setup for 2-D TAT in a cylindrical configuration is the same as that in [12]. The sample is shown in Fig. 2(a), which was photographed after the experiment. Microwave pulses were delivered to the sample from below. The imaging plane was 2 cm above the bottom of the tissue sample. Above the plane, there is another layer of fat about 1 cm thick. The sample consisted of five muscle cylinders with a diameter of about 3 mm and a height of 6 mm. The muscle cylinders were surrounded by pork fat. The electrical property of interest to this imaging technique is the microwave attenuation coefficient of the medium at the experimental microwave frequency, 3 GHz. The microwave attenuation coefficients of fat and muscle are 9 cm^{-1} and 1 cm^{-1}, respectively. The microwave absorption in mineral oil can be neglected, compared with the absorption in fat and muscle. During the experiment, the transducer scanned around the sample at a radius of 7.1 cm from 0° to 360° with a step size of 2.25°. The thermoacoustic signals were sampled for 60 μs at a sampling rate of 20 MHz. The time between the end of a microwave pulse and the acquisition of the thermoacoustic signal was between 10 μs and 20 μs in our system, depending on the distance of the transducer to the nearest sample surface.

Fig. 2(b) shows the reconstructed image from the experimental data. The reconstructed image is in good agreement with the real objects. The boundaries between the fat and the surrounding medium and the muscle cylinders are imaged clearly. However, it can be seen that the quality of the image decreases with the increasing distance of the objects from the center of the circle of detection. One possible reason is that the finite surface area of the detector, which has a 6-mm diameter in this experiment, may cause blurring of the image perpendicular to the radial direction, and this blurring is more serious when the object is farther from the center. Another possible reason is that the microwave field decreases when the radius increases in our irradiation configuration.

Our method can be applied to analyze the effect of the discrete sampling by the detector along the circle of detection on imaging. This can be illustrated by analyzing the signals from a point source located at radius ρ_1. According to (4)

$$\overline{p}_1(m, k) \propto J_m(k\rho_1). \tag{6}$$

Fig. 3 shows how $J_m(k\rho_1)$ changes with m, where $k = 8.37\ \mathrm{mm}^{-1}$ (the wave number of a 2-MHz acoustic wave) and $\rho_1 = 10$ mm. It is clear that $J_m(k\rho_1)$ has considerable value until $m \approx k\rho_1$, where the Bessel function makes a transition from near-field behavior to far-field behavior. Therefore, it is safe to claim that, with respect to variable ϕ, $\overline{p}(\mathbf{r}, k)$ is band-limited by $k\rho_1$. According to the Nyquist criteria, the number of scanning points per cycle should be at least $2k\rho_1$ to avoid aliasing. In other words, for a fixed number of scanning points N, the maximum wave number before aliasing occurs is $k_{\max} \approx N/(2\rho_1)$. It can be seen that the maximum wave number is inversely proportional to ρ_1. For the same N and temporal spectrum of signal, the aliasing may be more serious for signals coming from sources at a greater radial distance than for those closer to the center. The above analysis also points out a way to produce an aliasing-free image from the data obtained by discrete detection. That is to apply a filter in the temporal-frequency domain to the spectrum of the temporal data with a stopband at about $N/(2\rho_{\max})$, where $\rho_{\max}$ is the maximum radius of imaging range of interest. The application of the filter will decrease the resolution of the image; however, it can guarantee that there will be no aliasing in the image.

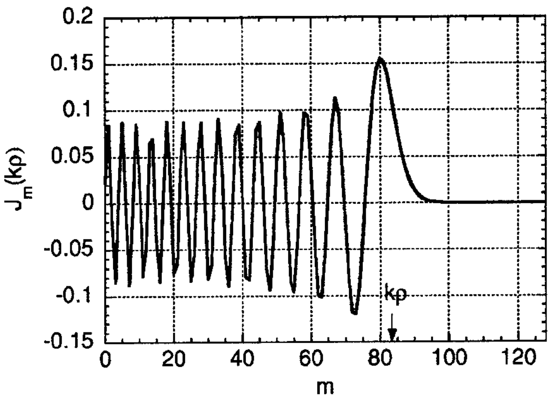

Fig. 3. $J_m(k\rho_1)$ versus m, where $k = 8.37\ \mathrm{mm}^{-1}$ (the wave number of a 2 MHz acoustic wave) and $\rho_1 = 10$ mm.

C. Discussion

Since our method is implemented in the frequency domain using the fast Fourier transform (FFT) technique, the computational efficiency is much greater than if implemented in the time domain. The most time-consuming computation in the numerical reconstruction lies in (5), which is a Hankel transform. Fortunately, a quasi-fast algorithm for it, which is as efficient as a one-dimensional FFT, is available [22]. Following the methods in [11], our method can explicitly include and further eliminate the effect of many limitations from the experiment, such as the finite size of the detector surface, the microwave pulse length, and the finite response frequency range of the detector. Additionally, combining our method and the techniques in [16], a new exact reconstruction algorithm for 3-D ultrasonic reflectivity imaging with a cylindrical aperture can be derived. Finally, we would like to point out that the reconstruction methods reported in this paper and the two companion papers [11], [12] are also applicable to photoacoustic or optoacoustic tomography as well as other diffraction-based inverse source problem.

The size of tissue samples that can be imaged by our system is mainly limited by the safety standard on microwave power, the microwave frequency, the microwave irradiation configuration, the sensitivity of the ultrasonic transducer, the dynamic range of the preamplifier and sampling system, and the affordable imaging time. The effect of microwave frequency on the imaging depth was addressed in reference [13]. A microwave irradiation configuration that renders a uniform microwave irradiation within the sample will also increase the capacity of the system to image larger samples. A large dynamic range of the preamplifier and the sampling system is necessary to accurately collect the thermoacoustic signals from both the surface and the inside of a sample. A more sensitive ultrasonic transducer and a longer imaging time can improve the signal-to-noise ratio of acoustic signals and make the weak signals from the inside of large samples detectable.

In our initial computation, the reconstruction of a single 2D image required about 2 min in a Dell Precision 330 computer (Intel Pentium 4 processor with a clock frequency of 1.5 GHz) with Matlab programs if there was no precomputation of Bessel and Hankel functions. However, our initial computation was aimed at verifying the proposed algorithm rather than demonstrating the computation efficiency. The proposed algorithm can be implemented with high computational efficiency as stated in the discussion section. For high computational efficiency, the program should be coded with languages such as C or Fortran, Bessel and Hankel functions should be precomputed, and the fast Hankel transform algorithm should be adopted. The evaluation of the computation efficiency of our algorithm is a topic for future studies.

IV. CONCLUSION

Using a new expansion of a spherical wave in the cylindrical coordinate system, we applied the Fourier transform and Hankel transform techniques to TAT with a cylindrical detection surface. The reconstruction algorithm is verified by both numerical simulations and experimental results in 2-D cases. The method was applied to analyze the effect of discrete sampling by the detector along the circle of detection on imaging; an aliasing-free reconstruction method for discrete sampling along the azimuth direction is proposed.

APPENDIX

The derivation of (2) will be presented here. The spherical wave $G_k(\mathbf{r}, \mathbf{r}') = \exp(-ik|\mathbf{r}-\mathbf{r}'|)/(4\pi|\mathbf{r}-\mathbf{r}'|)$ is a solution to the wave equation with a point source

$$\nabla_r^2 G_k(\mathbf{r}, \mathbf{r}') + k^2 G_k(\mathbf{r}, \mathbf{r}') = -\delta(\mathbf{r}-\mathbf{r}'). \quad \text{(A1)}$$

The solution can be expanded in terms of orthonormal functions of z and ϕ in a cylindrical coordinate system

$$G_k(\mathbf{r}, \mathbf{r}) = \left(\frac{1}{2\pi}\right)^2 \sum_{m=-\infty}^{\infty} \int_{-\infty}^{\infty} dk_z g_m(k, k_z, \rho, \rho') \cdot \exp[im(\phi-\phi') + ik_z(z-z')]. \quad \text{(A2)}$$

Substituting (A2) into (A1) results in an equation for the radial Green's function g_m

$$\frac{1}{\rho}\frac{d}{d\rho}\left(\rho\frac{dg_m}{d\rho}\right) + \left(k^2 - k_z^2 - \frac{m^2}{\rho^2}\right) g_m = -\frac{\delta(\rho-\rho')}{\rho}. \quad \text{(A3)}$$

When $|k| < |k_z|$, following the derivation of the series expansion of $1/|\mathbf{r}-\mathbf{r}'|$ [20], one obtains a similar expansion for the spherical wave

$$g_m = I_m(|\mu|\rho')K_m(|\mu|\rho). \quad \text{(A4)}$$

We next consider the case of $|k| \geq |k_z|$ and $k > 0$. Noticing that when $\rho \to \infty$, g_m behaves asymptotically as $\exp[-i\mu(\rho-\rho')]$ ($\rho > \rho'$ is implicit in our model), one can follow the derivation in [20] and obtain

$$g_m = \frac{\pi}{2i} J_m(\mu\rho')H_m^2(\mu\rho). \quad \text{(A5)}$$

Similarly, for $|k| \geq |k_z|$ and $k < 0$

$$g_m = \frac{\pi i}{2} J_m(|\mu|\rho')H_m^1(|\mu|\rho). \quad \text{(A6)}$$

Using the following identities of Bessel and Hankel functions [23]:

$$H_m^1(\mu\rho) = -(-1)^m H_m^2(-\mu\rho),$$
$$J_m(\mu\rho) = (-1)^m J_m(-\mu\rho)$$

and combining (A2) and (A4)–(A6), we obtain (2).

REFERENCES

[1] W. Joines, R. Jirtle, M. Rafal, and D. Schaeffer, "Microwave power absorption differences between normal and malignant tissue," *Radiation Oncol. Biol. Phys.*, vol. 6, pp. 681–687, 1980.

[2] S. Chaudhary, R. Mishra, A. Swarup, and J. Thomas, "Dielectric properties of normal human breast tissues at radiowave and microwave frequencies," *Indian J. Biochem. Biophys.*, vol. 21, pp. 76–79, 1984.

[3] W. Joines, Y. Zhang, C. Li, and R. Jirtle, "The measured electrical properties of normal and malignant human tissues from 50–900 MHz," *Med. Physics.*, vol. 21, pp. 547–550, 1994.

[4] L. E. Larsen and J. H. Jacobi, Eds., *Medical Applications of Microwave Imaging*. Piscataway, NJ: IEEE Press, 1986.

[5] S. Caorsi, A. Frattoni, G. L. Gragnani, E. Nortino, and M. Pastorino, "Numerical algorithm for dielectric-permittivity microwave imaging of inhomogeneous biological bodies," *Med. Biol. Eng. Comput.*, vol. NS-29, pp. 37–44, 1991.

[6] M. S. Hawley, A. Broquetas, L. Jofre, J. C. Bolomey, and G. Gaboriaud, "Microwave imaging of tissue blood content changes," *J. Biomed. Eng.*, vol. 13, pp. 197–202, 1991.

[7] P. M. Meaney, K. D. Paulsen, and J. T. Chang, "Near-field microwave imaging of biologically-based materials using a monopole transceiver system," *IEEE Trans. Microwave Theory Tech.*, vol. 46, pp. 31–45, Jan. 1998.

[8] R. A. Kruger, P. Liu, Y. R. Fang, and C. R. Appledorn, "Photoacoustic ultrasound (PAUS)-reconstruction tomography," *Med. Phys.*, vol. 22, pp. 1605–1609, 1995.

[9] C. G. A. Hoelen, F. F. M. Demul, R. Pongers, and A. Dekker, "Three-dimensional photoacoustic imaging of blood vessels in tissue," *Opt. Lett.*, vol. 23, pp. 648–650, 1998.

[10] G. Ku and L.-H. V. Wang, "Scanning thermoacoustic tomography in biological tissue," *Med. Phys.*, vol. 27, pp. 1195–1202, 2000.

[11] Y. Xu, D. Feng, and L.-H. V. Wang, "Exact frequency-domain reconstruction for thermoacoustic tomography—II: Planar geometry," *IEEE Trans. Med. Imag.*, vol. 21, no. 7, pp. 823–828, July 2002.

[12] M. Xu and L.-H. V. Wang, "Time-domain reconstruction for thermoacoustic tomography in a spherical geometry," *IEEE Trans. Med. Imag.*, vol. 21, no. 7, pp. 814–822, July 2002.

[13] G. Ku and L.-H. V. Wang, "Scanning microwave-induced thermoacoustic tomography: Signal, resolution, and contrast," *Med. Phys.*, vol. 28, pp. 4–10, 2001.

[14] Y. Xu and L.-H. V. Wang, "Signal processing in scanning thermoacoustic tomography in biological tissues," *Med. Phys.*, vol. 28, pp. 1519–1524, 2001.

[15] H. Stark, J. W. Woods, I. Paul, and R. Hingorani, "Direct Fourier reconstruction in computer tomography," *IEEE Trans. Acoust. Speech Signal Processing*, vol. ASSP-29, pp. 237–245, 1981.

[16] S. J. Nortan and M. Linzer, "Ultrasonic reflectivity imaging in three dimensions: Exact inverse scattering solution for plane, cylindrical and spherical aperture," *IEEE Trans. Biomed. Eng.*, vol. BME-28, pp. 202–220, 1981.

[17] K. Nagai, "A new synthetic-aperture focusing method for ultrasonic b-scan imaging by the Fourier transform," *IEEE Trans. Sonics Ultrason.*, vol. SU-32, pp. 531–536, 1985.

[18] J. Lu, "Experimental study of high frame rate imaging with limited diffraction beams," *IEEE Trans. Ultrason. Ferroelect. Freq. Contr.*, vol. 45, pp. 84–97, Jan. 1998.

[19] S. X. Pan and A. C. Kak, "A computational study of reconstruction algorithms for diffraction tomography: Interpolation versus filtered backprojection," *IEEE Trans. Acous. Speech Signal Processing*, vol. ASSP-31, pp. 1262–1275, 1983.

[20] J. D. Jackson, *Classical Electrodynamics*. New York: Wiley, 1975.

[21] G. J. Diebold, M. I. Khan, and S. M. Park, "Photoacoustic signatures of particulate matter: Optical production of acoustic monopole radiation," *Science*, vol. 250, pp. 101–104, 1990.

[22] A. E. Siegman, "Quasi fast Hankel transform," *Opt. Lett.*, vol. 1, pp. 13–15, 1977.

[23] M. Abramowitz and I. A. Stegun, *Handbook of Mathematical Functions*. New York: Dover, 1972.

Pulsed-microwave-induced thermoacoustic tomography: Filtered backprojection in a circular measurement configuration

Minghua Xu and Lihong V. Wang[a)]
Optical Imaging Laboratory, Biomedical Engineering Program, Texas A&M University, 3120 TAMU, College Station, Texas 77843-3120

(Received 12 December 2001; accepted for publication 7 May 2002; published 16 July 2002)

Our study on pulsed-microwave-induced thermoacoustic tomography in biological tissues is presented. A filtered backprojection algorithm based on rigorous theory is used to reconstruct the cross-sectional image from a thermoacoustic measurement in a circular configuration that encloses the sample under study. Specific details describing the measurement of thermoacoustic waves and the implementation of the reconstruction algorithm are discussed. A two-dimensional (2D) phantom sample with 2 mm features can be imaged faithfully. Through numerical simulation, the full width half-maximum (FWHM) of the point-spread function (PSF) is calculated to estimate the spatial resolution. The results demonstrate that the circular measurement configuration combined with the filtered backprojection method is a promising technique for detecting small tumors buried in biological tissues by utilizing microwave absorption contrast and ultrasound spatial resolution (~mm).
© *2002 American Association of Physicists in Medicine.* [DOI: 10.1118/1.1493778]

Key words: microwave, thermoacoustics, tomography, imaging, filtered backprojection

I. INTRODUCTION

Pulsed microwave-induced thermoacoustic tomography combines the advantages of both ultrasound spatial resolution and microwave absorption contrast.[1–4] The basic idea of this technique is that a very short microwave pulse (<1 μs) heats a sample; the sample then absorbs the microwave energy and simultaneously generates temporal thermoacoustic waves, which are strongly related to the locally absorbed microwave energy. The microwave pulse is so short that the heat diffusion's effect on the thermoacoustic wave can be ignored. The thermoacoustic signals have a wide frequency range up to MHz and carry the information of the microwave absorption distribution with millimeter spatial resolution. In practice, microwaves at 300 MHz–3 GHz with 0.1–1 μs pulse are often adopted, which offer penetration depths of several centimeters in biological tissues. For example, the penetration depths for fat and muscle tissues at 3 GHz microwaves are 9 and 1.2 cm, respectively.[3] Most other soft tissues have penetration depths in between those for muscle and fat tissues. The wide range of values among various tissues makes it possible to achieve high image contrast. In addition, the long penetration depth allows this technique to detect interior tumors.

In our initial studies, we used focused transducers with big apertures to detect thermoacoustic signals with both the linear scan[2,3] and the circular scan methods.[4] The big aperture gives us a good signal-to-noise ratio (SNR), because the SNR is inversely proportional to the square root of the aperture area. Each scan line is converted into a one-dimensional image along the axis of the transducer, and then cross-sectional images can be obtained by straightforward calculations. The axial resolution is obtained by measuring the temporal profiles of the thermoacoustic signals. However, the lateral resolution is mainly determined by the focal diameter of the transducer.[2,5] The image view is also limited by the focal length of the transducer.

An alternative method is to use unfocused transducers with small apertures to record the thermoacoustic signals and then reconstruct the microwave absorption distribution from the measured data. The different measurement configuration may, however, result in a different reconstruction algorithm. Under certain practical conditions, on a rigorous base, we theoretically reported a modified backprojection method for the planar, cylindrical, and spherical recording configurations.[6,7] These were computed through temporal spatial backprojection and coherent summation over spherical surfaces with spatial weighting factors. This method is something like synthetic aperture. Therefore, the SNR can be greatly improved through coherent summation, although the SNR of each detected temporal signal may be reduced due to the small aperture of the unfocused transducer as compared to focused transducers with big apertures.

In this paper, we present our study on pulsed-microwave-induced thermoacoustic tomography in biological tissues under a circular measurement configuration. A wide beam (~22 cm^2) of short-pulse (0.5 μs) microwave energy is used to illuminate a sample from the bottom. The sample absorbs the microwave energy and generates temporal thermoacoustic waves simultaneously. An unfocused ultrasonic transducer with a small aperture (6 mm) is used to record the thermoacoustic signals. A filtered backprojection (FBP) method based on rigorous theory is used to reconstruct the cross-sectional image from the measured data. Specific details describing the measurement of thermoacoustic waves and the implementation of the reconstruction algorithm are discussed. A phantom sample is investigated. The reconstructed image agrees with the original sample very well. Through

0094-2405/2002/29(8)/1661/9/$19.00

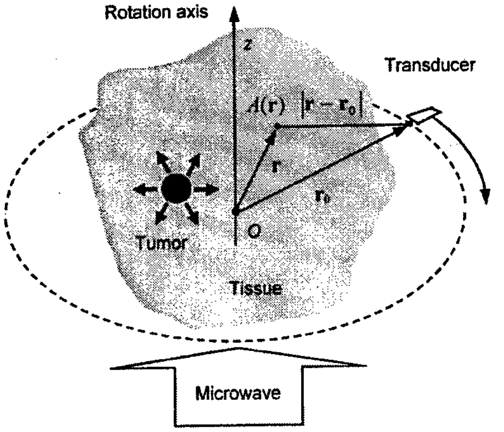

FIG. 1. Scheme of thermoacoustic circular measurement. Microwave pulses are transmitted to the sample from the bottom. The tumor inside absorbs the energy and generates thermoacoustic waves. An ultrasonic transducer at position $\mathbf{r}_0$ records the thermoacoustic signals.

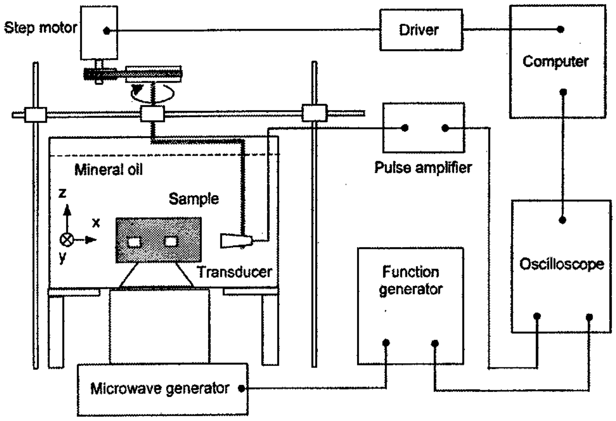

FIG. 2. Experimental setup.

numerical calculation of the point-spread function, the spatial resolution is estimated to reach ~mm.

II. METHOD OF MEASUREMENT

There are three typical measurement geometries: linear or planar configuration, circular or cylindrical configuration, and spherical configuration. The choice of measurement geometry depends on the practical need. For the purposes of investigating external organs, the second two choices are preferred. In practice, at least two restraints should be considered. One is that the space for delivering microwaves to the sample is physically limited. Ideally, the sample should be homogeneously illuminated as much as possible. Otherwise, the thermoacoustic signal will reflect not only the absorption differentiation, but also inhomogeneous illumination, which will result in reconstruction artifacts. The other restraint is that it is physically impossible to collect measurements over a 4π solid angular range. The developed reconstruction algorithm requires that the detectors receive outgoing thermoacoustic waves from all possible angular directions.[6,7] But, in reality, a limited angular range has to be tolerated, and the incomplete data also results in some reconstruction artifacts.

In this study, we chose a circular measurement configuration, as shown in Fig. 1. Tissue, such as breast tissue, is hard to compress but easy to deform. A slight force can make the external tissue nearly cylindrical in shape. Then, the microwave can be delivered to the tissue from its larger bottom and the detector can measure the outgoing thermoacoustic waves in a circular geometry around the tissue. The wavelength of microwaves below 3 GHz is relatively long, e.g., at 3 GHz, 10 cm in air, and 3 cm in soft tissue, compared to the typical size of tissue investigated in several centimeters diameter. That helps to illuminate the tissue homogeneously. However, because of attenuation, microwaves along the z axis decay exponentially and the generated thermoacoustic signal along the z axis decays exponentially, too, even in a homogenous sample. But the circular detection plane, i.e., the horizontal xy plane, is parallel with the incident plane of microwave pulses. Besides, due to the bounded water and salt in cancer cells,[8,9] the tumor will absorb more microwave energy and generate more intense thermoacoustic waves than the surrounding tissue. Therefore, the thermoacoustic signals from the circular plane have a significantly reduced dynamic range compared with those in any other planes. This improves the accuracy of both data acquisition and data reconstruction tremendously. As shown below, reasonable reconstruction images are achieved in the experiment.

Figure 2 shows the experimental setup we used for the circular measurement configuration. A Plexiglas container is filled with mineral oil. An unfocused transducer is immersed inside it and fixed on a rotation device. A step motor drives the rotation device and then moves the transducer scan around the sample on a horizontal x-y plane, where the transducer horizontally points to the rotation center. A sample is immersed inside the container and placed on a holder: it is made of a thin plastic material, which is transparent to microwaves. The transducer (V323, Panametrics) has a central frequency of 2.25 MHz and a diameter of 6 mm.

The microwave pulses transmitted from a 3 GHz microwave generator have a pulse energy of 10 mJ and a pulse width of 0.5 μs. A function generator (Protek, B-180) is used to trigger the microwave generator, control its pulse repetition frequency, and synchronize the oscilloscope sampling. In our experiments, the pulse repetition frequency is 50 Hz and the oscilloscope sampling frequency is 20 MHz. Microwave energy is delivered to the sample by a rectangular waveguide with a cross section of 72 mm×34 mm. A personal computer is used to control the steps. The signal from the transducer is first amplified through a pulse amplifier, then recorded and averaged 500 times by an oscilloscope (TDS640A, Tektronix), and finally transferred to a personal computer for imaging.

This system is within the IEEE standard for safety levels with respect to human exposure to radio frequency electromagnetic fields (see the Appendix). The waveguide is filled with air and has a mode of $\mathrm{TE}_{1,0}$. The wavelength of the emitted microwave is 10 cm in air. The microwave irradiates from the waveguide and then propagates through a thin layer of air into the container and the tissue sample. Due to the relatively long wavelength of microwave in tissue (~3 cm at 3 GHz), the diffraction causes only smooth variations on a scale comparable to 3 cm. As discussed later, in signal processing, we removed the low-frequency component below 50 KHz, which corresponds to an acoustic wavelength of ~3 cm. Therefore, the effect of mode structure of microwave irradiation on thermoacoustic imaging is minor.

III. METHOD OF RECONSTRUCTION

We assume a tissue with inhomogeneous microwave absorption but a relatively homogeneous acoustic property. When the microwave pulse duration is $<1\ \mu$s, the heat diffusion's effect on the thermoacoustic wave in the tissue can be ignored. The speed of sound in most soft tissue is relatively constant at ~1.5 mm/μs. Therefore, the pressure $p(\mathbf{r},t)$ produced by the heat source $H(\mathbf{r},t)$ obeys the following equation:[10]

$$c^2\nabla^2 p(\mathbf{r},t)-\frac{\partial^2}{\partial t^2}p(\mathbf{r},t)=-\Gamma(\mathbf{r})\frac{\partial H(\mathbf{r},t)}{\partial t}, \tag{1}$$

where the Grüneisen parameter $\Gamma(\mathbf{r})=\beta c^2/C_p$, c is the speed of sound; β is the isobaric volume expansion coefficient; C_p is the heat capacity; and $H(\mathbf{r},t)$ is the heating function defined as the thermal energy per unit time and unit volume deposited by the energy source. Basically, the heating function can be written as the product of a spatial absorption function and a temporal illumination function:

$$H(\mathbf{r},t)=A(\mathbf{r})I(t). \tag{2}$$

Suppose a delta illuminating function $\delta(t)$, the detected acoustic pressure $p(\mathbf{r}_0,t)$ on the circular surface $\mathbf{r}=\mathbf{r}_0=(\rho_0,\varphi_0,z_0)$, and time t can be written as[6]

$$p(\mathbf{r}_0,t)=\frac{1}{c}\frac{\partial}{\partial t}\int\int\int d^3r\,D(\mathbf{r})\frac{\delta(ct-|\mathbf{r}_0-\mathbf{r}|)}{4\pi|\mathbf{r}_0-\mathbf{r}|}, \tag{3}$$

where $D(\mathbf{r})=A(\mathbf{r})\Gamma(\mathbf{r})$. The inverse problem is to reconstruct the spatial distribution $D(\mathbf{r})$ from a set of data $p(\mathbf{r}_0,t)$ measured at a different position $\mathbf{r}_0$.

Due to the finite bandwidths of the transducer, the preamplifier and the microwave pulse, only a portion of the information about the absorption structure can be restored. The high-frequency component of the thermoacoustic signal primarily reflects the small size structure while the low-frequency component primarily reflects the large size structure. If challenged to detect small size tumors, we can safely remove the low-frequency component. Besides, the wavelengths of the high-frequency thermoacoustic waves are much smaller than the detecting distance between the thermoacoustic source and the transducer. Under the above conditions, i.e., $\rho_0 k\gg 1$ or $k|\mathbf{r}-\mathbf{r}_0|\gg 1$, where k is the wave number, we have shown theoretically that the distribution $D(\mathbf{r})$ can be calculated by the following 2D surface integral in the cylindrical configuration:[7]

$$D(\rho,\varphi,z)=-\frac{1}{2\pi c^2}\int\int_{S_0} dS_0[\mathbf{n}\cdot\mathbf{n}_0]\frac{1}{t}\frac{\partial p(\mathbf{r}_0,t)}{\partial t}\bigg|_{t=|\mathbf{r}-\mathbf{r}_0|/c}, \tag{4}$$

where

$$\mathbf{n}\cdot\mathbf{n}_0=\frac{|\boldsymbol{\rho}-\boldsymbol{\rho}_0|}{|\mathbf{r}-\mathbf{r}_0|}=\sqrt{\frac{\rho^2+\rho_0^2-2\rho\rho_0\cos(\varphi_0-\varphi)}{|\mathbf{r}-\mathbf{r}_0|^2}}$$
$$=\sqrt{1-\frac{(z_0-z)^2}{|\mathbf{r}-\mathbf{r}_0|^2}}, \tag{5}$$

$dS_0=\rho_0 d\varphi_0\, dz_0$, $\boldsymbol{\rho}$ and $\boldsymbol{\rho}_0$ are the projections of $\mathbf{r}$ and $\mathbf{r}_0$ on the z plane, respectively, and $\mathbf{n}$ and $\mathbf{n}_0$ are unit vectors pointing along the line joining $\boldsymbol{\rho}$ and $\boldsymbol{\rho}_0$ and along the line joining $\mathbf{r}$ and $\mathbf{r}_0$, respectively. This is a modified backprojection formula of quantity $-(1/t)[\partial p(\mathbf{r}_0,t)/\partial t]$. The weighting factor $[\mathbf{n}\cdot\mathbf{n}_0]$ is less than 1, except if $z=z_0$, $[\mathbf{n}\cdot\mathbf{n}_0]=1$. That indicates that the cross-sectional image of any z_0 plane is mainly determined by the data measured on the circle of the same z_0 plane. In other words, if some small absorption sources are located on a z_0 plane, a set of circular measurement data on the same plane would be sufficient to yield a good cross-sectional image.

The quantity $\partial p(\mathbf{r}_0,t)/\partial t$ can be calculated through the Fourier transform,

$$\frac{\partial p(\mathbf{r}_0,t)}{\partial t}=\mathrm{FFT}^{-1}\{-i\omega p(\mathbf{r}_0,\omega)W_\Omega(\omega)\}, \tag{6}$$

where FFT^{-1} denotes the fast inverse Fourier transform; ω is angular frequency and equal to $2\pi f$; $W_\Omega(\omega)$ is a window function; and the Fourier transform defines

$$\bullet(\omega)=\int_{-\infty}^{+\infty}\bullet(t)\exp(i\omega t)dt. \tag{7}$$

We want to point out that the factor ω in Eq. (6) actually represents a pure ramp filter, which will significantly depress the low-frequency signal. That is helpful to guarantee the validity of the reconstruction, Eq. (4). The ramp filter can also amplify the high-frequency noise in such a way that the reconstructed image is not acceptable from the physical point of view. In order to avoid this effect, it is necessary to introduce a relative low-pass filter $W_\Omega(\omega)$ characterized by a cutoff angular frequency $\Omega=2\pi f_\Omega$. A Hanning window is our choice in this case:

$$W_\Omega(\omega)=\begin{cases}0.5+0.5\cos\left(\pi\dfrac{\omega}{\Omega}\right), & \text{if } |\omega|<\Omega,\\ 0, & \text{otherwise.}\end{cases} \tag{8}$$

Thus, the reconstruction algorithm can also be termed a filtered backprojection (FBP) with the modified ramp filter $\omega W_\Omega(\omega)$. Unlike the FBP algorithm used in x-ray tomography,[11] which uses surface integration over intersecting planes, the method in our problem is calculated through temporal backprojection and coherent summation over spherical surfaces with a certain spatial weighting factor.

IV. EXPERIMENT

The experimental conditions necessitate special care. The reconstruction theory requires point detectors, and the real transducer must never be a point. But, we can ignore its size if we put it at a distance from the sample that is greater than the size of the transducer aperture. In addition, we must shield both the transducer and the electrical transmission cables from microwave illumination. Otherwise, the microwave pumping will cause harmful electrical signals via electromagnetic induction. If well shielded, the induced signal decays very rapidly. A time gate can cut out the induced signal before the arrival of the thermoacoustic signal. Suppose $p(\mathbf{r}_0,t)$ is the thermoacoustic signal with delta-pulse microwave pumping, then the measured thermoacoustic signal can be written as a convolution with the measurement system response $H(t)$:

$$S(\mathbf{r}_0,t)=p(\mathbf{r}_0,t)*H(t). \tag{9}$$

Considering the temporal response $M(t)$ of the amplifier, the impulse response $R(t)$ of the transducer and the temporal profile $I(t)$ of the microwave pulse, $H(t)$ can also be written as a convolution,

$$H(t)=M(t)*I(t)*R(t). \tag{10}$$

In the frequency domain, Eq. (9) can be written as

$$S(\mathbf{r}_0,\omega)=p(\mathbf{r}_0,\omega)H(\omega). \tag{11}$$

Basically, we cannot recover all of the available information because of the limited bandwidth of the detection system. The information we can acquire depends on the system response $H(\omega)$. In practice, $M(\omega)$ is very wide and ~ 1; $I(\omega)$ determines the bandwidth of the generated thermoacoustic signal, which is approximately inversely proportional to the width of its temporal profile; $R(\omega)$ is a wide-band transducer with a central frequency ω_c. If $H(\omega)$ is known, an appropriate deconvolution algorithm can be used to figure out $p(\mathbf{r}_0,\omega)$.

In our experiments, the illumination $I(t)$ is approximately a rectangular function with duration $\tau=0.5$ μs, and its temporal profile is shown as the short dashed line in Fig. 3(a), which determines the frequency of the generated thermoacoustic signal below 2 MHz. The transducer that we used is of the videoscan type with a central frequency of $f_c=2.25$ MHz, and its temporal profile is shown as the solid line in Fig. 3(a). In the frequency range below 2 MHz, the response of the transducer approximates a ramp filter. As shown in Fig. 3(b), the calculated $H(f)$ (solid line) was compared with a pure ramp filter f (short dashed line). In this special case for our measurement system, the filtered $\partial p(\mathbf{r}_0,t)/\partial t$ can be approximately calculated by an inverse Fourier transformation as

$$\frac{\partial p(\mathbf{r}_0,t)}{\partial t}\approx \mathrm{FFT}^{-1}\{S(\mathbf{r}_0,\omega)W_\Omega(\omega)\}. \tag{12}$$

Next, we imaged a phantom sample with a complex absorption structure using the following procedure. First, we used screwdrivers to carve a structure: the word "OIL" (abbreviation for Optical Imaging Lab) in a large fat base. The diameter of the dent was about 2 mm. In the meantime, we prepared a hot solution with 5% gelatin, 1% salt, and a drop of dark ink to improve the photographic properties. Then we used an injector to inject several drops of the hot solution into the dents and subsequently blew out the air to assure good coupling between the gelatin solution and the fat tissue. The gelatin word was cooled at room temperature until solidified. The photograph of the sample at this stage is shown in Fig. 4(a). Finally, we added a piece of fat both on the top and on the bottom of the sample so that the gelatin word was buried inside the fat tissue. The diagram of the structure in side view is shown in Fig. 4(b).

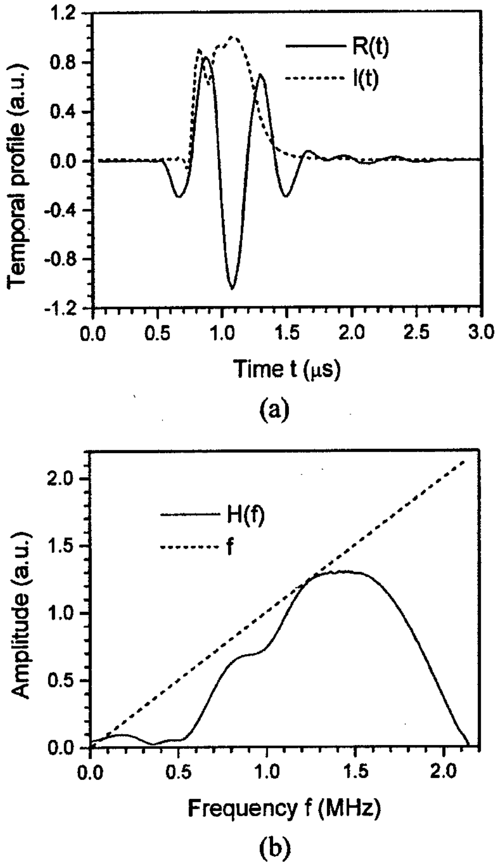

FIG. 3. (a) The impulse response of the transducer $R(t)$ and the temporal profile of the microwave pulse $I(t)$; (b) the system response $H(f)$ and the pure ramp filter f.

The transducer rotationally scanned the sample from 0°–360° with step size 2.25° in the plane, including the word "OIL." The distance between the transducer and the rotation center was 8 cm. The sampling frequency of the oscilloscope was 20 MHz. We chose the cutoff frequency $f_\Omega=4$ MHz in the filter W_Ω. The filtered temporal thermoacoustic signals are shown in Fig. 4(c). Because of some time delay in the oscilloscope, the rotation origin is at time $t=36.8$ μs. Unlike X-ray tomography,[11] these data have no symmetric property in a 2π period. The reconstructed image produced by our filtered backprojection method, which agrees with the original sample very well, is shown in Fig. 4(d). However, when

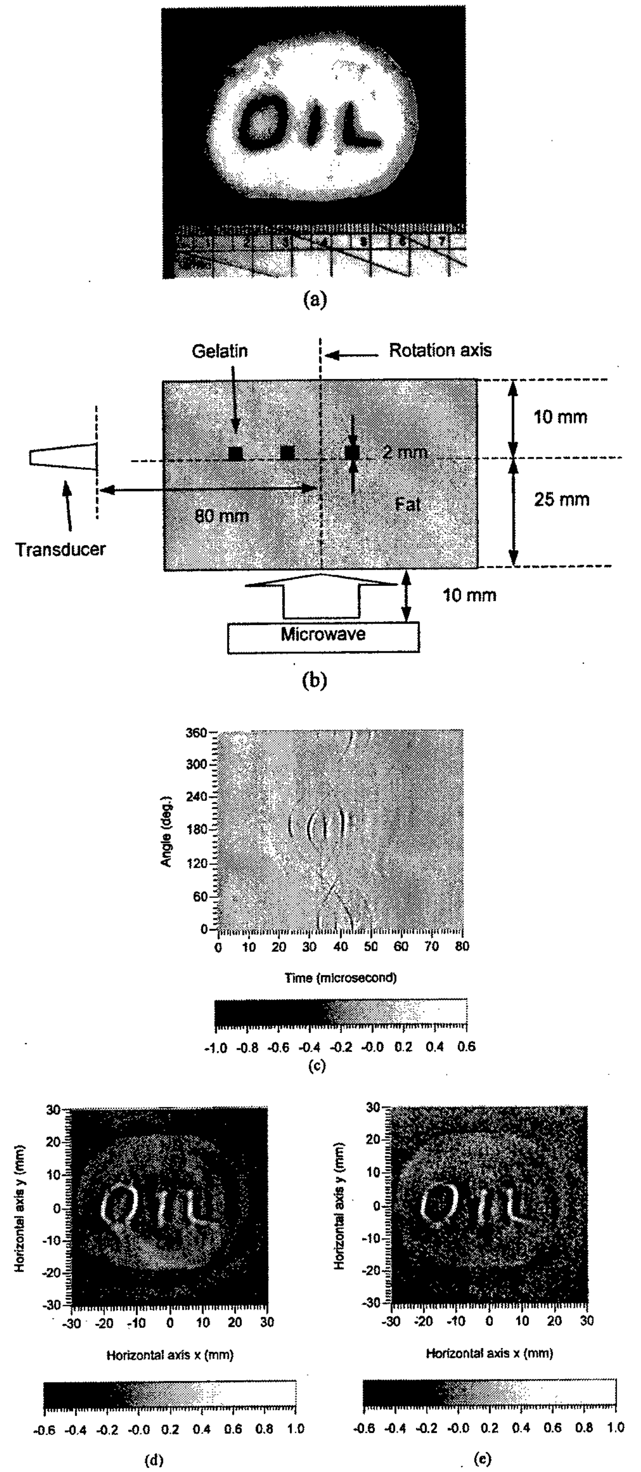

FIG. 4. (a) Cross-sectional photograph of the sample; (b) the diagram of the measurement in side view; (c) the filtered thermoacoustic temporal signals detected at different angular positions from 0°–360°; (d) the reconstructed image with filtering; (e) the reconstructed image without filtering.

the filter W_Ω was not used to depress the high-frequency noise, the reconstructed image displayed certain randomly distributed spots, as shown in Fig. 4(e), which degrade the image quality a lot.

In signal processing, we removed only the low-frequency component below 50 KHz. As shown in Fig. 4(d), the boundary and location of the large fat base with a 5 cm diameter was also faithfully imaged. Therefore, we conclude that the removal of low frequencies in signal processing will not have much effect on the detection of relatively large structures. The location and boundary of the microwave absorption structures are primarily determined by the relatively high-frequency component of the thermoacoustic signals.

V. NUMERICAL SIMULATION

The full width half-maximum (FWHM) of the point-spread-function (PSF) profile can be used to represent the spatial resolution.[12] Through numerical simulation, we can calculate the PSF profiles and then estimate the spatial resolution.

The limit band of the detection system is a primary factor in limiting the spatial resolution. Consider a point source at axis $x=x_p$, which can be written in the circular polar coordinates as

$$D(\mathbf{r}_p)=\frac{\delta(\rho-x_p)\,\delta(\varphi)\,\delta(z)}{\rho}. \tag{13}$$

Substituting it into Eq. (3), and taking the Fourier transform, it is easy to obtain the generated thermoacoustic wave in the frequency domain,

$$p(\mathbf{r}_0,\omega)=\frac{-i\omega}{4\pi c^2}\,\frac{\exp(ikd)}{d}, \tag{14}$$

where d is the distance between the point source and the detector,

$$d=\sqrt{\rho_0^2+x_p^2-2\rho_0 x_p\cos\varphi_0+z_0^2}. \tag{15}$$

For simplicity, we only consider a circular measurement in the plane $z_0=0$. We assume the sampling frequency is 20 MHz and use the Hanning window to simulate the limit band of the detection system. Figure 5(a) shows three examples of ramp filters modified by Hanning windows with cutoff frequencies at 4, 2, and 1 MHz, respectively. We use Eq. (6) to calculate derivatives of the temporal thermoacoustic signals. Finally, the FBP, Eq. (4), is employed to reconstruct images from the simulated data.

The numerical calculations demonstrate that the PSF is radially symmetric only when the point source is located at the origin. Such examples of PSF radial profiles with different cutoff frequencies are shown in Fig. 5(b). When a point source is off center, the PSF is not radially symmetric. Figure 5(c) shows some examples of PSF radial profiles when the point source is at $x_p=30$ mm. The farther the point is off the origin, the more distortion the PSF has. But the distortion is not significant and the PSF does not expand in either the lateral or axial direction by very much. Therefore, the PSF and FWHM can be regarded as nearly space invariant. Of course, if the detector system has a lower cutoff frequency, the width of the PSF profile has more extension and the spatial resolution becomes lower. Only a wide band signal at

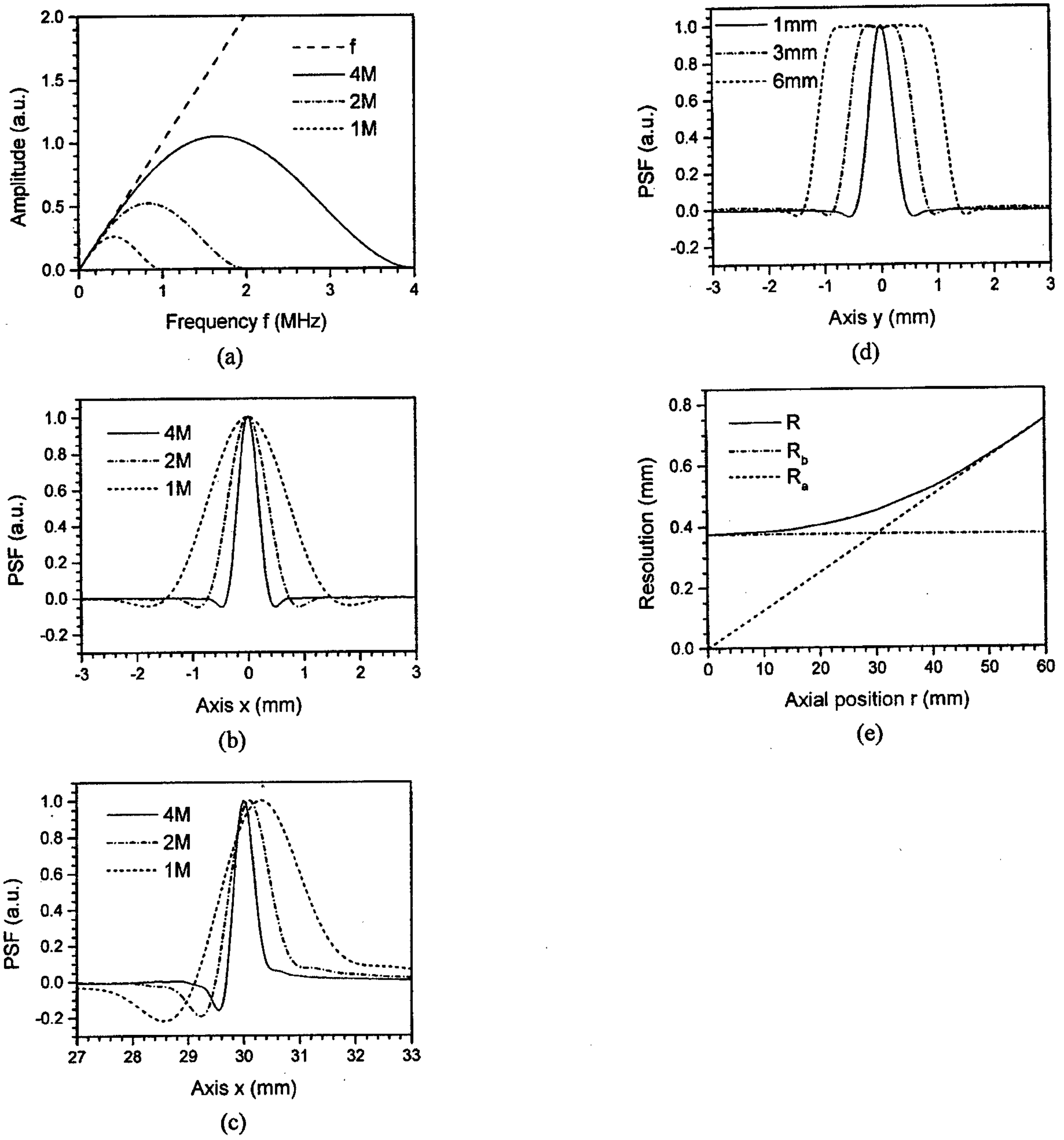

(a)

(b)

(c)

(d)

(e)

FIG. 5. (a) The pure ramp filter *f* (dashed line) and the modified filters by Hanning windows with different cutoff frequencies: 4 MHz (solid line), 2 MHz (short dash dotted line) and 1 MHz (short dashed line); Examples of PSF radial profiles with Hanning windows at cutoff frequencies: 4 MHz (solid line), 2 MHz (short dash dotted line) and 1 MHz (short dashed line), when the point source at (b) the origin and (c) the axis $x = 30$ mm; (d) examples of PSF profiles in lateral view with different detector aperture size $\delta = 1$ mm (solid line), 3 mm (short dash dotted line), and 6 mm (short dashed line), respectively; (e) an example of a comparison with R_a, R_b, and R, where $\delta = 1$ mm.

a sufficiently high frequency can restore good spatial resolution and accurate position orientation. Actually, the distortion of the PSF results from the approximation of the FBP algorithm.

For the PSF profiles in Fig. 5(b), the FWHM were measured to be 0.4, 0.9, and 1.5 mm for the cutoff frequencies 4, 2, and 1 MHz, respectively. These values are equivalent to the corresponding half-wavelengths of the central or dominative frequencies of the modified ramp filters: 1.7, 0.8, and 0.4 MHz, respectively. Therefore, the spatial resolution resulting from the bandwidth of the detection system can be estimated by

$$R_b \approx \frac{\lambda_c}{2}, \qquad (16)$$

where λ_c is the wavelength of the central or dominative high frequency of the detection system.

In addition to the limitations resulting from the bandwidth of the detection system, the size of the detector aperture is

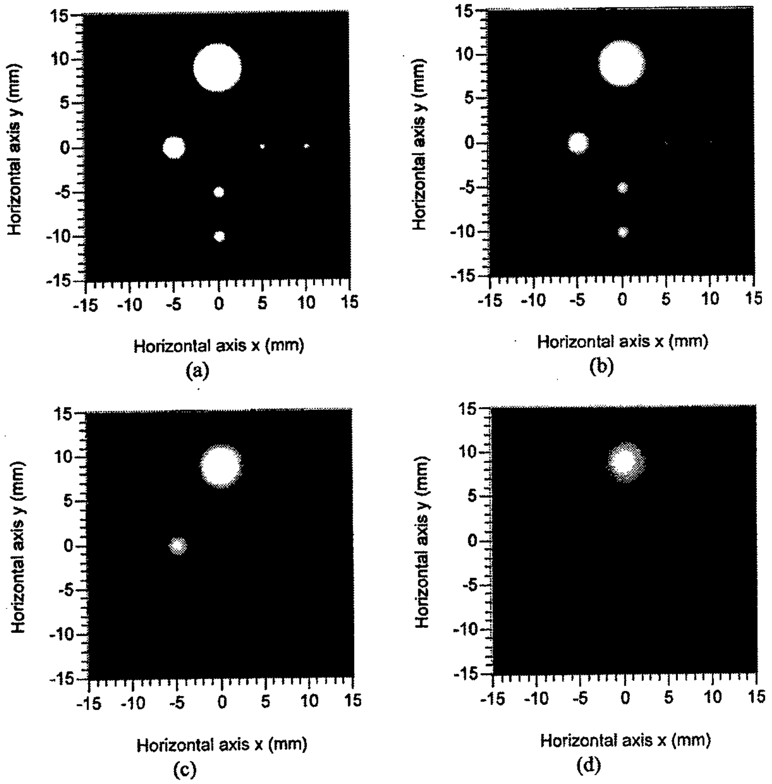

(a)

(b)

(c)

(d)

FIG. 6. Examples of reconstructed images with Hanning windows at different cutoff frequencies: (a) 4 MHz, (b) 2 MHz, (c) 1 MHz, and (d) 0.5 MHz respectively.

another factor, which limits spatial resolution. We also chose to investigate its effect through numerical simulation. The received signal in the detector can be simulated by a surface integral divided by its aperture. Then the PSF can be calculated through the FBP, Eq. (4). We assume that the detector has a flat surface with diameter δ.

The simulation demonstrates that the PSF gradually extends along the lateral side but changes very little along the axial direction. Figure 5(d) shows examples of lateral profiles for $\delta = 1$, 3, and 6 mm, respectively, where the point source at $x_p = 30\,\mathrm{mm}$ and $f_\Omega = 4\,\mathrm{MHz}$. It is expected that a big detector aperture will greatly blur the lateral resolution. For convenience, this kind of spatial resolution can be termed R_a, which can be estimated by

$$R_a \approx \frac{r}{r_0}\delta, \qquad (17)$$

where r_0 is the radius of the measurement geometry and r is the distance of the point source and the origin. Figure 5(e) shows an example of a comparison with R_a, R_b, and the lateral resolution R, where $\delta = 1$ mm; $r_0 = 80\,\mathrm{mm}$ and $f_\Omega = 4\,\mathrm{MHz}$. Near the origin, $R_a < R_b$, the lateral resolution R is still dominated by R_b. Beyond that where $R_a > R_b$, the lateral resolution R is greatly degraded by the aperture size δ and finally equals R_a. The result also indicates that either a large detector radius r_0 or a small detector aperture δ can improve the lateral resolution in the central region of the detection system. But R_b, i.e., the band limit of the detection system, determines the highest resolution we can obtain.

Let us review the experiment in the previous section. The detector aperture has a 6 mm diameter, and the image region is 30 mm in diameter. Therefore, the worst spatial resolution at $r = 30\,\mathrm{mm}$ still has ~2 mm. The dominative high frequency of the detection system is about 1.6 MHz, as shown in Fig. 3(b). Thus, the highest resolution is about 0.5 mm. That explains why the word "OIL" in 2 mm diameter can be clearly imaged.

Next, we conduct some numerical experiments. We consider a set of uniform spherical absorbers surrounded by a nonabsorbing background medium. For convenience, we use the centers of the absorbers to denote their positions. We also assume that the pulse duration is very short and can be regarded as a delta function, and, consequently, that the thermoacoustic signal received by the transducer can be calculated by Eq. (3). We employ the circular measurement configuration, as shown in Fig. 1(a). Suppose the circular ultrasonic array consists of 160 elements. The detection radius is 80 mm. There are six spherical absorbers in the $z = 0$ plane: a pair of tiny absorbers in diameter 0.75 mm at the positive x axis, a pair of small absorbers in diameter 1.5 mm at the negative y axis, a moderate absorber in diameter 3 mm at the negative x axis, and a big absorber in diameter 6 mm at the positive y axis. Equation (6) is used to compute the filtered thermoacoustic signals with Hanning windows. Figure 6 shows the reconstructed images with different cutoff frequencies: (a) 4 MHz, (b) 2 MHz, (c) 1 MHz, and (d) 0.5 MHz, respectively. As expected, all of the absorbers are clearly imaged, as shown in Fig. 6(a), when the frequency band is sufficiently wide. However, in the absence of a high-frequency signal, the small size structure is lost. For example, if the cutoff frequency is 1 MHz, the tiny absorbers disappear. For the even lower cutoff frequency of 0.5 MHz, not only do the small absorbers disappear, but also the originally sharp borders of the big absorbers are greatly degraded.

The above numerical simulations gives us clear directions for designing a good image system with ~mm spatial resolution. The duration of the microwave pulse should be less than 1 μs, which allows a thermoacoustic signal up to ~MHz frequency to be generated. The measurement detectors and the preamplifier should have sufficiently wide bands, and the central frequency of the detection system should reach 1–2 MHz. The transducer with a small aperture, such as 1 mm in diameter, is preferred. The small aperture will have less effect on the lateral resolution, and it will reduce the SNR as well. Alternatively, a big detection radius 10–15 cm can be adopted with the sacrifice of signal amplitude because of the acoustic wave propagation attenuation. A wide microwave frequency range from 300 MHz to 3 GHz can be used as the irradiation source. A lower-frequency microwave might be better to image relatively large size samples because it can penetrate deeper.

Finally, we must point out that incomplete measurement data will result in reconstruction artifacts and will degrade the spatial resolution. This topic will be addressed more completely in future work.

VI. CONCLUSION

We have presented our study on pulsed-microwave-induced thermoacoustic tomography in biological tissues by a circular measurement configuration. A filtered backprojection algorithm is used to reconstruct the cross-sectional images. The reconstructed image of a phantom sample agrees with the original values very well. Through numerical simulation, the point-spread function is calculated to estimate the spatial resolution. The results demonstrate that the circular measurement configuration combined with the filtered backprojection method is a promising technique for using microwave absorption contrast and ultrasound spatial resolution (~mm) to detect small tumors buried in biological tissues.

ACKNOWLEDGMENTS

This project was sponsored in part by the U.S. Army Medical Research and Material Command Grant No. DAMD17-00-1-0455, the National Institutes of Health Grant No. R01 CA71980, the National Science Foundation Grant No. BES-9734491, and Texas Higher Education Coordinating Board Grant No. ARP 000512-0123-1999.

APPENDIX

According to the IEEE standard for safety levels with respect to human exposure to radio frequency electromagnetic fields 3 KHz to 300 GHz (IEEE Std C95.1, 1999 edition), the peak power of maximum permissible exposure (Peak MPE) for a controlled environment in the frequency range f (300–3000 MHz) can be computed by

$$\text{Peak MPE}=\frac{0.24}{N}\times\frac{f}{\text{Pulse width}}\ (\text{mW/cm}^2),$$

where N is the pulse number per second ($N>5$) and the pulse width (<100 ms) is in seconds. In other words, the permissible pulse energy with illumination area S (cm^2) can be estimated by

$$\text{Pulse Energy}=\text{Peak MPE}\times\text{Pulse width}\times S$$
$$=\frac{0.24Sf}{N}\ (\text{mJ}).$$

In our system, $N=50$, pulse width$=0.5$ ms, and the area of the waveguide $S=7.2\times 3.4\,\text{cm}^2\approx 22\,\text{cm}^2$. Therefore, the permissible pulse energy$=0.24\times 22\times 3000/50\approx 300$ mJ. But the pulse energy that we used is only 10 mJ, which is much less than the above permissible value.

Actually, the pulse width is so short that only tiny energy is delivered to the sample. The microwave is not focused and the illumination area is so big that the energy density in the tissue is very low. Suppose the penetration depth of microwave is 1 cm, the energy density E_a due to a pulse microwave excitation can be estimated by

$$E_a=\text{Pulse energy}/(\text{Illumination area } S\times 1\ \text{cm})$$
$$=10\ \text{mJ}/22\ \text{cm}^3\approx 0.45\ \text{mJ/cm}^3.$$

Then, we can estimate the pressure and temperature rise excited by a pulse microwave in tissue. The muscle contains about 75% water. We take it as an example. In muscle, the volume expansion coefficient is $\beta\approx 3.8\times 10^{-4}\,\text{K}^{-1}$, the heat capacity is $C_p\approx 3.7\,\text{mJ/(g mK)}$, and the mass density is $\rho\approx 1$ g/cm^3. Therefore, the Grüneisen parameter$=\beta c^2/C_p\approx 0.23$, and the generated pressure rise,

$$p=0.23\times 0.45\ \text{mJ/cm}^3\approx 0.1\ \text{mJ/cm}^3=1\ \text{mbar},$$

and the temperature rise,

$$\delta T=E_a/(C_p\rho)=0.45/3.7\approx 0.1\ \text{mK}.$$

As discussed in the paper, the penetration depth in tissue for a microwave below 3 GHz is several centimeters. The Grüneisen parameter in other soft tissue should be close to the value 0.23 in muscle. Therefore, we can conclude that a microwave pulse only causes pressure rise with several millibars and temperature rise with millidegrees. Such tiny values are far beyond causing tissue damage.

[a] Author to whom all correspondence should be addressed. Telephone: 979-847-9040; fax: 979-845-4450; electronic mail: LWang@tamu.edu; URL: http://oilab.tamu.edu.

[1] R. A. Kruger, K. K. Kopecky, A. M. Aisen, D. R. Reinecke, G. A. Kruger, and W. L. Kiser, "Thermoacoustic CT with radio waves: A medical imaging paradigm," Radiology **211**, 275–278 (1999).

[2] G. Ku and L.-H. V. Wang, "Scanning thermoacoustic tomography in biological tissues," Med. Phys. **27**, 1195–1202 (2000).

[3] G. Ku and L.-H. V. Wang, "Scanning microwave-induced thermoacoustic tomography: Signal, resolution, and contrast," Med. Phys. **28**, 4–10 (2001).

[4] M. H. Xu, G. Ku, and L.-H. V. Wang, "Microwave-induced thermoacoustic tomography using multi-sector scanning," Med. Phys. **28**, 1958–1963 (2001).

[5] R. A. Kruger and P. Liu, "Photoacoustic ultrasound: Pulse production and detection in 0.5% Liposyn," Med. Phys. **21**, 1179–1184 (1994).

[6] M. H. Xu and L.-H. V. Wang, "Time-domain reconstruction for thermoacoustic tomography in a spherical geometry," IEEE Trans. Med. Imaging (in press).

[7] M. H. Xu, Y. Xu, and L.-H. V. Wang, "Thermoacoustic imaging in biological tissues: Time–domain reconstruction algorithms," IEEE Biomed. Eng. (submitted).

[8] S. Chaudhary, R. Mishra, A. Swarup, and J. Thomas, "Dielectric properties of normal human breast tissues at radiowave and microwave frequencies," Indian J. Biochem. Biophys. **21**, 76–79 (1984).

[9] W. Joines, Y. Zhang, C. Li, and R. Jirtle, "The measured electrical properties of normal and malignant human tissues from 50–900 MHz," Med. Phys. **21**, 547–550 (1994).

[10] A. C. Tam, "Application of photoacoustic sensing techniques," Rev. Math. Phys. **58**, 381–431 (1986).

[11] M. Bertero and P. Boccacci, *Introduction to Inverse Problems in Imaging* (Institute of Physics Publishing, London, 1998).

[12] R. A. Kruger, W. L. Kiser, K. D. Miller, H. E. Reynolds, D. R. Reinecke, G. A. Kruger, and P. J. Hofacker, "Thermoacoustic CT: Imaging principles," Proc. SPIE **3916**, 150–159 (2000).

Photoacoustic tomography of biological tissues with high cross-section resolution: Reconstruction and experiment

Xueding Wang, Yuan Xu, and Minghua Xu
Optical Imaging Laboratory, Biomedical Engineering Program, Texas A&M University, 3120 TAMU, College Station, Texas 77843-3120

Seiichirou Yokoo and Edward S. Fry
Department of Physics, Texas A&M University, 4242 TAMU, College Station, Texas 77843-4242

Lihong V. Wang[a)]
Optical Imaging Laboratory, Biomedical Engineering Program, Texas A&M University, 3120 TAMU, College Station, Texas 77843-3120

(Received 26 December 2001; accepted for publication 25 September 2002; published 27 November 2002)

A modified back-projection approach deduced from an exact reconstruction solution was applied to our photoacoustic tomography of the optical absorption in biological tissues. Pulses from a Ti:sapphire laser (4.7 ns FWHM at 789.2 nm) were employed to generate a distribution of photoacoustic sources in a sample. The sources were detected by a wide-band nonfocused ultrasonic transducer at different positions around the imaging cross section perpendicular to the axis of the laser irradiation. Reconstructed images of phantoms made from chicken breast tissue agreed well with the structures of the samples. The resolution in the imaging cross section was experimentally demonstrated to be better than 60 μm when a 10 MHz transducer (140% bandwidth at -60 dB) was employed, which was nearly diffraction limited by the detectable photoacoustic waves of the highest frequency. *© 2002 American Association of Physicists in Medicine.*
[DOI: 10.1118/1.1521720]

Key words: photoacoustic tomography, optoacoustic tomography, laser, reconstruction, imaging

I. INTRODUCTION

Recently, there has been considerable interest in photoacoustic tomography, a nonionizing imaging modality based upon differential absorption of electromagnetic waves for different tissue types. It is well known that some tissues, such as malignant tumors, melanin-pigmented lesions, and blood vessels have obviously higher absorption rates compared with surrounding tissues. For example, the absorption contrast between breast tumors and normal breast tissues can be as high as 300% for 1064 nm light;[1] the absorption contrast between the blood and the surrounding medium is around 1000% for 850 nm light.[2] The thermal expansion of an absorption structure in tissue creates acoustic waves according to the thermoelastic mechanism, which can be detected by high sensitive piezoelectric devices outside the sample. Photoacoustic tomography visualizes the high optical contrast between different soft biological tissues instead of the low acoustic contrast while retaining the satisfactory spatial resolution of pure ultrasound imaging.

The photoacoustic method to detect small deeply embedded tumors has been studied by Esenaliev *et al.*[3] and Oraevsky *et al.*[4,1] In an attempt to advance the *in vivo* detection of skin cancer, photoacoustic imaging of layered tissues with optical contrast has been studied by Beenen *et al.*,[5] Oraevsky *et al.*,[6] and Karabutov *et al.*[7] Axial resolution up to 10–20 μm has been achieved. Hoelen *et al.* applied photoacoustic tomography to the detection of blood concentrations.[2] The depth resolution of blood vessel imaging in highly scattering media is about 10 μm. Paltauf *et al.* adopted an optical method instead of piezoelectric devices for two-dimensional (2D) ultrasonic detection and achieved a spatial resolution around 10 μm.[8]

All of the above photoacoustic tomography systems can be categorized into two detection modes: (1) the forward mode, with the laser irradiation and ultrasound detection on opposite surfaces of the sample, and (2) the backward mode, with the laser irradiation and ultrasound detection on the same surface of the sample. Although high resolution along the axis of the laser irradiation can be easily achieved, the basic problem with these two modes is the poor lateral resolution, which is limited mainly by the scanning range of the detector.

When lateral resolution is the concern or the imaging purpose is to obtain a 2D image of a cross section of the sample perpendicular to the axis of the laser irradiation, a proper scheme is to arrange the receiver around the laser axis to detect the acoustic signals from the side of the sample. A focused ultrasonic transducer can be adopted to perform the linear, or sector, scan, and then the measured data is used to construct an image directly,[9] which is similar to the method used in early pulse-echo ultrasonography. An alternative method is to use a wide-band point detector to receive the acoustic signals and then reconstruct the absorption distribution based on a certain algorithm.[10,11]

On the other hand, when employing the nonfocused ultrasonic transducer for detection, the quality of the photoacoustic imaging is highly dependent on the reconstruction algorithm. Examples of approximate reconstruction algorithms include the weighted delay-and-sum method,[12] the optimal statistical approach,[13] and the Radon transform in far-field approximation.[10,14,15] Exact reconstruction algorithms were recently derived for various detection geometries.[16–19]

In this paper, a modified back-projection method based on the circular-scan geometry was applied to the photoacoustic tomography of optical absorption in biological tissues. The modified back-projection algorithm was deduced from an exact reconstruction solution in the time domain, which will be briefly introduced in the second section. In the third section, the experimental method, as well as the imaging results in tissue phantoms, will be shown. In the fourth section, the best resolution in the cross section of our photoacoustic tomography system will be demonstrated by experimental results. The final section will present our conclusions.

II. MODIFIED BACK-PROJECTION

We are interested in tissues with inhomogeneous optical absorption but relatively homogeneous acoustic properties. When the laser pulse is very short, which is the case in our experiments, the time required for thermal diffusion is much greater than the time for the thermoacoustic transition. Consequently, the effect of heat conduction in the thermoacoustic wave equations can be ignored. As has been described previously in the literatures,[20,21] the generation of a photoacoustic wave by deposition of light energy can be expressed as

$$\frac{\partial^2 p(\mathbf{r},t)}{\partial t^2}-v_s^2\nabla^2 p(\mathbf{r},t)=\frac{v_s^2\beta}{C_p}\frac{\partial H(\mathbf{r},t)}{\partial t}, \tag{1}$$

where v_s is the acoustic speed; C_p is the specific heat; β is the thermal coefficient of volume expansion; and $H(\mathbf{r},t)$ is the heat-producing radiation deposited in the tissue per unit volume per unit time, which can be expressed as

$$H(\mathbf{r},t)=\varphi(\mathbf{r})\eta(t), \tag{2}$$

where $\varphi(\mathbf{r})$ describes the optical energy deposition (also called optical absorption) within the tissue at position $\mathbf{r}$; $\eta(t)$ describes the shape of the irradiation pulse, which can be further expressed as $\eta(t)=\delta(t)$ for delta-function laser pulses.

The object of the image reconstruction is to estimate the distribution of the optical absorption $\varphi(\mathbf{r})$ of the tissue from a set of measured acoustic signals $p(\mathbf{r},t)$. For a circular scanning configuration, the exact inverse solution can be derived based on the spherical harmonic function,

$$\varphi(\mathbf{r})=\frac{1}{4\pi^2\lambda\nu_s r_0^2}\iint_{S_0} dS_0\int_{-\infty}^{+\infty}dk\,\overline{p}(\mathbf{r}_0,k)$$

$$\times\sum_{m=0}^{\infty}\frac{(2m+1)j_m(kr)}{h_m^{(1)}(kr_0)}P_m(\mathbf{n}\cdot\mathbf{n}_0), \tag{3}$$

where $\lambda=\beta/C_p$; $\mathbf{n}=\mathbf{r}/r$; $\mathbf{n}_0=\mathbf{r}_0/r_0$; $\mathbf{r}_0$ is the detector position in respect to the imaging center; $k=\omega/v_s$ is the wave number; $\overline{p}(\mathbf{r}_0,k)$ is the Fourier transform of the pressure function $p(\mathbf{r}_0,t)$; S_0 is the measurement surface including the object under investigation; $j_l(\cdot)$ and $h_l^{(1)}(\cdot)$ are the spherical Bessel and Hankel functions, respectively; and $P_l(\ )$ represents the Legendre polynomial. The detailed derivation of this exact inverse solution can be found elsewhere.

This inverse solution involves a summation of a series that is computationally time consuming. Therefore, it is desirable to simplify the solution. In the experiments, the detection radius r_0 is much larger than the wavelengths of the photoacoustic waves that are used for imaging. Therefore, we can assume $|k|r_0\gg 1$ and use the asymptotic form of the Hankel function to simplify the above exact inverse solution Eq. (3). The approximate inverse solution has the form of

$$\varphi(\mathbf{r})=-\frac{1}{2\pi\nu_s^4\lambda}\iint_{S_0} dS_0\frac{1}{t}\frac{\partial p(\mathbf{r}_0,t)}{\partial t}\bigg|_{t=|\mathbf{r}_0-\mathbf{r}|\nu_s}. \tag{4}$$

Actually, two compensation factors are implicit in this solution. Firstly, we introduce a weighting factor "*t*," which compensates for the $1/t$ attenuation of a spherical pressure wave as it propagates through a homogeneous medium. At the same time, we consider that in this type of reconstruction geometry, the contribution to a certain point P from an element of receiving area S is proportional to the subtended solid angle of this element S when viewed from the point P. The solid angle is inversely proportional to the square of the distance between the receiving element S and the point P, which leads to a compensation factor of "$1/t^2$." Combining the above two factors, we obtain a compensation factor of "$1/t$" as shown in Eq. (4).

Reference 15 gave an approximate solution of $\varphi(\mathbf{r})$ based on a three-dimensional inverse Radon transformation with the assumption that the size of an absorption object is much less than the distance between the source and the detector. In that case, the spherical surface over which the surface integral is computed approximates a plane. Actually, with the above assumption, t is nearly a constant compared to the size of the absorption object. However, in most cases, for example, the situation in our experiments, the size of an absorption object can be comparable to the distance between the source and the detector. Under this condition, the solution given by Ref. 15 is not appropriate, while our solution shown in Eq. (4) still holds and therefore is more general.

Although the modified back-projection reconstruction shown in Eq. (4) is valid for three-dimensional distributions of photoacoustic sources, we here consider only the imaging of thin slices of absorption objects in turbid media to evaluate our imaging system. The slices of absorption objects lie in the imaging plane perpendicular to the axis of laser irradiation. The photoacoustic signals from turbid media outside the imaging plane are regarded as background that will not provide information for the imaging of absorption objects. In this case, the detection of acoustic pressures over the 2π angle in the imaging plane is sufficient to achieve high resolution in the imaged cross section. For 2D imaging, the approximate inverse solution for the circular-scan geometry can be represented by

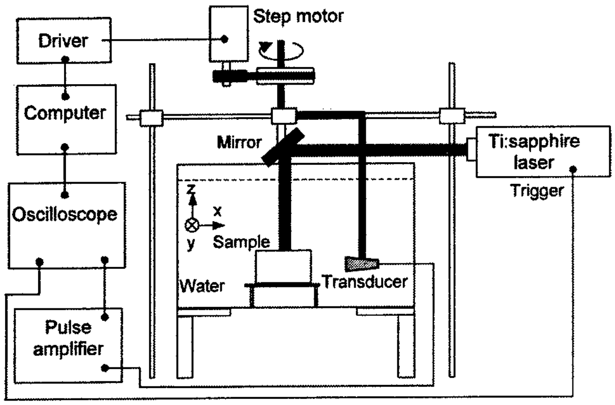

FIG. 1. Experimental setup.

$$\varphi(\mathbf{r}) = -\frac{r_0^2}{2\pi\lambda v_s^4}\int_{\theta_0} d\theta_0 \frac{1}{t}\frac{\partial p(\mathbf{r}_0,t)}{\partial t}\bigg|_{t=|\mathbf{r}_0-\mathbf{r}|/v_s}, \qquad (5)$$

which is an integral over θ_0 around the thin slice of the object. From Eqs. (4) and (5), we see that the reconstruction of the absorption distribution can be fulfilled by back-projection of the quantity

$$-\frac{1}{t}\frac{\partial p(r_0,t)}{\partial t}\bigg|_{t=|r_0-r|/v_s}$$

instead of the acoustic pressure $p(\mathbf{r}_0,t)$.

If $R(t)$ is the impulse response of the detector and $P(t)$ is the pulse duration of the laser, in the time domain, we have

$$T(\mathbf{r}_0,t) = p(\mathbf{r}_0,t) * R(t) * P(t), \qquad (6)$$

where $T(\mathbf{r}_0,t)$ is the piezoelectric signal detected by the transducer, and $*$ represents convolution. Then, $\partial p(\mathbf{r}_0,t)/\partial t$ in Eq. (5) can be calculated by an inverse Fourier transformation,

$$\frac{\partial p(\mathbf{r}_0,t)}{\partial t} = \mathbf{FFT}^{-1}\left[\frac{-i\omega T(\mathbf{r}_0,\omega)W(\omega)}{P(\omega)R(\omega)}\right]$$
$$= \frac{1}{2\pi}\int_{-\infty}^{+\infty}\frac{-i\omega T(\mathbf{r}_0,\omega)W(\omega)}{P(\omega)R(\omega)}\exp(-i\omega t)dt, \qquad (7)$$

where $W(\omega)$ is a band-pass window function that suppresses the frequency component outside the detectable spectrum of the transducer.

III. TOMOGRAPHY IN BIOLOGICAL TISSUES

A. Experimental method

A schematic diagram of our experimental setup for photoacoustic tomography is shown in Fig. 1, where a laboratory coordinate system $[x,y,z]$ is also depicted. A flash-lamp-pumped Ti:sapphire laser operating at a wavelength of 789.2 nm with a pulse energy of approximately 30 mJ, a pulse duration of 4.7 ns FWHM, and a repetition rate of 10 Hz, was used as the light source. The laser is expanded to a 1.5 cm diameter beam when heating the sample surface from above along the laser axis; this provides an incident power density within the limit of safety for human skin (100 mJ/cm^2) according to the ANSI standard.[22] In our experiments, the area in a cross section of the sample that is imaged is defined by the size of the laser beam. The wave form and the frequency spectrum of the laser pulse are demonstrated in Figs. 2(a) and 2(b), respectively, where the curve in (b) shows the component of $R(\omega)$ in Eq. (7).

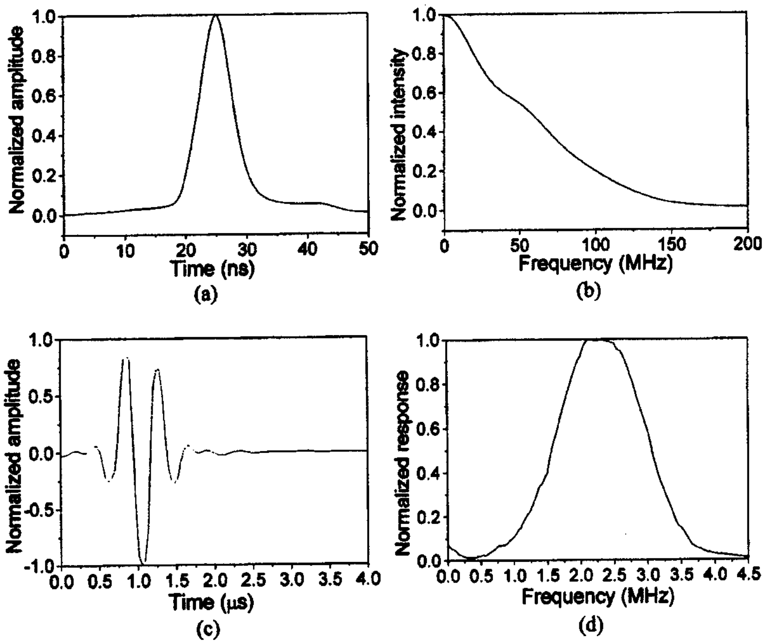

FIG. 2. (a) Wave form and (b) frequency spectrum of the 4.7 ns laser pulse. (c) Impulse response and (d) frequency response of the 2.25 MHz transducer.

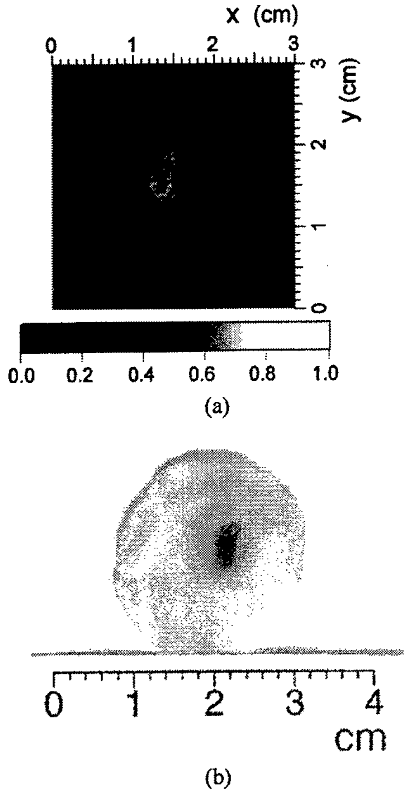

(a)

(b)

FIG. 3. Photoacoustic tomography of a slice of chicken gizzard that was buried 0.5 cm deep in the chicken breast slab. (a) Reconstructed image; (b) picture of the imaged cross-section of the sample.

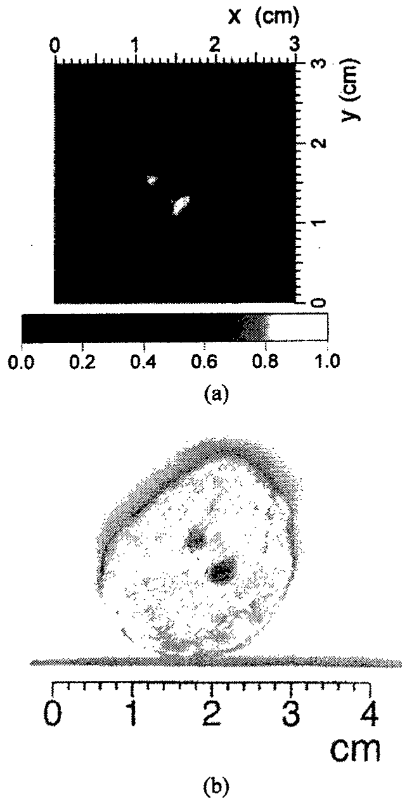

(a)

(b)

FIG. 4. Photoacoustic tomography of two slices of chicken gizzard that were buried 0.5 cm deep in the chicken breast slab. (a) Reconstructed image; (b) picture of the imaged cross-section of the sample.

The wide-band nonfocused transducer (V323, Panametrics) has a 2.25 MHz central frequency and a 6 mm diameter of the active element. The impulse response and the frequency response of the transducer are demonstrated in Figs. 2(c) and 2(d), respectively, where the curve in Fig. 2(d) shows the component of $P(\omega)$ in Eq. (7). Because the frequency bandwidth of the laser pulse is much broader than that of the transducer, $P(\omega)$ is constant and Eq. (7) can be simplified as

$$\frac{\partial p(\mathbf{r}_0,t)}{\partial t} \propto \frac{1}{2\pi}\int_{-\infty}^{+\infty} \frac{-i\omega T(\mathbf{r}_0,\omega)W(\omega)}{R(\omega)} \exp(-i\omega t)dt. \quad (8)$$

The transducer was mounted on a rotation stage that was driven by a computer-controlled step motor. The transducer scanned around the sample with a rotational step size of 1.125° and a rotational radius of 5 cm. The transducer and the sample were immersed in water. A low-noise pulse preamplifier (500 PR, Panametrics) amplified the acoustic signals received by the transducer and sent signals to an oscilloscope (TDS-640A, Tektronix). Then, 30 times averaged digital signals were transferred to a computer for imaging.

The experiments were performed with thin slices of gizzard tissues or red rubber pieces placed 0.5 cm deep in fresh chicken breast muscle slabs. For 789.2 nm light the reduced scattering coefficient μ_s' and the absorption coefficient μ_a for chicken breast tissue are about 1.9 cm^{-1} and 0.1 cm^{-1}, respectively.[23] Under this condition, the effective optical attenuation coefficient μ_{eff} is 0.77 cm^{-1}. The blood concentration in the chicken gizzard tissue is much higher than that in the chicken breast muscle. According to our measurements, the absorption contrast between them is greater than 200%. In the experiments, the sizes of the chicken breast slabs were larger than the size of the laser beam. Therefore, the imaged area is only a part of a cross section of the sample.

B. Imaging results

Image reconstruction utilized the 2D modified backprojection algorithm described in Eq. (5). We used 1.5 mm/μs as the estimated sound velocity ν_s in soft tissues. When a detected sample has nearly homogeneous acoustic properties, the small difference between the actual sound velocity and the estimated value will not cause any distortion in the relative location of the absorption distribution in the sample. In other words, the absolute locations and sizes of the detected targets inside the sample may be changed; however, their relative positions will not be altered.

Figure 3(a) shows the reconstructed image of a thin slice of gizzard tissue buried 0.5 cm deep in a chicken breast slab. The gizzard tissue has a nearly rectangular shape (3 mm×6 mm) in the imaging plane and a thickness of about 1 mm. The picture of the cross section of this sample is shown in Fig. 3(b) for comparison. In the second sample, two slices of

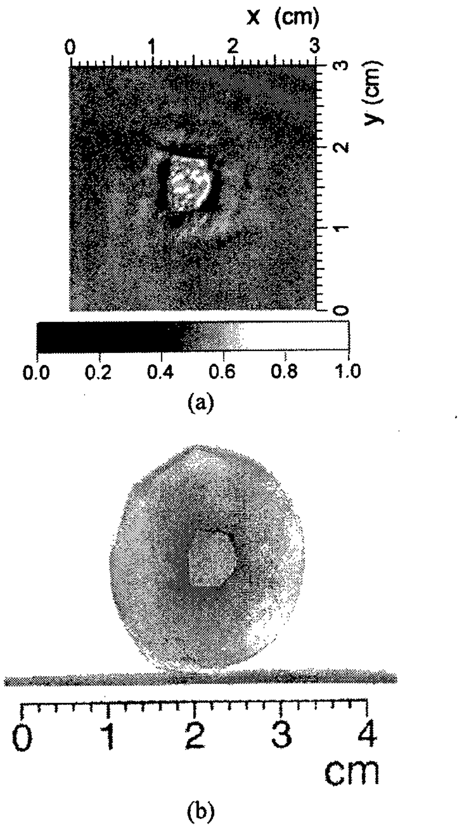

(a)

(b)

FIG. 5. Photoacoustic tomography of a slice of rubber that was buried 0.5 cm deep in the chicken breast slab. (a) Reconstructed image; (b) picture of the imaged cross-section of the sample.

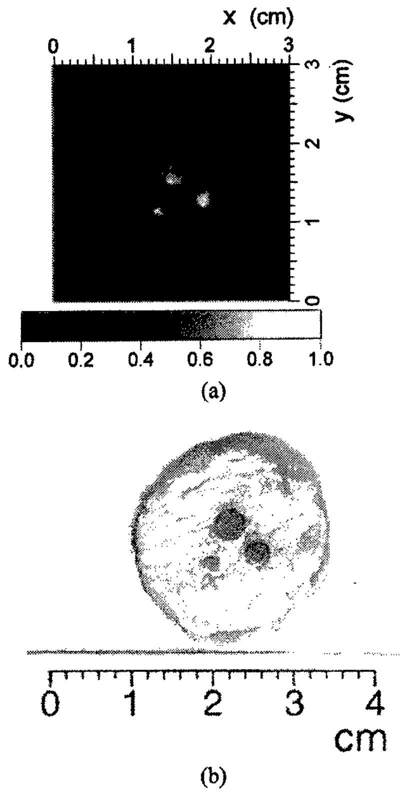

(a)

(b)

FIG. 6. Photoacoustic tomography of three slices of rubber circles that were buried 0.5 cm deep in the chicken breast slab. The radii of the three circles are 0.4 cm, 0.3 cm, and 0.1 cm, respectively. (a) Reconstructed image; (b) picture of the imaged cross-section of the sample.

gizzard tissues are placed 0.5 cm deep in a chicken breast slab, where the sizes of the two gizzard pieces are different. The reconstructed imaging is shown in Fig. 4(a) for comparison with the picture of the sample in Fig. 4(b).

Based on our experimental system as well as the reconstruction algorithm, the results of the 2D photoacoustic tomography are satisfying. The highly absorbing objects in turbid media with comparatively low absorption were localized well. The boundaries between the gizzards and the chicken breast are clearly imaged.

Because both the gizzards and the chicken breast muscles are soft biological tissues, it is difficult to avoid deformation when the samples were photographed. For this reason, the shapes of the gizzard slices in the reconstructed imaging have minor discrepancies with those appearing in the photographs. To overcome this problem, slices of red rubber pieces were used as absorption objects in some of our experiments. Figure 5(a) shows the reconstructed image of a slice of rubber (with a 1 mm thickness) that was buried 0.5 cm deep in a chicken breast slab; it fits perfectly with the picture of the sample shown in Fig. 5(b). In another sample, three circles of rubber slices with a 1 mm thickness, where the radii of the three circles are about 4 mm, 3 mm, and 1 mm, respectively, were adopted as absorption objects. In Figure 6(a), the shapes and sizes as well as the localizations of the three rubber slices are all imaged well compared with the picture in Fig. 6(b). In the reconstructed images in Figs. 3–6, we can see some intensity fluctuations around the absorption objects, which come mainly from the photoacoustic signals generated in the background chicken breast tissues.

IV. TESTING FOR RESOLUTION

In order to quantify the actual resolution of our detection system as well as the reconstruction algorithm, well-controlled samples with high absorption contrast in transparent media were measured for imaging. Usually, the expected highest spatial resolution is estimated to be the half wavelength at the center frequency of the transducer. However, when the frequencies of the detected photoacoustic signals determining the spatial resolution are higher than the center frequency, the achievable spatial resolution is better than the estimated resolution at the center frequency. Therefore, we estimate the possible best resolution to be the half wavelength at the highest detectable photoacoustic frequency.

Pairs of parallel lines printed on transparencies were adopted as ideal testing samples, as shown in Fig. 7(a). The length and width of the dark lines was 8 mm and 0.3 mm, respectively. The gap *d* between the two lines was set to be 0.1 mm, 0.2 mm, and 0.3 mm, respectively. Each piece of transparency with a pair of dark lines was placed in the imaging plane. The 2.25 MHz nonfocused transducer scanned-

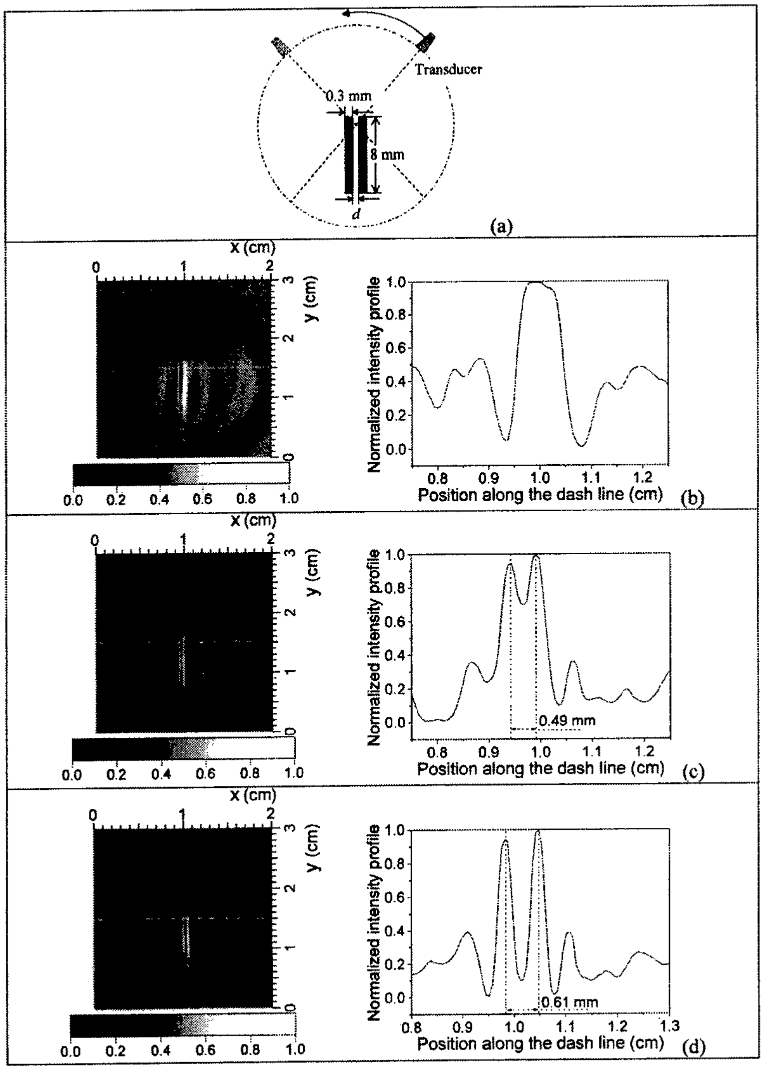

FIG. 7. (a) Schematic of a pair of parallel lines printed on transparency. The length of the two lines is 8 mm; the width of the two lines is 0.3 mm; and the gap between the two lines was *d*. The radius of the circular-scan is 50 mm. (b), (c), and (d) are the reconstructed images of the pairs of parallel lines with a gap *d* of 0.1 mm, 0.2 mm, and 0.3 mm, respectively. The profiles of reconstructed absorption intensities along the dash lines in 2D images are demonstrated as the right pictures in (b), (c), and (d), respectively.

around the transparency with a radius of 5 cm. The detectable frequency band of the transducer is from 0 to 4.5 MHz. Therefore, the estimated highest spatial resolution is 0.17 mm. The reconstructed 2D images of these pairs of lines are shown in Figs. 7(b), 7(c), and 7(d) for *d* equals 0.1 mm, 0.2 mm, and 0.3 mm, respectively. The intensity profiles along the dashed lines ($y=1.5$ cm) in the 2D images are also presented. When *d* equals 0.2 mm or 0.3 mm, the two parallel lines can be recognized with an obvious gap between them. However, when *d* equals 0.1 mm, we can see only one line in the reconstructed image. In each image, there are some weak intensity fluctuations around the pair of lines, which come mainly from acoustic reflection at the edge of the transparency piece. The results in Fig. 7 show that with the circular-scan method and the modified back-projection algorithm, we can achieve a spatial resolution of ~0.2 mm.

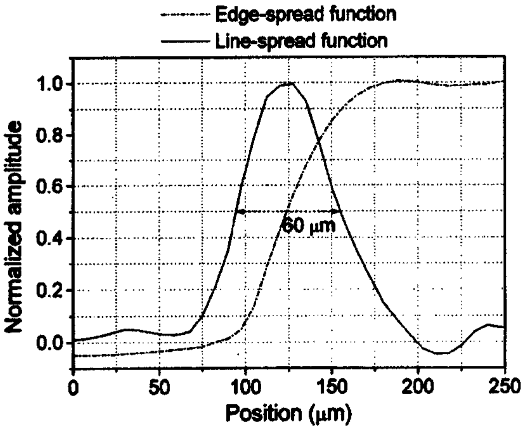

FIG. 8. Edge-spread function and line-spread function of our photoacoustic imaging system with a 10 MHz transducer.

The center of the circular scan in the experiments is taken at the center of each reconstructed image. We can see that in these 2D images, the spatial resolution at a position near the imaging center is higher than that at a longer distance from the imaging center. This kind of blur in the reconstructed image is mainly caused by the physical size of the transducer. The blur is greater when the physical size of the transducer is larger, or the distance from the imaging center is larger.

We quantified the spatial resolution of our imaging system with a 10 MHz wide-band (140% at −60 dB) cylindrically focused transducer (V312, Panametrics). The transducer has a 6 mm diameter active element and is nonfocused in the imaging plane. The estimated highest spatial resolution of our imaging system with this transducer is about 45 μm. A well-controlled phantom made from red rubber with a high optical absorption contrast and a sharp edge has been imaged to obtain the edge-spread function. A line-spread function was obtained through differentiating the profile of the edge-spread function. Both the two profiles are shown in Fig. 8. The line-spread function shows a full width at half maximum of about 60 μm, which shows that the spatial resolution of our photoacoustic imaging system is near the diffraction limit of the detected photoacoustic signals.

V. CONCLUSION

Pulsed-laser induced photoacoustic tomography of absorption in biological tissues has been studied. A modified back-projection algorithm derived from an exact inverse solution was used to reconstruct the signals received by a wide-band nonfocused transducer that scanned circularly around the sample under detection. Reconstructed images of gizzard slices and rubber slices buried in chicken breast tissues agree well with the pictures of samples. Experiments also quantified the highest 2D resolution that can be achieved by this imaging system: using a detection of 2π view, the spatial resolution is nearly diffraction limited by the detected photoacoustic waves.

Our photoacoustic detection system with the modified back-projection reconstruction algorithm is proved to be an effective method for biological tissue imaging with high contrast and high spatial resolution. If a high resolution along the laser axis is required at the same time, scanning of acoustic signals along the axis will be necessary.

ACKNOWLEDGMENTS

This project was sponsored in part by the U.S. Army Medical Research and Material Command Grant No. DAMD 17-00-1-0455, the National Institutes of Health Grant No. R01 CA71980, the National Science Foundation Grant No. BES-9734491, Texas Higher Education Coordinating Board Grant No. ARP 000512-0123-1999, and the Robert A. Welch Foundation Grant No. A-1218.

---

[a] Author to whom correspondence should be addressed. Electronic mail: lwang@tamu.edu (URL: http//oilab.tamu.edu).

[1] A. A. Oraevsky, V. A. Andreev, A. A. Karabutov, D. R. Fleming, Z. Gatalica, H. Singh, and R. O. Esenaliev, "Laser opto-acoustic imaging of the breast: detection of cancer angiogenesis," Proc. SPIE **3597**, 352–363 (1999).

[2] C. G. A. Hoelen, F. F. M. de Mul, R. Pongers, and A. Dekker, "Three-dimensional photoacoustic imaging of blood vessels in tissue," Opt. Lett. **23**, 648–650 (1998).

[3] R. O. Esenaliev, A. A. Karabutov, and A. A. Oraevsky, "Sensitivity of laser opto-acoustic imaging in detection of small deeply embedded tumors," IEEE J. Sel. Top. Quantum Electron. **5**, 981–988 (1999).

[4] R. O. Esenaliev, F. K. Tittel, S. L. Thomsen, B. Fornage, C. Stelling, A. A. Karabutov, and A. A. Oraevsky, "Laser optoacoustic imaging for breast cancer diagnostics: Limit of detection and comparison with x-ray and ultrasound imaging," Proc. SPIE **2979**, 71–82 (1997).

[5] A. Beenen, G. Spanner, and R. Niessner, "Photoacoustic depth-resolved analysis of tissue models," Appl. Spectrosc. **51**, 51–57 (1997).

[6] A. A. Oraevsky, R. O. Esenaliev, and A. Karabutov, "Laser optoacoustic tomography of layered tissues: Signal processing," Proc. SPIE **2979**, 59–70 (1997).

[7] A. A. Karabutov, E. V. Savateeva, and A. A. Oraevsky, "Imaging of layered structures in biological tissues with opto-acoustic front surface transducer," Proc. SPIE **3601**, 284–295 (1999).

[8] G. Paltauf and H. Schmidt-Kloiber, "Optical method for two-dimensional ultrasonic detection," Appl. Phys. Lett. **75**, 1048–1050 (1999).

[9] M. H. Xu, G. Ku, and L. V. Wang, "Microwave-induced thermoacoustic tomography using multi-sector scanning," Med. Phys. **28**, 1958–1963 (2001).

[10] R. A. Kruger, P. Liu, Y. R. Fang, and C. R. Appledorn, "Photoacoustic ultrasound (PAUS)–Reconstruction tomography," Med. Phys. **22**, 1605–1609 (1995).

[11] A. M. Reyman, I. V. Yahovlev, A. G. Kirillov, and V. V. Lozhkarev, "Deep tomography of biological tissues by optoacoustic method," Proc. SPIE **4256**, 159–166 (2001).

[12] C. G. A. Hoelen and de F. F. M. Mul, "Image reconstruction for photoacoustic scanning of tissue structures," Appl. Opt. **39**, 5872–5883 (2000).

[13] Y. V. Zhulina, "Optimal statistical approach to optoacoustic image reconstruction," Appl. Opt. **39**, 5971–5977 (2000).

[14] R. A. Kruger, D. R. Reinecke, and G. A. Kruger, "Thermoacoustic computed tomography–technical considerations," Med. Phys. **26**, 1832–1837 (1999).

[15] R. A. Kruger, W. L. Kiser, K. D. Miller, H. E. Reynolds, D. R. Reinecke, G. A. Kruger, and P. J. Hofacker, "Thermoacoustic CT: imaging principles," Proc. SPIE **3916**, 150–159 (2000).

[16] K. Kostli, M. Frenz, H. Bebie, and H. Weber, "Temporal backward projection of optoacoustic pressure transients using Fourier transform methods," Phys. Med. Biol. **46**, 1863–1872 (2001).

[17] M. Xu and L. V. Wang, "Time-domain reconstruction for thermoacoustic tomography in a spherical geometry," IEEE Trans. Med. Imaging **21**, 814–822 (2002).

[18] Y. Xu, D. Feng, and L. V. Wang, "Exact frequency-domain reconstruction for thermoacoustic tomography: I. Planar geometry," IEEE Trans. Med. Imaging **21**, 823–828 (2002).

[19] Y. Xu, M. Xu, and L. V. Wang, "Exact frequency-domain reconstruction for thermoacoustic tomography: II. Cylindrical geometry," IEEE Trans. Med. Imaging **21**, 829–833 (2002).

[20] G. J. Diebold, T. Sun, and M. I. Khan, "Photoacoustic waveforms generated by fluid bodies," in *Photoacoustic and Photothermal Phenomena III*, edited by D. Bicanic (Springer-Verlag, Berlin, Heidelberg, 1992), pp. 263–269.

[21] V. E. Gusev and A. A. Karabutov, *Laser Optoacoustics* (American Institute of Physics, New York, 1993).

[22] American National Standards Institute, American national standard for the safe use of lasers. Standard Z136.1-2000 (ANSI, Inc., New York, NY, 2000).

[23] G. Marquez, L. V. Wang, S. P. Lin, J. A. Schwartz, and S. L. Thomsen, "Anisotropy in the absorption and scattering spectra of chicken breast tissue," Appl. Opt. **37**, 798–804 (1998).

PHYSICAL REVIEW E **67**, 056605 (2003)

Analytic explanation of spatial resolution related to bandwidth and detector aperture size in thermoacoustic or photoacoustic reconstruction

Minghua Xu and Lihong V. Wang*
Optical Imaging Laboratory, Department of Biomedical Engineering, Texas A&M University, 3120 TAMU,
College Station, Texas 77843-3120

(Received 31 October 2002; published 9 May 2003)

An analytic explanation of the spatial resolution in thermoacoustic or photoacoustic reconstruction is presented. Three types of specific recording geometries, including spherical, planar, and cylindrical surface, as well as other general cases, are investigated. Analytic expressions of the point-spread functions (PSF's), as a function of the bandwidth of the measurement system and the finite size of the detector aperture, are derived based on rigorous reconstruction formulas. The analyses clearly reveal that the dependence of the PSF's on the bandwidth of all recording geometries shares the same space-invariant expression while the dependence on the aperture size of the detector differs. The bandwidth affects both axial and lateral resolutions; in contrast, the detector aperture blurs the lateral resolution greatly but the axial resolution only slightly.

DOI: 10.1103/PhysRevE.67.056605 PACS number(s): 43.35.+d, 87.57.Ce, 43.60.+d, 43.80.+p

I. INTRODUCTION

In the last decade, thermoacoustic or photoacoustic tomography of soft tissue utilizing excitation from a pulsed electromagnetic (EM) energy source, such as radio frequency or laser, has attracted considerable attention [1–12]. With this technique, it is assumed that, following a short pulse of EM illumination, a spatial distribution of acoustic pressure inside the tissue is simultaneously excited by thermoelastic expansion, which acts as a source for acoustic response. The intensity of the acoustic pressure is strongly related to the locally absorbed EM energy. A wide range of EM absorption coefficients in soft tissue contributes to a good contrast between different types of tissues. The effect of thermal diffusion on thermoacoustic or photoacoustic waves in tissue is always ignored, since the EM pulse duration is often so short that the thermal conduction time is far greater than the acoustic transit time through the heterogeneities of the EM energy depositions. The acoustic waves from the initial acoustic source propagate toward the surface of the tissues with various time delays. Ultrasound detectors are placed around the tissue to record the outgoing acoustic waves, referred to as the thermoacoustic or photoacoustic signals, which carry information about EM absorption as well as about the acoustic properties of the tissue. For medical imaging and diagnostics, an appropriate reconstruction algorithm is required to map the initial acoustic sources, or EM absorption distribution.

To detect thermoacoustic signals, one approach is to use focused ultrasound transducers, in which the lateral resolution is determined by the focal diameter of the transducer and the axial resolution by the bandwidth [5,6]. Another approach is to use small-aperture unfocused detectors—ideally, point detectors—that can receive ultrasound from a large angle of acceptance. Thus far, rigorous reconstruction algorithms have been reported with point-detector measurements from idealized recording configurations, including the fully enclosing spherical recording surface [7], the planar recording surface of an infinite extent [3,8], and the cylindrical recording surface of an infinite length [9]. In these algorithms, the acoustic property of the tissue is often assumed to be homogenous as the speed of sound in soft tissue is relatively constant at ~1.5 mm/μs. Details can be found in Ref. [7] of the reconstruction formulas for spherical geometry and in Refs. [8,9,11] for the planar and cylindrical geometries.

Spatial resolution is one of the most important parameters in thermoacoustic reconstruction. Acoustic inhomogeneity blurs the reconstructed image, but in some cases, the blurring can be corrected. A limited view also affects spatial resolution due to lack of sufficient data; in this case, the reconstruction is incomplete and reconstruction artifacts occur [12]. These two topics will not be addressed in this paper. There are two other main factors that limit spatial resolution—the finite bandwidth of the detection system and the size of the detector aperture. Past research work has only estimated the spatial resolution in thermoacoustic tomography based on measurements or numerical simulations. No theoretical analysis has been reported.

In this paper, a complete theoretical explanation of the degree of spatial resolution that results from varying the bandwidth as well as the detector aperture will be presented. Analytic expressions of point-spread functions (PSF's) on the spherical, planar, and cylindrical recording surfaces will be explicitly derived. The paper is organized as follows. In Sec. II, the inverse problem and the reconstruction formulas for thermoacoustic tomography will be briefly reviewed. Detailed derivations of bandwidth-limited PSF's in the above three measurement geometries as well as more general cases will be presented in Secs. III A, III B, III C, and III D, respectively; and resolution will be discussed in Sec. III E. In Sec. IV, detailed derivations of PSF's as a function of detector aperture size will be shown in Secs. IV A, IV B, and IV C. Section V will provide discussion and conclusions.

---

[*] Author to whom all correspondence should be addressed. FAX: 979-845-4450; electronic address: LWang@tamu.edu; URL: http://oilab.tamu.edu

1063-651X/2003/67(5)/056605(15)/$20.00

©2003 The American Physical Society

II. RECONSTRUCTION FORMULAS

We will first briefly review the inverse problem and the rigorous reconstruction formulas for thermoacoustic tomography. It is well known that, in response to a heat source, the pressure $p(\mathbf{r},t)$ at position $\mathbf{r}$ and time t in an acoustically homogeneous medium obeys the following equation [13]:

$$\nabla^2 p(\mathbf{r},t)-\frac{1}{c^2}\frac{\partial^2}{\partial t^2}p(\mathbf{r},t)=-\frac{\beta}{C_p}\frac{\partial}{\partial t}H(\mathbf{r},t), \qquad (1)$$

where C_p is the specific heat, $H(\mathbf{r},t)$ is the heating function defined as the thermal energy deposited by the EM radiation per time and volume, β is the isobaric volume expansion coefficient, and c is the speed of sound. The heating function can be written as the product of a spatial absorption function and a temporal illumination function:

$$H(\mathbf{r},t)=A(\mathbf{r})I(t). \qquad (2)$$

Assuming that the illumination is a Dirac δ function such as $I(t)=\delta(\bar{t})$, and taking the following Fourier transform on variable $\bar{t}=ct$,

$$\tilde{p}(\mathbf{r},k)=\int_{-\infty}^{+\infty}p(\mathbf{r},\bar{t})\exp(ik\bar{t})d\bar{t}, \qquad (3)$$

the solution of Eq. (1) becomes the integral

$$\tilde{p}(\mathbf{r}_0,k)=-ikc^2\eta\int\int\int_V d^3r\,A(\mathbf{r})\tilde{G}_k(\mathbf{r},\mathbf{r}_0), \qquad (4)$$

where $\eta=\beta/C_p$ and $\tilde{G}_k(\mathbf{r},\mathbf{r}_0)$ is the Green's function satisfying the following equation:

$$(\nabla^2+k^2)\tilde{G}_k(\mathbf{r},\mathbf{r}_0)=-\delta(\mathbf{r}-\mathbf{r}_0). \qquad (5)$$

In general, the Green's function in three-dimensional free space can be written as [14]

$$\tilde{G}_k(\mathbf{r},\mathbf{r}_0)=\frac{\exp(ik|\mathbf{r}-\mathbf{r}_0|)}{4\pi|\mathbf{r}-\mathbf{r}_0|}. \qquad (6)$$

Actually, the initial thermoacoustic pressure excited by the $\delta(t)$ EM illumination is equal to $p_0(\mathbf{r})=\Gamma(\mathbf{r})A(\mathbf{r})$, where the Grüneisen parameter $\Gamma(\mathbf{r})=\eta(\mathbf{r})c^2$ may be inhomogeneous. Then, Eq. (4) can be expressed by the following form:

$$\tilde{p}(\mathbf{r}_0,k)=-ik\int\int\int_V d^3r\,\tilde{G}_k(\mathbf{r},\mathbf{r}_0)p_0(\mathbf{r}). \qquad (7)$$

The inverse problem is to reconstruct the absorption distribution $A(\mathbf{r})$ or the initial thermoacoustic pressure distribution $p_0(\mathbf{r})$ from a set of data $p(\mathbf{r}_0,t)$ or $\tilde{p}(\mathbf{r}_0,k)$ measured at position $\mathbf{r}_0$. In general, the Green's function can be expanded in terms of some appropriate functions for the corresponding recording geometries. Then, based on the orthogonality of the appropriate functions, reconstruction formulas can be derived.

In spherical recording geometry, it is assumed that the recording surface is a spherical surface $\mathbf{r}_0=(r_0,\theta_0,\varphi_0)$ in the spherical polar coordinates $\mathbf{r}=(r,\theta,\varphi)$, where θ is the polar angle from the z axis and φ is the azimuthal angle in the x-y plane from the x axis. The sample under study lies inside the sphere, i.e., $A(\mathbf{r})=A(r,\theta,\varphi)$ where $r<r_0$ and $A(\mathbf{r})=0$ when $r>r_0$. The rigorous reconstruction formula for $A(\mathbf{r})$ can be written as [7]

$$A(\mathbf{r})=\frac{1}{2\pi^2c^2\eta}\int\int_{\Omega_0}d\Omega_0\int_0^{+\infty}dk\,\tilde{p}(\mathbf{r}_0,k)\times\sum_{m=0}^{\infty}\frac{(2m+1)j_m(kr)}{h_m^{(1)}(kr_0)}P_m(\mathbf{n}_0\cdot\mathbf{n}), \qquad (8)$$

where $d\Omega_0=\sin\theta_0\,d\theta_0 d\varphi_0$; $\mathbf{n}=\mathbf{r}/r$ and $\mathbf{n}_0=\mathbf{r}_0/r$ are unit vectors; $j_m(\cdot)$, $h_m^{(1)}(\cdot)$, and $P_m(\cdot)$ are the spherical Bessel function of the first kind, the spherical Hankel function of the first kind, and the Legendre polynomial function, respectively. In addition, the integral range over variable k in Eq. (8) can extend to from $-\infty$ to 0 by simply taking the complex conjugate and using the following properties: $\tilde{p}^*(\mathbf{r}_0,k)=\tilde{p}(\mathbf{r}_0,-k)$, $[j_n(z)]^*=j_n(z)$, and $[h_n^{(1)}(z)]^*=h_n^{(2)}(z)$ when z is real and positive, where "$*$" stands for the complex conjugate.

In planar recording geometry, it is assumed that the measurement surface is the $z=0$ plane, i.e., $\mathbf{r}_0=(x_0,y_0,0)$ in the Cartesian coordinates $\mathbf{r}=(x,y,z)$. The sample lies above the plane, i.e., $A(\mathbf{r})=A(x,y,z)$ where $z>0$ and $A(\mathbf{r})=0$ when $z<0$. The rigorous reconstruction formula for $A(\mathbf{r})$ can be written as [8,11]

$$A(x,y,z)=\frac{1}{4\pi^3c^2\eta}\int\int_{-\infty}^{+\infty}dx_0dy_0\int_{-\infty}^{+\infty}dk\,\tilde{p}(\mathbf{r}_0,k)\times\int\int_{\rho=0}^{\rho=|k|}du\,dv\times\exp[-iz\,\mathrm{sgn}(k)\sqrt{k^2-\rho^2}]\exp[iu(x_0-x)+iv(y_0-y)], \qquad (9)$$

where $\rho=\sqrt{u^2+v^2}$, sgn$(k)=1$ when $k>0$, and sgn$(k)=-1$ when $k<0$.

In cylindrical recording geometry, it is assumed that the measurement surface is a circular cylindrical surface $\mathbf{r}_0=(\rho_0,\varphi_0,z_0)$ in the circular cylindrical coordinates $\mathbf{r}=(\rho,\varphi,z)$. The sample lies in the cylinder, i.e., $A(\mathbf{r})=A(\rho,\varphi,z)$ when $\rho<\rho_0$, and $A(\mathbf{r})=0$ when $\rho>\rho_0$. The rigorous reconstruction formula for $A(\mathbf{r})$ can be written as [9,11]

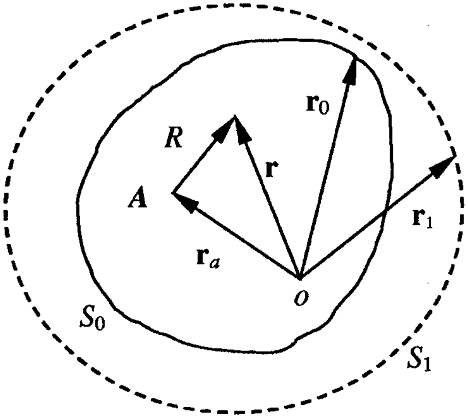

FIG. 1. Diagram of the recording geometry: a recording surface S_1 completely encloses another recording surface S_0; there is a point source A at $\mathbf{r}_a$ inside S_0; R is the distance between an arbitrary point at $\mathbf{r}$ and the point source A; $\mathbf{r}_0$ and $\mathbf{r}_1$ point to a detection element on the surfaces S_0 and S_1, respectively.

$$A(\rho,\varphi,z)=\frac{1}{2\pi^3c^2\eta}\int_0^{2\pi}d\varphi_0\int_{-\infty}^{+\infty}dz_0\int_0^{+\infty}dk\tilde{p}(\mathbf{r}_0,k)$$
$$\times\int_{-k}^{+k}d\gamma\exp[i\gamma(z_0-z)]$$
$$\times\sum_{n=-\infty}^{+\infty}\exp[in(\varphi_0-\varphi)]\frac{J_n(\rho\sqrt{k^2-\gamma^2})}{H_n^{(1)}(\rho_0\sqrt{k^2-\gamma^2})},\qquad(10)$$

where $J_n(\cdot)$ and $H_n^{(1)}(\cdot)$ are the Bessel function of the first kind and the Hankel function of the first kind, respectively. In addition, the integral range over variable k in Eq. (10) can extend to from $-\infty$ to 0, by simply taking the complex conjugate and using the following properties: $\tilde{p}^*(\mathbf{r}_0,k)=\tilde{p}(\mathbf{r}_0,-k)$, $[J_n(z)]^*=J_n(z)$, and $[H_n^{(1)}(z)]^*=H_n^{(2)}(z)$ when z is real and positive.

III. BANDWIDTH-LIMITED PSF

As shown in Fig. 1, assuming a point source $A(\mathbf{r})=\delta(\mathbf{r}-\mathbf{r}_a)$ at $\mathbf{r}_a$, the pressure at the recording point $\mathbf{r}_0$ can be expressed as

$$\tilde{p}(\mathbf{r}_0,k)=-ikc^2\eta\tilde{G}_k(\mathbf{r}_a,\mathbf{r}_0).\qquad(11)$$

Suppose the detection system is bandlimited in the temporal-frequency domain and characterized by a low-pass function $\tilde{H}(k)$. The amplitude of the acoustic wave vector $k=\omega/c$, where ω is the acoustic angular frequency. The detected signal at the recording surface $\mathbf{r}_0$ becomes $\tilde{p}'(\mathbf{r}_0,k)=\tilde{H}(k)\tilde{p}(\mathbf{r}_0,k)$ instead of $\tilde{p}(\mathbf{r}_0,k)$. But the reconstruction formulas, Eqs. (8)–(10), for point-detector measurements in the spherical, planar, and cylindrical recording geometries, respectively, remain the same. Replacing $\tilde{p}(\mathbf{r}_0,k)$ by $\tilde{p}'(\mathbf{r}_0,k)$ in these reconstruction formulas will give us the bandwidth-limited analytic expressions of the PSF's to be derived below for the different geometries.

A. Spherical geometry

The point source at $\mathbf{r}_a=(r_a,\theta_a,\varphi_a)$ in the spherical coordinates can be written as

$$A(\mathbf{r})=\frac{1}{r^2}\delta(r-r_a)\delta(\varphi-\varphi_a)\delta(\cos\theta-\cos\theta_a).\qquad(12)$$

The Green's function can be expanded according to the following identity $(r_0>r_a,k>0)$ [14]:

$$\tilde{G}_k(\mathbf{r}_a,\mathbf{r}_0)=\frac{ik}{4\pi}\sum_{l=0}^{\infty}(2l+1)j_l(kr_a)h_l^{(1)}(kr_0)P_l(\mathbf{n}_a\cdot\mathbf{n}_0),\qquad(13)$$

where $\mathbf{n}_a=\mathbf{r}_a/r_a$.

Replacing $\tilde{p}(\mathbf{r}_0,k)$ by $\tilde{p}'(\mathbf{r}_0,k)$ in Eq. (8) and considering the following identity [14]:

$$\int\int_{\Omega_0}d\Omega_0P_l(\mathbf{n}_a\cdot\mathbf{n}_0)P_m(\mathbf{n}_0\cdot\mathbf{n})=\frac{4\pi}{2l+1}\delta_{lm}P_l(\mathbf{n}_a\cdot\mathbf{n}),\qquad(14)$$

the resulting reconstruction for $A(\mathbf{r})$ is

$$A_b(\mathbf{r})=\frac{1}{2\pi^2}\int_0^{+\infty}\tilde{H}(k)k^2dk\sum_{m=0}^{\infty}(2m+1)$$
$$\times P_m(\mathbf{n}_a\cdot\mathbf{n})j_m(kr_a)j_m(kr).\qquad(15)$$

Further, taking into account the following identity [15]:

$$\sum_{m=0}^{\infty}(2m+1)P_m(\mathbf{n}_a\cdot\mathbf{n})j_m(kr_a)j_m(kr)=\frac{\sin(kR)}{kR}=j_0(kR),\qquad(16)$$

where $R=\sqrt{r_a^2+r^2-2r_ar\cos(\mathbf{n}_a\cdot\mathbf{n})}$, one can obtain

$$A_b(\mathbf{r})=\frac{1}{2\pi^2}\int_0^{+\infty}\tilde{H}(k)j_0(kR)k^2dk.\qquad(17)$$

Particularly, if $\tilde{H}(k)\equiv1$ for $k=0\rightarrow\infty$, considering the following identities [14]:

$$\int_0^{+\infty}j_m(kr)j_m(kr_a)k^2dk=\frac{\pi}{2r^2}\delta(r-r_a),\qquad(18)$$

$$\sum_{m=0}^{\infty}(2m+1)P_m(\mathbf{n}_a\cdot\mathbf{n})=4\pi\delta(\varphi-\varphi_a)\delta(\cos\theta-\cos\theta_a),\qquad(19)$$

Eq. (15) reduces to a point source the same as the expression in Eq. (12), which actually verifies the reconstruction Eq. (8).

B. Planar geometry

The point source at $\mathbf{r}_a=(x_a,y_a,z_a)$ in the Cartesian coordinates can be written as

$$A(x,y,z)=\delta(x-x_a)\delta(y-y_a)\delta(z-z_a). \tag{20}$$

The Green's function can be expanded as [14]

$$\tilde{G}_k(\mathbf{r}_a,\mathbf{r}_0)=\frac{1}{(2\pi)^3}\int\int\int_{-\infty}^{+\infty}d^3K\frac{\exp[i\mathbf{K}\cdot(\mathbf{r}_0-\mathbf{r}_a)]}{K^2-k^2}, \tag{21}$$

where $\mathbf{K}=(K_x,K_y,K_z)$.

Using the detected signal at the recording surface $\mathbf{r}_0$, $\tilde{p}'(\mathbf{r}_0,k)=\tilde{H}(k)\tilde{p}(\mathbf{r}_0,k)$, to replace $\tilde{p}(\mathbf{r}_0,k)$ in the reconstruction Eq. (9), and considering the following identities:

$$\int_{-\infty}^{+\infty}\exp[i(u+K_x)x_0]dx_0=2\pi\delta(K_x+u), \tag{22}$$

$$\int_{-\infty}^{+\infty}\exp[i(\nu+K_y)y_0]dy_0=2\pi\delta(K_y+\nu), \tag{23}$$

$$\int_{-\infty}^{+\infty}dK_z\frac{\exp(-iK_zz_a)}{K_z^2+\rho^2-k^2}=i\pi\,\mathrm{sgn}(k)\frac{\exp[iz_a\,\mathrm{sgn}(k)\sqrt{k^2-\rho^2}]}{\sqrt{k^2-\rho^2}},\quad |k|>\rho, \tag{24}$$

the resulting reconstruction for $A(\mathbf{r})$ is

$$\begin{aligned}A_b(x,y,z)=&\frac{1}{(2\pi)^3}\int_{-\infty}^{+\infty}k\,dk\,\tilde{H}(k)\int\int_{\rho=0}^{\rho=|k|}du\,d\nu\\&\times\exp(-iu\Delta x-i\nu\Delta y)\\&\times\mathrm{sgn}(k)\frac{\exp[-i\,\mathrm{sgn}(k)\Delta z\sqrt{k^2-\rho^2}]}{\sqrt{k^2-\rho^2}},\end{aligned} \tag{25}$$

where $\Delta x=x-x_a$, $\Delta y=y-y_a$, and $\Delta z=z-z_a$.

In the evaluation of the integral in Eq. (24), we replaced k with $k+i\gamma$ as suggested in Ref. [14], where γ is a small positive real number. Since there will be some damping of the wave in a physical system, we then complete a contour integral in the complex plane and let γ approach zero.

Changing the integration order of $du\,dv$ and dk, and further letting $w=\mathrm{sgn}(k)\sqrt{k^2-\rho^2}$, Eq. (25) reduces to

$$\begin{aligned}A_b(x,y,z)=&\frac{1}{(2\pi)^3}\int\int\int_{-\infty}^{+\infty}du\,d\nu\,dw\\&\times\exp(-iu\Delta x-i\nu\Delta y-iw\Delta z)\tilde{H}(k),\end{aligned} \tag{26}$$

where $k^2=u^2+v^2+w^2$.

Particularly, if $\tilde{H}(k)\equiv1$ for $-\infty<k<\infty$, Eq. (26) becomes a point source as the original one in Eq. (20).

In general, by changing the integral from the Cartesian coordinates into the spherical coordinates,

$$(u,v,w)\rightarrow\mathbf{k}=(k,\theta,\varphi),$$

$$(\Delta x,\Delta y,\Delta z)\rightarrow\mathbf{R}=(R,\alpha,\beta),$$

where $R^2=(\Delta x)^2+(\Delta y)^2+(\Delta z)^2$, one can rewrite Eq. (26) as

$$A_b(x,y,z)=\frac{1}{(2\pi)^3}\int\int\int\exp(-i\mathbf{k}\cdot\mathbf{R})\tilde{H}(k)d^3\mathbf{k}. \tag{27}$$

The integration of Eq. (27) can be further simplified to

$$\begin{aligned}A_b(x,y,z)=&\frac{1}{(2\pi)^3}\int_0^{+\infty}\tilde{H}(k)k^2dk\\&\times\int_0^{\pi}\exp(-ikR\cos\gamma)\sin\gamma d\gamma 2\pi,\end{aligned} \tag{28}$$

where γ is the angle between $\mathbf{k}$ and $\mathbf{R}$, i.e.,

$$A_b(x,y,z)=\frac{1}{2\pi^2}\int_0^{+\infty}\tilde{H}(k)j_0(kR)k^2dk. \tag{29}$$

C. Cylindrical geometry

The point source at $\mathbf{r}_a=(\rho_a,\varphi_a,z_a)$ in the cylindrical coordinates can be written as

$$\begin{aligned}A(\rho,\varphi,z)&=\frac{1}{\rho}\delta(\rho-\rho_a)\delta(\varphi-\varphi_a)\delta(z-z_a)\\&=\frac{1}{\rho}\delta(\rho-\rho_a)\frac{1}{2\pi}\sum_{m=-\infty}^{+\infty}\exp[im(\varphi-\varphi_a)]\\&\quad\times\frac{1}{2\pi}\int_{-\infty}^{+\infty}\exp[ik_z(z-z_a)]dk_z.\end{aligned} \tag{30}$$

The Green's function can be expanded as $(k>0)$ [11,14,17]

$$\begin{aligned}\tilde{G}_k(\mathbf{r}_a,\mathbf{r}_0)=&\frac{i}{8\pi}\sum_{m=-\infty}^{+\infty}\exp[im(\varphi_a-\varphi_0)]\\&\times\int_{-\infty}^{+\infty}dk_z\exp[ik_z(z_a-z_0)]\\&\times J_m(\mu\rho_a)H_m^{(1)}(\mu\rho_0),\end{aligned} \tag{31}$$

where $\mu=\sqrt{k^2-k_z^2}$ when $k_z^2<k^2$, and $\mu=i\sqrt{k_z^2-k^2}$ when $k_z^2>k^2$.

Using the detected signal at the recording surface $\mathbf{r}_0$, $\tilde{p}'(\mathbf{r}_0,k)=\tilde{H}(k)\tilde{p}(\mathbf{r}_0,k)$ to replace $\tilde{p}(\mathbf{r}_0,k)$ in the reconstruction Eq. (10), and considering the following identities:

$$\int_0^{2\pi} d\varphi_0 \exp[i\varphi_0(n-m)] = 2\pi\delta_{nm}, \tag{32}$$

$$\int_{-\infty}^{+\infty} dz_0 \exp[iz_0(\gamma - k_z)] = 2\pi\delta(\gamma - k_z), \tag{33}$$

the resulting reconstruction for $A(\mathbf{r})$ is

$$A_b(\rho,\varphi,z) = \frac{1}{4\pi^2}\int_0^{+\infty} k\,dk\,\tilde{H}(k)\int_{-k}^{+k} dk_z \exp[ik_z(z_a - z)] \times \sum_{m=-\infty}^{+\infty} \exp[im(\varphi_a - \varphi)] J_m(\mu\rho_a) J_m(\mu\rho). \tag{34}$$

Changing the integration order of variables k and k_z and taking into account the following identity [15]:

$$\sum_{m=-\infty}^{+\infty} \exp[im(\varphi_a - \varphi)] J_m(\mu\rho_a) J_m(\mu\rho) = J_0(\mu D), \tag{35}$$

where $D = \sqrt{\rho_a^2 + \rho^2 - 2\rho_a\rho\cos(\varphi_a - \varphi)}$, one can simplify Eq. (34) to

$$A_b(\rho,\varphi,z) = \frac{1}{4\pi^2}\int_{-\infty}^{+\infty} dk_z \exp[ik_z(z_a - z)] \times \int_{|k_z|}^{+\infty} k\tilde{H}(k)\,dk\,J_0(\mu D). \tag{36}$$

By changing the integral variable k with $\mu = \sqrt{k^2 - k_z^2}$, one can get

$$A_b(\rho,\varphi,z) = \frac{1}{4\pi^2}\int_{-\infty}^{+\infty} dk_z \exp[-ik_z\Delta z] \times \int_0^{+\infty} \tilde{H}(k)\mu\,d\mu\,J_0(\mu D), \tag{37}$$

where $k^2 = k_z^2 + \mu^2$, $\Delta z = z - z_a$.

Then, one can denote $\Delta x = x - x_a = D\cos\beta$ and $\Delta y = y - y_a = D\sin\beta$, and introduce $k_x = \mu\cos\alpha$ and $k_y = \mu\sin\alpha$, where $D = \sqrt{(\Delta x)^2 + (\Delta y)^2}$ and $\mu = \sqrt{k_x^2 + k_y^2}$, and rewrite the far right integral in Eq. (37) as

$$\int_0^{+\infty} \mu\,d\mu\,H(k) J_0(\mu D) = \frac{1}{2\pi}\int\int_{-\infty}^{+\infty} dk_x dk_y \times \exp(-ik_x\Delta x - ik_x\Delta y)\tilde{H}(k), \tag{38}$$

where $k^2 = k_z^2 + \mu^2 = k_x^2 + k_y^2 + k_z^2$.

Therefore, Eq. (37) can be rewritten as

$$A_b(\rho,\varphi,z) = \frac{1}{(2\pi)^3}\int\int\int_{-\infty}^{+\infty} dk_z dz_x dk_y \tilde{H}(k) \times \exp(-ik_x\Delta x - ik_z\Delta y - ik_z\Delta z), \tag{39}$$

which is the same as Eq. (26). Thus, $A_b(\rho,\varphi,z)$ takes the same form as Eq. (29),

$$A_b(\rho,\varphi,z) = \frac{1}{2\pi^2}\int_0^{+\infty} \tilde{H}(k) j_0(kR) k^2 dk, \tag{40}$$

where

$$R = \sqrt{(\Delta x)^2 + (\Delta y)^2 + (\Delta z)^2} = \sqrt{\rho_a^2 + \rho^2 - 2\rho_a\rho\cos(\varphi_a - \varphi) + (\Delta z)^2}.$$

Particularly, if $\tilde{H}(k) \equiv 1$ for $k = 0 \to \infty$, Eq. (39) reduces to a point source the same as the original one.

D. General geometry

We have proved that the bandwidth-limited PSF's in the three different geometries share the same expression as shown in Eqs. (17), (29), and (40). As described in these equations, the PSF is independent of the position of the point source but dependent on the distance R from the point source. Therefore, the PSF due to bandwidth is space invariant.

Actually, the space invariance of PSF due to bandwidth can be extended to more general recording geometries. As mentioned in Ref. [11], the reconstruction for $A(\mathbf{r})$ can be expressed by a linear integral:

$$A(\mathbf{r}) = \int\int_{S_0} dS_0 \int_k dk\,\tilde{K}_k(\mathbf{r}_0,\mathbf{r})\tilde{p}(\mathbf{r}_0,k), \tag{41}$$

where S_0 is the recording surface, which covers the object under study.

The inverse problem for thermoacoustic reconstruction is to seek such an integral kernel $\tilde{K}_k(\mathbf{r}_0,\mathbf{r})$ for a particular recording surface. For the spherical, planar, and cylindrical recording geometries, the integral kernel $\tilde{K}_k(\mathbf{r}_0,\mathbf{r})$ can be explicitly given as shown in Eqs. (8), (9), and (10), respectively. For other recording geometries, the integral kernel $\tilde{K}_k(\mathbf{r}_0,\mathbf{r})$ is more complicated or even nonexistent analytically.

As shown in Fig. 1, suppose another recording surface S_1, which could be a spherical, planar, or cylindrical recording surface, can completely enclose surface S_0. Then, based on Green's theorem [17], the pressure $\tilde{p}(\mathbf{r}_1,k)$ at S_1 can be computed by the pressure $\tilde{p}(\mathbf{r}_0,k)$ on surface S_0,

$$\tilde{p}(\mathbf{r}_1,k) = \int\int_{S_0} dS_0 \left(\tilde{p}(\mathbf{r}_0,k)\frac{\partial\tilde{G}_k(\mathbf{r}_1,\mathbf{r}_0)}{\partial n_0^s} - \tilde{G}_k(\mathbf{r}_1,\mathbf{r}_0)\frac{\partial\tilde{p}(\mathbf{r}_0,k)}{\partial n_0^s} \right), \tag{42}$$

where $\partial/\partial n_0^s$ is the normal component of the gradient on surface S_0 and points outward away from the acoustic source; and $\mathbf{r}_0$ and $\mathbf{r}_1$ represent detection positions on surfaces S_0 and S_1, respectively. Since the reconstruction based on Eq. (41) from the measurement on surface S_0 is exact, the pressure $\tilde{p}(\mathbf{r}_1,k)$ on surface S_1 must be identical to the thermoacoustic pressure directly generated by the source $A(\mathbf{r})$:

$$\tilde{p}(\mathbf{r}_1,k)=\int\int\int_{V_0} dV_0 A(\mathbf{r})\tilde{G}_k(\mathbf{r}_1,\mathbf{r}), \tag{43}$$

where V_0 is the volume enclosed by S_0.

Now, considering the bandwidth characterized by $\tilde{H}(k)$, one can rewrite the reconstruction Eq. (41) as

$$A_b(\mathbf{r})=\int\int_{S_0} dS_0 \int_{-\infty}^{+\infty} dk \tilde{K}_k(\mathbf{r}_0,\mathbf{r})[\tilde{H}(k)\tilde{p}(\mathbf{r}_0,k)]. \tag{44}$$

In other words, Eq. (44) gives the exact reconstruction of a new and unique source $A_b(\mathbf{r})$ from $\tilde{H}(k)\tilde{p}(\mathbf{r}_0,k)$ measured on surface S_0:

$$\tilde{H}(k)\tilde{p}(\mathbf{r}_0,k)=\int\int\int_{V_0} dV_0 A_b(\mathbf{r})\tilde{G}_k(\mathbf{r}_0,\mathbf{r}). \tag{45}$$

Based on Green's theorem, the pressure on surface S_1 can be computed by the pressure $\tilde{H}(k)\tilde{p}(\mathbf{r}_0,k)$ on surface S_0, which is found equal to $\tilde{H}(k)\tilde{p}(\mathbf{r}_1,k)$ with considering Eq. (42):

$$\begin{aligned}\int\int_{S_0} dS_0\bigg(& [\tilde{H}(k)\tilde{p}(\mathbf{r}_0,k)]\frac{\partial \tilde{G}_k(\mathbf{r}_1,\mathbf{r}_0)}{\partial n_0^s} \\ & -\tilde{G}_k(\mathbf{r}_1,\mathbf{r}_0)\frac{\partial[\tilde{H}(k)\tilde{p}(\mathbf{r}_0,k)]}{\partial n_0^s}\bigg) \\ =\tilde{H}(k)\int\int_{S_0} dS_0\bigg(& \tilde{p}(\mathbf{r}_0,k)\frac{\partial \tilde{G}_k(\mathbf{r}_1,\mathbf{r}_0)}{\partial n_0^s} \\ & -\tilde{G}_k(\mathbf{r}_1,\mathbf{r}_0)\frac{\partial \tilde{p}(\mathbf{r}_0,k)}{\partial n_0^s}\bigg) \\ =\tilde{H}(k)\tilde{p}(\mathbf{r}_1,k). &\end{aligned} \tag{46}$$

This pressure must be identical to the thermoacoustic pressure directly generated by the new source $A_b(\mathbf{r})$ in volume V_0,

$$\int\int\int_{V_0} dV_0 A_b(\mathbf{r})\tilde{G}_k(\mathbf{r}_1,\mathbf{r})=\tilde{H}(k)\tilde{p}(\mathbf{r}_1,k), \tag{47}$$

i.e.,

$$\tilde{H}(k)\tilde{p}(\mathbf{r}_1,k)=\int\int\int_{V_1} dV_1 A_b(\mathbf{r})\tilde{G}_k(\mathbf{r}_1,\mathbf{r}), \tag{48}$$

since there is no source in the volume between the surfaces S_0 and S_1.

Equation (48) indicates that the new source $A_b(\mathbf{r})$ could be restored from the value $\tilde{H}(k)\tilde{p}(\mathbf{r}_1,k)$ on surface S_1, if an exact reconstruction from data only on surface S_1 does exist. In other words, the reconstruction for $A(\mathbf{r})$ from the measurement with the bandwidth $\tilde{H}(k)$ on surface S_0 is identical to the reconstruction from the measurement with the same bandwidth $\tilde{H}(k)$ on surface S_1 that fully encloses S_0. Fortunately, we have already obtained the exact reconstruction formulas from measurements on such a surface S_1 as the spherical, planar, or cylindrical recording geometries. Therefore, the PSF of the point source at $\mathbf{r}_a$ as a function of bandwidth $\tilde{H}(k)$ from the measurement on surface S_0 is nothing but the same expression as Eqs. (17), (29), and (40) for the above three specific recording geometries, respectively.

E. Resolution

For convenience, we can denote the PSF symbolically as $\mathcal{F}_b^{\mathrm{PSF}}$,

$$\mathcal{F}_b^{\mathrm{PSF}}(R)=\frac{1}{2\pi^2}\int_0^{+\infty}\tilde{H}(k)j_0(kR)k^2 dk, \tag{49}$$

where the subscript b represents bandwidth, and $R=|\mathbf{r}-\mathbf{r}_a|$. Equation (49) can be rewritten in another form as

$$\mathcal{F}_b^{\mathrm{SPF}}(R)=\frac{-1}{4\pi R}\left[\frac{dH(R)}{dR}+\frac{dH(-R)}{dR}\right], \tag{50}$$

if we let $H(-\bar{t})=H(\bar{t})$ and define the following Fourier transform:

$$H(\bar{t})=\frac{1}{2\pi}\int_{-\infty}^{+\infty}\tilde{H}(k)\exp(-ik\bar{t})dk, \tag{51}$$

where $H(\bar{t})$ is the corresponding temporal signal of $\tilde{H}(k)$.

If $\tilde{H}(k)$ has a cutoff frequency k_c, $\tilde{H}(k)=1$ when $k\leqslant k_c$, $\tilde{H}(k)=0$ when $k>k_c$, the integral in Eq. (49) can be carried out,

$$\begin{aligned}\mathcal{F}_b^{\mathrm{PSF}}(R)&=\frac{1}{2\pi^2}\int_0^{k_c} j_0(kR)k^2 dk \\ &=\frac{k_c}{2\pi^2R^2}\left(\frac{\sin(k_cR)}{k_cR}-\cos(k_cR)\right),\end{aligned} \tag{52}$$

i.e.,

$$\mathcal{F}_b^{\mathrm{PSF}}(R)=\frac{k_c^3}{2\pi^2}\frac{j_1(k_cR)}{k_cR}=\frac{k_c^3}{6\pi^2}\frac{3j_1(k_cR)}{k_cR}. \tag{53}$$

By normalizing the PSF of Eq. (53), one can get

$$\mathcal{F}_b^{\mathrm{PSF}}(R)=\frac{3j_1(k_cR)}{k_cR}. \tag{54}$$

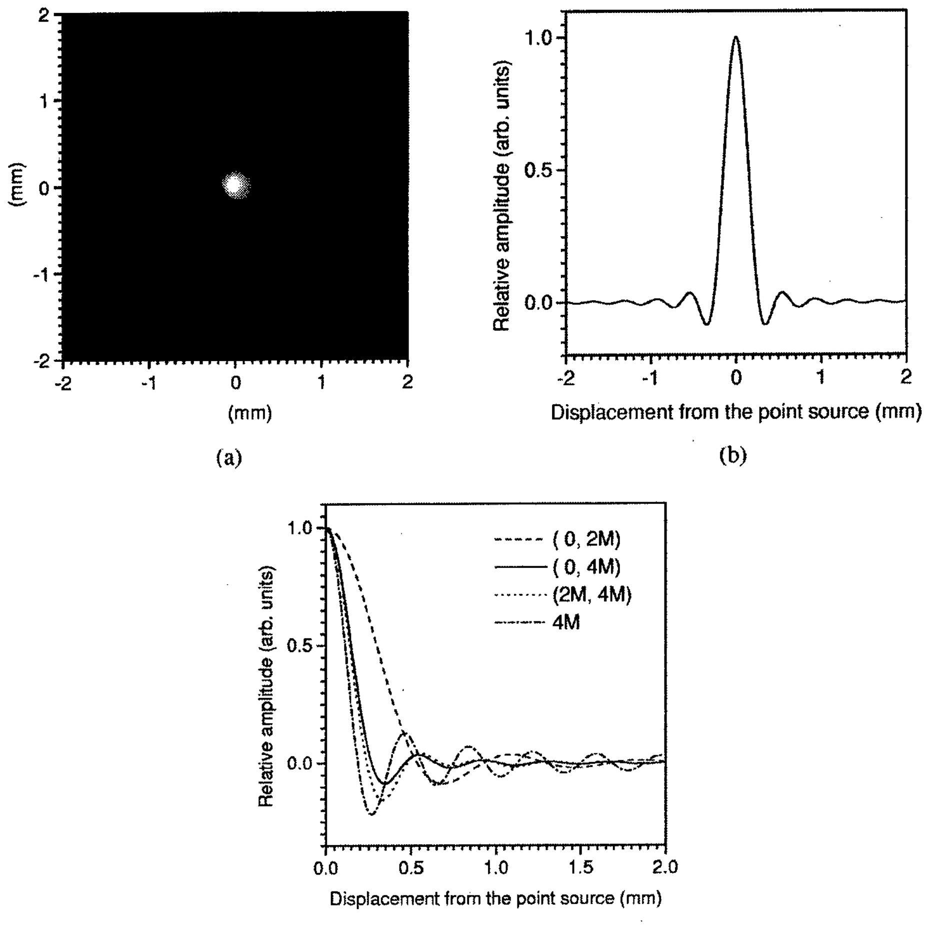

(a) (b)

(c)

FIG. 2. An example of the PSF as a result of the bandwidth (0, 4 MHz): (a) a gray scale view and (b) a profile through the point source. (c) Comparison of the PSF's with different bandwidths: dashed line, (0, 2 MHz); solid line, (0, 4 MHz); dotted line, (2 MHz, 4 MHz); dot-dashed line, 4 MHz.

The full width at half maximum (FWHM) of the PSF is often used to represent the spatial resolution. It is easy to show $3j_1(x)/x=0.5$ when $x=2.4983$. Therefore,

$$\mathcal{W}_{\mathrm{FWHM}}=2\times\frac{2.4983}{k_c}=2\times\frac{2.4983}{2\pi f_c/c}=0.7952c/f_c\approx 0.8\lambda_c, \tag{55}$$

where λ_c is the wavelength at the cutoff frequency of the bandwidth. For example, if $c=1.5$ mm/μs, $f_c=4$ MHz, then $\mathcal{W}_{\mathrm{FWHM}}\approx 0.3$ mm. The corresponding $\mathcal{F}_b^{\mathrm{PSF}}(R)$ is plotted in Figs. 2(a) and 2(b).

Sometimes, a detection system has a finite bandwidth characterized by a central frequency f_0 with a low cutoff frequency f_{Lc} and a high cutoff frequency f_{Hc}. For simplicity, suppose $\tilde{H}(k)=1$ is in the above frequency range, and then the PSF can be expressed by

$$\mathcal{F}_b^{\mathrm{PSF}}(R)=\frac{k_{\mathrm{Hc}}^3}{2\pi^2}\frac{j_1(k_{\mathrm{Hc}}R)}{k_{\mathrm{Hc}}R}-\frac{k_{\mathrm{Lc}}^3}{2\pi^2}\frac{j_1(k_{\mathrm{Lc}}R)}{k_{\mathrm{Lc}}R}, \tag{56}$$

where $k_{\mathrm{Lc}}=2\pi f_{\mathrm{Lc}}/c$ and $k_{\mathrm{Hc}}=2\pi f_{\mathrm{Hc}}/c$.

For example, a system is with $f_0=3$ MHz, and $f_{\mathrm{Lc}}=2$ MHz and $f_{\mathrm{Hc}}=4$ MHz. The corresponding PSF is plotted as the dotted line in Fig. 2(c). As shown in Fig. 2(c), the FWHM of the PSF with a bandwidth of (2 MHz, 4 MHz) is slightly narrower than the FWHM of the PSF with a wider bandwidth of (0, 4 MHz) [solid line in Fig. 2(c)]. In other words, due to the absence of a low frequency component, the high frequency component will cause the FWHM to be narrower. The minimum value of the FWHM can be estimated in the PSF with a single frequency f_c and zero bandwidth. The PSF in this case is nothing but the integral kernel in Eq. (49): the zero-order spherical Bessel function $j_0(k_cR)$. Such an example, with $f_c=4$ MHz, is plotted as the dash-dot line in Fig. 2(c). Since $j_0(1.895)\approx 0.5$, the minimum $\mathcal{W}_{\mathrm{FWHM}}\approx 0.6\lambda_c$, where λ_c is the wavelength at the cutoff frequency f_c. But, as shown in Fig. 2(c), a PSF that lacks a low frequency component does not concentrate in the center beam anymore, and the side beams of the PSF slowly attenuate as the position gets farther away from the point source, thereby introducing significant artifacts in the investigation of large objects.

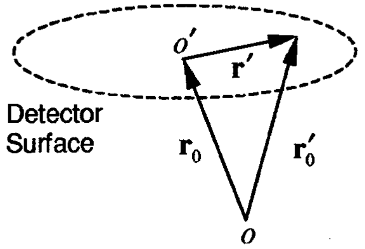

FIG. 3. Diagram of the detector surface $\mathbf{r}'$ with origin o'. The vector $\mathbf{r}_0$ represents the center of detector o' in the recording geometry with origin o. The vector $\mathbf{r}_0'$ points to an element of the detector aperture.

In conclusion, the obtainable spatial resolution approximates to a value between $0.6\lambda_c$ and $0.8\lambda_c$, where λ_c is the wavelength at the high cutoff frequency f_c. If the bandwidth is too narrow, the reconstruction based on the wide bandwidth measurement becomes inappropriate and the FWHM of the reconstructed PSF does not properly describe the real spatial resolution.

IV. EFFECT OF DETECTOR APERTURE

Next, let us derive the analytic expressions of the PSF's related to detector aperture size. As shown in Fig. 3, the real signal detected at position $\mathbf{r}_0$ can be expressed as a surface integral over the detector aperture

$$\tilde{p}'(\mathbf{r}_0,k)=\int\int \tilde{p}(\mathbf{r}_0',k)W(\mathbf{r}_0')d^2\mathbf{r}_0', \tag{57}$$

where $W(\mathbf{r}_0')$ is a weighting factor, which represents the contribution from different elements of the detector surface to the total signal of the detector.

Since $\mathbf{r}_0'=\mathbf{r}_0+\mathbf{r}'$, Eq. (57) can be rewritten as

$$\tilde{p}'(\mathbf{r}_0,k)=\int\int \tilde{p}(\mathbf{r}_0+\mathbf{r}',k)W(\mathbf{r}')d^2\mathbf{r}'. \tag{58}$$

One can assume a point source at $\mathbf{r}_a$ and then get the detected signal at position $\mathbf{r}_0$ using Eq. (57) or (58). If the signal is not bandlimited, by substituting $\tilde{p}'(\mathbf{r}_0,k)$ for $p(\mathbf{r}_0,k)$ in the rigorous reconstruction formulas such as Eqs. (8)–(10), one can get analytic expressions of the PSF's for the spherical, planar, and cylindrical geometries, respectively. In general, the analytic expressions cannot be thoroughly simplified for arbitrary detector apertures. In order to explicitly demonstrate the effects of the detector apertures on spatial resolution, we will make some assumptions about the detector apertures.

A. Spherical geometry

As shown in Fig. 4(a), $\mathbf{r}_0$ represents the center of detector o' in the global spherical coordinates (r,θ,φ) with the origin at the recording geometry center o. A local spherical coordinate system aligned with $\mathbf{r}_0$ is used as well. Assume that the detector is circularly symmetric about its center o'; in this case, the weighting factor depends only on θ', $W(\mathbf{r}')=W(\theta')$, where the angle θ' between $\mathbf{r}_0'$ and $\mathbf{r}_0$—the polar angle of $\mathbf{r}_0'$ in the local coordinate system—varies from 0 to Θ depending on the size of the detector. The azimuthal angle φ' of $\mathbf{r}_0'$ in the local coordinate system varies from 0 to 2π. The normal of the detector surface at point o' is assumed to point to the center of the recording geometry o. The surface integral in Eq. (58) can be transformed into an integral over a curve radiating from the center o' on the surface l' and the azimuthal angle φ':

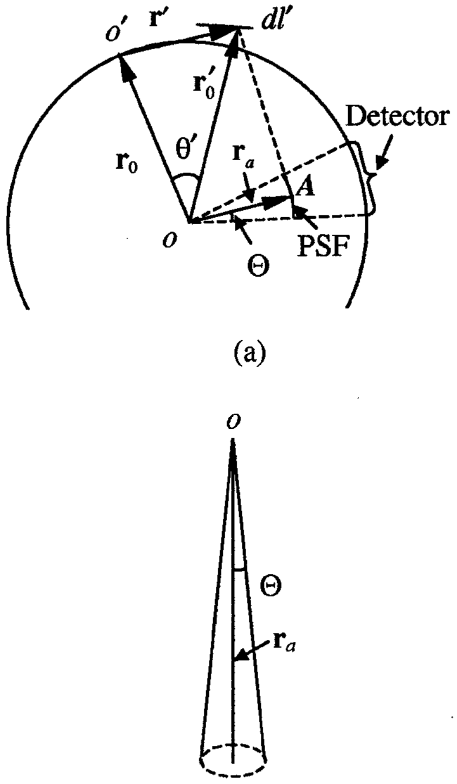

(a)

(b)

FIG. 4. (a) Diagram of the spherical recording geometry: θ' is the angle between $\mathbf{r}_0$ and $\mathbf{r}_0'$; dl' is an integral element on the detector surface; Θ is the angle of the radius of the detector aperture to the recording geometry origin o; the extension of the PSF at point A is indicated; other denotations of the symbols are the same as in Figs. 1 and 3. (b) Perspective view of the lateral extension of the PSF's of all the point sources along a radial axis in the spherical recording geometry.

$$\begin{aligned}\tilde{p}'(\mathbf{r}_0,k)&=\int\int \tilde{p}(\mathbf{r}_0+\mathbf{r}',k)W(\theta')r'\sqrt{1-(\mathbf{n}_0\cdot\mathbf{n}')^2}d\varphi' dl'\\&=\int_{l'}W(\theta')\sqrt{1-(\mathbf{n}_0\cdot\mathbf{n}')^2}r'dl'\\&\quad\times\int_0^{2\pi}\tilde{p}(\mathbf{r}_0+\mathbf{r}',k)d\varphi',\end{aligned} \tag{59}$$

where $\mathbf{n}'=\mathbf{r}'/r'$ and

$$\tilde{p}(\mathbf{r}_0+\mathbf{r}',k)=-ikc^2\eta\frac{\exp(ik|\mathbf{r}_a-\mathbf{r}_0-\mathbf{r}'|)}{4\pi|\mathbf{r}_a-\mathbf{r}_0-\mathbf{r}'|}. \tag{60}$$

Considering the expansion in the local spherical coordinates, and denoting $\mathbf{n}'_0=\mathbf{r}'_0/r'_0$, $\mathbf{n}'_0=(\theta',\varphi')$, and $\mathbf{n}_a=(\theta'_a,\varphi'_a)$, one obtains

$$\frac{\exp(ik|\mathbf{r}_a-\mathbf{r}'_0|)}{4\pi|\mathbf{r}_a-\mathbf{r}'_0|}=\frac{ik}{4\pi}\sum_{l=0}^{\infty}(2l+1)j_l(kr_a)\times h_l^{(1)}(kr'_0)P_l(\mathbf{n}_a\cdot\mathbf{n}'_0), \tag{61}$$

where $P_l(\mathbf{n}_a\cdot\mathbf{n}'_0)$ can be expanded as [14]

$$P_l(\mathbf{n}_a\cdot\mathbf{n}'_0)=P_l(\cos\theta'_a)P_l(\cos\theta')+2\sum_{m=1}^{l}\frac{(l-m)!}{(l+m)!}P_l^m(\cos\theta'_a)P_l^m(\cos\theta')\times\cos[m(\varphi'_a-\varphi')]. \tag{62}$$

Then, one can evaluate the following integral:

$$\int_0^{2\pi}P_l(\mathbf{n}_a\cdot\mathbf{n}'_0)d\varphi'=2\pi P_l(\cos\theta')P_l(\cos\theta'_a). \tag{63}$$

Actually, θ'_a is the angle between $\mathbf{r}_0$ and $\mathbf{r}_a$, i.e., $\cos\theta'_a=\mathbf{n}_a\cdot\mathbf{n}_0$.

Combining the results of Eqs. (61)–(63), Eq. (59) can be rewritten as

$$\tilde{p}'(\mathbf{r}_0,k)=\frac{k^2c^2\eta}{2}\int_{l'}W(\theta')\sqrt{1-(\mathbf{n}_0\cdot\mathbf{n}')^2}r'dl'\times\sum_{l=0}^{\infty}(2l+1)P_l(\cos\theta')P_l(\mathbf{n}_a\cdot\mathbf{n}_0)j_l(kr_a)\times h_l^{(1)}(kr'_0). \tag{64}$$

By replacing $p(\mathbf{r}_0,k)$ with $\tilde{p}'(\mathbf{r}_0,k)$ in the reconstruction formula Eq. (8) and considering identity (14), one obtains the reconstruction for $A(\mathbf{r})$:

$$A_a(\mathbf{r})=\frac{1}{\pi}\int_{l'}W(\theta')\sqrt{1-(\mathbf{n}_0\cdot\mathbf{n}')^2}r'dl'\times\sum_{m=0}^{\infty}(2m+1)P_m(\mathbf{n}_a\cdot\mathbf{n})P_m(\cos\theta')\times\int_0^{+\infty}j_m(kr_a)j_m(kr)\frac{h_m^{(1)}(kr'_0)}{h_m^{(1)}(kr_0)}k^2dk. \tag{65}$$

Letting $\tilde{\theta}$ and $\tilde{\varphi}$ be the polar and azimuthal angles of vector $\mathbf{n}$ with respect to vector $\mathbf{n}_a$, and using an identity similar to the one shown in Eq. (63), one can rewrite Eq. (65) as

$$A_a(\mathbf{r})=\int\int W(\theta')r'\sqrt{1-(\mathbf{n}_0\cdot\mathbf{n}')^2}d\varphi'dl'\times\frac{1}{2\pi^2}\sum_{m=0}^{\infty}(2m+1)P_m(\cos\tilde{\gamma})\times\int_0^{+\infty}j_m(kr_a)j_m(kr)\frac{h_m^{(1)}(kr'_0)}{h_m^{(1)}(kr_0)}k^2dk, \tag{66}$$

where $\cos\tilde{\gamma}=\cos\tilde{\theta}\cos\theta'+\sin\tilde{\theta}\sin\theta'\cos(\tilde{\varphi}-\varphi')$.

1. Special spherical aperture

For simplicity, assume that the detector is a small section of the spherical measurement surface, i.e., $r'_0=|\mathbf{r}'_0|=|\mathbf{r}_0+\mathbf{r}'|=|\mathbf{r}_0|=r_0$. Therefore, one obtains

$$\sqrt{1-(\mathbf{n}_0\cdot\mathbf{n}')^2}r'dl'=r_0^2\sin\theta'd\theta', \tag{67}$$

and

$$h_m^{(1)}(kr'_0)/h_m^{(1)}(kr_0)=1. \tag{68}$$

Substituting the identity Eq. (18) and the following identity (see the Appendix) into Eq. (65),

$$\sum_{m=0}^{\infty}(2m+1)P_m(\mathbf{n}_a\cdot\mathbf{n})P_m(\cos\theta')=2\delta(\cos\theta'-\mathbf{n}_a\cdot\mathbf{n}), \tag{69}$$

one obtains

$$A_a(\mathbf{r})=\frac{r_0^2}{r^2}\delta(r-r_a)\int_0^{\Theta}\sin\theta'W(\theta')d\theta'\,\delta(\cos\theta'-\mathbf{n}_a\cdot\mathbf{n}). \tag{70}$$

Letting γ be the angle between $\mathbf{n}_a$ and $\mathbf{n}$, i.e., $\mathbf{n}_a\cdot\mathbf{n}=\cos\gamma$,

$$\begin{aligned}A_a(\mathbf{r})&=\frac{r_0^2}{r^2}\delta(r-r_a)\int_0^{\Theta}\sin\theta'W(\theta')d\theta'\,\delta(\cos\theta'-\cos\gamma)\\&=\frac{r_0^2}{r^2}\delta(r-r_a)\int_0^{\Theta}\sin\theta'W(\theta')d\theta'\frac{\delta(\theta'-\gamma)}{\sin\theta'}\\&=\frac{r_0^2}{r^2}\delta(r-r_a)\int_0^{\Theta}W(\theta')\delta(\theta'-\gamma)\delta\theta'\\&=\frac{r_0^2}{r^2}\delta(r-r_a)W(\gamma).\end{aligned} \tag{71}$$

If letting $W(\theta')=1$,

$$A_a(\mathbf{r})=\frac{r_0^2}{r^2}\delta(r-r_a)[U(\gamma)-U(\gamma-\Theta)], \tag{72}$$

where U is the step function, $U(x)=1$ when $x>0$ and $U(x)=0$ when $x<0$.

Equation (72) indicates that, in this special case, the PSF only extends along the lateral direction, which is proportional to the solid angle of the detector aperture to the origin of the measurement geometry. The perspective view of the lateral extension of all the points in a radial axis looks like a cone as shown in Fig. 4(b). The farther the point source is away from the origin, the more extension the PSF has. Therefore, the lateral resolution is worse when the point is close to the detector. But, a lateral resolution superior to the aperture size can still be achieved if the object under study is close to the center of the geometry.

2. Small flat aperture

Now, let us consider flat apertures. Sometimes, a set of small flat detectors is used to form a spherical recording surface. Suppose the detector aperture is disklike and its radius is P. Since $\mathbf{n}_0\cdot\mathbf{n}'=0$ in this case,

$$\sqrt{1-(\mathbf{n}_0\cdot\mathbf{n}')^2}r'dl'=r'dr', \tag{73}$$

where $r'=r_0\tan\theta'$. If the aperture is small relative to the radius of the detection surface, i.e., $r'\leq P\ll r_0$, the following approximation holds:

$$r_0'-r_0=\sqrt{r_0^2+r'^2}-r_0\approx\frac{r'^2}{2r_0}. \tag{74}$$

Neglecting the second-order and higher small quantities, one can approximate $h_m^{(1)}(kr_0')/h_m^{(1)}(kr_0)\approx1$. Then, one can follow the derivation for the special spherical aperture and obtain

$$A_a(\mathbf{r})=\frac{1}{r^2}\delta(r-r_a)\int_0^P W(r')r'dr'\ \delta(\cos\theta'-\mathbf{n}_a\cdot\mathbf{n}). \tag{75}$$

Letting $W(r')=1$ and approximating $r'=r_0\tan\theta'\approx r_0\theta'$ for the small-aperture case, one reaches

$$\begin{aligned}A_a(\mathbf{r})&\approx\frac{r_0^2}{r^2}\delta(r-r_a)\int_0^{P/r_0}\theta'\frac{\delta(\theta'-\gamma)}{\sin\theta'}d\theta'\\&=\frac{r_0^2}{r^2}\delta(r-r_a)\int_0^{P/r_0}\delta(\theta'-\gamma)\delta\theta'\\&=\frac{r_0^2}{r^2}\delta(r-r_a)[U(\gamma)-U(\gamma-P/r_0)].\end{aligned} \tag{76}$$

Equation (76) indicates that, for the small flat aperture, the extension of the PSF is primarily along the lateral axis. In fact, if we substitute Θ for P/r_0, Eq. (76) becomes identical to Eq. (72) for the special spherical aperture.

Particularly, at the center of the recording geometry, i.e., $r_a=0$, we have $j_m(0)=\delta_{m0}$, $P_0(\cdot)=1$, and $h_0^{(1)}(kr)=-i\exp(ikr)/(kr)$. Assuming $W(r')=1$, Eq. (65) reduces to

$$\begin{aligned}A_a(\mathbf{r})=\frac{1}{\pi}\int_0^{+\infty}&j_0(kr)\exp(-ikr_0)k^2dk\\&\times\int_0^P\frac{r_0}{r_0'}r'dr'\ \exp(ikr_0').\end{aligned} \tag{77}$$

Using the relation $r_0'=\sqrt{r_0^2+r'^2}$, one can simplify Eq. (77) to

$$A_a(\mathbf{r})=\frac{1}{\pi}\int_0^{+\infty}j_0(kr)k^2dk\frac{r_0[\exp(ik\sqrt{P^2+r_0^2}-ikr_0)-1]}{ik}. \tag{78}$$

Because $P\ll r_0$, the imaginary part is much less than the real part and hence can be neglected; as a result, one can obtain

$$A_a(\mathbf{r})\approx\frac{r_0}{\pi}\int_0^{+\infty}j_0(kr)\sin[k(\sqrt{P^2+r_0^2}-r_0)]k\,dk. \tag{79}$$

Using the following identity [14]:

$$\begin{aligned}\int_0^{+\infty}j_0(ka)\sin(kb)k\,dk&=b\int_0^{+\infty}j_0(ka)j_0(kb)k^2dk\\&=\frac{\pi}{2b}\delta(b-a),\end{aligned} \tag{80}$$

in the small-aperture case, i.e., $P\ll r_0$, Eq. (79) reduces to

$$A_a(r)=\frac{r_0^2}{P^2}\delta\left(r-\frac{P^2}{2r_0}\right). \tag{81}$$

Equation (79) indicates that the point source at the center becomes a circle with a diameter P^2/r_0.

Next, we want to estimate the lateral extension at an arbitrary point. Taking the asymptotic form of the Hankel function to approximate

$$\frac{h_m^{(1)}(kr_0')}{h_m^{(1)}(kr_0)}\approx\frac{\exp(ikr_0')/(kr_0')}{\exp(ikr_0)/(kr_0)}=\frac{r_0}{r_0'}\exp(ikr_0'-ikr_0), \tag{82}$$

one can rewrite Eq. (65) as

$$\begin{aligned}A_a(\mathbf{r})=\frac{1}{\pi}\int_0^P W(r')r'dr'\int_0^{+\infty}&\frac{r_0}{r_0'}\exp(ikr_0'-ikr_0)k^2dk\\&\times\sum_{m=0}^{\infty}(2m+1)P_m(\mathbf{n}_a\cdot\mathbf{n})\\&\times P_m(\cos\theta')j_m(kr_a)j_m(kr).\end{aligned} \tag{83}$$

The above integral is still complicated. Here, we consider only the spread along $\mathbf{r}_a$ with the assumption of $W(r')=1$. Substituting $P_m(\mathbf{n}_a\cdot\mathbf{n})=P_m(1)=1$ into Eq. (83) and considering identity (16), and further approximating $j_0(k\sqrt{r_a^2+r^2-2r_ar\cos\theta'})\approx j_0(k|r-r_a|)$ for the small-aperture case ($r'\ll r_0$, i.e., $\theta'\ll1$), one obtains

$$\begin{aligned}A_a(r\mathbf{n}_a)=\frac{1}{\pi}\int_0^{+\infty}&j_0(k|r-r_a|)\exp(-ikr_0)k^2dk\\&\times\int_0^P\frac{r_0}{r_0'}r'dr'\ \exp(ikr_0').\end{aligned} \tag{84}$$

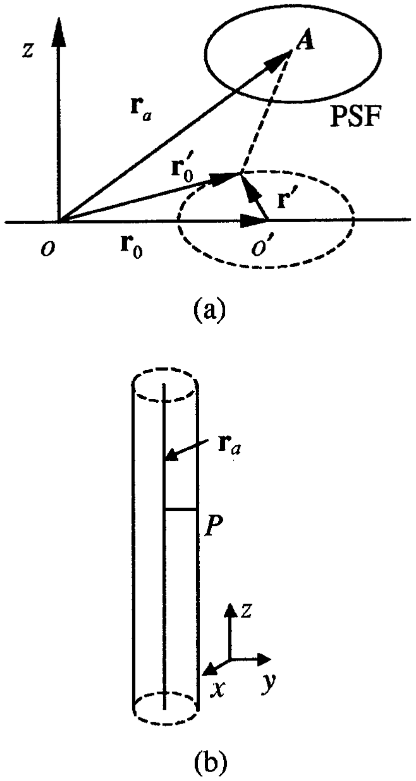

FIG. 5. (a) Diagram of the planar recording geometry: P is the radius of the detector aperture; the extension of the PSF at point A is indicated; other denotations of the symbols are the same as in Figs. 1 and 3; (b) perspective view of the lateral extension of the PSF's of all the point sources along a line parallel to the z axis in the planar recording geometry.

If we substitute $|r-r_a|$ for r, Eq. (84) becomes identical to Eq. (77). Thus, in the small-aperture case ($P \ll r_0$), Eq. (84) reduces to Eq. (81) with the replacement of r by $|r-r_a|$:

$$A_a(r\mathbf{n}_a)\approx\frac{r_0^2}{P^2}\delta\left(|r-r_a|-\frac{P^2}{2r_0}\right). \tag{85}$$

Equation (85) indicates that the point source at which $\mathbf{r}_a$ extends in the radial direction to a region with diameter P^2/r_0 is the same as the extension of the PSF at the recording geometry center as shown in Eq. (81). But, in most cases, this extension is negligible. For example, when using a transducer with even a 6 mm diameter to image a 10-cm-size breast on a recording geometry surface with a 15 cm diameter, $P^2/r_0=3^2/150=0.06$ mm. However, the lateral extension at r is on the order of $2rP/r_0$ as shown in Eq. (76). For example, even at $r=1$ cm, $2rP/r_0=(2)(10)(3)/150=0.4$ mm>0.06 mm.

B. Planar geometry

In this case, we reasonably assume that the detector surface is flat. As shown in Fig. 5(a), $\mathbf{r}_0$ represents the center of the detector o' in the global Cartesian coordinates (x,y,z) with the origin at the recording geometry center o. Let x', y', and z' be the differences of the coordinates between $\mathbf{r}_0'$ and $\mathbf{r}_0$, respectively. For the following two linear translations:

$$\mathbf{r}_0\rightarrow\mathbf{r}_0':\ x_0\rightarrow x_0+x'=x_0',\quad y_0\rightarrow y_0+y'=y_0', \tag{86}$$

$$\mathbf{r}_a\rightarrow\mathbf{r}_a':\ x_a\rightarrow x_a-x'=x_a',\quad y_a\rightarrow y_a-y'=y_a', \tag{87}$$

there exist the following translational invariances, $|\mathbf{r}_a-\mathbf{r}_0'|=|\mathbf{r}_a'-\mathbf{r}_0|$.

The detected signal at $\mathbf{r}_0$ can be written as

$$\begin{aligned}\tilde{p}'(\mathbf{r}_0,k)&=\int\int W(\mathbf{r}')\tilde{p}(\mathbf{r}_0+\mathbf{r}',k)d^2\mathbf{r}'\\&=\int\int W(x',y')\tilde{p}(x_0+x',y_0+y',k)dx'dy'.\end{aligned} \tag{88}$$

Using $\tilde{p}'(\mathbf{r}_0,k)$ to replace $p(\mathbf{r}_0,k)$ in the reconstruction formula Eq. (9), and following the similar derivation shown in Sec. III B, one gets the reconstruction for $A(\mathbf{r})$ as

$$\begin{aligned}A_a(x,y,z)&=\int\int W(x',y')\,\delta(x-x_a')\,\delta(y-y_a')\\&\quad\times\delta(z-z_a)dx'dy'\\&=\int\int W(x',y')\,\delta(x-x_a+x')\,\delta(y-y_a+y')\\&\quad\times\delta(z-z_a)dx'dy',\end{aligned} \tag{89}$$

i.e.,

$$A_a(x,y,z)=W(x-x_a,y-y_a)\,\delta(z-z_a). \tag{90}$$

Assuming that the detector surface is a disk with radius P, and $W(x',y')=1$ when $\sqrt{x'^2+y'^2}<P$, Eq. (90) reduces to

$$A_a(x,y,z)=U(P-D)\,\delta(\Delta z), \tag{91}$$

where $D=\sqrt{(\Delta x)^2+(\Delta y)^2}$, and $\Delta x=x-x_a$, etc.

Equation (91) indicates that without considering the bandwidth, the PSF does not extend along the axial direction, but it greatly extends in the lateral direction. Moreover, the lateral extension is proportional to the detector aperture. The perspective view of the lateral extension of all the PSF's in a line parallel with the z axis looks like a cylinder as shown in Fig. 5(b). Therefore, the lateral resolution is totally blurred by the detector aperture, no matter where the point is.

C. Cylindrical geometry

1. Special cylinder aperture

We first assume that the detector surface is a section of the cylindrical measurement surface. As shown in Fig. 6(a), $\mathbf{r}_0$ represents the center of the detector o' in the global cylindrical coordinates (ρ,φ,z) with the origin at the recording geometry center o. Let φ' be the difference between the polar angles of $\mathbf{r}_0$ and $\mathbf{r}_0'$, and ρ' and z' be the projections of

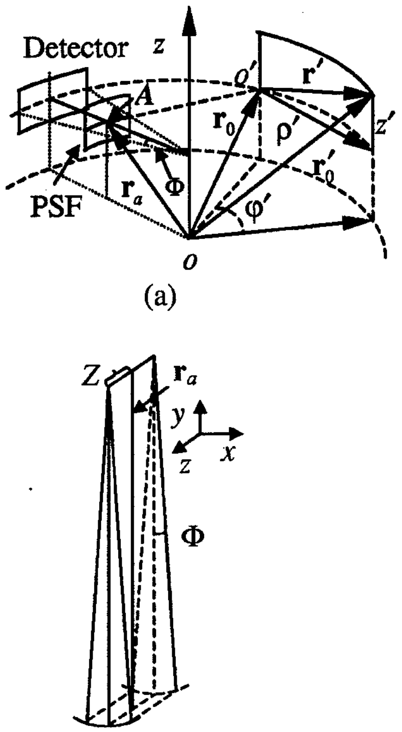

(a)

(b)

FIG. 6. (a) Diagram of the cylindrical geometry: φ' is the difference between the polar angles of $\mathbf{r}_0$ and $\mathbf{r}_0'$; ρ' and z' are the projections of $\mathbf{r}'$ in the x-y plane and the z axis, respectively; Z is the half width of the detector aperture along the z axis and Φ is the half angle of the width of the detector aperture parallel to the x-y plane to the center of the recording geometry; the extension of the PSF at point A is indicated; other denotations of the symbols are the same as in Figs. 1 and 3. (b) Perspective view of the lateral extension of the PSF's of all the point sources along a radial axis in the cylindrical recording geometry.

$\mathbf{r}'$ in the x-y plane and the z axis, respectively. Two sides of the detector are along the z axis from $-Z$ to Z, and the other two sides are parallel with the x-y plane and the polar angle φ' varies from $-\Phi$ to Φ. For the following two translations:

$$\mathbf{r}_0\to\mathbf{r}_0'\colon\ \varphi_0\to\varphi_0+\varphi'=\varphi_0',\quad z_0\to z_0+z'=z_0', \tag{92}$$

$$\mathbf{r}_a\to\mathbf{r}_a'\colon\ \varphi_a\to\varphi_a-\varphi'=\varphi_a',\quad z_a\to z_a-z'=z_a', \tag{93}$$

there exist the following translational invariances, $|\mathbf{r}_a-\mathbf{r}_0'|=|\mathbf{r}_a'-\mathbf{r}_0|$.

The detected signal can be written as

$$\begin{aligned}\tilde{p}_a(\mathbf{r}_0,k)&=\int\int\tilde{p}(\mathbf{r}_0+\mathbf{r}',k)W(\mathbf{r}')d^2\mathbf{r}'\\&=\int\int\tilde{p}(\varphi_0+\varphi',z_0+z',k)W(\varphi',z')\rho_0 d\varphi' dz'.\end{aligned} \tag{94}$$

Replacing $p(\mathbf{r}_0,k)$ by $\tilde{p}'(\mathbf{r}_0,k)$ in the reconstruction formula Eq. (10), and following the derivation shown in Sec. III C, one can get the reconstruction for $A(\mathbf{r})$ as

$$\begin{aligned}A_a(\rho,\varphi,z)&=\int\int\frac{1}{\rho}\delta(\rho-\rho_a)\delta(\varphi-\varphi_a')\\&\quad\times\delta(z-z_a')W(\varphi',z')\rho_0 d\varphi' dz'\\&=\frac{\rho_0}{\rho}\delta(\rho-\rho_a)\int\int\delta(\varphi-\varphi_a+\varphi')\\&\quad\times\delta(z-z_a+z')W(\varphi',z')d\varphi' dz',\end{aligned} \tag{95}$$

i.e.,

$$A_a(\rho,\varphi,z)=\frac{\rho_0}{\rho}\delta(\rho-\rho_a)W(\varphi-\varphi_a,z-z_a). \tag{96}$$

If $W(\varphi',z')=1$, φ' from $-\Phi$ to Φ, and z' from $-Z$ to Z, Eq. (96) can be rewritten as

$$A_a(\rho,\varphi,z)=\frac{\rho_0}{\rho}\delta(\rho-\rho_a)U(\Phi-|\varphi-\varphi_a|)U(Z-|z-z_a|). \tag{97}$$

Equation (97) indicates that the extension of the PSF in the cylindrical geometry combines the properties of the PSF's in the spherical and planar geometries. In this special case, the PSF does not extend along the radial direction. The perspective view of the lateral extension of all the point sources in a radial axis looks like a wedge of pie as shown in Fig. 6(b). In the z-axis direction, the PSF extension is proportional to the detector size along the z axis, just like the planar geometry. While parallel with the x-y plane, the lateral extension is proportional to the angle of the detector width to the z axis, just like in the spherical case. Therefore, a lateral resolution that is better than the aperture size can be obtained parallel to the x-y plane if the object under study is close to the center of the geometry; however, the lateral resolution along the z axis is determined by the detector size.

2. Small rectangle aperture

Sometimes a set of small rectangle detectors is used to form a cylindrical array. The normal of the detector at the center point o' is assumed to point to the center of the recording geometry. Two sides of the detector are along the z axis from $-Z$ to Z, and the other two sides are parallel with the x-y plane and have a length of $2P$. One can follow the similar derivation in Sec. III C, and get the reconstruction for $A(\mathbf{r})$ as

$$A_a(\rho,\varphi,z)=\frac{1}{2\pi}\int_{-Z}^{Z}\delta(z_a-z-z')dz'\int_{-P}^{P}d\rho'\,W(\varphi',z')$$
$$\times\sum_{m=-\infty}^{+\infty}\exp[im(\varphi_a-\varphi-\varphi')]$$
$$\times\int_0^{+\infty}\mu\,d\mu$$
$$\times J_m(\mu\rho_a)J_m(\mu\rho)\frac{H_m^{(1)}(\mu\sqrt{\rho_0^2+\rho'^2})}{H_m^{(1)}(\mu\rho_0)},\quad(98)$$

where $\rho'=\rho_0\tan\varphi'$. Let $W(\varphi',z')=1$.

For the small-aperture case, $\rho'\ll\rho_0$, one can approximate

$$\frac{H_m^{(1)}(\mu\sqrt{\rho_0^2+\rho'^2})}{H_m^{(1)}(\mu\rho_0)}\approx 1.\quad(99)$$

Further, taking the small-aperture approximation $\rho'=\rho_0\tan\varphi'\simeq\rho_0\varphi'$, and considering the following identity [14]:

$$\int_0^{+\infty}\mu\,d\mu\,J_m(\mu\rho_a)J_m(\mu\rho)=\frac{1}{\rho}\delta(\rho-\rho_a),\quad(100)$$

one can rewrite Eq. (98) as

$$A_a(\rho,\varphi,z)=U(Z-|z-z_a|)\frac{1}{\rho}\delta(\rho-\rho_a)$$
$$\times\int_{-P/\rho_0}^{P/\rho_0}\rho_0 d\varphi'\,\delta(\varphi_a-\varphi-\varphi'),\quad(101)$$

i.e.,

$$A_a(\rho,\varphi,z)=\frac{\rho_0}{\rho}\delta(\rho-\rho_a)U\left(\frac{P}{\rho_0}-|\varphi-\varphi_a|\right)U(Z-|z-z_a|).\quad(102)$$

Equation (102) indicates that, for the small flat aperture, the extension of the PSF is primarily along the lateral axis. In fact, if we substitute Φ for P/ρ_0, Eq. (102) becomes identical to Eq. (97) in the special cylinder aperture case.

Next, we want to estimate the lateral extension of the PSF. One can also take the asymptotic form of the Hankel function to approximate

$$\frac{H_m^{(1)}(\mu\sqrt{\rho_0^2+\rho'^2})}{H_m^{(1)}(\mu\rho_0)}\approx\exp[i\mu(\sqrt{\rho_0^2+\rho'^2}-\rho_0)],\quad(103)$$

and then rewrite Eq. (98) as

$$A_a(\rho,\varphi,z)=\frac{1}{2\pi}U(Z-|z-z_a|)\int_0^{+\infty}\mu\,d\mu$$
$$\times\int_{-P}^{P}d\rho'\,\exp[i\mu(\sqrt{\rho_0^2+\rho'^2}-\rho_0)]$$
$$\times\sum_{m=-\infty}^{+\infty}J_m(\mu\rho_a)J_m(\mu\rho)$$
$$\times\exp[im(\varphi_a-\varphi-\varphi')].\quad(104)$$

Considering identity (35), Eq. (104) can be rewritten as

$$A_a(\rho,\varphi,z)=\frac{1}{2\pi}U(Z-|z-z_a|)\int_0^{+\infty}\mu\,d\mu$$
$$\times\int_{-P}^{P}d\rho'\,\exp[i\mu(\sqrt{\rho_0^2+\rho'^2}-\rho_0)]$$
$$\times J_0(\mu\sqrt{\rho_a^2+\rho^2-2\rho_a\rho\cos(\varphi_a-\varphi-\varphi')}).\quad(105)$$

Equation (105) is still complicated. Here, by only considering the points along $\mathbf{r}_a$, i.e., letting $\varphi=\varphi_a$, and then taking the small-aperture approximation ($\varphi'\ll 1$),

$$J_0(u\sqrt{\rho_a^2+\rho^2-2\rho_a\rho\cos(\varphi_a-\varphi-\varphi')})\approx J_0(\mu|\rho-\rho_a|),\quad(106)$$

and

$$\sqrt{\rho_0^2+\rho'^2}-\rho_0\approx\frac{\rho'^2}{2\rho_0},\quad(107)$$

one can rewrite Eq. (105) as

$$A_a(\rho,\varphi_a,z)=U(Z-|z-z_a|)\int_{-P}^{P}d\rho'\int_0^{+\infty}\mu\,d\mu$$
$$\times J_0(\mu|\rho-\rho_a|)\exp(i\mu\rho'^2/2\rho_0).\quad(108)$$

Because $\rho'\ll\rho_0$, the imaginary part is much less than the real part and hence can be neglected,

$$A_a(\rho,\varphi_a,z)=U(Z-|z-z_a|)\int_{-P}^{P}d\rho'\int_0^{+\infty}\mu\,d\mu$$
$$\times J_0(\mu|\rho-\rho_a|)\cos(\mu\rho'^2/2\rho_0)$$
$$=U(Z-|z-z_a|)\int_{-P}^{P}d\rho'\left(\frac{\rho_0}{\rho'}\right)\frac{\partial}{\partial\rho'}$$
$$\times\int_0^{+\infty}d\mu\,J_0(\mu|\rho-\rho_a|)\sin(\mu\rho'^2/2\rho_0).\quad(109)$$

Using the following identity [15]:

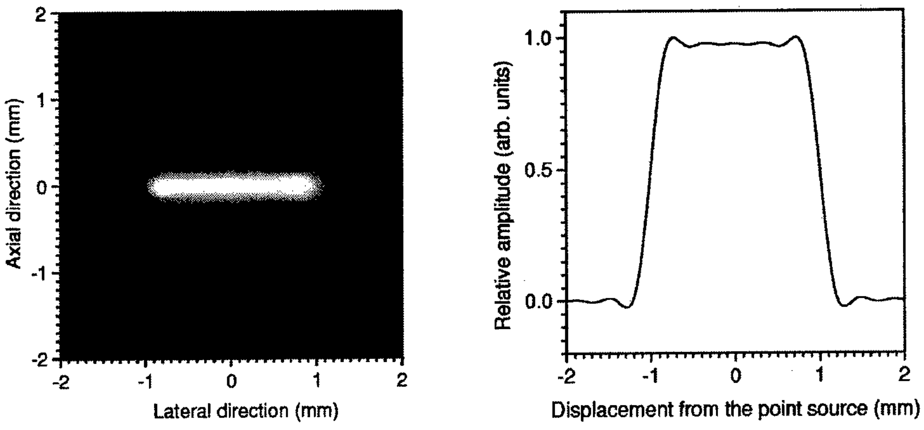

(a) (b)

FIG. 7. An example of the PSF due to the detector aperture: (a) a gray scale view and (b) a lateral profile through the point source.

$$\int_0^{+\infty} dt\, J_0(ta)\sin(tb) = \begin{cases} \dfrac{1}{\sqrt{b^2-a^2}}, & 0<a<b \\ 0 & \text{otherwise,} \end{cases} \tag{110}$$

one can get the integral in Eq. (109),

$$\begin{aligned} &\int_{-P}^{P} d\rho' \left(\frac{\rho_0}{\rho'}\right)\frac{\partial}{\partial\rho'}[\sqrt{(\rho'^2/2\rho_0)^2-|\rho-\rho_a|^2}]^{-1} \\ &= \left(\frac{\rho_0}{\rho'}\right)[\sqrt{(\rho'^2/2\rho_0)^2-|\rho-\rho_a|^2}]^{-1}\Big|_{-P}^{P} \\ &\quad - \int_{-P}^{P}[\sqrt{(\rho'^2/2\rho_0)^2-|\rho-\rho_a|^2}]^{-1} d\left(\frac{\rho_0}{\rho'}\right). \end{aligned} \tag{111}$$

The integral of Eq. (111) only exists in the range $P^2/2\rho_0 > |\rho-\rho_a|$. Therefore, the PSF extends to a region with a diameter P^2/ρ_0, which is negligible compared to the lateral extension as we discussed in the spherical geometry explanation.

So far, we have derived the analytic PSF's due to the detector apertures for the specific spherical, planar, and cylindrical recording geometries. The explicit expressions can be given when the detector surfaces are assumed to have the same geometric properties as the recording geometries. Otherwise, it appears that explicitly carrying out the analytic derivations is impossible. But, in reality, the detector aperture is very small compared to the recording surface. We have also estimated axial extension in this case and found that it was negligible compared to lateral extension.

V. DISCUSSION AND CONCLUSIONS

In Sec. III, we proved that the PSF as a function of bandwidth is space invariant. In Sec. IV, we demonstrated that the finite aperture of the detector extends the PSF for different recording geometries.

Finally, we attempt to analyze the combined effects of bandwidth and detector size together. Assume that the detected signal is bandlimited, characterized by $\tilde{H}(k)$ with a cutoff frequency k_c, and the detectors have the same geometries as the recording surfaces. One can then follow the derivations in Secs. III and IV and reach the following results.

(1) Spherical geometry:

$$A_{ba}(\mathbf{r}) = \int\int W(\theta')\mathcal{F}_b^{\mathrm{PSF}}(R')r_0^2 \sin\theta' d\theta' d\varphi', \tag{112}$$

where $R' = \sqrt{r^2+r_a^2-2rr_a\cos\tilde{\gamma}}$, $\cos\tilde{\gamma} = \cos\tilde{\theta}\cos\theta' + \sin\tilde{\theta}\sin\theta'\cos(\tilde{\varphi}-\varphi')$, and $\tilde{\theta}$ and $\tilde{\varphi}$ are the polar and azimuthal angles of vector $\mathbf{n}$ with respect to vector $\mathbf{n}_a$, respectively.

(2) Planar geometry:

$$A_{ba}(x,y,z) = \int\int W(x',y')\mathcal{F}_b^{\mathrm{PSF}}(R')dx'dy', \tag{113}$$

where $R' = \sqrt{(x-x_a+x')^2+(y-y_a+y')^2+(z-z_a)^2}$.

(3) Cylindrical geometry:

$$A_{ba}(\rho,\varphi,z) = \int\int W(\varphi',z')\mathcal{F}_b^{\mathrm{PSF}}(R')\rho_0 d\varphi' dz', \tag{114}$$

where $R' = \sqrt{\rho^2+\rho_a^2-2\rho\rho_a\cos(\varphi-\varphi_a+\varphi')+(z-z_a+z')^2}$.

Equations (112)–(114) clearly reveal that the PSF can be regarded as a convolution of the detector aperture with the space invariant $\mathcal{F}_b^{\mathrm{PSF}}$. However, in the spherical geometry case, the convolution becomes complicated as shown in Eq. (112). Further, we can imagine how complicated the convolution could be with an arbitrary recording geometry using arbitrary-aperture detectors.

Let us take the PSF in the planar geometry case as an example, which is shown in Fig. 7. The detector aperture is assumed to be a disk with a radius of 1 mm and a cutoff frequency $f_c = 4$ MHz. In the axial direction, the extension of the PSF is similar to that shown in Fig. 2(b), which is determined by the bandwidth. However, as shown Fig. 7(b), the PSF greatly expands in the lateral direction, and its corresponding $\mathcal{W}_{\mathrm{FWHM}} \approx 2$ mm, which is physically limited by the detector size.

In conclusion, spatial resolution as a function of bandwidth is space invariant for any recording geometry when the reconstruction is linear and exact. The bandwidth limits the obtainable spatial resolution. The detector aperture blurs lateral resolution greatly at different levels for different recording geometries but the effect on axial resolution is slight. The results offer clear instruction for designing appropriate thermoacoustic imaging systems with predefined spatial resolutions.

ACKNOWLEDGMENTS

This project was sponsored in part by the U.S. Army Medical Research and Material Command Grant No. DAMD17-00-1-0455, the National Institutes of Health Grant Nos. R21 EB00319-02 and R01 EB000712, the National Science Foundation Grant No. BES-9734491, and the Texas Higher Education Coordinating Board Grant No. ARP 000512-0063-2001.

APPENDIX

The completeness relation of the spherical harmonics $Y_{lm}(\theta,\varphi)$ [14,16] is

$$\sum_{l=0}^{\infty}\sum_{m=-1}^{l} Y_{lm}^{*}(\theta',\varphi')Y_{lm}(\theta,\varphi) = \delta(\varphi-\varphi')\delta(\cos\theta-\cos\theta'), \tag{A1}$$

where

$$Y_{lm}(\theta,\varphi)=\sqrt{\frac{2l+1}{4\pi}\frac{(l-m)!}{(l+m)!}}P_l^m(\cos\theta)\exp(im\varphi). \tag{A2}$$

Then, do an integral over φ from 0 to 2π of both sides of Eq. (A1),

$$\sum_{l=0}^{\infty}\sum_{m=-l}^{l}\frac{2l+1}{4\pi}\frac{(l-m)!}{(l+m)!}P_l^m(\cos\theta)P_l^m(\cos\theta') \times\int_0^{2\pi}\exp[im(\varphi-\varphi')]d\varphi$$
$$=\sum_{l=0}^{\infty}\sum_{m=-l}^{l}\frac{2l+1}{4\pi}\frac{(l-m)!}{(l+m)!}P_l^m(\cos\theta)P_l^m(\cos\theta')2\pi\delta_{m0}$$
$$=\sum_{l=0}^{\infty}\frac{2l+1}{4\pi}P_l(\cos\theta)P_l(\cos\theta')2\pi$$
$$=\delta(\cos\theta-\cos\theta')\int_0^{2\pi}\delta(\varphi-\varphi')d\varphi=\delta(\cos\theta-\cos\theta'), \tag{A3}$$

i.e.,

$$\sum_{l=0}^{\infty}(2l+1)P_l(\cos\theta)P_l(\cos\theta')=2\delta(\cos\theta-\cos\theta'). \tag{A4}$$

---

[1] C. G. A. Hoelen, F. F. M. de Mul, R. Pongers, and A. Dekker, Opt. Lett. **23**, 648 (1998).

[2] R. A. Kruger, W. L. Kiser, K. D. Miller, H. E. Reynolds, D. R. Reinecke, G. A. Kruger, and P. J. Hofacker, Proc. SPIE **3916**, 150 (2000).

[3] K. P. Köstli, D. Frauchiger, J. J. Niederhauser, G. Paltauf, H. P. Weber, and M. Frenz, IEEE J. Sel. Top. Quantum Electron. **7**, 918 (2001).

[4] R. O. Esenaliev, A. A. Karabutov, and A. A. Oraevsky, IEEE J. Sel. Top. Quantum Electron. **5**, 981 (1999).

[5] G. Ku and L.-H. V. Wang, Med. Phys. **28**, 4 (2001).

[6] M. Xu, G. Ku, and L.-H. V. Wang, Med. Phys. **28**, 1958 (2001).

[7] M. Xu and L.-H. V. Wang, IEEE Trans. Med. Imaging **21**, 814 (2002).

[8] Y. Xu, D.-Z. Feng, and L.-H. V. Wang, IEEE Trans. Med. Imaging **21**, 823 (2002).

[9] Y. Xu, M. Xu, and L.-H. V. Wang, IEEE Trans. Med. Imaging **21**, 829 (2002).

[10] M. Xu and L.-H. V. Wang, Med. Phys. **29**, 1661 (2002).

[11] M. Xu, Y. Xu, and L.-H. V. Wang, IEEE Trans. Biomed. Eng. (to be published).

[12] Y. Xu and L.-H. Wang (unpublished).

[13] A. C. Tam, Rev. Mod. Phys. **58**, 381 (1986).

[14] G. B. Arfken and H. J. Weber, *Mathematical Methods for Physicists* (Academic, San Diego, 1995).

[15] M. Abramowitz and I. A. Stegun, *Handbook of Mathematical Functions with Formulas, Graphs, and Mathematical Tables* (Dover, New York, 1965).

[16] J. D. Jackson, *Classical Electrodynamics* (Wiley, New York, 1999).

[17] P. M. Morse and K. U. Ingard, *Theoretical Acoustics* (McGraw-Hill, New York, 1968).

1086 IEEE TRANSACTIONS ON BIOMEDICAL ENGINEERING, VOL. 50, NO. 9, SEPTEMBER 2003

Time-Domain Reconstruction Algorithms and Numerical Simulations for Thermoacoustic Tomography in Various Geometries

Minghua Xu, Yuan Xu, and Lihong V. Wang*, *Senior Member, IEEE*

***Abstract*—In this paper, we present time-domain reconstruction algorithms for the thermoacoustic imaging of biological tissues. The algorithm for a spherical measurement configuration has recently been reported in another paper. Here, we extend the reconstruction algorithms to planar and cylindrical measurement configurations. First, we generalize the rigorous reconstruction formulas by employing Green's function technique. Then, in order to detect small (compared with the measurement geometry) but deeply buried objects, we can simplify the formulas when two practical conditions exist: 1) that the high-frequency components of the thermoacoustic signals contribute more to the spatial resolution than the low-frequency ones, and 2) that the detecting distances between the thermoacoustic sources and the detecting transducers are much greater than the wavelengths of the high-frequency thermoacoustic signals (i.e., those that are useful for imaging). The simplified formulas are computed with temporal back projections and coherent summations over spherical surfaces using certain spatial weighting factors. We refer to these reconstruction formulas as modified back projections. Numerical results are given to illustrate the validity of these algorithms.**

***Index Terms*—Algorithm, geometry, imaging, photoacoustics, reconstruction, thermoacoustics, time-domain, tomography.**

I. INTRODUCTION

RECENT research has suggested that thermoacoustic tomography using either pulsed radio-frequency (RF) [1]–[8] or pulsed laser [9]–[12] can be a powerful imaging technology with good spatial resolution. Within this technique, when a pulsed electromagnetic irradiation is absorbed by a tissue, the heating and subsequent expansion of the tissue give rise to an instantaneous acoustic stress or pressure distribution inside the tissue. Directly following the pulse irradiation, the induced pressure distribution prompts acoustic wave propagation toward the surface of the tissue with various time delays. Ultrasound detectors are placed around the tissue to record the outgoing acoustic waves. These detected acoustic waves can be used to inversely compute the distribution of the initial acoustic pressure or electromagnetic absorption, which is related to the properties of the tissue.

In fact, electromagnetic fields in the RF range of 300 to 3000 MHz are the most useful in the study of soft tissues sized in centimeters. The RF penetration depth at this frequency range varies depending on the tissue properties and the RF frequency [3], [13], [14]. For example, the penetration depths for muscle and fat are about 1.2 and 9 cm at 3 GHz, respectively, and about 4 and 30 cm at 300 MHz, respectively; most other soft tissues have penetration depths that fall between these values. In addition, in this frequency range, there is very little scattering by the tissues [13].

In a typical application of thermoacoustic imaging using RF, a short-pulsed RF field illuminates the tissue. The most investigated and documented effect of RF power on biological tissues is the transformation of energy entering the tissues into increased kinetic energy in the absorbing molecules, thereby producing a general heating in the medium [13]. The heating results from both ionic conduction and vibration of the dipole molecules of water and proteins [13]. The energy absorbed by the tissue produces a temperature rise that is dependent on the cooling mechanism of tissue [13]. Human exposure to RF power must be limited for safety reasons, and within the mandated safety limits, the temperature rise per short pulse (such as 1 μs) in soft tissue is very small (on the order of milli-degrees) [6].

Nevertheless, this small temperature rise causes linear expansion of the tissue. The heating and expansion are greatest in those regions of the tissue that absorb the most RF power. Therefore, a distribution of acoustic pressure or stress inside the tissue is induced immediately during the short RF-pulse irradiation period due to heterogeneities of the RF energy deposition and the Grüneisen parameter inside the inhomogeneous tissue. Thermal expansion due to energy deposition is commonly referred to as the *thermoelastic effect* [15]. The generated acoustic pressure is on the order of mBar [6]. Such a small value does not cause tissue damage.

Subsequently, after the RF-pulse irradiation, the acoustic stresses inside the tissue relax. They act as instantaneous acoustic sources inside the tissue, which promote acoustic wave propagation. These acoustic waves contain acoustic frequencies ranging from very low frequencies to high frequencies that approximate the reciprocal of the RF pulse duration. The acoustic detectors, called ultrasound transducers [16], which can convert mechanical stresses into electrical signals, are placed around the tissue to record these outgoing acoustic waves, commonly

---

Manuscript received September 24, 2001; revised February 8, 2003. This work was sponsored in part by the U.S. Army Medical Research and Materiel Command under Grant DAMD17-00-1-0455, in part by the National Institutes of Health (NIH) under Grant R01 CA71980, in part by the National Science Foundation (NSF) under Grant BES-9734491, and in part by the Texas Higher Education Coordinating Board under Grant ARP 000512-0123-1999. *Asterisk indicates corresponding author.*

M. Xu and Y. Xu are are with the Optical Imaging Laboratory, Department of Biomedical Engineering, Texas A&M University, College Station, TX 77843-3120 USA.

*L. V. Wang is with the Optical Imaging Laboratory, Department of Biomedical Engineering, Texas A&M University, 3120 TAMU, College Station, TX 77843-3120 USA(e-mail: LWang@tamu.edu; URL: http://oilab.tamu.edu).

Digital Object Identifier 10.1109/TBME.2003.816081

0018-9294/03$17.00 © 2003 IEEE

referred to as *thermoacoustic or photoacoustic signals*. These thermoacoustic signals carry information about the RF absorption or initiated stress as well as about the acoustic properties of the tissue. Since the RF absorption or initiated stress is directly related to certain tissue properties (i.e., ionic conductivity and water components, etc.), the key problem is how to reconstruct the distribution of the RF absorption or initiated stress from the measured thermoacoustic signals around the tissue surface.

The short duration of the RF pulse allows one to restrict the RF energy deposition within the absorbing volume and minimize the thermal diffusion effect on the thermoacoustic waves. In thermoacoustic imaging, the RF pulse duration, τ_p, is typically shorter than the thermal transport time of absorbed RF energy in thermal conduction, τ_{th}, the condition that is commonly referred to as *thermal confinement* [17]. The condition for thermal confinement can be expressed as $\tau_p < \tau_{\text{th}} \sim l_p^2/\alpha$, where α is the thermal diffusivity of the irradiated material and l_p is the RF penetration depth or the size of the absorbing structure. For most soft tissues, $\alpha \sim 10^3 \text{ cm}^2 \cdot \text{s}^{-1}$ [14]. For example, we are interested in the detection of small absorbers in sizes from submillimeters to centimeters inside the tissue. We choose $l_p \sim$ mm to underestimate the thermal transport time $\tau_{\text{th}} \sim 10\ \mu$s. The RF pulse used, τ_p, is typically less than 1 μs, which is much less than τ_{th}. Moreover, the time required for an acoustic wave to traverse the absorption depth l_p approximates to $\sim l_p/c \approx 0.7\ \mu$s, which is also much shorter than τ_{th}, where c is the sound speed that is around 1.5 mm/μs in most soft tissues [14]. In other words, even in 1 μs of RF pulse duration, the heat transports a length of $\sqrt{\alpha\tau_p} \sim 0.3$ mm, while in the same amount of time, the acoustic wave propagates a distance of $c\tau_p \sim 1.5$ mm, which is far away from the thermal diffusion region of 0.3 mm. Of course, thermal diffusion will slightly blur the reconstructed images. But, when we try to investigate targets that are bigger than the thermal diffusion region, for instance, > 0.3 mm, if the RF pulse duration is less than 1 μs, the thermal effect on the thermoacoustic waves in soft tissue can be ignored. In addition, the thermoacoustic signal excited by a RF pulse with finite width can be regarded as a convolution with the RF pulse profile and the thermoacoustic signal excited by a $\delta(t)$ RF irradiation. For theoretical analysis, the short pulse can be regarded as a delta function.

In general, thermoacoustic imaging can be used for the investigation of soft tissues with inhomogeneous RF absorption but relatively homogeneous acoustic properties including the speed of sound and low acoustic attenuation. For practical purposes, speed dispersion can be neglected in soft tissues; typically, the speed increases by about 0.01% MHz^{-1} [16]. In most soft tissues, the speed of sound is relatively constant at ~ 1.5 mm/μs with a small variation about 5% [14], [16]. Acoustic attenuation in soft tissues is primarily due to the spectra of the relaxation processes, which account for the nearly linear frequency dependence [16]. The total acoustic attenuation in soft tissues results from combined losses due to absorption and scattering [14], [16]. In the low megahertz range, acoustic scattering in soft tissues accounts for only about 10% of the total acoustic attenuation [14]. A mean value of the acoustic energy attenuation in soft tissue is equal to $0.6 \text{ dB} \cdot \text{cm}^{-1} \cdot \text{MHz}^{-1}$ [16]. Typically, the total energy attenuation for a 1-MHz signal after a 5-cm propagation is about 3 dB, and the corresponding amplitude attenuates approximately to 70% of the initial value. Such attenuation is still acceptable, although the spatial resolution will be blurred at a certain level due to the loss of the high-frequency signal. For simplicity, the acoustic attenuation is neglected here. Pure acoustic property differentiation should appeal to conventional ultrasound imaging [16]. The unique advantage of thermoacoustic imaging is its ability to detect the inhomogeneous RF absorption property of tissues when the acoustic property is homogeneous. An obvious application is the detection of breast cancer tumors. People have observed that tumors in the breast have a stronger rate of RF absorption than the surrounding tissues; by contrast, the ultrasonic contrast in soft tissues is quite low [8].

In previous papers [2]–[4], the authors have presented studies on scanning thermoacoustic tomography using focused ultrasonic transducers as in conventional pulse-echo ultrasound imaging [16]. Each scan line is converted into a one-dimensional (1-D) image along the axis of the focused transducer, and only a simple calculation is required to construct cross-sectional images from all of the scan lines. However, the lateral resolution of this approach is determined by the focal diameter of the transducer as with conventional ultrasound, and the imaging region is also limited to the focal length of the transducer. To obtain a larger imaging view, we use unfocused wide-band point transducers to record the thermoacoustic signals. In this approach, a complicated reconstruction algorithm has to be derived for computing the images from a set of data measured around the tissue under study. Different recording geometric configurations result in different reconstruction formulas.

The puzzle of finding good reconstruction algorithms has not yet been resolved. Some researchers have resorted to approximated reconstruction algorithms, such as the Radon transform in the far-field approximation [7], [9], the weighted delay-and-sum method with experiential weighting factors [10], or the optimal statistical approach [18]. To date, some rigorous reconstruction algorithms have been reported for idealized measurement configurations, such as for the fully enclosing spherical recording surface [5], the planar recording surface of an infinite extent [19], [20] and the cylindrical recording surface of an infinite length [21]. However, in practical applications, the recording surfaces are generally finite and partially enclosing.

In this paper, we will first discuss the inverse problem of thermoacoustic imaging. Then, by employing the Green's function technique, we will generalize the rigorous reconstruction formulas for three types of recording surfaces: a planar, a spherical, and a cylindrical surface, which enclose the sample under study. In order to detect small but relatively deeply buried targets, we will introduce the following two conditions (details given in Section II): the high-frequency components of thermoacoustic signals contribute more to spatial resolution than the low-frequency ones, and the detecting distances between the thermoacoustic sources and the detecting transducers are much larger than the wavelengths of the high-frequency thermoacoustic signals that are useful for imaging. Taking these conditions into account, we will simplify the rigorous formulas and present time-domain reconstruction algorithms, which can be computed by temporal back projections and coherent summations over spherical surfaces with certain spatial weighting factors. Finally, numerical experiments will be conducted to demonstrate the validity of these formulas.

II. INVERSE PROBLEM

As discussed in Section I, in typical thermoacoustic measurements, the RF pulse duration is so short that the thermal conduction time is far greater than the thermoacoustic transit time and the effect of thermal diffusion on the thermoacoustic wave in the tissue can be ignored. We focus on small-amplitude thermoacoustic propagation using safe levels of RF irradiation. Thus, the inverse problem that we want to solve is a linear acoustic-wave equation.

The pressure $p(\mathbf{r}, t)$ at position $\mathbf{r}$ and time t in an acoustically homogeneous medium in response to a heat source $H(\mathbf{r}, t)$ obeys the following equation [5], [23]:

$$\nabla^2 p(\mathbf{r}, t) - \frac{1}{c^2}\frac{\partial^2}{\partial t^2} p(\mathbf{r}, t) = -\frac{\beta}{C_p}\frac{\partial}{\partial t} H(\mathbf{r}, t) \tag{1}$$

where C_p is the specific heat, $H(\mathbf{r}, t)$ is the heating function defined as the thermal energy deposited by the energy source per time and volume, β is the isobaric volume expansion coefficient, and c is the speed of sound. The heating function can be written as the product of a spatial absorption function and a temporal illumination function of the RF source

$$H(\mathbf{r}, t) = A(\mathbf{r}) I(t). \tag{2}$$

As discussed in Section I, the short RF pulse can be regarded as a Dirac delta function

$$I(t) = \delta(t). \tag{3}$$

Substituting (2) and (3) into (1) and taking the Fourier transform on variable $\bar{t} = ct$ of (1), one gets

$$(\nabla^2 + k^2)\tilde{p}(\mathbf{r}, k) = ikc^2\eta A(\mathbf{r}) \tag{4}$$

where $\eta = \beta / C_p$, and the following Fourier transform pair exists:

$$\tilde{p}(\mathbf{r}, k) = \int_{-\infty}^{+\infty} p(\mathbf{r}, \bar{t}) \exp(ik\bar{t}) d\bar{t}, \tag{5}$$

$$p(\mathbf{r}, \bar{t}) = \frac{1}{2\pi} \int_{-\infty}^{+\infty} \tilde{p}(\mathbf{r}, k) \exp(-ik\bar{t}) dk \tag{6}$$

where the acoustic wave number $k = \omega / c$ and ω is the angular frequency and equal to $2\pi f$; and $\tilde{p}(\mathbf{r}, k)$ is the frequency spectrum of the thermoacoustic signal $p(\mathbf{r}, \bar{t})$. Equation (4) is a nonhomogeneous Helmholtz equation. Assume that the thermoacoustic signals are measured on a surface S_0 that encloses the sample under study, the frequency spectrum of the thermoacoustic pressure measured at the position $\mathbf{r}_0$ on surface S_0 can be expressed as [22]

$$\tilde{p}(\mathbf{r}_0, k) = -ikc^2\eta \iiint_V d^3r A(\mathbf{r}) \tilde{G}_k(\mathbf{r}, \mathbf{r}_0) \tag{7}$$

where $\tilde{G}_k(\mathbf{r}, \mathbf{r}_0)$ is the Green's function of the nonhomogeneous equation

$$(\nabla^2 + k^2)\tilde{G}_k(\mathbf{r}, \mathbf{r}_0) = -\delta(\mathbf{r} - \mathbf{r}_0). \tag{8}$$

In general, Green's function in three dimensions can be written as [22]

$$\tilde{G}_k(\mathbf{r}, \mathbf{r}_0) = \frac{\exp(ik|\mathbf{r} - \mathbf{r}_0|)}{4\pi|\mathbf{r} - \mathbf{r}_0|}. \tag{9}$$

Now, the inverse problem is to reconstruct the absorption distribution $A(\mathbf{r})$ from a set of data $p(\mathbf{r}_0, t)$ or $\tilde{p}(\mathbf{r}_0, k)$ measured at position $\mathbf{r}_0$. Equation (7) shows a linear mapping connecting $A(\mathbf{r})$ and $\tilde{p}(\mathbf{r}_0, k)$. The solution of $A(\mathbf{r})$ can be expected in a similar form—a linear integral

$$A(\mathbf{r}) = \iint_{S_0} dS_0 \int_k dk \tilde{p}(\mathbf{r}_0, k) \tilde{K}_k(\mathbf{r}_0, \mathbf{r}) \tag{10}$$

where $dS_0 = d^2\mathbf{r}_0$, S_0 is the total recording surface, and the integral kernel $\tilde{K}_k(\mathbf{r}_0, \mathbf{r})$ needs to be determined. As shown in Section III, the integral kernel is complicated. But under most practical conditions, as discussed below, it can be simplified to a linear relation with the Green's function.

The greatest challenge is to detect small (compared with measurement geometry) but deeply buried targets inside the tissue. Let us check the property of the frequency spectrum of acoustic waves generated from a small object. Assume there is a homogeneous RF absorption sphere with a size of $2a$ in diameter, i.e., the spatial absorption function $A(\mathbf{r}) = U(a - r)$, where the step function $U(\xi) = 1, \xi \geq 0$ and $U(\xi) = 0, \xi < 0$. With a $\delta(t)$ RF illumination, the radiated acoustic wave from this sphere can be expressed as $p(r, t) = \eta c^2 U(a - |r - ct|)(r - ct)/(2r)$ [23]. Applying the Fourier transform gives the frequency spectrum $\sim j_1(ka)$, where $j_1(ka)$ is the spherical Bessel function of the first kind. The main beam of the above spectrum is in a belly shape with maximum amplitude at the central frequency $f_c \approx 0.7c/(2a)$. For example, for an object with a size of 1 mm, $f_c = 0.7 \times 1.5\ (\text{mm}/\mu\text{s})/(1\ \text{mm}) \approx 1$ MHz. Below 100 KHz, the spectrum amplitude is less than 0.1 of the maximum value, and particularly at 0 Hz, the spectrum amplitude is zero, which can be proved using (7) letting $k = 0$. In general, the frequency spectrum of acoustic waves generated from a small object concentrates in the relatively high-frequency region. The dominating frequency or central frequency f_c can be approximated by the reciprocal of the required time τ for an acoustic wave to traverse the object length l, i.e., $f_c \approx 1/\tau = c/l$. In addition, the boundaries of large objects can also be regarded as small structures, which are also determined by relatively high-frequency signals. In other words, only the relatively high-frequency thermoacoustic signals can restore small absorbers as well as the boundaries of big absorbers.

During measurement, the transducer for ultrasonic imaging [16] can be employed to receive thermoacoustic signals. The ideal transducer for receiving ultrasound would have a wide dynamic range and a wide frequency response. Most commonly, transducers are operated over a band of frequencies containing a resonant frequency, which is determined by the physical property of the transducer [16]. A transducer with a resonant or central frequency of 1–3 MHz could be perfectly matched to millimeter-sized small absorbers in soft tissues. The real-time localization of targets should employ transducer arrays, in which all of the small elements serve independent ultrasound detectors and simultaneously receive thermoacoustic signals at different positions around the investigated tissue [16]. Currently, a linear or circular array with hundreds of small elements, in which each element has a size of ~sub-mm with a total length of perhaps ~10 cm, is available on the market or can be customized and manufactured in a research lab [16]. In addition, the measurement geometry is relatively big compared with the small targets. For example, when using a spherical measurement configuration with a radius $r_0 = 5$ cm, even at $f = 100$ KHz, $kr_0 \approx 20 \gg 1$. In another example, for a target inside a tissue with a distance to the nearest detection element $d = 1$ cm, at $f = 1$ MHz, $kd \approx 40 \gg 1$ and even at $f = 100$ KHz, $kd \approx 4 > 1$.

Therefore, for practical applications, we introduce the following two conditions: the high-frequency components of the thermoacoustic signals contribute more to the spatial resolution than the low-frequency ones, and the detecting distances between the thermoacoustic sources and the detecting transducers are much larger than the wavelengths of the high-frequency thermoacoustic signals. Taking these conditions into account, we will simplify the rigorous formulas and present time-domain reconstruction algorithms in the following sections.

III. RECONSTRUCTION FORMULAS

A. Planar Measurement Configuration

The Cartesian coordinate system $\mathbf{r} = (x, y, z)$ suits this situation. As shown in Fig. 1(a), we assume that the measurement surface is the $z = 0$ plane, i.e., $\mathbf{r}_0 = (x_0, y_0, 0)$. The sample lies above the plane, i.e., $A(\mathbf{r}) = A(x, y, z)$ where $z > 0$ and $A(\mathbf{r}) = 0$ when $z < 0$. Taking Fourier transforms on both sides of (8) on variables x, y and z, it can be shown that the Green's function is a triple Fourier integral [22]

$$\widetilde{G}_k(\mathbf{r},\mathbf{r}_0) = \frac{1}{(2\pi)^3}\iiint_{-\infty}^{+\infty} dK_x dK_y dK_z \cdot \frac{\exp\left[iK_x(x_0-x)+iK_y(y_0-y)-iK_z z\right]}{K_x^2+K_y^2+K_z^2-k^2}. \quad (11)$$

Considering the above expansion, and referencing the mathematical techniques in Norton's work on ultrasonic reflectivity imaging [24], we can derive a rigorous reconstruction formula in the form of (10) as (see Appendix A)

$$A(x,y,z) = \iint_{-\infty}^{+\infty} dx_0 dy_0 \int_{-\infty}^{+\infty} dk\, \widetilde{p}(x_0,y_0,k)\widetilde{K}_k(\mathbf{r}_0,\mathbf{r}) \quad (12)$$

with

$$\widetilde{K}_k(\mathbf{r}_0,\mathbf{r}) = \frac{1}{4\pi^3 c^2 \eta}\iint_{\rho=0}^{\rho=|k|} du\,dv \exp\left[-iz\,\mathrm{sgn}(k)\sqrt{k^2-\rho^2}\right] \cdot \exp[iu(x_0-x)+iv(y_0-y)] \quad (13)$$

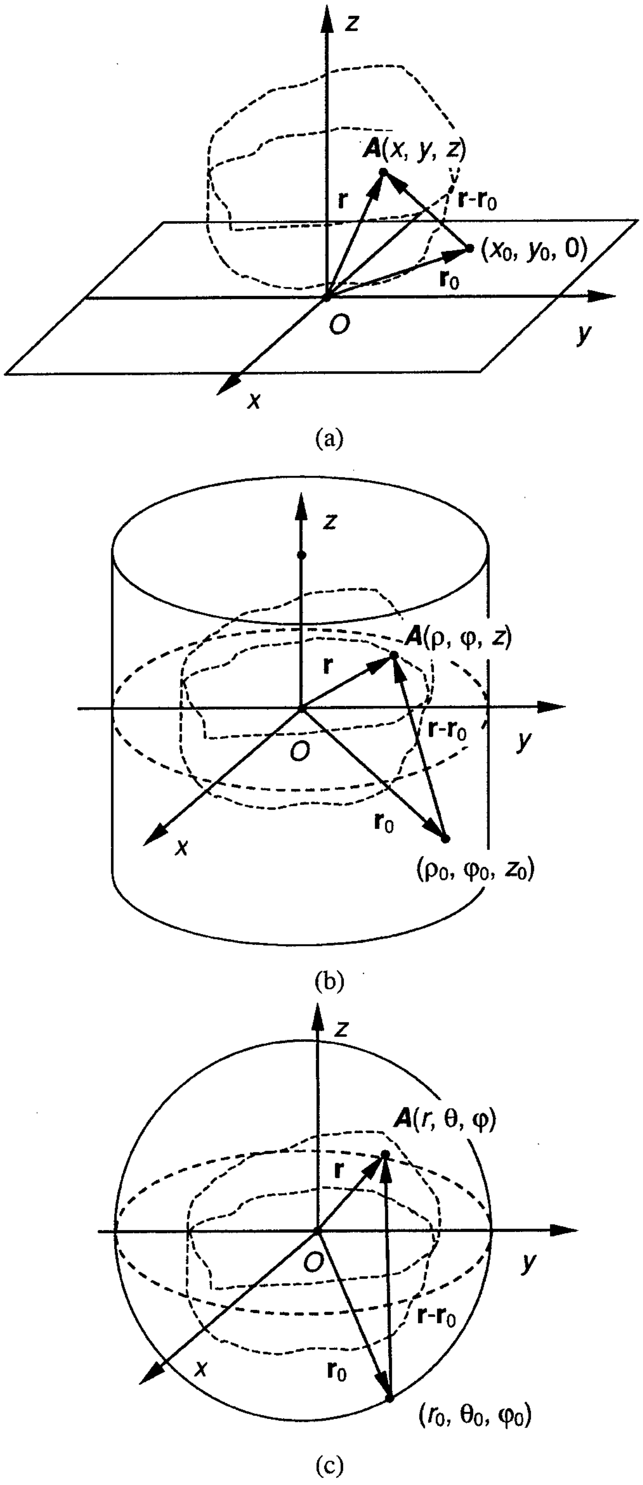

Fig. 1. Diagram of the measurement: (a) planar measurement configuration, (b) cylindrical measurement configuration, and (c) spherical measurement configuration.

where $\rho = \sqrt{u^2+v^2}$, and the sign function: $\mathrm{sgn}(k) = 1$ if $k > 0$, and $\mathrm{sgn}(k) = -1$ if $k < 0$.

Under the condition $|k||\mathbf{r}-\mathbf{r}_0| \gg 1$, which means that the detecting distances between the thermoacoustic sources and the detecting transducers are much greater than the wavelengths of the thermoacoustic signals that are useful for imaging, (13) reduces to (see Appendix A)

$$\widetilde{K}_k(\mathbf{r}_0,\mathbf{r}) \approx \frac{i2k}{\pi c^2\eta}\frac{z}{|\mathbf{r}-\mathbf{r}_0|}\widetilde{G}_k^*(\mathbf{r},\mathbf{r}_0), \tag{14}$$

where "$*$" stands for the complex conjugate.

It can be shown that $\mathbf{n}\cdot\mathbf{n}_0 = z/|\mathbf{r}-\mathbf{r}_0|$, where $\mathbf{n}$ and $\mathbf{n}_0$ are unit vectors pointing along the z axis and along the line joining $\mathbf{r}$ and $\mathbf{r}_0$, respectively. Substituting (14) into (12), we get

$$\begin{aligned} A(\mathbf{r}) &= \iint_{S_0} dS_0 \int_{-\infty}^{+\infty} dk \frac{i2k}{\pi c^2\eta}\widetilde{p}(\mathbf{r}_0,k)\widetilde{G}_k^*(\mathbf{r},\mathbf{r}_0)[\mathbf{n}\cdot\mathbf{n}_0] \\ &= -\frac{1}{\pi c^2\eta}\iint_{S_0} dS_0\cdot\frac{1}{2\pi}\int_{-\infty}^{+\infty} dk(-ik)\widetilde{p}(\mathbf{r}_0,k) \\ &\quad\times\frac{\exp(-ik|\mathbf{r}-\mathbf{r}_0|)}{|\mathbf{r}-\mathbf{r}_0|}[\mathbf{n}\cdot\mathbf{n}_0] \end{aligned} \tag{15}$$

where $dS_0 = dx_0dy_0$. Recalling the inverse Fourier transform of (6), (15) reduces to

$$A(\mathbf{r}) = -\frac{1}{\pi c^4\eta}\iint_{S_0} dS_0[\mathbf{n}\cdot\mathbf{n}_0]\frac{1}{t}\left.\frac{\partial p(\mathbf{r}_0,t)}{\partial t}\right|_{t=\frac{|\mathbf{r}_0-\mathbf{r}|}{c}}. \tag{16}$$

This is a modified back projection formula of quantity $-(1/t)(\partial p(\mathbf{r}_0,t)/\partial t)$ with a weighting factor $[\mathbf{n}\cdot\mathbf{n}_0]$. The required condition is $|k||\mathbf{r}-\mathbf{r}_0| >> 1$.

B. Cylindrical Measurement Configuration

In this case, a circular cylindrical coordinate system $\mathbf{r} = (\rho,\varphi,z)$ is convenient. As shown in Fig. 1(b), we assume that the measurement surface is a circular cylindrical surface $\mathbf{r}_0 = (\rho_0,\varphi_0,z_0)$. The sample (of a finite size) lies inside the cylinder. The Green's function can be expressed in the cylindrical coordinates ($k > 0$) (see Appendix B for detail)

$$\begin{aligned} \widetilde{G}_k(\mathbf{r},\mathbf{r}_0) &= \frac{1}{4\pi^2}\sum_{m=-\infty}^{+\infty}\exp[im(\varphi-\varphi_0)] \\ &\quad\cdot\int_{-\infty}^{+\infty} dk_z\exp[ik_z(z-z_0)]\,g_{mk}(\rho,\rho_0,k_z) \end{aligned} \tag{17}$$

where if $k_z^2 < k^2$, $g_{mk}(\rho,\rho_0,k_z) = (i\pi/2)J_m(\mu\rho)H_m^{(1)}(\mu\rho_0)$ with $\mu = \sqrt{k^2-k_z^2}$; if $k_z^2 > k^2$, $g_{mk}(\rho,\rho_0,k_z) = I_m(-i\mu\rho)K_m(-i\mu\rho_0)$ with $\mu = i\sqrt{k_z^2-k^2}$. $J_m(\cdot)$, $H_m^{(1)}(\cdot)$, $I_m(\cdot)$ and $K_m(\cdot)$ are the Bessel function of the first kind, the Hankel function of the first kind, the modified Bessel function of the first kind, and the modified Bessel function of the second kind, respectively.

After some deduction (see Appendix B), we get the reconstruction formula in the form of (10) as

$$A(\rho,\varphi,z) = \iint_{S_0} dS_0\int_0^{+\infty} dk\widetilde{p}(\mathbf{r}_0,k)\widetilde{K}_k(\mathbf{r}_0,\mathbf{r}) \tag{18}$$

where $dS_0 = \rho_0d\varphi_0dz_0$, and

$$\begin{aligned} \widetilde{K}_k(\mathbf{r}_0,\mathbf{r}) &= \frac{1}{2\pi^3c^2\eta\rho_0}\int_{-k}^{+k} d\gamma\exp[i\gamma(z_0-z)] \\ &\quad\cdot\sum_{n=-\infty}^{+\infty}\exp[in(\varphi_0-\varphi)]\frac{J_n(\rho\sqrt{k^2-\gamma^2})}{H_n^{(1)}(\rho_0\sqrt{k^2-\gamma^2})}. \end{aligned} \tag{19}$$

Under the conditions introduced in Section II, i.e., $\rho_0k \gg 1$, (19) approximates to (see Appendix B)

$$\widetilde{K}_k(\mathbf{r}_0,\mathbf{r}) \approx \frac{i2k}{\pi c^2\eta}\sqrt{1-\frac{(z_0-z)^2}{|\mathbf{r}-\mathbf{r}_0|^2}}\,\widetilde{G}_k^*(\mathbf{r},\mathbf{r}_0). \tag{20}$$

Adding the complex conjugate of (18) onto itself and then dividing the summation by two, and further considering $\widetilde{p}^*(\mathbf{r}_0,k) = \widetilde{p}(\mathbf{r}_0,-k)$ and the approximation (20), one gets

$$\begin{aligned} A(\rho,\varphi,z) &= \iint_{S_0} dS_0\int_{-\infty}^{+\infty} dk\frac{ik}{c^2\eta\pi}\widetilde{p}(\mathbf{r}_0,k) \\ &\quad\cdot\frac{\exp(-ik|\mathbf{r}-\mathbf{r}_0|)}{4\pi|\mathbf{r}-\mathbf{r}_0|}\sqrt{1-\frac{(z_0-z)^2}{|\mathbf{r}-\mathbf{r}_0|^2}} \\ &= -\frac{1}{2\pi c^2\eta}\iint_{S_0} dS_0\sqrt{1-\frac{(z_0-z)^2}{|\mathbf{r}-\mathbf{r}_0|^2}} \\ &\quad\cdot\frac{1}{2\pi}\int_{-\infty}^{+\infty}(-ik)dk\widetilde{p}(\mathbf{r}_0,k)\frac{\exp(-ik|\mathbf{r}-\mathbf{r}_0|)}{|\mathbf{r}-\mathbf{r}_0|}. \end{aligned} \tag{21}$$

It can be shown that

$$\begin{aligned} \mathbf{n}\cdot\mathbf{n}_0 &= \frac{|\boldsymbol{\rho}-\boldsymbol{\rho}_0|}{|\mathbf{r}-\mathbf{r}_0|} \\ &= \sqrt{\frac{\rho^2+\rho_0^2-2\rho\rho_0\cos(\varphi_0-\varphi)}{|\mathbf{r}-\mathbf{r}_0|^2}} \\ &= \sqrt{1-\frac{(z_0-z)^2}{|\mathbf{r}-\mathbf{r}_0|^2}} \end{aligned} \tag{22}$$

where $\boldsymbol{\rho}$ and $\boldsymbol{\rho}_0$ are the projections of $\mathbf{r}$ and $\mathbf{r}_0$ on z plane, respectively, and $\mathbf{n}$ and $\mathbf{n}_0$ are unit vectors pointing along the line joining $\boldsymbol{\rho}$ and $\boldsymbol{\rho}_0$ and along the line joining $\mathbf{r}$ and $\mathbf{r}_0$, respectively. Recalling the inverse transformation (6), we can rewrite (21) as

$$A(\rho,\varphi,z) = -\frac{1}{2\pi c^4\eta}\iint_{S_0} dS_0[\mathbf{n}\cdot\mathbf{n}_0]\frac{1}{t}\left.\frac{\partial p(\mathbf{r}_0,t)}{\partial t}\right|_{t=\frac{|\mathbf{r}-\mathbf{r}_0|}{c}}. \tag{23}$$

This is a modified back projection formula of quantity $-(1/t)(\partial p(\mathbf{r}_0,t)/\partial t)$ with a weighting factor $[\mathbf{n}\cdot\mathbf{n}_0]$. The required condition is $\rho_0|k| \gg 1$ and $|k||\mathbf{r}-\mathbf{r}_0| \gg 1$.

C. Spherical Measurement Configuration

This instance has been reported in another paper [5]. As a consequence, we only briefly review the results here for completeness.

We use the spherical polar coordinate system $\mathbf{r} = (r, \theta, \varphi)$. As shown in Fig. 1(c), we assume that the recording surface is a spherical surface $\mathbf{r}_0 = (r_0, \theta_0, \varphi_0)$. The sample lies inside the sphere, i.e., $A(\mathbf{r}) = A(r, \theta, \varphi)$ where $r < r_0$ and $A(\mathbf{r}) = 0$ when $r > r_0$. The Green's function can be expanded as a series based on the spherical Bessel function of the first kind $j_l(\cdot)$, the spherical Hankel function of the first kind $h_l(\cdot)$, and the Legendre polynomial $P_l(\cdot)$

$$\widetilde{G}_k(\mathbf{r}, \mathbf{r}_0) = \frac{ik}{4\pi} \sum_{l=0}^{\infty} (2l+1) j_l(kr) h_l^{(1)}(kr_0) P_l(\mathbf{n} \cdot \mathbf{n}_0), \ (k>0) \tag{24}$$

where $\mathbf{n} = \mathbf{r}/r$, and $\mathbf{n}_0 = \mathbf{r}_0/r_0$.

We find the rigorous reconstruction formula as

$$A(r, \theta, \varphi) = \iint\limits_{S_0} dS_0 \int_0^{+\infty} dk \widetilde{p}(\mathbf{r}_0, k) \widetilde{K}_k(\mathbf{r}_0, \mathbf{r}) \tag{25}$$

where $dS_0 = r_0^2 \sin\theta_0 d\theta_0 d\varphi_0$, and

$$\widetilde{K}_k(\mathbf{r}_0, \mathbf{r}) = \frac{1}{2\pi^2 c^2 \eta r_0^2} \sum_{m=0}^{\infty} \frac{(2m+1) j_m(kr)}{h_m^{(1)}(kr_0)} P_m(\mathbf{n} \cdot \mathbf{n}_0). \tag{26}$$

Under the condition $kr_0 \gg 1$, one can approximate

$$\widetilde{K}_k(\mathbf{r}_0, \mathbf{r}) \approx \frac{i2k}{\pi c^2 \eta} \widetilde{G}_k^*(\mathbf{r}, \mathbf{r}_0). \tag{27}$$

Adding the complex conjugate of (25) onto itself and then dividing the summation by two, and further considering $\widetilde{p}^*(\mathbf{r}_0, k) = \widetilde{p}(\mathbf{r}_0, -k)$ and the approximation (27), we get

$$A(r, \theta, \varphi) = -\frac{1}{2\pi c^2 \eta} \iint\limits_{S_0} dS_0 \cdot \frac{1}{2\pi} \int_{-\infty}^{+\infty} dk \widetilde{p}(\mathbf{r}_0, k)(-ik) \frac{\exp(-ik|\mathbf{r}_0 - \mathbf{r}|)}{|\mathbf{r}_0 - \mathbf{r}|}. \tag{28}$$

Recalling the inverse Fourier transform (6), (28) reduces to

$$A(r, \theta, \varphi) = -\frac{1}{2\pi c^4 \eta} \iint\limits_{S_0} dS_0 \frac{1}{t} \left. \frac{\partial p(\mathbf{r}_0, t)}{\partial t} \right|_{t = \frac{|\mathbf{r}_0 - \mathbf{r}|}{c}}. \tag{29}$$

Equation (29) shows that the absorption distribution can be calculated by means of back projection of the quantity $-(1/t)(\partial p(\mathbf{r}_0, t)/\partial t)$. The required condition is $|k| r_0 \gg 1$.

As expected, all of the reconstruction formulas—(16) for the planar measurement configuration, (23) for the cylindrical measurement configuration, and (29) for the spherical measurement configuration—can be carried out in the time domain. They share a similar expression, except for the weighting factor $[\mathbf{n} \cdot \mathbf{n}_0]$. These formulas can be referred to as modified back-projections. Compared with (16), (23) and (29) have an additional factor 1/2. This is because the planar measurement configuration can cover a solid angle of up to 2π only while the other two configurations can cover a full 4π solid angle.

IV. NUMERICAL EXPERIMENTS

Now we want to conduct some numerical experiments to demonstrate the validity of the above time-domain reconstruction formulas for thermoacoustic imaging.

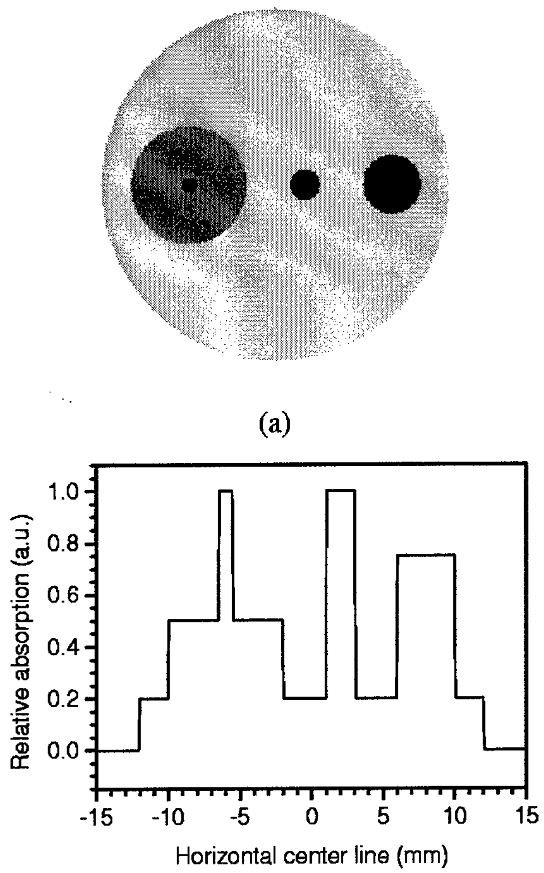

(a)

(b)

Fig. 2. Original sample. (a) Cross-sectional image. (b) Profile along the horizontal center line.

We consider uniform spherical absorbers surrounded by a nonabsorbing background medium. For convenience, we use the centers of the absorbers to denote their positions. The uniform spherical absorber can be written as $A(\mathbf{r}) = A_0 U(a - |\mathbf{r} - \mathbf{r}_a|)$, where A_0 is the absorption intensity, and a and $\mathbf{r}_a$ are the radius and the center of the sphere, respectively. As shown in Fig. 2(a), assume a sample contains five spherical absorbers with different absorption intensities and the centers of these spheres lie in a line parallel to the x axis. For convenience, we call this line the horizontal center line. As shown in Fig. 2(b), from the smallest to the biggest, the radii are 0.5, 1, 2, 4, and 12 mm, respectively, and the relative absorption intensities are 1, 1, 0.75, 0.5, and 0.2, respectively. We also assume that the RF pulse duration is very short and can be regarded as a delta function, and, consequently, that the thermoacoustic signal $p(\mathbf{r}_0, t)$ irradiated from a uniform sphere can be calculated by $\eta c^2 U(a - |R - ct|)(R - ct)/(2R)$, where R is the distance between the detection position $\mathbf{r}_0$ and the absorber center $\mathbf{r}_a (R = |\mathbf{r}_0 - \mathbf{r}_a|)$ [23]. The quantity $\partial p(\mathbf{r}_0, t)/\partial t$ in the reconstruction formulas (16), (23), and (29) can be calculated through the Fourier transform

$$\frac{\partial p(\mathbf{r}_0, t)}{\partial t} = \text{IFFT}\left\{-i\omega p(\mathbf{r}_0, \omega) W_\Omega(\omega)\right\} \tag{30}$$

where IFFT denotes the inverse fast Fourier transform, $W_\Omega(\omega)$ is a window function, and the Fourier transform defines

$$\bullet(\omega) = \int_{-\infty}^{+\infty} \bullet(t)\exp(i\omega t)dt. \tag{31}$$

As we discussed in [6], the factor ω in (30) actually represents a pure ramp filter, which will significantly depress the low-frequency signal. It is helpful for guaranteeing the validity of the reconstruction (16), (23), and (29). It also indicates that the relatively high-frequency component of the signals play the primary role in the restoration of the RF absorption distribution inside the tissue. But, the ramp filter can also amplify the high-frequency noise in such a way that the reconstructed image is not acceptable from the physical point of view. In order to avoid this effect, it is necessary to introduce a relatively low-pass filter $W_\Omega(\omega)$ characterized by a cutoff angular frequency $\Omega = 2\pi f_\Omega$. A Hanning window is our choice in this case

$$W_\Omega(\omega) = \begin{cases} 0.5 + 0.5\cos\left(\pi\frac{\omega}{\Omega}\right), & \text{if } |\omega| < \Omega, \\ 0, & \text{otherwise.} \end{cases} \tag{32}$$

In addition, $W_\Omega(\omega)$ also reflects the limited bandwidth of the detected thermoacoustic signals that is due to the finite bandwidth of the detector. We assume the thermoacoustic waves to be in a frequency range below 4 MHz, and choose $f_\Omega = 4$ MHz; then the dominative frequency in $\omega W_\Omega(\omega)$ is 1.7 MHz. Here, the data sampling frequency is 20 MHz.

A. Planar Measurement Configuration

We use the planar measurement configuration as shown in Fig. 1(a). Assume that the measurement area is 120 mm × 120 mm in the $z = 0$ plane and that the thermoacoustic signals are collected at 3600 total detection positions that are evenly distributed in the measurement area. Such a measurement can be realized by using a rectangular ultrasonic array or by scanning a linear array or even by scanning a single detector to cover the measurement area. The center of the measurement area is (0, 0, 0). The sample center (0, 0, 30) lies 30 mm above the measurement area. Fig. 3(a) shows the reconstructed RF absorption distribution of the $z = 30$ mm plane, and Fig. 3(b) shows the comparison of the original and reconstructed absorption profiles along the horizontal center line.

B. Cylindrical Measurement Configuration

We employ the cylindrical measurement configuration as shown in Fig. 1(b). Assume the measurement area is a cylindrical surface with a length of 90 mm and a radius of 50 mm. One can use a linear ultrasound array, which is vertically placed and has 30 elements evenly distributed a length of 90 mm, to horizontally scan the sample, with a step size of 3° to cover the measurement area. One can also vertically scan a circular ultrasound array with a step size of 3 mm, where the circular array may have 120 elements evenly distributed in the array. In these ways, the measurement covers 3600 detection positions, which are approximately evenly distributed in the measurement area. The sample center lies at (0, 0, 0), the center of the measurement cylindrical surface. Fig. 4(a) shows the reconstructed RF absorption distribution in the $z = 0$ mm plane and Fig. 4(b) shows the comparison of the original and reconstructed absorption profiles along the horizontal center line.

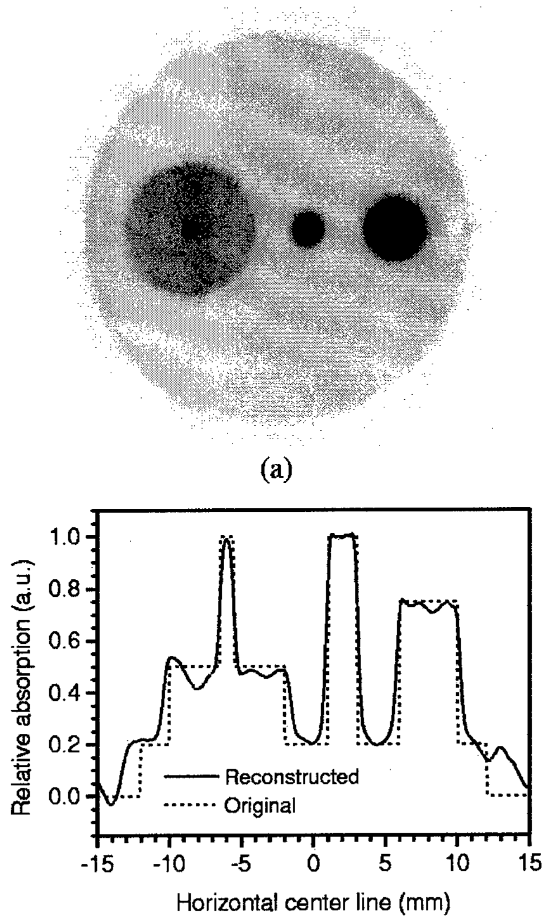

(b)

Fig. 3. Reconstructed image from planar measurement configuration using 3600 detector positions with high cutoff frequency 4 MHz. (a) Cross-sectional image at the $z = 30$ mm plane. (b) Comparison of the original and reconstructed absorption profiles along the horizontal center line.

C. Spherical Measurement Configuration

Fig. 1(c) shows the spherical measurement configuration. To simulate a practical condition, we adopt only a half-spherical measurement area in the upper half space ($z > 0$). Suppose a quarter circular array has 30 elements and the radius of the array is 50 mm. Then one can rotationally scan the array along its radius with a step size of 3° to cover a half spherical measurement area. In this way, the, the measurement contains 3600 detection positions, which are approximately evenly distributed in the measurement area. The sample center lies (0, 0, 12 mm) inside the measurement surface. Fig. 5(a) shows the reconstructed RF absorption distribution of the $z = 12$ mm plane, and Fig. 5(b) shows the comparison of the original and reconstructed absorption profiles along the horizontal center line.

The above examples demonstrate the performance of the time-domain formulas for different measurement configurations. The reconstructed profiles are in good agreement with the original distributions. As mentioned before, with a cutoff

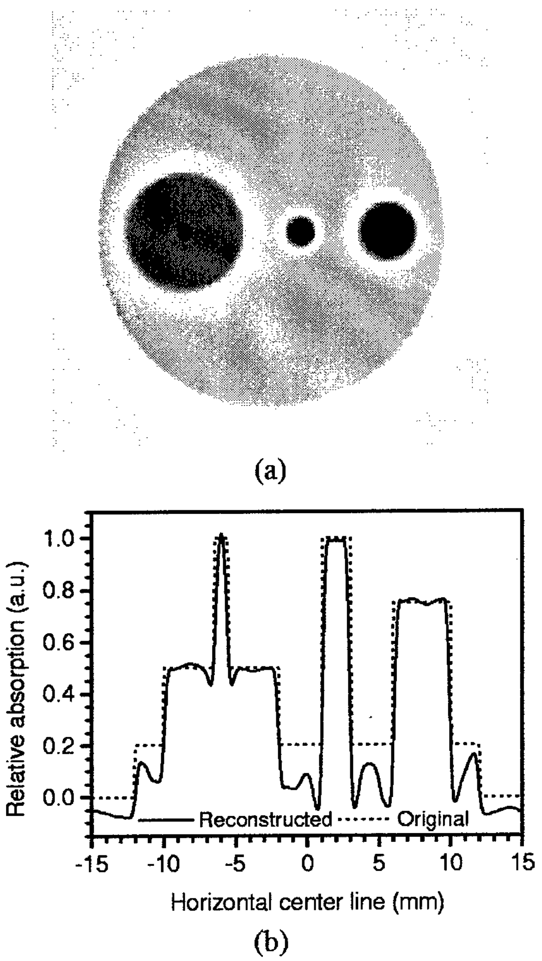

Fig. 4. Reconstructed image from cylindrical configuration using 3600 detector positions with high cutoff frequency 4 MHz. (a) Cross-sectional image at the $z = 0$ mm plane. (b) Comparison of the original and reconstructed absorption profiles along the horizontal center line.

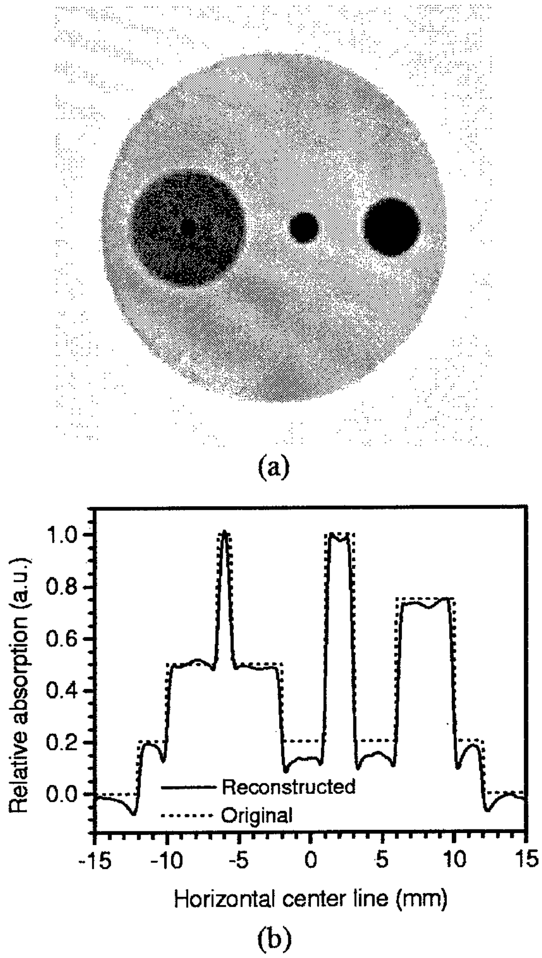

Fig. 5. Reconstructed image from spherical measurement configuration using 3600 detector positions with high cutoff frequency 4 MHz. (a) Cross-sectional image at the $z = 12$ mm plane. (b) Comparison of the original and reconstructed absorption profiles along the horizontal center line.

frequency $f_\Omega = 4$ MHz, the dominative frequency in $\omega W_\Omega(\omega)$ is 1.7 MHz, which corresponds to an acoustic wavelength of 0.9 mm. That explains why the small absorbers, as well as the boundaries of the big absorbers, can be faithfully reconstructed. As predicted, the flat bases of the big absorbers are not faithfully recovered, which results from the approximations of the algorithms.

However, in the absence of a high-frequency signal, the small size structure will be lost. For example, if the cutoff frequency $f_\Omega = 1.5$ MHz, the dominative frequency in $\omega W_\Omega(\omega)$ is about 0.6 MHz, which corresponds to an acoustic wavelength of 2.5 mm. Without loss of generality, we will take the spherical measurement configuration as an example. The other parameters in the numerical experiment are the same as the example shown in Fig. 5. As shown in Fig. 6, not only is the small absorber nearly corrupted, but also the originally sharp borders of the big absorbers are greatly degraded.

Only a small number of detector positions affect the reconstructed images. We will again take the spherical measurement configuration as an example. Suppose a quarter circular array has only eight elements and the radius of the array is 50 mm. One must rotationally scan the array along its radius with a step size of 11.25° to cover a half spherical measurement area. The other parameters in the numerical experiment are the same as in the example shown in Fig. 5. In this way, the measurement has only 256 detection positions. As shown in Fig. 7, the main structure of the sample is recovered in the reconstructed image, but a lot of noisy artifacts occur.

In addition, the signal-to-noise ratio (SNR) should be carefully considered in thermoacoustic imaging, since the amplitude of the thermoacoustic signal is small as was mentioned in Section I. In general, white noise can be suppressed by averaging over many identical data acquisitions. Denoising can also be accomplished with more elaborate methods including Fourier-based filtering and wavelet-based filtering [25]. Fortunately, reconstruction in thermoacoustic imaging is a linear addition process as shown in (16), (23), and (29). The white noise in each detector is independent of every other. If there are n detectors, the SNR in the image will be improved by the square root of n times through summation of the data. Of course, more detectors and more data acquisitions will increase the cost of the data acquisition time as well as the detection equipment. Actu-

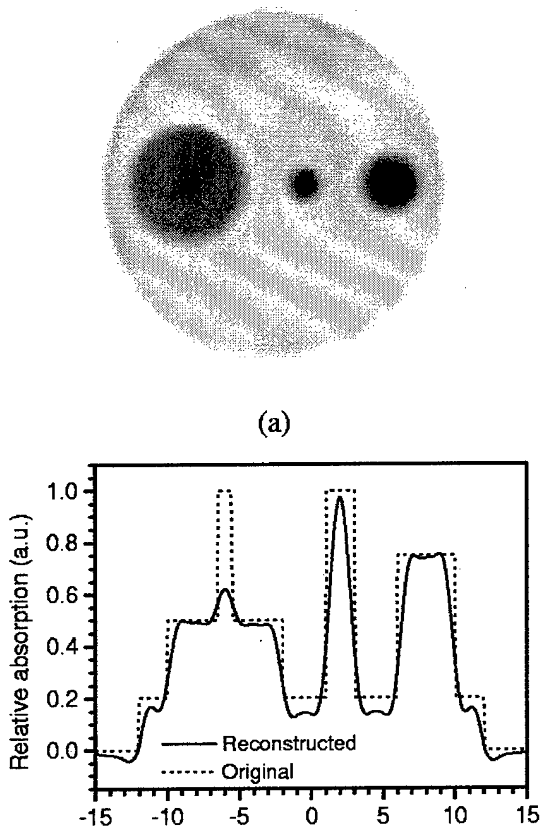

(a)

(b)

Fig. 6. Reconstructed image from spherical measurement configuration using 3600 detector positions with high cutoff frequency 1.5 MHz. (a) Cross-sectional image at the $z = 12$ mm plane. (b) Comparison of the original and reconstructed absorption profiles along the horizontal center line.

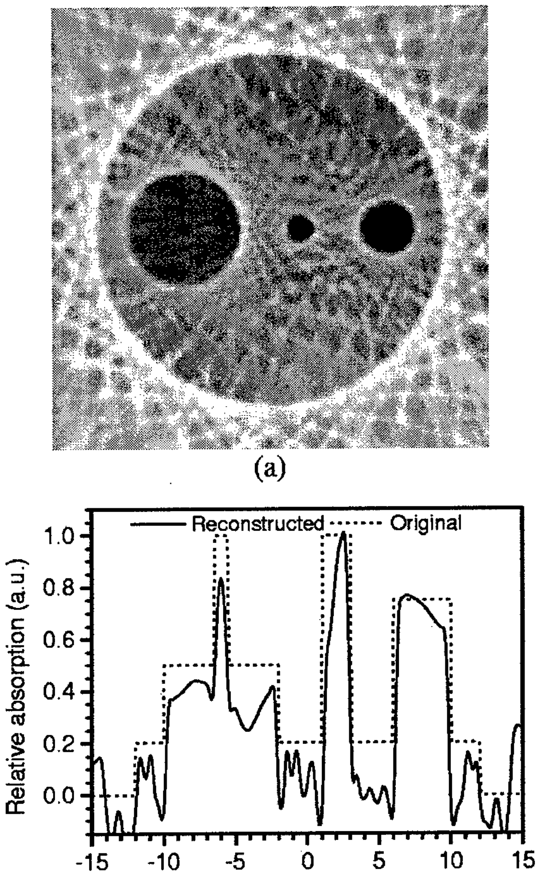

(a)

(b)

Fig. 7. Reconstructed image from spherical measurement configuration using 256 detector positions with high cutoff frequency 4 MHz. (a) Cross-sectional image at the $z = 12$ mm plane. (b) Comparison of the original and reconstructed absorption profiles along the horizontal center line.

ally, as with other imaging modalities, such as magnetic resonance imaging, there is a tradeoff between SNR and the cost of data acquisition time and equipment.

In the above simulations, we consider the point-detectors. In fact, a finite detector area will limit the lateral spatial resolution and affect the axial resolution slightly [6]. A complete analytical explanation of spatial resolution related to bandwidth and detector aperture size will be reported in another paper [26].

V. PRACTICAL APPLICATIONS

The time-domain reconstruction formulas—termed modified back projections—can be derived under the practical conditions discussed above. We have shown that modified back projection formulas closely approximate the rigorous formulas under the above conditions. Unlike the filtered back projection algorithm used in X-ray tomography, which uses the surface integration over intersecting planes, the modified formulas in our problems are calculated through temporal back projection and coherent summation over spherical surfaces with certain spatial weighting factors. Fortunately, due to the advantage of coherent summation, these formulas are still applicable to practical conditions with a finite extension or partial enclosure even though they are derived from idealized recording surfaces. Of course, finite recording surfaces only provide limited spatial views, but that is adequate in practical applications.

The planar, spherical, and cylindrical recording surfaces may cover most measurement configurations. Among them the planar measurement geometry may be the easiest to implement. A two-dimensional (2-D) planar ultrasonic transducer array can be used to detect the thermoacoustic signals as in conventional ultrasound imaging. For example, Hoelen *et al.* [10] used this kind of recording geometry in their photoacoustic imaging. They adopted a delay-and-sum algorithm with experiential weighting factors, which worked well in dealing with their experimental data. Our research shows that the spatial weighting factor $[\mathbf{n}, \mathbf{n}_0]$ does exist in the back projection formula of (16) for the planar recording configuration. This is an interesting result in our theoretical analysis, which indicates that (16) should be a more accurate form than the one used by Hoelen *et al.*.

The spherical recording configuration may be more suitable for external organ imaging such as breast cancer detection where in practice, only a semispherical measurement surface can be implemented. For example, Kruger *et al.* employed this kind of measurement geometry [7]. In their experimental system, multiple discrete transducers were mounted on a hemispherical bowl and could scan nearly a 2π solid angle surrounding the breast volume. In the data processing, they assumed that the size of a typical absorbing object was much smaller than the detecting distance, and that the spherical surface, on which the surface integral was computed, approximated a plane. Therefore, the inverse Radon transform was approximately used to reconstruct the image as in X-ray tomography. Obviously, the above far-field condition is not strict, especially when the absorption source is far away from the center of the spherical geometry and results in reconstruction artifacts. Our theoretical analysis gives a more reasonable reconstruction formula (29), which can improve the quality of the reconstructed images.

The cylindrical recording configuration partially combines the properties of planar geometry and of spherical geometry. The reconstruction formula (23) shows a spatial weighting factor $[\mathbf{n}, \mathbf{n}_0] \leq 1$, which is dependent on $|z - z_0|$. The weighting factor reaches the maximum value $[\mathbf{n}, \mathbf{n}_0] = 1$ at $z = z_0$, which indicates that the cross-sectional image of any z_0 plane is primarily determined by the data measured on the circle of the same plane. For example, if some small strong absorption sources at a size of several millimeters lie on the z_0 plane inside a weak absorption background at a size of several centimeters in diameter, a set of circular measurement data detected on a circle with a radius of several centimeters on the z_0 plane would be sufficient to yield a good cross-sectional image. In our initial work [5], [6], we used this kind of circular measurement to investigate some phantom samples and the reconstructed images agreed with the samples very well. But, if there are other absorbers outside the z_0 plane, the thermoacoustic signals from these absorbers also reach the detectors in the z_0 plane. Thus, a set of circular measurement data on the z_0 plane only could not distinguish between the absorbers on or outside of the plane. In this case, three-dimensional measurement and reconstruction must be used.

In fact, the choice of measurement configuration depends on the practical needs. From the physical point of view, these reconstruction formulas, (16), (23), and (29) for planar, cylindrical, and spherical configurations, respectively, are the same, except that the spatial weighting factors resulted from the measurement geometries. In addition, the weighting factors in the above equations are obtained through first-order approximations. In principle, high-order approximations can be derived.

Finally, it has to be pointed out that an inhomogeneous acoustic property, such as the speed of sound variation, might blur the reconstructed images. The experiments as shown in [5] and [6] demonstrated that the small speed variations between fat and muscle or gelatin did not result in significant reconstruction artifacts. The reason is that thermoacoustic waves are produced internally by RF absorption and are propagated one-way to the detectors. Thus, a small speed variation does not affect the travel time of the sound very much in a finite-length path, for example, 10 cm, which is a typical breast diameter. Therefore, in thermoacoustic tomography, satisfactory contrast and resolution are obtainable even in tissue with a small degree of acoustic inhomogeneity.

VI. CONCLUSION

In this paper, we have presented time-domain reconstruction algorithms for the thermoacoustic imaging of biological tissues. They are computed through temporal back projections and coherent summations over spherical surfaces with certain spatial weighting factors. Numerical experiments have demonstrated the validity of their applications. These formulas (or high-order approximations of the rigorous reconstruction formulas) can serve as the basis for time-domain thermoacoustic or photoacoustic imaging in biological tissues.

APPENDIX A

The delta function can be written in the Cartesian coordinates as

$$\delta(\mathbf{r} - \mathbf{r}_0) = \delta(x - x_0)\delta(y - y_0)\delta(z). \tag{A1}$$

Taking Fourier transforms on both sides of (8) on variables x, y, and z, it can be shown that the Green's function is a triple Fourier integral of (11). If the recording surface S_0 is infinite, we may take 2-D Fourier transforms on x_0 and y_0 of $\tilde{p}(x_0, y_0, k)$, i.e., multiplying both sides of (7) by $\exp(iux_0 + ivy_0)$ and integrating with respect to x_0 and y_0 from $-\infty$ to $+\infty$, one gets

$$\begin{aligned}\iint_{-\infty}^{+\infty} & dx_0 dy_0 \exp(iux_0 + ivy_0)\tilde{p}(x_0, y_0, k) \\ &= \frac{-ikc^2\eta}{2\pi} \int_0^{+\infty} dz \iint_{-\infty}^{+\infty} dx dy A(x, y, z) \exp(iux + ivy) \\ &\quad \cdot \int_{-\infty}^{+\infty} dK_z \frac{\exp(-iK_z z)}{K_z^2 + \rho^2 - k^2}\end{aligned} \tag{A2}$$

where $\rho = \sqrt{u^2 + v^2}$, $(\rho \geq 0)$.

The integral of the far right of (A2) can be computed by the contour integration $(z > 0)$, because there will always be some damping of the wave in a physical system [22], [24]

$$\begin{aligned}\int_{-\infty}^{+\infty} & dK_z \frac{\exp(-iK_z z)}{K_z^2 + \rho^2 - k^2} \\ &= \begin{cases} i\pi \operatorname{sgn}(k) \dfrac{\exp\left[iz \operatorname{sgn}(k)\sqrt{k^2 - \rho^2}\right]}{\sqrt{k^2 - \rho^2}}, & |k| > \rho \\ -\pi \dfrac{\exp\left[-z\sqrt{\rho^2 - k^2}\right]}{\sqrt{\rho^2 - k^2}}, & |k| < \rho \end{cases}\end{aligned} \tag{A3}$$

where $\operatorname{sgn}(k) = 1$ for $k \geq 0$ and $\operatorname{sgn}(k) = -1$ for $k < 0$.

Here, we use the values of k for $|k| > \rho$ to do the reconstruction. Those of k for $|k| < \rho$ correspond to evanescent waves and will have no contribution to the reconstruction.

In the case $|k| > \rho$ and $z > 0$, (A2) becomes

$$\begin{aligned}\iint_{-\infty}^{+\infty} & dx_0dy_0 \exp(iux_0 + ivy_0)\frac{2}{kc^2\eta}\widetilde{p}(x_0, y_0, k)\\ &= \int_{0}^{+\infty} dz \iint_{-\infty}^{+\infty} dxdyA(x, y, z)\exp(iux + ivy)\\ &\quad\cdot \operatorname{sgn}(k)\frac{\exp\left[iz\operatorname{sgn}(k)\sqrt{k^2-\rho^2}\right]}{\sqrt{k^2-\rho^2}}.\end{aligned} \tag{A4}$$

Multiplying both sides of (A4) by $\exp(-iux' - ivy')$ and integrating with respect to u and v letting ρ from 0 to $|k|$, and further multiplying both sides of (A4) by $k\exp\left[-iz'\operatorname{sgn}(k)\sqrt{k^2-\rho^2}\right]$ and integrating with respect to k from $-\infty$ to $+\infty$, gives

$$\begin{aligned}\iint_{-\infty}^{+\infty} & dx_0dy_0 \int_{-\infty}^{+\infty} dk \iint_{\rho=0}^{\rho=|k|} dudv\\ &\times \exp\left[iu(x_0 - x')\right]\exp\left[iv(y_0 - y')\right]\\ &\cdot \frac{2\widetilde{p}(x_0, y_0, k)}{kc^2\eta}k\exp\left[-iz'\operatorname{sgn}(k)\sqrt{k^2-\rho^2}\right]\\ &= \int_{0}^{+\infty} dz \iint_{-\infty}^{+\infty} dxdyA(x, y, z)\\ &\quad\cdot \int_{-\infty}^{+\infty} kdk\operatorname{sgn}(k)\frac{\exp\left[i(z-z')\operatorname{sgn}(k)\sqrt{k^2-\rho^2}\right]}{\sqrt{k^2-\rho^2}}\\ &\quad\cdot \iint_{\rho=0}^{\rho=|k|} dudv\exp\left[iu(x - x')\right]\exp\left[iv(y - y')\right].\end{aligned} \tag{A5}$$

Rearranging the orders of integration of the right-hand side of (A5), we get

$$\begin{aligned}\text{right} &= \int_{0}^{+\infty} dz \iint_{-\infty}^{+\infty} dxdyA(x, y, z)\iint_{-\infty}^{+\infty} dudv\\ &\quad\times \exp\left[iu(x - x')\right]\exp\left[iv(y - y')\right]\\ &\quad\cdot \left[\int_{\rho}^{+\infty} kdk\frac{\exp\left[i(z-z')\sqrt{k^2-\rho^2}\right]}{\sqrt{k^2-\rho^2}}\right.\\ &\qquad\left. + \int_{-\infty}^{-\rho} kdk\frac{\exp\left[-i(z-z')\sqrt{k^2-\rho^2}\right]}{-\sqrt{k^2-\rho^2}}\right].\end{aligned} \tag{A6}$$

If we let $w = \operatorname{sgn}(k)\sqrt{k^2-\rho^2}$, (A6) reduces to

$$\begin{aligned}\text{right} &= \int_{0}^{+\infty} dz \iint_{-\infty}^{+\infty} dxdyA(x, y, z) \cdot \iiint_{-\infty}^{+\infty} dudvdw\\ &\quad\times \exp\left[iu(x - x')\right]\exp\left[iv(y - y')\right]\exp\left[i(z - z')w\right]\\ &= \int_{0}^{+\infty} dz \iint_{-\infty}^{+\infty} A(x, y, z)dxdy\\ &\quad\cdot (2\pi)^3\delta(x - x')\delta(y - y')\delta(z - z')\\ &= (2\pi)^3A(x', y', z').\end{aligned} \tag{A7}$$

Then, substituting (A7) into (A5) and dropping the primes, we get (12) and (13).

Next, we want to show that under certain practical conditions, (12) reduces to a modified back projection formula. Replacing K_x and K_y in (11) with u and v, and then taking complex conjugates of (11) and (A3), one gets

$$\begin{aligned}\widetilde{G}_k^*(\mathbf{r}, \mathbf{r}_0) &= \frac{1}{(2\pi)^3}\iint_{-\infty}^{+\infty} dudv\exp\left[iu(x_0 - x) + iv(y_0 - y)\right]\\ &\quad\cdot \int_{-\infty}^{+\infty} dK_z\frac{\exp(iK_zz)}{K_z^2 + \rho^2 - k^2}\end{aligned} \tag{A8}$$

and

$$\begin{aligned}\int_{-\infty}^{+\infty} & dK_z\frac{\exp(iK_zz)}{K_z^2 + \rho^2 - k^2}\\ &= \begin{cases} -i\pi\operatorname{sgn}(k) & \\ \quad\times\dfrac{\exp\left[-iz\operatorname{sgn}(k)\sqrt{k^2-\rho^2}\right]}{\sqrt{k^2-\rho^2}}, & |k| > \rho,\\ -\pi\dfrac{\exp\left[-z\sqrt{\rho^2-k^2}\right]}{\sqrt{\rho^2-k^2}}, & |k| < \rho.\end{cases}\end{aligned} \tag{A9}$$

Then, substituting (A9) into (A8), taking the first derivative on variable z of (A8) and then making a comparison with (13), one finds

$$\frac{\partial}{\partial z}\widetilde{G}_k^*(\mathbf{r}, \mathbf{r}_0) = -\frac{\pi c^2\eta}{2}\widetilde{K}_k(\mathbf{r}_0, \mathbf{r}) + \widetilde{\varepsilon}_k(\mathbf{r}_0, \mathbf{r}), \tag{A10}$$

where

$$\begin{aligned}\widetilde{\varepsilon}_k(\mathbf{r}, \mathbf{r}_0) &= \frac{1}{8\pi^2}\iint_{\rho=|k|}^{\rho=+\infty} dudv\exp\left[iu(x_0 - x)\right]\\ &\quad\times \exp\left[iv(y_0 - y)\right]\\ &\quad\cdot \exp\left[-z\sqrt{\rho^2 - k^2}\right].\end{aligned} \tag{A11}$$

If letting $u = \rho\cos\psi$, $v = \rho\sin\psi$, $x_0 - x = R\cos\alpha$, and $y_0 - y = R\sin\alpha$, where $\rho = \sqrt{u^2 + v^2}$ and $R = \sqrt{(x_0 - x)^2 + (y_0 - y)^2}$, through changing the variables of integration, using the identity

$$\frac{1}{2\pi}\int_{0}^{2\pi} d\phi\exp\left[i\rho\phi\cos(\phi - \alpha)\right] = J_0(\rho R) \tag{A12}$$

one can rewrite (A11) as

$$\widetilde{\varepsilon}_k(\mathbf{r}, \mathbf{r}_0) = \frac{1}{4\pi}\int_{|k|}^{+\infty} \rho d\rho J_0(\rho R)\exp\left[-z\sqrt{\rho^2 - k^2}\right]. \tag{A13}$$

As [24] shows

$$\begin{aligned}|\widetilde{\varepsilon}_k(\mathbf{r}, \mathbf{r}_0)| \le |\widetilde{\varepsilon}_0(\mathbf{r}, \mathbf{r}_0)| &= \frac{1}{4\pi}\int_{0}^{+\infty} \rho d\rho J_0(\rho R)\exp(-z\rho)\\ &= \frac{z}{4\pi(z^2 + \rho^2)^{\frac{3}{2}}}\\ &= \frac{z}{4\pi|\mathbf{r} - \mathbf{r}_0|^3}.\end{aligned} \tag{A14}$$

However

$$\frac{\partial}{\partial z}\widetilde{G}_k^*(\mathbf{r},\mathbf{r}_0)=\frac{\partial}{\partial z}\left[\frac{\exp\left(-ik|\mathbf{r}-\mathbf{r}_0|\right)}{4\pi|\mathbf{r}-\mathbf{r}_0|}\right] =\frac{-z}{|\mathbf{r}-\mathbf{r}_0|}\left(\frac{1}{|\mathbf{r}-\mathbf{r}_0|}+ik\right)\widetilde{G}_k^*(\mathbf{r},\mathbf{r}_0). \tag{A15}$$

Therefore, under the condition $|k||\mathbf{r}-\mathbf{r}_0|\gg 1$, one gets

$$\left|\frac{\partial}{\partial z}\widetilde{G}_k^*(\mathbf{r},\mathbf{r}_0)\right| > \frac{z|k|}{4\pi|\mathbf{r}-\mathbf{r}_0|^2} \gg \frac{z}{4\pi|\mathbf{r}-\mathbf{r}_0|^3} \geq |\widetilde{\varepsilon}_k(\mathbf{r},\mathbf{r}_0)|. \tag{A16}$$

This means that the evanescent contribution $\widetilde{\varepsilon}$ is negligible when $|k||\mathbf{r}-\mathbf{r}_0|\gg 1$ holds. Then, from (A10), we get

$$\widetilde{K}_k(\mathbf{r}_0,\mathbf{r}) \approx -\frac{2}{\pi c^2\eta}\frac{\partial}{\partial z}\widetilde{G}_k^*(\mathbf{r},\mathbf{r}_0) \approx \frac{i2k}{\pi c^2\eta}\frac{z}{|\mathbf{r}-\mathbf{r}_0|}\widetilde{G}_k^*(\mathbf{r},\mathbf{r}_0). \tag{A17}$$

APPENDIX B

The delta function can be expressed in the circular cylindrical coordinates [22]

$$\begin{aligned}\delta(\mathbf{r}-\mathbf{r}_0) &= \frac{1}{\rho}\delta(\rho-\rho_0)\delta(\varphi-\varphi_0)\delta(z-z_0)\\ &= \frac{1}{\rho}\delta(\rho-\rho_0)\frac{1}{2\pi}\sum_{m=-\infty}^{+\infty}\exp\left[im(\varphi-\varphi_0)\right]\\ &\quad\cdot\frac{1}{2\pi}\int_{-\infty}^{+\infty}\exp\left[ik_z(z-z_0)\right]dk_z.\end{aligned} \tag{B1}$$

Assuming a similar expansion of the Green's function as

$$\widetilde{G}_k(\mathbf{r},\mathbf{r}_0)=\frac{1}{4\pi^2}\sum_{m=-\infty}^{+\infty}\exp\left[im(\varphi-\varphi_0)\right] \int_{-\infty}^{+\infty}dk_z\exp\left[ik_z(z-z_0)\right]\cdot g_{mk}(\rho,\rho_0,k_z). \tag{B2}$$

Substituting (B1) and (B2) into (8), we get

$$\rho^2\frac{d^2g_{mk}}{d\rho^2}+\rho\frac{dg_{mk}}{d\rho}+\left[\left(k^2-k_z^2\right)\rho^2-m^2\right]g_{mk}=-\rho\delta(\rho-\rho_0). \tag{B3}$$

For the $k>0$ case, by letting $\mu=\sqrt{k^2-k_z^2}$, one obtains

$$g_{mk}(\rho,\rho_0,k_z)=\frac{i\pi}{2}J_m(\mu\rho)H_m^{(1)}(\mu\rho_0) \tag{B4}$$

where if $k_z^2>k^2$, $g_{mk}(\rho,\rho_0,k_z)=I_m(-i\mu\rho)K_m(-i\mu\rho_0)$ with $\mu=i\sqrt{k_z^2-k^2}$. Therefore, (7) can be expressed in the following form:

$$\frac{\widetilde{p}(\mathbf{r}_0,k)}{-ikc^2\eta}=\frac{1}{4\pi^2}\iiint_V d^3rA(\mathbf{r})\sum_{m=-\infty}^{+\infty}\exp\left[im(\varphi-\varphi_0)\right] \cdot\int_{-\infty}^{+\infty}dk_z\exp\left[ik_z(z-z_0)\right]g_{mk}(\rho,\rho_0,k_z). \tag{B5}$$

For the idealized cylindrical recording geometry, $\widetilde{p}(\mathbf{r}_0,k)$ is a periodical function of angular variable φ_0 with a 2π period and its extent along z is infinite. Therefore, we may take a series expansion of the recorded data on variable φ_0 and a 1-D Fourier transform on variable z_0. Multiplying both sides of (B5) by $\exp(i\gamma z_0)$ and integrating with respect to z_0 from $-\infty$ to $+\infty$, and further multiplying both sides by $\exp(in\varphi_0)$ and integrating with respect to φ_0 from 0 to 2π, one obtains

$$\begin{aligned}&\int_0^{2\pi}d\varphi_0\int_{-\infty}^{+\infty}dz_0\frac{\widetilde{p}(\mathbf{r}_0,k)}{-ikc^2\eta}\exp(in\varphi_0)\exp(i\gamma z_0)\\ &=\frac{1}{4\pi^2}\iiint_V d^3rA(\mathbf{r})\sum_{m=-\infty}^{+\infty}\exp(im\varphi)\\ &\quad\times\int_0^{2\pi}d\varphi_0\exp\left[i(n-m)\varphi_0\right]\\ &\quad\cdot\int_{-\infty}^{+\infty}dk_z\exp(ik_zz)g_{mk}(\rho,\rho_0,k_z)\\ &\quad\times\int_{-\infty}^{+\infty}dz_0\exp\left[i(\gamma-k_z)\varphi_0\right]\\ &=\frac{1}{4\pi^2}\iiint_V d^3rA(\mathbf{r})\sum_{m=-\infty}^{+\infty}\exp(im\varphi)2\pi\delta_{nm}\\ &\quad\cdot\int_{-\infty}^{+\infty}dk_z\exp(ik_zz)g_{mk}(\rho,\rho_0,k_z)2\pi\delta(\gamma-k_z)\\ &=\iiint_V d^3rA(\mathbf{r})\exp(in\varphi)\\ &\quad\times\exp(i\gamma z)g_{nk}(\rho,\rho_0,\gamma).\end{aligned} \tag{B6}$$

Here we use the values of k for $\gamma^2<k^2$ to do the reconstruction. Those values of k for which $\gamma^2>k^2$ represent the evanescent waves play no role in the reconstruction. In the case of $\gamma^2<k^2$, we can rewrite (B6) as

$$\begin{aligned}&\int_0^{2\pi}d\varphi_0\int_{-\infty}^{+\infty}dz_0\frac{2}{\pi}\frac{\widetilde{p}(\mathbf{r}_0,k)}{kc^2\eta}\\ &\quad\times\exp(in\varphi_0)\exp(i\gamma z_0)=\iiint_V d^3rA(\mathbf{r})\exp(in\varphi)\\ &\quad\times\exp(i\gamma z)J_n(\mu\rho)\\ &\quad\times H_n^{(1)}(\mu\rho_0).\end{aligned} \tag{B7}$$

Multiplying both sides of (B7) by $\mu J_n(\mu\rho')/H_n^{(1)}(\mu\rho_0)$ and integrating them with respect to μ from 0 to $+\infty$, then multiplying both sides by $\exp(-in\varphi')$ and summing n from $-\infty$ to $+\infty$, and further multiplying both sides by $\exp(-i\gamma z')$ and integrating them with respect to γ from $-\infty$ to $+\infty$, one gets

$$\int_0^{2\pi}d\varphi_0\int_{-\infty}^{+\infty}dz_0\int_{-\infty}^{+\infty}d\gamma\exp\left[i\gamma(z_0-z')\right]\int_0^{+\infty}\mu d\mu\frac{2}{\pi}\frac{\widetilde{p}(\mathbf{r}_0,k)}{kc^2\eta} \cdot\sum_{n=-\infty}^{+\infty}\exp\left[in(\varphi_0-\varphi')\right]\frac{J_n(\mu\rho')}{H_n^{(1)}(\mu\rho_0)}$$

$$
\begin{aligned}
&= \int_{-\infty}^{+\infty} dz \int_{0}^{\rho_0} \rho d\rho \int_{0}^{2\pi} d\varphi A(\mathbf{r}) \int_{0}^{+\infty} d\gamma \exp\left[i\gamma(z-z')\right] \\
&\quad \cdot \sum_{n=-\infty}^{+\infty} \exp\left[in(\varphi-\varphi')\right] \int_{0}^{+\infty} \mu d\mu J_n(\mu\rho) J_n(\mu\rho') \\
&= \int_{-\infty}^{+\infty} dz \int_{0}^{\rho_0} \rho d\rho \int_{0}^{2\pi} d\varphi A(\mathbf{r}) \cdot 2\pi\delta(z-z') \\
&\quad \cdot 2\pi\delta(\varphi-\varphi') \cdot \frac{\delta(\rho-\rho')}{\rho} \\
&= (2\pi)^2 A(\rho', \varphi', z'). \qquad \text{(B8)}
\end{aligned}
$$

By dropping the primes, changing the integral variable from μ to k according to $\mu = \sqrt{k^2-\gamma^2}$ and rearranging the orders of the integration, one can rewrite the (B8) as

$$
\begin{aligned}
A(\rho,\varphi,z) &= \frac{1}{2\pi^3} \int_{0}^{2\pi} d\varphi_0 \int_{-\infty}^{+\infty} dz_0 \int_{-\infty}^{+\infty} d\gamma \int_{+|\gamma|}^{+\infty} k dk \frac{\widetilde{p}(\mathbf{r}_0,k)}{kc^2\eta} \\
&\quad \cdot \sum_{n=-\infty}^{+\infty} \exp\left[in(\varphi_0-\varphi)\right] \\
&\quad \times \frac{J_n\left(\rho\sqrt{k^2-\gamma^2}\right)}{H_n^{(1)}\left(\rho_0\sqrt{k^2-\gamma^2}\right)} \exp\left[i\gamma(z_0-z)\right] \\
&= \frac{1}{2\pi^3} \int_{0}^{2\pi} d\varphi_0 \int_{-\infty}^{+\infty} dz_0 \int_{0}^{+\infty} dk \frac{\widetilde{p}(\mathbf{r}_0,k)}{c^2\eta} \\
&\quad \cdot \sum_{n=-\infty}^{+\infty} \exp\left[in(\varphi_0-\varphi)\right] \\
&\quad \times \int_{-k}^{+k} d\gamma \frac{J_n\left(\rho\sqrt{k^2-\gamma^2}\right)}{H_n^{(1)}\left(\rho_0\sqrt{k^2-\gamma^2}\right)} \exp\left[i\gamma(z_0-z)\right]. \qquad \text{(B9)}
\end{aligned}
$$

Equation (B9) can be easily written in the forms of (18) and (19).

Next, we want to show that (18) can be reduced to a modified back projection under certain conditions. When $\xi \gg 1$, according to the asymptotic expansions of the Hankel function, we get

$$
H_n^{(1)}(\xi) H_n^{(2)}(\xi) \approx \frac{2}{\pi\xi}. \qquad \text{(B10)}
$$

Assuming $\rho_0\sqrt{k^2-\gamma^2} \gg 1$, i.e., $\rho_0 k \gg 1$, one can approximate

$$
\frac{1}{H_n^{(1)}\left(\rho_0\sqrt{k^2-\gamma^2}\right)} \approx \frac{\pi}{2}\rho_0\sqrt{k^2-\gamma^2} H_n^{(2)}\left(\rho_0\sqrt{k^2-\gamma^2}\right). \qquad \text{(B11)}
$$

Therefore

$$
\begin{aligned}
\widetilde{K}_r(\mathbf{r},\mathbf{r}_0) &\approx \frac{1}{4\pi^2 c^2\eta} \sum_{n=-\infty}^{+\infty} \exp\left[in(\varphi_0-\varphi)\right] \\
&\quad \times \int_{-k}^{+k} d\gamma \exp\left[i\gamma(z_0-z)\right] \\
&\quad \cdot \sqrt{k^2-\gamma^2} J_n\left(\rho\sqrt{k^2-\gamma^2}\right) \\
&\quad \times H_n^{(2)}\left(\rho_0\sqrt{k^2-\gamma^2}\right). \qquad \text{(B12)}
\end{aligned}
$$

We can argue that the values of γ for $\gamma^2 > k^2$ do not contribute to the reconstruction. Taking the complex conjugate of the Green's function in (B2) and replacing k_z by γ, we may exclude these γ satisfying $\gamma^2 > k^2$ and approximate the Green's function as

$$
\begin{aligned}
\widetilde{G}_k^*(\mathbf{r},\mathbf{r}_0) &\approx -\frac{i}{8\pi} \sum_{n=-\infty}^{+\infty} \exp\left[in(\varphi_0-\varphi)\right] \int_{-k}^{+k} d\gamma \exp\left[i\gamma(z_0-z)\right] \\
&\quad \cdot J_n\left(\rho\sqrt{k^2-\gamma^2}\right) H_n^{(2)}\left(\rho\sqrt{k^2-\gamma^2}\right). \qquad \text{(B13)}
\end{aligned}
$$

Letting $z_1 = z_0 - z$, the second-order partial derivative of (B13) with respect to z_1 has the following relation:

$$
\frac{\partial^2}{\partial z_1^2} \sim -\gamma^2. \qquad \text{(B14)}
$$

Comparing (B12) with (B13), we get

$$
\widetilde{K}_k(\mathbf{r}_0,\mathbf{r}) = \frac{i2k}{\pi c^2\eta} \sqrt{1 + \frac{1}{k^2}\frac{\partial^2}{\partial z_1^2}} \widetilde{G}_k^*(\mathbf{r},\mathbf{r}_0). \qquad \text{(B15)}
$$

Under the condition $k|\mathbf{r}-\mathbf{r}_0| \gg 1$

$$
\begin{aligned}
\frac{1}{k^2}\frac{\partial^2}{\partial z_1^2} \widetilde{G}_k^*(\mathbf{r},\mathbf{r}_0) &= \frac{1}{k^2}\frac{\partial^2}{\partial z_1^2} \left[\frac{\exp\left(-ik|\mathbf{r}-\mathbf{r}_0|\right)}{4\pi|\mathbf{r}-\mathbf{r}_0|}\right] \\
&\approx -\frac{(z_0-z)^2}{|\mathbf{r}-\mathbf{r}_0|^2} \widetilde{G}_k^*(\mathbf{r},\mathbf{r}_0). \qquad \text{(B16)}
\end{aligned}
$$

Then, (B15) approximates to

$$
\widetilde{K}_k(\mathbf{r},\mathbf{r}_0) \approx \frac{i2k}{\pi c^2\eta} \sqrt{1 - \frac{(z_0-z)^2}{|\mathbf{r}-\mathbf{r}_0|^2}} \widetilde{G}_k^*(\mathbf{r},\mathbf{r}_0). \qquad \text{(B17)}
$$

REFERENCES

[1] R. A. Kruger, K. K. Kopecky, A. M. Aisen, D. R. Reinecke, G. A. Kruger, and W. L. Kiser, "Thermoacoustic CT with radio waves: A medical imaging paradigm," *Radiology*, vol. 211, pp. 275–278, 1999.

[2] G. Ku and L.-H. V. Wang, "Scanning thermoacoustic tomography in biological tissues," *Med. Phys.*, vol. 27, pp. 1195–1202, 2000.

[3] ——, "Scanning microwave-induced thermoacoustic tomography: Signal, resolution, and contrast," *Med. Phys.*, vol. 28, pp. 4–10, 2001.

[4] M.-H. Xu, G. Ku, and L.-H. V. Wang, "Microwave-induced thermoacoustic tomography using multi-sector scanning," *Med. Phys.*, vol. 28, pp. 1958–1963, 2001.

[5] M.-H. Xu and L.-H. V. Wang, "Time-domain reconstruction for thermoacoustic tomography in a spherical geometry," *IEEE Med. Imag.*, vol. 21, pp. 814–822, July 2002.

[6] ——, "Pulsed-microwave-induced thermoacoustic tomography: Filtered backprojection in a circular measurement configuration," *Med. Phys.*, vol. 29, pp. 1661–1669, 2002.

[7] R. A. Kruger, D. R. Reinecke, and G. A. Kruger, "Thermoacoustic computed tomography—technical considerations," *Med. Phys.*, vol. 26, pp. 1832–1837, 1999.

[8] R. A. Kruger, K. D. Miller, H. E. Reynolds, W. L. Kiser, Jr, D. R. Reinecke, and G. A. Kruger, "Breast cancer *in vivo*: Contrast enhancement with thermoacoustic CT at 434 MHz—feasibility study," *Radiology*, vol. 216, pp. 279–283, 2000.

[9] P. Y. Liu, "The P-transform and photoacoustic image reconstruction," *Phys. Med. Biol.*, vol. 43, pp. 667–674, 1998.
[10] C. G. A. Hoelen and F. F. M. de Mul, "Image reconstruction for photoacoustic scanning of tissue structures," *Appl. Opt.*, vol. 39, no. 31, pp. 5872–5883, Nov. 2000.
[11] R. O. Esenaliev, A. A. Karabutov, and A. A. Oraevsky, "Sensitivity of laser opto-acoustic imaging in detection of small deeply embedded tumors," *IEEE J. Sel. Top. Quantum Electron.*, vol. 5, pp. 981–988, July-Aug. 1999.
[12] K. P. Kostli, M. Frenz, H. P. Weber, G. Paltauf, and H. Schmidt-Kloiber, "Optoacoustic infrared spectroscopy of soft tissue," *J. Appl. Phys.*, vol. 88, pp. 1632–1637, 2000.
[13] C. C. Johnson and A. W. Guy, "Nonionizing elecromagnetic wave effects in biological materials and systems," *Proc. IEEE*, vol. 60, pp. 692–718, 1972.
[14] F. A. Duck, *Physical Properties of Tissue*. San Diego, CA: Academic, 1990.
[15] V. E. Gusev and A. A. Karabutov, *Laser Optoacoustics*. New York: American Institute of Physics, 1993.
[16] P. N. T. Wells, "Ultrasonic imagining of the human body," *Rep. Prog. Phy.*, vol. 62, pp. 671–722, 1999.
[17] L. V. Zhigilei and B. J. Garrison, "Microscopic mechanisms of laser ablation of organic solids in the thermal and stress confinement irradiation regimes," *J. Appl. Phys.*, vol. 88, pp. 1281–1298, 2000.
[18] Y. V. Zhulina, "Optimal statistical approach to optoacoustic image reconstruction," *Appl. Opt.*, vol. 39, no. 32, pp. 5971–5977, Nov. 2000.
[19] K. P. Kostli, M. Frenz, H. Bebie, and H. P. Weber, "Temporal backward projection of optoacoustic pressure transients using Fourier transform methods," *Phys. Med. Biol.*, vol. 46, pp. 1863–1872, 2001.
[20] Y. Xu, D. Feng, and L.-H. V. Wang, "Exact frequency-domain reconstruction for thermoacoustic tomography-I: Planar geometry," *IEEE Med. Imag.*, vol. 21, pp. 823–828, July 2002.
[21] Y. Xu, M.-H. Xu, and L.-H. V. Wang, "Exact frequency-domain reconstruction for thermoacoustic tomography-II: Cylindrical geometry," *IEEE Med. Imag.*, vol. 21, pp. 829–833, July 2002.
[22] G. B. Arfken and H. J. Weber, *Mathematical Methods for Physicists*. San Diego, CA: Academic, 1995.
[23] G. J. Diebold, T. Sun, and M. I. Khan, "Photoacoustic monopole radiation in one, two, and three dimensions," *Phys. Rev. Lett.*, vol. 67, pp. 3384–3387, 1991.
[24] S. J. Norton and M. Linzer, "Ultrasonic reflectivity imaging in three dimensions: Exact inverse scattering solutions for plane, cylindrical, and spherical apertures," *IEEE Trans. Biomed. Eng.*, vol. BME-28, pp. 202–220, 1981.
[25] *The Image Processing Handbook*, CRC, Boca Raton, FL, 1992.
[26] M.-H. Xu and L.-H. V. Wang, "Analytic explanation of spatial resolution related to bandwidth and detector aperture size in thermoacoustic or photoacoustic reconstruction," *Phys. Rev. E*, vol. 67, no. 056605, 2003.

Minghua Xu received the B.S. degree in physics from Qingdao University of Oceanography, Qingdao, China, in 1994, and the M.S. and Ph.D. degrees in acoustics from Nanjing University, Jiangsu, China, in 1996 and 1999, respectively. He is working towards the Ph.D. degree in biomedical engineering at Texas A&M University, College Station.

His main research topic is biomedical imaging.

Yuan Xu received the B.S. degree in physics from Wuhan University, Wuhan, P. R. China, in 1992, the M.S. degree in physics from Shanghai Institute of Optics and Fine Mechanics, Shanghai, P. R. China, in 1995, and the Ph.D. degree in physics from Institute of Physics, Chinese Academy of Sciences, Beijing, P. R. China, in 1999. He is now a graduate student with the department of Biomedical Engineering in Texas A&M University, College Station.

His special fields of interest are thermoacoustic tomography and ultrasound tomography, and their applications to medical imaging.

Lihong V. Wang (M'96–SM'00) received the Ph.D. degree in electrical engineering from Rice University, Houston, TX, in 1992.

He worked for University of Texas M.D. Anderson Cancer Center, a top-ranked cancer institution, as an Assistant Professor. He was promoted to Professor of Biomedical Engineering and Electrical Engineering at Texas A&M University, College Station, in 2002. His research focus is on nonionizing biophotonic imaging for early cancer detection. His group pioneered acousto-optical tomography, spectroscopic oblique-incidence reflectometry, thermo-acoustic tomography, photo-acoustic tomography, and Mueller-matrix optical coherence tomography. His program for Monte Carlo modeling of photon transport in biological tissues has been used worldwide (available at http://oilab.tamu.edu).

Dr. Wang is a fellow of American Institute for Medical and Biological Engineering, and a member of American Physical Society, Biomedical Engineering Society, Engineering in Medicine and Biology, Society Optical Society of America, and Society of Photo-Optical Instrumentation Engineers. He received the NIH FIRST Award, NSF CAREER Award, Johnson & Johnson Outstanding Young Scientist Award, Texas A&M TEES Select Young Faculty Award, Texas A&M TEES Faculty Fellow Award (twice), Texas A&M Ernest A. Baetz Faculty Fellow Award, Texas A&M TEES Senior Faculty Fellow Award, and Texas A&M University Faculty Fellow. He is listed in *Who's Who in Science and Engineering*. He has been an associate editor for the *Annals of Biomedical Engineering*, *Journal of Biomedical Optics*, and *Applied Optics*.

1134 IEEE TRANSACTIONS ON ULTRASONICS, FERROELECTRICS, AND FREQUENCY CONTROL, VOL. 50, NO. 9, SEPTEMBER 2003

Effects of Acoustic Heterogeneity in Breast Thermoacoustic Tomography

Yuan Xu and Lihong V. Wang, *Senior Member, IEEE*

Abstract—**The effects of wavefront distortions induced by acoustic heterogeneities in breast thermoacoustic tomography (TAT) are studied. Amplitude distortions are shown to be insignificant for different scales of acoustic heterogeneities. For wavelength-scale, or smaller, heterogeneities, amplitude distortion of the wavefront is minor as a result of diffraction when the detectors are placed in the far field of the heterogeneities. For larger-scale heterogeneities at the parenchyma wall, by using a ray approach (geometric optics), we show that no refraction-induced multipath interference occurs and, consequently, that no severe amplitude distortion, such as is found in ultrasound tomography, exists. Next, we consider the effects of phase distortions (errors in time-of-flight) in our numerical studies. The numerical results on the spreads of point sources and boundaries caused by the phase distortions are in good agreement with the proposed formula. After that, we demonstrate that the blurring of images can be compensated for by using the distribution of acoustic velocity in the tissues in the reconstructions. The effects of the errors in the acoustical velocities on this compensation also are investigated. An approach to implement the compensation using only TAT data is proposed. Lastly, the differences in the effects of acoustic heterogeneity and the generation of speckles in breast TAT and breast ultrasound imaging are discussed.**

I. Introduction

When an electromagnetic pulse is absorbed by biological tissue, the heating and subsequent expansion causes the emission of acoustic signals; this phenomenon is called the thermoacoustic effect. In thermoacoustic tomography (TAT), the thermoacoustic signals from a tissue sample are collected to map the distribution of the radiation absorption within the sample. Radiation absorption is closely related to the physiological and pathological status of the tissue. For example, the microwave absorption rate of cancerous breast tissue is two to five times greater than that of the surrounding normal breast tissue. This difference has been attributed to an increase in the amount of bound water and sodium within malignant cells [1]-[3].

The TAT combines good imaging resolution with high imaging contrast. Microwave imaging alone has the advantage of good imaging contrast but suffers from poor spatial resolution [4]–[7]. On the other hand, purely ultrasonic imaging has good spatial resolution but poor contrast. TAT capitalizes on the advantages of both methods.

There are a variety of reconstruction algorithms for TAT [8]–[13]. By using the approximation that the distance between the detector and the absorbing object is much larger than the dimensions of the absorbing object, a three-dimensional (3-D) radon transform has been used to reconstruct objects in TAT [8]. A time-domain, focused-beam-forming technique also has been applied to image reconstruction in the photoacoustic scanning of tissue structures [9], and a delay-and-sum algorithm has been applied to microwave-induced TAT [12]. The above reconstructions were implemented in the time domain. In the frequency domain, exact reconstruction algorithms for TAT have been implemented in planar, cylindrical, and spherical configurations with series expansion techniques [11]–[13].

An important assumption in the above reconstruction algorithms is that the tissue is acoustically homogeneous. For many medical imaging applications, including imaging of the female breast, this assumption is an approximation. For example, the speed of sound in the breast can vary from 1400 m/s to 1550 m/s. Errors due to the assumption of a constant acoustic speed, which has never been studied in TAT, potentially can have a pronounced effect on image quality. In breast ultrasound tomography (UT), however, wavefront distortion has been studied extensively [14]–[17]. The amplitude distortion caused by refraction dominates the phase distortion induced by acoustic speed variation in the breast UT [15]. Refraction occurs where there is a speed mismatch across a tissue interface. Because of refraction, rays from a single source can reach the same receiver by different paths, as shown in Fig. 1. The interference between these rays causes strong amplitude distortions in breast UT. Different deaberration methods have been proposed to compensate for phase distortion in UT [18], [19]. However, so far they have been inadequate to correct the strong amplitude distortion caused by refraction [20].

The effects of acoustic heterogeneity on breast TAT are estimated to be weaker than those in breast UT for the following reasons. First, signals in breast TAT are primarily in a lower frequency range (usually below 1.5 MHz [21]) than those in UT. Ultrasound scattering in this frequency range is weak. Second, in TAT, the acoustic source is induced by electromagnetic absorption; therefore, only one-way distortion on reception wave propagation occurs. As shown in Fig. 2, an acoustic ray, for example SB_1D, needs to pass through interface Σ only once. In contrast, in pure

Manuscript received March 8, 2002; accepted February 25, 2003. This project was sponsored in part by the U.S. Army Medical Research and Material Command Grant No. DAMD17-00-1-0455, the National Institutes of Health Grants No. R01 CA71980 and No. R21 CA83760, the National Science Foundation Grant No. BES-9734491, and Texas Higher Education Coordinating Board Grant No. ARP 000512-0063-2001.

The authors are with the Optical Imaging Laboratory, Department of Biomedical Engineering, Texas A&M University, College Station, TX 77843-3120 (e-mail: lwang@tamu.edu).

0885–3010/$10.00 © 2003 IEEE

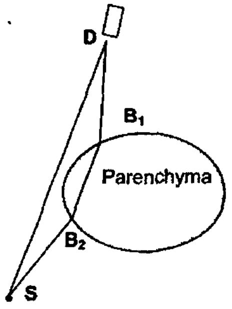

Fig. 1. Multipath interference caused by refraction at boundary points B_1 and B_2 in breast ultrasound imaging in transmission mode. S is a point source and D is a detector.

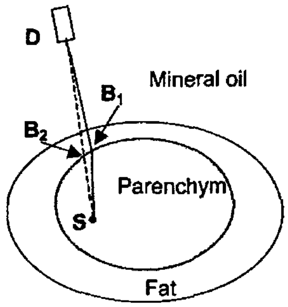

Fig. 2. Ray refraction at the parenchyma wall with breast TAT. The outer oval represents the breast surface, in which there is negligible refraction due to the good match of acoustic speed between fat and mineral oil. The solid line SB_1D represents a ray in the heterogeneous model; the dashed line SB_2D represents that in a homogeneous model. S is a point source and D is a detector; B_1, B_2 are two points at the parenchyma wall.

ultrasound imaging, either in the pulse-echo mode or in the transmission mode, ultrasound distortion includes two parts: distortion during both transmission and reception wave propagation. Therefore, the acoustic wave has to pass through the interface at least twice, as shown in SB_2B_1D in Fig. 1. Third, if the detection distance from the objects are properly chosen, the effects of amplitude distortion can be minimized in breast TAT, as will be shown in Section III.

In our work, we analyze the effects of amplitude distortion and numerically simulate the effects of phase distortion with the truncated conjugate gradient [22] (TCG) method. In Section II, we derive equations for the forward problem in an acoustically homogeneous model, which yields acoustic pressure from a known distribution of microwave absorption. In Section III, we investigate the effects of refraction on the wavefront amplitude and phase in breast TAT. We prove that, in breast TAT, a convex parenchyma wall (when observed from the outside of the parenchyma tissue) does not cause multipath interference and that the effects of amplitude distortion also are not severe for a concave boundary. An equation for the forward problem in an acoustically heterogeneous model also is introduced at the end of Section III. The inversion algorithm of TCG, and the model and parameters used in the numerical simulations, are presented in Section IV. In Section V, the effects of phase distortion are studied numerically. We show how the degradation of the reconstructed images depends on acoustic heterogeneity when acoustic heterogeneity is not considered in the reconstruction algorithm. Correction of phase distortion should be the first step for improving image quality in breast TAT because phase is much more important in imaging than amplitude when there is no severe amplitude distortion [23], [24]. Therefore, the reconstructions are implemented with consideration of acoustic velocity heterogeneity to illustrate how the imaging degradation can be compensated for. The effects of the errors in the acoustical velocities on this compensation also are investigated. In Section VI, an approach to implement compensation with only TAT data is proposed. The differences between breast TAT and breast ultrasound imaging on the effects of acoustic heterogeneity and speckles are explained by their differences in central ultrasound frequency and detection geometry. Section VII presents conclusions.

II. THE FORWARD PROBLEM IN A HOMOGENEOUS MODEL

We begin by deriving a formula for the forward problem for an acoustically homogeneous model, then modify it at the end of Section III to consider velocity heterogeneity. In the case of thermal confinement, the acoustic wave at point $\mathbf{r}$ and time t, $p(\mathbf{r},t)$, is related to the microwave absorption $H(\mathbf{r},t)$ by the following wave equation [25]:

$$\frac{\partial^2 p(\mathbf{r},t)}{\partial t^2} - v_{s0}^2\nabla^2 p(\mathbf{r},t) = \frac{\beta}{C}\frac{\partial H(\mathbf{r},t)}{\partial t}, \qquad (1)$$

where v_{s0} is the acoustic speed, C is the specific heat, and β is the coefficient of the volume thermal expansion. (1) can be rewritten in terms of $H(\mathbf{r},t)$:

$$p(\mathbf{r},t) = \frac{\beta}{4\pi C}\iiint \frac{\partial H(\mathbf{r}',t')}{\partial t'}\frac{d\mathbf{r}'}{|\mathbf{r}-\mathbf{r}'|}, \qquad (2)$$

where $t' = t - |\mathbf{r}-\mathbf{r}'|/v_s$. The source term $H(\mathbf{r},t)$ can further be written as the product of a spatial component and a temporal component, i.e.:

$$H(\mathbf{r},t) = I_0\varphi(\mathbf{r})\eta(t), \qquad (3)$$

where I_0 is a scaling factor proportional to the incident radiation intensity, $\varphi(\mathbf{r}')$ describes the to-be-reconstructed microwave absorption properties of the medium at $\mathbf{r}'$, and $\eta(t)$ describes the shape of the irradiating pulse. Substituting (3) into (4) results in:

$$p(\mathbf{r},t) = \frac{\beta I_0}{4\pi C}\iiint \varphi(\mathbf{r}')\frac{d\eta(t')}{dt'}\frac{d\mathbf{r}'}{|\mathbf{r}-\mathbf{r}'|}. \qquad (4)$$

We proceed by transforming the time-dependent wave equation into the temporal-frequency domain. Denoting the Fourier transforms of p and η by $\overline{p}$ and $\overline{\eta}$, respectively, we have:

$$\begin{aligned} p(\mathbf{r},t) &= \int_{-\infty}^{\infty} \overline{p}(\mathbf{r},k)\exp(ikt)dk, \\ \eta(t) &= \int_{-\infty}^{\infty} \overline{\eta}(k)\exp(ikt)dk. \end{aligned} \tag{5}$$

Substituting (5) into (4) results in:

$$\overline{p}(\mathbf{r},k) = \frac{i\beta I_0 k\overline{\eta}(k)}{4\pi C}\iiint \varphi(\mathbf{r}')\frac{\exp\left(-ik|\mathbf{r}-\mathbf{r}'|/v_{s0}\right)}{|\mathbf{r}-\mathbf{r}'|}d\mathbf{r}'. \tag{6}$$

Define $\overline{p}_1(\mathbf{r},k) = \overline{p}(\mathbf{r},k)/(2\pi\eta(k))$, substitute it into (6), apply an inverse Fourier transform to both sides of the equation, and obtain the following equation:

$$p_1(\mathbf{r},t) = \frac{v_{s0}\beta I_0}{4\pi C}\frac{\partial}{\partial t}\iint\limits_{t=t_f(\mathbf{r}',\mathbf{r})} \frac{\varphi(\mathbf{r}')}{|\mathbf{r}-\mathbf{r}'|}d\mathbf{r}', \tag{7}$$

where

$$t_f(\mathbf{r}',\mathbf{r}) = |\mathbf{r}-\mathbf{r}'|/v_{s0}; \tag{8}$$

is the time-of-flight (TOF) from to $\mathbf{r}'$ to $\mathbf{r}$; $p_1(\mathbf{r},t)$ is the deconvolution of $p(\mathbf{r},t)$ with respect to the length of the microwave pulse and can be interpreted as the detected pressure signal when the microwave pulse is infinitely narrow. The physical meaning of this equation is that, in an acoustically homogenous medium, the pressure p_1, at a spatial point $\mathbf{r}$ and time t, is proportional to the first-order temporal derivative of the integration of the absorbed microwave energy over a spherical surface [a circle in the two-dimensional (2-D) case]. The spherical surface is centered at $\mathbf{r}$ and has a radius of tv_{s0}.

III. The Effect of Acoustic Heterogeneity in TAT

A TAT model is shown in Fig. 2. In our imaging system, mineral oil is chosen as the coupling medium for both microwaves and ultrasonic waves. The acoustic speed in mineral oil is 1437 m/s [26], which is very close to that in fat [27]. Therefore, there should be negligible refraction at the boundary between the breast and the mineral oil; consequently, we will consider only the effects of the acoustical heterogeneity within the breast. More details on our TAT experimental setup can be found in [12].

A. Amplitude Distortion Caused by Refraction

Fig. 1 shows the multipath interference in breast ultrasound imaging in transmission mode. The acoustic ray from source S can travel to detector D by two different paths, SD and SB_2B_1D, due to refraction at the interfaces between different tissues. The interference between the two rays can cause amplitude distortion [15]. In the following subsections, we will first prove that there is no multipath interference in the case of a convex parenchyma wall in breast TAT. Then, we will show that the amplitude distortion also is not severe for a concave parenchyma wall.

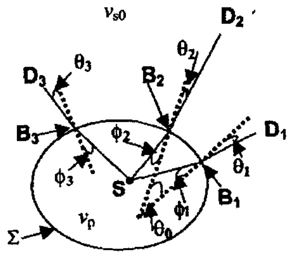

Fig. 3. Diagram showing that no two rays from a point source S will intersect with each other after being refracted at a convex boundary Σ and entering a medium with a slower acoustic speed. S is a point source; D_1 and D_2 are detectors; ϕ_1, ϕ_2, and ϕ_3 are the incidence angles; θ_1, θ_2, and θ_3 are the transmission angles; the solid lines represent acoustic rays; B_1, B_2, B_3 are three points at the parenchyma wall; v_p, v_{s0} are the mean acoustic speeds in the parenchyma tissue and the fat tissue, respectively; and $v_p > v_{s0}$.

1. Convex Boundary: In this subsection, we will show that there is no multipath interference in the TAT of the breast with a convex parenchyma wall by proving that no two rays from a source within the parenchyma will intersect with each other after refractions at the wall. The model is shown in Fig. 3, where S is an acoustic source; v_p and v_{s0} are the acoustic speed in the breast parenchyma and the medium (also the fat), respectively ($v_p > v_{s0}$); the dashed lines are the normals of the boundary at points B_1, B_2, B_3, respectively; ϕ_1, ϕ_2, and ϕ_3 are the angles of incidence; θ_1, θ_2, and θ_3 and are the angles of transmission; and the solid lines represent the acoustic rays. Because the boundary is convex, it can be inferred that rotation from the normal at point B_2 to the normal at point B_1 is clockwise and the angle is θ_0 (positive). We also have $\phi_2 < \theta_0 + \phi_1$, which can be seen by extending lines SB_2 and SB_1 to the outside of the boundary and noticing that SB_2 and SB_1 will never intersect outside the boundary. To prove B_2D_2 and B_1D_1 will not intersect outside the boundary, we need to show $\theta_2 < \theta_0 + \theta_1$. According to Snell's law, we have:

$$\begin{aligned} \sin\theta_2 &= (1-\alpha)\sin\phi_2, \\ \sin\theta_1 &= (1-\alpha)\sin\phi_1, \end{aligned} \tag{9}$$

where $\alpha = 1 - v_{s0}/v_p$, which is positive when $v_p > v_{s0}$. The problem can be discussed under two conditions:

$\phi_2 < \phi_1$. In this case, according to (9), we have $\theta_2 < \theta_1$ and therefore $\theta_2 < \theta_0 + \theta_1$. And

$\phi_2 \geq \phi_1$. (9) can be transformed to:

$$\begin{aligned} \sin\left(\frac{\theta_1-\phi_1}{2}\right) &= -\frac{\alpha\sin(\phi_1)}{2\cos\left((\theta_1+\phi_1)/2\right)}, \\ \sin\left(\frac{\theta_2-\phi_2}{2}\right) &= -\frac{\alpha\sin(\phi_2)}{2\cos\left((\theta_2+\phi_2)/2\right)}. \end{aligned} \tag{10}$$

Because $\phi_2 \geq \phi_1$ and consequently $\theta_2 \geq \theta_1$, it is straightforward to obtain $\theta_2 - \phi_2 \leq \theta_1 - \phi_1$ from (10). Using $\phi_2 < \theta_0 + \phi_1$, we have $\theta_2 < \theta_0 + \theta_1$. In conclusion, we prove that, after the rays from a point source go into another medium with a slower acoustic speed, the rays cannot intersect with each other when the interface is convex. In another words, for any pairing of point source and detector, there is only one acoustic path that satisfies Snell's law. Consequently, no multipath interference occurs and amplitude distortion can be ignored. This conclusion also can be applied to a boundary with wavelength-scale concave segments. This kind of boundary can be treated as a convex boundary approximately because the effects of the small concave segments can be neglected when the detectors are placed in the far field of the segments, as will be shown in the following subsection. In contrast, multipath interference does occur after rays pass a convex parenchyma wall in ultrasound imaging, as shown in Fig. 1. This difference makes the amplitude distortion in TAT of the breast with a convex, or approximately convex parenchyma wall, smaller than that in pure ultrasound imaging.

2. Concave Boundary: We realize that, in reality, the boundary between mammary tissue and subcutaneous fat tissue might be concave and quite irregular. In this subsection, we will show that the amplitude distortion caused by a concave boundary is not severe. Basically, this conclusion can be explained as follows. With wavelength-scale or smaller heterogeneities, amplitude distortion of the wavefronts is minor due to diffraction when the detectors are placed in the far field of the irregular boundary segment. When the size of the concave segment is larger, according to the imaging formula of concave boundaries shown below, only imaginary images exist after the wavefronts from real objects pass through the concave boundary. Equivalently, no two rays from a point source will intersect with each other after passing through the concave boundary segment and no strong amplitude distortion occurs. In the following subsection, we will define two kinds of multipath interference: focusing-type and nonfocusing-type interferences. The former can induce amplitude distortion in both narrowband and broadband signals; the latter can induce only amplitude distortion in narrowband signals. As a consequence, we need only examine in detail the focusing-type interference, because signals in breast TAT are broadband.

Definition of focusing-type and nonfocusing-type interferences. Fig. 4 shows the two different kinds of multipath interferences. Three different ray paths SB_1D, SB_2D, SB_3D from source S to detector D are shown, and each of them is assumed to satisfy the refraction law. The SB_1D and SB_2D can be considered as a small modification of the straight line SD due to weak heterogeneity, and SB_3D is far away from SD. We use focusing-type interference to refer to the interference between pulses along the paths with the same TOFs. The interference between SB_1D and SB_2D is of this type. This is because SB_1D and SB_2D satisfy the refraction law, and their TOFs are local minima according to Fermat's principle [28]. Consequently the rays around SB_1D and SB_2D should have almost the same TOF. After noticing that B_1 and B_2 are close to each other, it can be inferred that SB_1D and SB_2D have the same TOFs. Actually, the boundary segment around B_1B_2 can be considered a focusing lens and can produce strong amplitude distortion even for broadband pulses, as verified by the strong amplitude distortion in broadband breast ultrasound imaging [15]. As a contrast, we use nonfocusing-type interference to refer to the interference between the pulses along paths with different TOFs. The interference between SB_3D and SB_1D (SB_2D) is a nonfocusing-type interference, because B_3 is far from B_1 and B_2, and generally it can be assumed that $|t_{SB_1D} - t_{SB_3D}|$ and $|t_{SB_2D} - t_{SB_3D}|$ (t_{SB_1D}, t_{SB_2D}, and t_{SB_3D} are the TOFs along ray paths SB_1D, SB_2D, and SB_3D, respectively) are larger than 1 μs, the average pulse width of thermoacoustic signals in our RF TAT experiments. Consequently, the pulse along SB_3D is separated temporally from the pulses along SB_1D, SB_2D, and the interference between SB_3D and SB_1D (SB_2D) is insignificant. Similar analyses can be found in the pure ultrasound imaging literature [15].

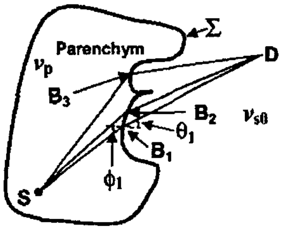

Fig. 4. Diagram to show two types of multipath interferences caused by a concave boundary: focusing-type interference between SB_1D and SB_2D and nonfocusing-type interference between SB_1D (SB_2D) and SB_3D. In a focusing-type interference, the different rays have approximately the same TOF, which consequently yields constructive interference and strong amplitude distortion. In this case, the boundary segment around B_1B_2 can be considered as a lens. In nonfocusing-type interference, the difference of the TOFs along two rays is larger than the pulse width; consequently, the pulses are separated temporally and no strong amplitude distortion occurs. See Fig. 3 for the symbols' definitions.

The signals along SB_3D may introduce artifacts in the reconstructed images because detector D receives two pulses from source S—one along SB_1D and SB_2D, and the other along SB_3D. To estimate the effects of signals along path SB_3D, we numerically simulate refractions at arbitrary boundaries, at which the locations of source S and detector D are randomly chosen. We find that the SB_3D-type refraction rarely occurs. Therefore, we expect the artifacts introduced by the signals along SB_3D to be insignificant; and, in the following studies, we consider only focusing-type interference.

Analysis of focusing-type interference. For a boundary segment with a size of $2a$ much larger than the wavelength of interest λ, we will use a ray model to study the effects of refraction. To have focusing-type interference, the positions of the source and detector must satisfy the following equation:

$$\frac{1}{l_{SB_1}/\cos\phi_1}+\frac{1}{l_{B_1D}(1-\alpha)/\cos\phi_1}=\frac{\alpha}{R_l}=\frac{1}{f}, \tag{11}$$

where f is the focal length of segment B_1B_2 in Fig. 4 and $f=R_l/\alpha$; R_l is the radius of the segment; and l_{SB_1} and l_{B_1D} are the lengths of line SB_1 and DB_1, respectively. The derivation of (11) can be found in Appendix A. To have a real image, or equivalently to have two rays intersect after passing through boundary segment B_1B_2, (11) requires:

$$l_{SB_1}/\cos(\phi_1) > R_l/\alpha. \tag{12}$$

Next, we derive another requirement due to diffraction for the occurrence of strong amplitude distortion. The smallest beam width after a wavefront passes through a boundary segment with a size of $2a$ is $l_{B_1D}\lambda/a$, where λ is the wavelength of the acoustic wavefront. To induce strong focusing, for example, to have a beam width smaller than a at D, we need to have:

$$l_{B_1D} < a^2/\lambda. \tag{13}$$

The right-hand side of the above inequality is the same as the definition of the near-field length of a plain transducer when a is considered as the radius of the transducer. It is well-known that the amplitude can change rapidly in the near field due to the acoustic interference, but it is much smoother in the far field. Similarly, if the detector is placed within the far field of the concave boundary segment, the amplitude distortion will be less severe in TAT.

Eq. (13) is derived for the case in which a wavefront propagates perpendicularly to the boundary segment. When a wavefront is incident obliquely upon the segment B_1B_2, the effective size of the lens in (13) should be the projection of its geometrical size onto the plane perpendicular to the propagation direction of the incident wave. Then we have:

$$l_{B_1D} < (a\cos\phi_1)^2/\lambda. \tag{14}$$

By combining (14), (12), and $R_l > a$, we obtain the following requirement for inducing strong amplitude distortion after passing through the boundary:

$$l_{SB_1} > \frac{\sqrt{l_{B_1D}\lambda}}{\alpha}. \tag{15}$$

It can be seen from this equation that when l_{B_1D} is large enough:

$$l_{B_1D} > \frac{(l_{SB_1}\alpha)^2}{\lambda}, \tag{16}$$

the strong amplitude distortion can be minimized. Notice that the required minimum detection distance in (16) increases linearly with the frequency of the wave.

In the derivation of (11), ray theory is utilized. Ray theory is valid under the following conditions [29]:

$$l_{B_1D} \ll 4a^2/\lambda, \tag{17}$$

and

$$2a \gg \lambda. \tag{18}$$

Eq. (17) is similar to (13), but the former is stronger; (17) states that the ray model is valid when the wave propagation distance from the heterogeneity is much smaller than $4a^2/\lambda$; beyond that distance, diffraction must be considered. In our analysis of amplitude distortion in TAT, we extend the effective range of the ray model from (17) to (13). This is based on the assumption that the ray model overestimates the wavefront distortions due to ignorance of the diffraction effect. Therefore, if the analysis using ray theory shows that there is only minor amplitude distortion when (16) and (18) are met, the analysis from the exact wave equation should yield the same result.

For a wavelength-scale boundary segment (e.g., $2a < 4\lambda$), (18) is violated, and (16) cannot be applied. In this case, strong amplitude distortion can be minimized by placing the detector within the far field of the heterogeneity:

$$l_{B_1D} > 4\lambda, \tag{19}$$

where we have substituted $2a < 4\lambda$ into (13). Combining (16) and (19), we obtain the minimum detection distance for avoiding strong amplitude distortion induced by different scales of heterogeneities:

$$l_{B_1D} > \max\left[\frac{(l_{SB_1}\alpha)^2}{\lambda}, 4\lambda\right], \tag{20}$$

where max[] represents computing the maximum. Using the following parameters, $l_{SB_1} < 10$ cm (the assumed size of the breast parenchyma), and $\alpha = 0.07$, in which the mean velocity in the subcutaneous zone v_f and the breast parenchyma v_p are assumed to be 1437 m/s [28] and 1546 m/s [30], respectively, we have $l_{B_1D} > 4.9$ cm for 1.5 MHz ultrasound and $l_{B_1D} > 1.63$ cm for 0.5 MHz ultrasound. These requirements can be met easily in TAT experiments. For ultrasound waves with a frequency less than 0.5 MHz, it is not necessary to apply (20), because ultrasound scattering by soft tissue in this frequency range can be neglected and no severe amplitude distortion is expected.

The above analysis is made for 2-D TAT. This corresponds to the experimental configuration in which a linear, or ring array of transducers with a cylindrical surface is used, and a section image of the breast in the detection plane is desired. However, because of the refraction at the parenchyma wall, the thermoacoustic waves from the objects within the detection plane might deviate out of the plane. On the other hand, the signals collected in the detection plane are transmitted by the objects out of the detection plane rather than within it. Consequently, the obtained image is actually a projection of the out-of-plane objects onto the detection plane. To reduce this kind of error, we can use the technique of compressing the breast against the chest wall, which has proven to be effective in reducing wavefront distortions in breast ultrasound imaging. After the compression, the acoustic signals can pass through the interface more or less perpendicularly. However, the ultimate solution to this problem is 3-D TAT. Most of the 2-D results on amplitude distortions (e.g., (14), (16), (20), and the results on phase distortions shown later) can be directly applied to 3-D TAT; (11) also can be applied to analyze a 3-D convex boundary locally by substituting $-R_l$ for R_l. Then, it is straightforward to see that in a 3-D case no two rays can intersect with each other after passing a convex boundary segment.

In summary, our analysis shows that, in RF breast TAT, if the detection is made at a distance to the breast surface required by (20), the amplitude distortion caused by the refraction at the parenchyma wall is not important because of the diffraction effect and the fact that TAT signals are broadband, have low central frequency, and experience only one-way transmission through the parenchyma wall. The effect of intramammary fat lobules will be addressed in Section VI. Therefore, in the following analysis and simulations, we will consider only phase distortion.

B. Phase Distortion Caused by Refraction and Speed Variation

If the background is acoustically homogeneous, an acoustic ray from source S in Fig. 2 goes along the straight line SD to reach detector D. When there is acoustic heterogeneity, an acoustic ray goes along line SB_1D because of refraction at the interface. Assume there is no change in the shape of the acoustic pulse caused by acoustic heterogeneity. The TOF from source S to detector D in the acoustically heterogeneous model is:

$$t_{SB_1D} = \int_{SB_1D} dl/v_s(\mathbf{r}''), \qquad (21)$$

where $v_s(\mathbf{r}'')$ is the local acoustic speed, and $\mathbf{r}''$ is a point within line SB_1D. Now, we will show that t_{SB_1D} can be approximated to the second order of a small value $\varepsilon = (v_s(\mathbf{r}'') - v_{s0})/v_{s0}$ by $t_{SD} = \int_{SD} dl/v_s(\mathbf{r}'')$, where v_{s0} is the velocity used in the acoustically homogeneous model. According to Fermat's principle, an acoustic ray travels on the fastest path. In other words, SB_1D is a local minimum of TOF. Now assume B_1 is displaced to B' by a small distance $q = |BB'|$,

$$\frac{q}{l_{SD}} = o(\varepsilon). \qquad (22)$$

After expanding $t_{SB'D}$ around t_{SB_1D} with respect to q, we have:

$$t_{SB'D} = t_{SB_1D} + q\left.\frac{\partial t_{SB'D}}{\partial q}\right|_{q=0} + o(\varepsilon^2). \qquad (23)$$

Recalling that SB_1D is a local minimum, we have $\left.\frac{\partial t_{SB'_1D}}{\partial q}\right|_{q=0}$. Substituting it into (23) and assuming $l_{B_2B_1}/l_{SD} = o(\varepsilon)$ due to the weak acoustic heterogeneity in breast tissue, we have:

$$t_{SD} = \int_{SD} dl/v_s(\mathbf{r}'') = t_{SB_1D} + o(\varepsilon^2). \qquad (24)$$

The above result can be understood in the following way. Although the path length of SB_1D in Fig. 2 is longer than that of SD and $(l_{SB_1} + l_{DB_1} - l_{SD})/l_{SD} = o(\varepsilon)$, path SD has a longer part within the slow-speed area than path SB_1D. The combination of the two opposite effects leads to the cancellation of the first-order term of ε in (24).

Next we will show that the approximation of t_{SB_1D} by t_{SD} includes most of the flight-time variation induced by acoustic heterogeneity. The TOF from source S to detector D in an acoustically homogeneous and heterogeneous model is l_{SD}/v_{s0} and t_{SB_1D}, respectively. The difference between them is:

$$\begin{aligned}\delta t &= |t_{SB_1D} - l_{SD}/v_{s0}| \\ &= |t_{SB_1D} - t_{SD} + t_{SD} - l_{SD}/v_{s0}| \\ &\approx \left|o(\varepsilon^2) + t_{SD} - l_{SD}/v_{s0}\right| \approx o(\varepsilon),\end{aligned} \qquad (25)$$

where we used (24). Combining δt with (24), we have:

$$\frac{|t_{SD} - t_{SB_1D}|}{\delta t} = o(\varepsilon). \qquad (26)$$

Therefore, the error in the approximation of t_{SB_1D} by t_{SD} is not important. At last, it should be pointed out that our analysis of TOF can be applied to both 2-D and 3-D TAT.

C. Forward Formula in an Acoustically Heterogeneous Model

In our analysis of TOF, we consider only a single interface. The results can be extended to the case involving several interfaces. In general, the TOF from $\mathbf{r}$ to $\mathbf{r}'$ can be expressed as:

$$t_f(\mathbf{r}', \mathbf{r}) = \int_{L(\mathbf{r}', \mathbf{r})} dl/v_s(\mathbf{r}'') + o(\varepsilon^2), \qquad (27)$$

where $L(\mathbf{r}', \mathbf{r})$ is the straight line from $\mathbf{r}'$ to $\mathbf{r}$, and $\mathbf{r}''$ lies within the line L. Combining (27) and (7), we obtain the forward formula for acoustically heterogeneous TAT.

Our analysis of TOF is in agreement with the results from a more rigid model [31]. It was reported that the variation in travel time caused directly by acoustic speed heterogeneity is a first-order perturbation, and that the effect of the ray bending on the travel times is a second-order one. For breast tissue, which is weakly acoustically heterogeneous, it is enough to consider the first-order perturbation by computing the integral of the slowness perturbation along straight lines, as shown in (27).

IV. Implementation and Modeling of Numerical Simulations

A. Numerical Implementation

It can be seen from (7) that $p_1(\mathbf{r},t)$ can be obtained from $\varphi(\mathbf{r}')$ after applying two linear operations to it: one is integration over the object space, the other is differentiation over t. Therefore, in its discrete form, (7) is a set of linear equations:

$$\mathbf{M}\varphi=\mathbf{p}, \tag{28}$$

where $\mathbf{M}$ is the matrix representing the product of the two linear operators. The standard techniques of solving a linear equation system can be used. We adopted the TCG method to minimize the object function $\|\mathbf{M}\varphi-\mathbf{p}\|$ in the sense of least square root and no preconditioner is used. In the implementation of TCG, instead of the whole matrix $\mathbf{M}$, a function that gives the multiplication of matrix $\mathbf{M}$ and its adjoin with an arbitrary vector is required. Consequently, the demand on computer memory is reduced greatly, compared with many other techniques that require storing the whole matrix $\mathbf{M}$ in memory. Another advantage of TCG is that an approximate result can be obtained by stopping the iteration before reaching the full convergence. The truncation not only saves computation time but also provides a way of regularization for stabilizing the results. In (28), we use the Savitzky-Golay smoothing method [32], rather than the finite differentiation method to implement the operation of the first-order temporal derivative, as the former yields a much smoother and more accurate result than the latter when data are noisy. We truncated our simulations after 15 iterations, which corresponds to the relative changes in the norms of the results, about 0.7% for the acoustically homogeneous model and up to 6% for the acoustically heterogeneous model. In both cases, further iterations yield little visible improvement to image and may induce instability.

In our simulations, we choose the 2-D case rather than the 3-D case because the computational complexity can be reduced and because it is much easier to interpret and graph a 2-D image. For the 2-D case, the integration in (7) is over a curve instead of a spherical surface:

$$p_1(\mathbf{r},t)=\frac{\beta I_0 v_{s0}}{4\pi C}\frac{\partial}{\partial t}\oint_{t=t_f(\mathbf{r}',\mathbf{r})}\frac{\varphi(\mathbf{r}')}{|\mathbf{r}-\mathbf{r}'|}d\mathbf{r}', \tag{29}$$

where t_f is determined by (27). Nevertheless, the conclusions of a 2-D case can be extended to a 3-D one.

B. Model and Parameters in Numerical Simulations

Fig. 5(a) and (b) illustrate the acoustic and RF absorption models of the breast, respectively. The acoustic model of the breast in our simulations is based on experimental results on the distribution of acoustic speed in the breast [27]–[30]. Acoustic speed in the breast may vary from 1400 m/s to 1550 m/s. Generally, a zone of low velocity (1400–1450 m/s) characterizes subcutaneous fat [33]. The speed in normal dense parenchyma is higher, varying from 1500 m/s to 1550 m/s [30]. In Fig. 5 the outer circles, with a radius of 50 mm, represent the breast surface. The inner irregular boundaries, which are generated by randomly modifying a circle, represent the walls of the breast parenchyma. The size of the parenchyma tissue was changed in different simulations because the ratio of breast parenchyma to subcutaneous fat may change with age. Usually, a young female breast has less fat than an older one does. The mean velocity in the subcutaneous zone v_f and the breast parenchyma v_p are set to be 1437 m/s [27] and 1546 m/s [30], respectively. A random component, which is a normal distribution with a mean of zero and a variance of 33 m/s, is added to the velocity distribution to simulate the velocity fluctuations in the subcutaneous zone [33] and the breast parenchyma [30]. Later, our simulation results show that the random component of velocity will induce little spread in the images due to the cancellation after integration. To ensure that the acoustic speed does not change sharply within each tissue, the random component is smoothed spatially by introducing a correlation length as shown below. The imaged area is divided into patches with side dimensions of a correlation length. The value of the random component at the center of each patch is determined according to the normal distribution mentioned above; then the random component within the patch decreases linearly to zero at the boundary of the patch. We tried different correlation lengths in our simulations, from 12 mm (about the size of fat lobules in parenchyma tissue) to 3 mm. The image degrades more with increasing correlation length, but the difference is minor. The correlation length was chosen to be about 6 mm for the reported results. The speed distribution in Fig. 5 was normalized to 1437 m/s, which is assumed to be the acoustic velocity in the medium surrounding the breast and the mean acoustic speed in the subcutaneous fat.

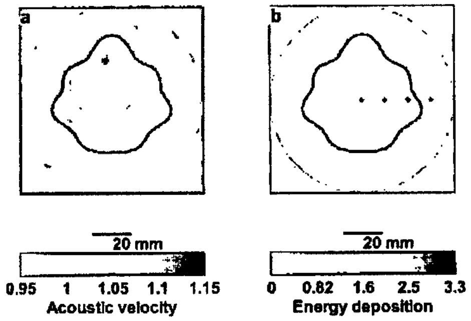

Fig. 5. (a) Distribution of acoustic velocity normalized to v_{s0} for a breast model. The breast surface is represented by the outer circle; the wall between the breast parenchyma and the subcutaneous fat is represented by the inner irregular boundary. (b) The microwave absorption distribution in our model. The four small spots represent the assumed tumors.

The RF absorption model of the breast is shown in Fig. 5(b). The boundary shapes are the same as in Fig. 5(a). The RF absorption coefficients in fat, tumors, and the coupling oil are set to be 0.3, 3, and 0 after being normalized to that in the parenchyma. The tumors, shown in Fig. 5(b) as dark spots, are placed evenly along the horizontal direction to study the dependence of the distortions in the images on the tumor locations. We set the radii of the four tumors to about 1.2 mm to simulate approximately the point-source spread caused by acoustic heterogeneity.

The parenchyma wall in our simulation is generated as the following equation: $r(\theta) = r_p(1 + Ag(\theta))$, where $r(\theta)$ is the radius of the boundary at angle θ, r_p is the mean radius of the boundary and is used to represent the size of the parenchyma tissue, A is the distortion amplitude, and $g(\theta)$ generates random numbers within $[-1, 1]$.

The parameters in our simulations are chosen as follows unless stated otherwise. Noise is added to the generated signals so that the frequency range with signal-to-noise ratio (SNR) larger than unity is from 0 to 1.5 MHz, which approximates our experimental results [21]. The radius of the circle of detection is set to be 125 mm to meet (16); the angle range of detection is 2π with 400 steps. An insufficient number of scanning steps can cause radial aliases in the reconstructed image [13]. Thermoacoustic signals are sampled for 108 μs at a sampling rate of about 14 MHz, which is sufficient to meet the Nyquist criteria. The 100 mm by 100 mm imaging field is mapped with a 256 by 256 mesh. In our simulations, the thermoacoustic signals are generated in an acoustically inhomogeneous model, and the reconstruction is implemented for two cases—with and without the consideration of acoustic heterogeneity.

V. NUMERICAL RESULTS

We first study the effect of acoustic heterogeneity on imaging when acoustic heterogeneity is considered in the forward problem but not in the reconstruction. In the reconstruction, $v_s(\mathbf{r})$ in (27) is set to be v_{s0}. Then we show how to improve image resolution after considering acoustic heterogeneity in the reconstructions. And, the effects of measurement errors in v_f, v_p and Σ on the improvement are investigated.

A. Reconstruction Without Considering Heterogeneity

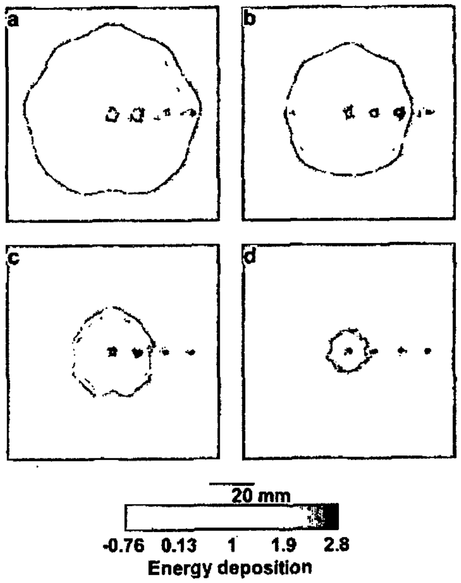

Fig. 6. Images when acoustic heterogeneity is not considered in the reconstructions. The mean radii of the parenchyma wall are set to be (a) 0.8, (b) 0.6, (c) 0.4, and (d) 0.2 of the breast radius, respectively. The point-spread width and the boundary-spread width increase linearly with the size of the parenchyma tissue. Note that the spread of points outside the parenchyma tissue are much smaller than the spread inside.

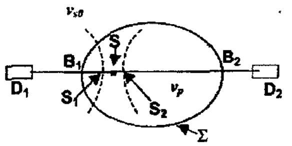

Fig. 7. Diagram for deriving (30), which estimates the spread of a point source S along line D_1D_2 due to TOF error. S_1 is the intersection of D_1D_2 with the backprojection arch of the signal transmitted by source S and detected by detector D_1; S_2 is the corresponding one at D_2.

Fig. 6(a)–(d) shows the results when acoustic heterogeneity is not considered in the reconstructions. In the four simulations, the mean radii of the parenchyma wall r_p are set to be 0.8, 0.6, 0.4, and 0.2 of the breast radius. The wall is distorted randomly in the simulations, and the distortion amplitude is 0.1. We measure the point-spread width (PSW), which is the width of the image of a point source along a specific direction minus its real size, 2.4 mm, and the boundary spread width (BSW), which is the width of the blurred parenchyma wall Σ in an image. It is clear from Fig. 6 that PSW and BSW increase with the radius of the parenchyma wall. It is proved in Appendix B that the two widths can be estimated by the following equation:

$$w = l_p\alpha, \tag{30}$$

where l_p is $2r_p$ in the case of BSW; in the case of PSW, l_p is the length of a ray within the parenchyma tissue along a specific direction (for example the length of B_1B_2 in Fig. 7). The PSW is anisotropic because l_p depends on direction. This anisotropy of PSW can be verified by the observation that the three tumors within the parenchyma tissue in Fig. 6(a) and (b) have the same spread along the horizontal direction, and their spreads along the vertical direction decrease when the tumors are located away from the center.

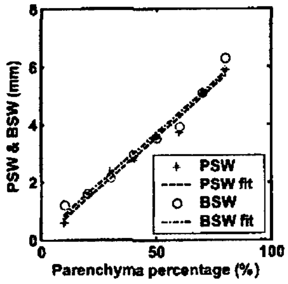

Fig. 8. Quantitative results of the point-spread width and boundary-spread width along the horizontal direction in eight simulations in which the mean radius of the parenchyma wall changes from 0.1 to 0.8 of the breast radius using a step of 0.1. The corresponding linear fittings of PSW (dashed) and BSW (dash-dotted) are in good agreement with the proposed formula (30).

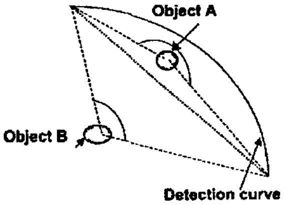

Fig. 9. Diagram showing that in TAT a π or wider view can provide complete data for reconstruction. A view means the angle subtended by the detection curve when observed from the to-be-imaged object. Object A has a view larger than π, and object B has a view less than π.

Fig. 8 shows the quantitative results (with an error of ±0.8 mm) of the PSW and BSW along the horizontal direction in eight simulations in which the radius changes from 0.1 to 0.8 of the breast radius with a step of 0.1. The corresponding linear fitting results for the PSW and BSW are shown as dashed and dash-dotted lines, respectively. The slopes of the two lines are 0.071 and 0.0705, respectively, both of which are close to the estimated rate of 0.07 derived from (30) after substituting the parameters used in our simulations, the radius of the breast $r_b = 50$ mm and $\alpha = 0.07$.

Another interesting point in Fig. 6 is that the PSW of the objects outside the parenchyma tissue are affected little by acoustic heterogeneity. Only minor artifacts are observed near them. This is because in TAT a π or wider view can provide complete data for reconstruction [34]. Here, a view means the angle subtended by the detection curve when observed from the to-be-imaged object. For example, object A in Fig. 9 has a view larger than π, and object B's is less than π. If an object is outside the parenchyma tissue, it has at least a π-view detection range in which the medium between the object and the detectors is acoustically homogeneous. Therefore, a perfect image can be reconstructed from this part of the data. On the other hand, the image reconstructed from the part of signals that experience the heterogeneous medium is weak in amplitude because the flight-time errors compromise the build-up strength of the signals.

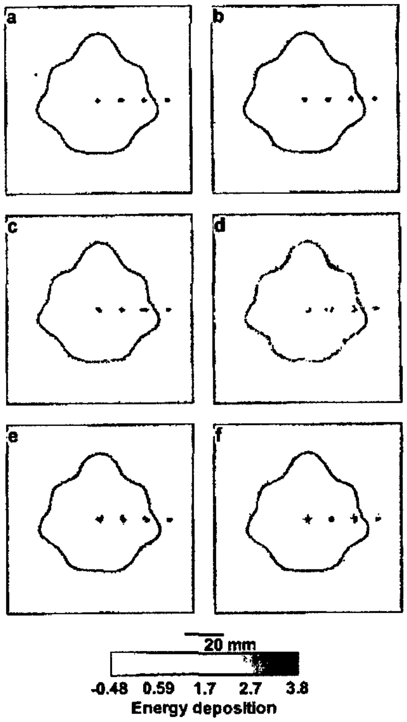

Fig. 10. (a) Compensation for the degradation in images when complete acoustic heterogeneity information is included in the reconstructions. (b) Only exact v_p, v_f, and Σ are included to show the insensitivity of improvement to a random component of the acoustic-velocity distribution. (c) and (d) Images in which there are (c) 1% and (d) 3% errors in v_p, respectively. (e) Images in which Σ is scaled down by 10%. (f) Images in which 20% random error is introduced in Σ. These results show the stability of the improvement to the errors in v_p, v_f, and Σ.

In addition to blurring of images, acoustic heterogeneity increases the background noise level and decreases the values of reconstructed tumors, which consequently reduces the contrast of tumors in the images and the detectability of small tumors. A comprehensive quantitative study of this issue will depend on the SNR of the hardware of the imaging system, the parameters of the imaging system and reconstruction algorithms, and the contrast of the to-be-imaged objects. Meaningful conclusions should be made based on relevant experimental data which we leave for future study.

B. Reconstruction with the Consideration of Heterogeneity

The exact distribution of acoustic velocity is included in the model in Fig. 10(a). Although the result is good, it is not practical, because it is not feasible to obtain the exact distribution of velocity in the breast by current technology. A much more practical situation is when the mean velocities v_f, v_p, and boundary profile Σ are approximately known and the velocity fluctuation within each area is un-

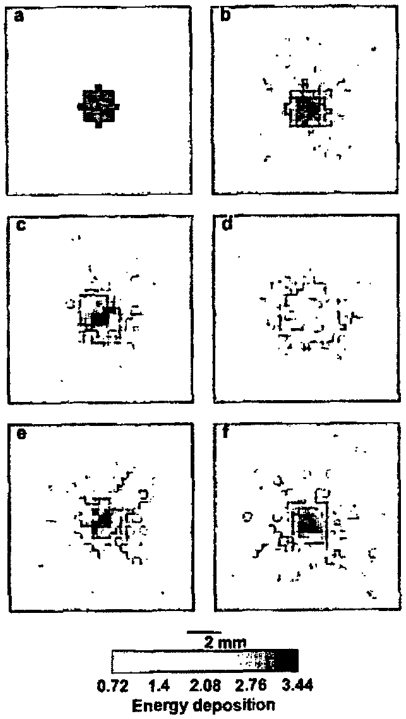

Fig. 11. (a)–(f) Close-up images around the central tumor in Fig. 10. Compensation for the degradation in images when complete acoustic heterogeneity information is included in the reconstructions. (b) Only exact v_p, v_f, and Σ are included to show the insensitivity of improvement to a random component of the acoustic-velocity distribution. (c) and (d) Images in which there are (c) 1% and (d) 3% errors in v_p, respectively. (e) Image in which Σ is scaled down by 10%. (f) Image in which 20% random error is introduced in Σ.

known. Different approaches to obtain v_f, v_p, and boundary profile Σ will be explored in Section VI. Here, we will show the effectiveness of our compensation method. Figs. 10(b)–(f) show the images reconstructed from the same data as in Fig. 10(a), but the reconstruction algorithm used only v_f, v_p, and Σ to study the effects of the measurement errors in v_f, v_p, and Σ on the improvement. In Figs. 10(b)–(f), the random component of the acoustic-velocity distribution is ignored. In addition, v_p is decreased by 1% and 3% in Figs. 10(c) and (d), respectively; Σ is scaled down by 10% in Fig. 10(e); and a 20% random error is introduced to Σ in Fig. 10(f). Figs. 11(a)–(f) are the corresponding close-up images around the central tumor in Fig. 10. The r_p in these simulations is 0.6 of the breast radius, and the distortion amplitude of the parenchyma wall is 0.2.

1. Effect of Errors in Velocities: There is little difference between the resolution of the reconstructed images when we consider [Fig. 11(a)] and do not consider [Fig. 11(b)] the random component of velocity distribution, although the artifacts in the background in Fig. 11(b) are a little stronger than those in Fig. 11(a). The good resolution, after ignoring the random component of the acoustic-velocity distribution in Fig. 11(b), can be explained by modifying (30) to:

$$w = \int_{B_1 B_2} \alpha(\mathbf{r}'') dl_p, \qquad (31)$$

where $\alpha(\mathbf{r}'') = 1 - v_{s0}/v_p(\mathbf{r}'')$ and is spatially dependent; the integration is over the line B_1B_2 in Fig. 7. It can be found that the contributions of the random component of velocity are canceled in some degree after the integration over an acoustic ray.

Comparing Figs. 11(c) and (d) with Fig. 11(b), it can be noticed that a 1% error in v_p does not degrade the imaging quality much, but a 3% error in v_p greatly deteriorates the imaging resolution and contrast. This is because in our model the difference between v_f and v_p is about 7% of their speeds, and a 3% error in v_p actually accounts for 42% of the difference between v_f and v_p. Therefore, we conclude that an accuracy of 1% in the determination of v_p is sufficient for significant improvement in imaging resolution.

2. Effects of Errors in Determining Σ: In the model in Fig. 11(e), the boundary Σ is scaled down by 10%. In Fig. 11(f), a random component is added to the real boundary, which is implemented by multiplying the real radii of a boundary with uniform random numbers within [0.8, 1.2]. After comparing Figs. 11(e) and (f) with other components of Fig. 11, it is found that compensation is less sensitive to error in determining Σ as v_p. This is because a 10% error, which is about 6 mm in the diameter of the parenchyma wall, adds an error of at most 0.42 mm to the PSW and BSW according to (30).

VI. DISCUSSION

A. Effect of Small Fat Lobules

In breast UT, centimeter-scale fat lobules in the parenchyma tissue also can cause significant distortion. In breast TAT, the amplitude distortion due to centimeter-scale fat lobules is estimated to be insignificant because of the diffraction effect, as discussed in Section III-A,2. For example, substituting $a = 1$ cm, $\lambda = 1.5$ mm in (13), we obtain a near-field length of 6.7 cm. Therefore, no strong amplitude distortion is expected when detectors are placed farther than 6.7 cm from the lobule. In addition, Figs. 6 (b)–(d) show that the images of point sources outside an acoustic heterogeneity are affected little by the acoustic heterogeneity due to the completeness of the π-view detection in TAT. This explanation also can be applied to the distortion caused by fat lobules. When a fat lobule on one side of an acoustic source causes severe distortion, the signals that are spared from severe distortion in other directions still can produce good images.

B. Determine v_f and v_p in Experiments

Our simulation results in Fig. 10(c) and Fig. 11(c) show that a 1% error in v_f and v_p will lead to minor blurring but that we still have enough definition to determine the configuration and location of the imaged objects. To determine v_f and v_p within 1% accuracy, we can try different speeds around the averages, which are 1437 m/s and 1546 m/s for fat and breast tissue, respectively, with a step size of 1% velocity. Optimum speeds can be determined by choosing the reconstructed image with the sharpest parenchyma wall, because errors in v_f and v_p will cause the spread of this boundary. Because the variations of v_f and v_p between individuals are about 2% and 4%, respectively, only 15 trials are needed to scan all the combinations. Furthermore, the backprojection method [12] can be used in each trial because the boundary of the reconstructed image can be recovered well with this method [34], [35]. Therefore, the additional computation cost in the trials is estimated to be only double the total computation complexity.

C. Determine Σ in Experiments

There are two ways to obtain Σ. The first method uses only TAT signals. It takes advantage of the fact that fat and parenchyma have both acoustic and microwave contrasts. A TAT image is first reconstructed with an acoustically homogeneous model. Then an approximate Σ can be extracted from the image and plugged into an acoustically heterogeneous reconstruction model to obtain a more accurate TAT image. As shown in Fig. 6, the boundary spread of the parenchyma wall in TAT images is at most 7% of its real size (if $\alpha = 0.07$) when an acoustically homogeneous reconstruction model is used. Our studies of the effects on the reconstruction of the errors in the boundary profile, shown in Fig. 10(e) and Fig. 11(e), reveal that this level of error has little effect on the images reconstructed from a heterogeneous model. We intend to implement this method in our future work.

The second method for determining Σ is the coregistration of ultrasound B-scan imaging and TAT. In principle, this can be accomplished in the same set-up. The TAT data is acquired, then the transducers work in pulse-echo mode to determine an approximate Σ. This boundary information can be included in the reconstruction algorithm of TAT.

D. Differences Between TAT and UT

The studies we presented in Section III show that there should be no severe amplitude distortion in breast TAT, but severe amplitude distortion caused by refraction has been observed in both narrowband and broadband breast UT [15]. The difference between the effects of acoustic heterogeneity on TAT and UT can be explained by the different central frequencies. In UT, the central frequency is above 3 MHz, and in TAT the central frequency is below 1 MHz. The higher frequency in UT results in stronger wavefront distortion due to the following reasons. First, the scattering effect increases rapidly with frequency; second, the minimum detection distance for avoiding strong amplitude distortion caused by an acoustic lens, which can be a boundary segment or a small inclusion, extends farther with increasing frequency. Substituting the following parameters for UT, $l_{SB_1} < 10$ cm, $\lambda = 0.5$ mm, and $\alpha = 0.07$ into (20), we have $l_{B_1D} > 9.8$ cm. We notice that the transducer or array was placed closer than the required distance to the breast [15], [16]. Therefore, it is not surprising to observe the strong interference effect in UT.

Another important difference between TAT and UT is that there is no speckle in our TAT images [11]. Speckle is an important factor limiting the quality of pure ultrasonic imaging. In our technology, the detected signals are primary acoustic waves rather than reflective or scattered waves as in UT. Furthermore, the temporal frequency of the acoustic signals lies in a range from 0 to 1.5 MHz, which is only weakly scattered in the tissues. However, the issue of image speckle in more realistic medical imaging applications is a topic for future consideration.

E. Miscellaneous

Our analysis and numerical simulations have shown that breast TAT images can survive acoustic heterogeneity. The ultimate test, however, will come from clinical experiments on the breast in which the motion artifacts due to breathing and cardiac movement may introduce blurring. Such blurring of images is estimated to be on the order of the movement amplitude. To correct the blurring, we can monitor the breast motion, for example, placing a microwave absorber on the breast surface as a marker. Then the data on the breast motion can be used in the reconstructions to shift the detectors' positions and, consequently, compensate for the breast's displacement.

VII. CONCLUSIONS

The effects of acoustic heterogeneity on TAT in the breast are studied. Our analysis shows that the amplitude distortion in the breast TAT is minor. There is no multipath interference in the breast TAT with a convex parenchyma wall, and the amplitude distortion also is not severe for concave boundary, because the TAT signals are broadband, have low central frequency, and experience only one-way transmission through the parenchyma wall. Therefore we consider only phase distortion in our numerical studies. The numerical results on the spread of point sources and boundaries caused by the phase distortion are in good agreement with the predictions of the proposed formula. It is shown that phase distortion can be compensated for when complete or partial information on the distribution of acoustic velocity in the breast is included in the reconstruction. It is found that improvement in the results is more sensitive to measurement error in v_f, v_p than Σ. Based on this sensitivity study, an approach to implement our compensation method using only TAT data is proposed. The differences between breast TAT and breast ultrasound imaging in relation to the effects of acoustic heterogeneity and speckles are accounted for by differences in their central frequency of ultrasound and detection configuration.

Appendix A
Derivation of (11)

Assume that the concave boundary can be approximated by an arch with a radius $R_l > a$, where a is half the size of the boundary segment. Two rays are refracted at points B_1 and B_2 in Fig. 4, where B_2 has a small displacement from B_1 along the boundary. According to the refraction law, we have:

$$\begin{aligned} \sin\theta_1 &= (1-\alpha)\sin\phi_1, \\ \cos\theta_1 d\theta_1 &= (1-\alpha)\cos\phi_1 d\phi_1, \end{aligned} \tag{32}$$

where $d\phi_1$ is the difference between the incidence angles of the two rays and $d\theta_1$ is the transmission one. They can be expressed as:

$$\begin{aligned} d\theta_1 &= \left(1 - \frac{R_l\cos\theta_1}{l_{B_1D}}\right)d\theta, \\ d\phi_1 &= \left(\frac{R_l\cos\phi_1}{l_{SB_1}} + 1\right)d\theta, \end{aligned} \tag{33}$$

where l_{SB_1} and l_{B_1D} are the distances from the boundary point B_1 to source S and detector D, respectively, and $d\theta = l_{B_1B_2}/R_l$. Combining the above equations, we have the imaging formula for the boundary segment:

$$\frac{\cos^2}{l_{SB_1}} + \frac{\cos^2\theta_1}{l_{DB_1}(1-\alpha)} = \frac{\cos\theta_1/(1-\alpha) - \cos\phi_1}{R_l}. \tag{34}$$

Because in our breast model $\alpha \approx 0.1$ is small, the above equation can be further simplified to (11) after using $\theta_1 \approx \phi_1$.

Appendix B
Derivation of (30)

The first iteration in TCG is equivalent to the backprojection method [34]. In backprojection for an acoustically homogeneous TAT, $p(\mathbf{r}, t)$, the signal detected at $\mathbf{r}$ and time t is projected back to a sphere with a radius of tv_{s0} and a center at $\mathbf{r}$. It is shown that the boundaries of objects can be reconstructed correctly with the backprojection method [35]. Let us consider a model illustrated in Fig. 7 to estimate the spread of source S along line D_1D_2, where D_1 and D_2 are two detectors, S_1 is the intersection of D_1D_2 with the backprojection arch of the signal transmitted by source S and detected by detector D_1, S_2 is the corresponding one at D_2, and Σ represents the parenchyma wall. If there is no error in computing TOFs, S_1, S_2, and S will be one point; therefore, a point image of source S can be recovered. In an acoustically heterogeneous model, however, the flight-time errors caused by the approximation of v_p by v_{s0} in the reconstruction result in the splitting of S_1 and S_2 from S, where l_{S_1S} and l_{S_2S} can be estimated by the multiplication of the flight-time errors with v_{s0}, $l_{S_1S} = l_{B_1S}(1 - v_{s0}/v_p) = \alpha l_{B_1S}$ and $l_{S_2S} = l_{B_2S}(l - v_{s0}/v_p) = \alpha l_{B_2S}$. Combining them, we have (30) for the spread width of source S along line D_1D_2. Similar analysis can be applied to estimating BSW as well.

Acknowledgments

We would like to thank Dr. Q. Zhu for many useful discussions. We also are indebted to the anonymous reviewers, whose constructive comments lead us to a more comprehensive investigation of the problem.

References

[1] W. Joines, R. Jirtle, M. Rafal, and D. Schaeffer, "Microwave power absorption differences between normal and malignant tissue," *Radiation Oncology-Biology-Physics*, vol. 6, pp. 681–687, 1980.

[2] S. Chaudhary, R. Mishra, A. Swarup, and J. Thomas, "Dielectric properties of normal human breast tissues at radiowave and microwave frequencies," *Indian J. Biochem. Biophys.*, vol. 21, pp. 76–79, 1984.

[3] W. Joines, Y. Zhang, C. Li, and R. Jirtle, "The measured electrical properties of normal and malignant human tissues from 50–900 MHz," *Med. Phys.*, vol. 21, pp. 547–550, 1994.

[4] L. E. Larsen and J. H. Jacobi, Eds. *Medical Applications of Microwave Imaging*. Piscataway, NJ: IEEE Press, 1986.

[5] S. Caorsi, A. Frattoni, G. L. Gragnani, E. Nortino, and M. Pastorino, "Numerical algorithm for dielectric-permittivity microwave imaging of inhomogeneous biological bodies," *Med. Biol. Eng. Comput.*, vol. NS-29, pp. 37–44, 1991.

[6] M. S. Hawley, A. Broquetas, L. Jofre, J. C. Bolomey, and G. Gaboriaud, "Microwave imaging of tissue blood content changes," *J. Biomed. Eng.*, vol. 13, pp. 197–202, 1991.

[7] P. M. Meaney, K. D. Paulsen, and J. T. Chang, "Near-field microwave imaging of biologically-based materials using a monopole transceiver system," *IEEE Trans. Microwave Theory Tech.*, vol. 46, pp. 31–45, 1998.

[8] R. A. Kruger, P. Liu, Y. R. Fang, and C. R. Appledorn, "Photoacoustic ultrasound (PAUS)—reconstruction tomography," *Med. Phys.*, vol. 22, pp. 1605–1609, 1995.

[9] C. G. A. Hoelen, F. F. M. Demul, R. Pongers, and A. Dekker, "Three-dimensional photoacoustic imaging of blood vessels in tissue," *Op. Lett.*, vol. 23, pp. 648–650, 1998.

[10] G. Ku and L.-H. V. Wang, "Scanning thermoacoustic tomography in biological tissue," *Med. Phys.*, vol. 27, pp. 1195–1202, 2000.

[11] Y. Xu, D. Feng, and L.-H. V. Wang, "Exact frequency-domain reconstruction for thermoacoustic tomography: I. Planar geometry," *IEEE Trans. Med. Imag.*, vol. 21, pp. 823–828, 2002.

[12] M. Xu and L.-H. V. Wang, "Time-domain reconstruction for thermoacoustic tomography in a spherical geometry," *IEEE Trans. Med. Imag.*, vol. 21, pp. 814–822, 2002.

[13] Y. Xu, M. Xu, and L.-H. V. Wang, "Exact frequency-domain reconstruction for thermoacoustic tomography: II. Cylindrical geometry," *IEEE Trans. Med. Imag.*, vol. 21, pp. 829–833, 2002.

[14] M. Moshfeghi and R. C. Waag, "In vivo and in vitro ultrasound beam distortion measurements of a large aperture and a conventional aperture focused transducer," *Ultrasound Med. Biol.*, vol. 5, pp. 415–428, 1988.

[15] Q. Zhu and B. D. Steinberg, "Large-transducer measurements of wavefront distortion in the female breast," *Ultrason. Imag.*, vol. 14, pp. 276–299, 1992.

[16] C. W. Manry and S. L. Broschat, "FDTD simulations for ultrasound propagation in a 2-D breast model," *Ultrason. Imag.*, vol. 18, pp. 25–34, 1996.

[17] P. D. Freiburger, D. C. Sullivan, B. H. Leblanc, S. W. Smith, and G. E. Trahey, "Two dimensional ultrasonic beam distortion in the breast: In vivo measurements and effects," *Ultrason. Imag.*, vol. 14, pp. 398–414, 1992.

[18] S. W. Flax and M. O'Donnell, "Phase aberration correction using signals from point reflectors and diffuse scatterers: Basic principles," *IEEE Trans. Ultrason., Ferroelect., Freq. Contr.*, vol. 35, pp. 758–767, 1988.

[19] G. E. Trahey, D. Zhao, J. A. Miglin, and S. W. Smith, "Experimental results with a real-time adaptive ultrasonic imaging system for viewing through distorting media," *IEEE Trans. Ultrason., Ferroelect., Freq. Contr.*, vol. 37, pp. 418–427, 1990.

[20] Q. Zhu and B. D. Steinberg, "Deaberration of incoherent wavefront distortion: An approach toward inverse filtering," *IEEE Trans. Ultrason., Ferroelect., Freq. Contr.*, vol. 44, pp. 575–589, 1997.

[21] Y. Xu and L.-H. V. Wang, "Signal processing in scanning thermoacoustic tomography in biological tissues," *Med. Phys.*, vol. 28, pp. 1519–1524, 2001.

[22] P. C. Hansen, *Rank-Deficient and Discrete Ill—Posed Problems.* Philadelphia, PA: SIAM Press, 1998.

[23] A. V. Oppenheim and J. S. Lim, "The importance of phase in signals," *Proc. IEEE*, pp. 529–541, 1981.

[24] B. D. Steinberg, "A theory of the effect of hard limiting and other distortions upon the quality of microwave images," *IEEE Trans. Acoust. Speech Signal Processing*, vol. ASSP-35, pp. 1462–1472, 1987.

[25] V. E. Gusev and A. A. Karabutov, *Laser Optoacoustics.* New York: American Institute of Physics, 1993.

[26] A. R. Selfridge, "Approximate properties in isotropic materials," *IEEE Trans. Sonics Ultrason.*, vol. SU-32, pp. 381–394, 1985.

[27] F. S. Foster, M. Strban, and G. Austin, "The ultrasound microscope: Initial studies of the breast tissue," *Ultrason. Imag.*, vol. 6, pp. 243–261, 1984.

[28] M. Born and E. Wolf, *Principles of Optics.* New York: Cambridge University Press, 1997.

[29] L. A. Chernov, *Wave Propagation in a Random Medium.* New York: Dover, 1960.

[30] G. Kossoff, E. K. Fry, and J. Jellins, "Average velocity of ultrasound in the human female breast," *J. Acoust. Soc. Amer.*, vol. 53, pp. 1730–1736, 1973.

[31] R. Sneider and D. F. Aldridge, "Perturbation theory for travel times," *J. Acoust. Soc. Amer.*, vol. 98, pp. 1565–1569, 1995.

[32] H. P. William, A. T. Saul, T. V. William, and P. F. Brian, *Numerical Recipes in C.* Cambridge: Cambridge Univ. Press, 1992.

[33] J. F. Greenleaf and R. C. Bahn, "Clinical imaging with transmissive ultrasonic computerized tomography," *IEEE Trans. Biomed. Eng.*, vol. BME-28, no. 2, pp. 177–185, 1981.

[34] Y. Xu and L.-H. V. Wang, "Limited-view thermoacoustic tomography and reconstruction by truncated-conjugate gradient," *IEEE Trans. Med. Imag.*, submitted for publication.

[35] A. K. Louis and E. T. Quinto, "Local tomographic methods in sonar," in *Surveys on Solution Methods for Inverse Problems.* Vienna: Springer, 2000, pp. 147–154.

Yuan Xu was born in Guangshui, China in 1971, received his Ph.D. degree in physics from the Institute of Physics, Chinese Academy of Sciences, Beijing, China, in 1999. He is studying for a Ph.D. degree in Biomedical Engineering at Texas A&M University, College Station, Texas.

His research interest is thermoacoustic tomography.

Lihong V. Wang (M'96–SM'00) was born in Guangshui, China on March 8, 1964, received his Ph.D. degree in electrical engineering from Rice University, Houston, TX, in 1992.

Dr. Wang worked for Dr. Steven Jacques initially as a postdoctoral research associate and was shortly promoted to assistant professor at the University of Texas M. D. Anderson Cancer Center, Houston, TX, a top-ranked cancer institution. He was promoted to professor in biomedical and electrical engineering, Texas A&M University, College Station, TX, in 2002.

He is a senior member of the Institute of Electrical and Electronics Engineers (IEEE), and a member of the American Physical Society (APS), Society of Photo-Optical Instrumention Engineers (SPIE), Optical Society of America (OSA), and Engineering in Medicine and Biology Society (EMBS). He received the National Institutes of Health (NIH) First award, National Science Foundation (NSF) Career award, Johnson & Johnson Outstanding Young Scientist award, Texas A&M Texas Engineering Experiment Station (TEES) Select Young Faculty award, Texas A&M TEES Faculty Fellow award (twice), Texas A&M Ernest A. Baetz Faculty Fellow award, and Texas A&M University Faculty Fellow award. He is listed in *Who's Who in Science and Engineering.* He served as a grant reviewer for NIH, NSF, the Navy, and other funding agencies. He is an associate editor for the *Annals of Biomedical Engineering*, *Journal of Biomedical Optics*, and *Applied Optics*.

VOLUME 92, NUMBER 3 PHYSICAL REVIEW LETTERS week ending 23 JANUARY 2004

Time Reversal and Its Application to Tomography with Diffracting Sources

Yuan Xu and Lihong V. Wang*
Optical Imaging Laboratory, Department of Biomedical Engineering, Texas A&M University,
3120 TAMU, College Station, Texas 77843-3120, USA

(Received 22 August 2003; published 23 January 2004)

An exact time-domain method is proposed to time reverse a transient scalar wave using only the field measured on an arbitrary closed surface enclosing the initial source. Under certain conditions, a time-reversed field can be approximated by retransmitting the measured signals in a reversed temporal order. Exact reconstruction for three-dimensional broadband diffraction tomography (a linearized inverse scattering problem) is proposed by time-reversing the measured field back to the time when each secondary source is excited. The algorithm is verified by a numerical simulation. Extension to the case using Green's function in a heterogeneous medium is discussed.

DOI: 10.1103/PhysRevLett.92.033902 PACS numbers: 42.30.Wb, 42.25.Fx

Time reversal of an acoustic or electromagnetic wave is based on the invariance of the wave equation in a lossless medium under the transform $t \rightarrow -t$ (t represents the time). Time reversal of a wave can be understood as generating the back-propagation field from the measured forward-propagation field and/or its normal derivative after removing the initial sources. The concept of time reversal has been implemented experimentally and applied to a wide range of studies such as inverse scattering [1], wave-front distortion correction [2,3], and multiple scattering phenomena [4].

However, no formula is available for computing the time-reversed (TR) field using only the measured field on a closed surface enclosing the initial source. When both the field and its normal gradient on a closed surface are available, there are formulas [3,5] to derive the TR field. However, it is not practical to measure both the field and its normal gradient simultaneously. For example, the output signal from a piezoelectric transducer is generally a complex combination of these two effects. There are two challenges in deriving the TR field using only the field. First, it is not obvious that Green's function, which is widely used to derive the field in space from the field on a closed surface, can be applied here. This is because the TR field on the closed surface includes both diverging and converging components [3,5]. While the converging component of the TR wave is just the measured signals in the forward propagation in a reversed temporal order (RTO), the diverging component has no counterpart in the forward propagation and, consequently, is not available from measurement in general. Second, in a free space, retransmission of the measured signals in RTO from the detection surface does not reproduce the TR field. This is because the waves retransmitted in one position propagate to the other positions on the surface and change the field there, and, consequently, the field on the surface does not equal the field in the forward propagation in RTO.

In this Letter, we find that when time reversal is considered in the time domain, an exact time-reversal method that uses only the field on an arbitrary closed surface can be derived for a wide variety of applications such as tomography with diffracting sources, inverse diffraction, and ultrasound therapy. Under certain conditions, a TR field can be approximated by retransmitting the measured signals in RTO in a free space. Acoustic waves are used as an example to present our results and methods, but their application to other scalar or vector waves is straightforward.

Next, we show that exact reconstruction for broadband diffraction tomography (DT) in a weakly scattering medium can be essentially represented by a time-reversal process in a homogeneous medium. Although exact reconstruction algorithms have been proposed for DT in some special geometries [6], no exact algorithm for broadband DT using only pressure measured on an arbitrary closed surface has been proposed. In the forward problem of our DT model, the objects [shaded in (Fig. 1)] are irradiated by an illuminating source of $\delta(t)\delta(\mathbf{r} - \mathbf{r}_s)$ at $\mathbf{r}_s$, and the scattered field is measured on an arbitrary closed surface Σ enclosing the objects to reconstruct their heterogeneity. This DT model is a single-view one; therefore, it is very efficient for collecting data. The total field $\bar{p}_t(\mathbf{r}, \omega)$ in an acoustically heterogeneous medium is [7]

$$\bar{p}_t(\mathbf{r}, \omega) = \bar{p}_{\text{in}}(\mathbf{r}, \omega) + \int_R d\mathbf{r}_1 k^2 \gamma(\mathbf{r}_1) \bar{p}_t(\mathbf{r}_1, \omega) G_\omega(\mathbf{r}|\mathbf{r}_1), \tag{1}$$

where $G_\omega(\mathbf{r}|\mathbf{r}_0) = \exp(-i\omega|\mathbf{r} - \mathbf{r}_0|/v_s)/(4\pi|\mathbf{r} - \mathbf{r}_0|)$,

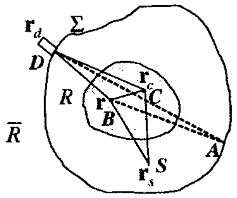

FIG. 1. Illustration of diffraction tomography. S represents the illuminating source, D represents a detector scanning across surface Σ, and the to-be-imaged object is shaded. R and $\bar{R}$ are the spaces inside and outside Σ, respectively.

© 2004 The American Physical Society

$\bar{p}_{\text{in}}(\mathbf{r}, \omega) = G_\omega(\mathbf{r}|\mathbf{r}_s)/2\pi$ is the temporal spectrum of the incidence field, ω is the temporal angular frequency, $k = \omega/v_s$, $\gamma(\mathbf{r}) = (\kappa - \kappa_0)/\kappa_0$ describes the normalized deviation of compressibility κ from the average κ_0, and v_s is the acoustic speed corresponding to κ_0. Equation (1) can be rewritten as

$$\bar{\varphi}_n(\mathbf{r}, \omega) = \int_R d\mathbf{r}_1 \gamma(\mathbf{r}_1) \bar{p}_t(\mathbf{r}_1, \omega) G_\omega(\mathbf{r}|\mathbf{r}_1)/v_s, \tag{2}$$

where $\bar{\varphi}_n(\mathbf{r}, \omega) = [\bar{p}_t(\mathbf{r}, \omega) - \bar{p}_{\text{in}}(\mathbf{r}, \omega)]v_s/\omega^2$. Equation (2) shows that point $\mathbf{r}_1$ of the objects can be considered as a secondary source $\gamma(\mathbf{r}_1)\bar{p}_t(\mathbf{r}_1, \omega)/v_s$ for $\bar{\varphi}_n$. In our reconstruction of DT, we first time reverse $\bar{\varphi}_n$ back to time $t_e(\mathbf{r}) = |\mathbf{r} - \mathbf{r}_s|/v_s$ at point $\mathbf{r}$ [$t_e(\mathbf{r})$ is the time the secondary source at $\mathbf{r}$ is excited] and then derive the heterogeneity. Here, we first derive the formulas for time reversing a wave in a homogeneous medium and treat DT under first Born approximation (FBA), which involves replacing $\bar{p}_t(\mathbf{r}_1, \omega)$ with $\bar{p}_{\text{in}}(\mathbf{r}_1, \omega)$ on the right-hand side of (2). Then the extensions to the case using Green's function in a heterogeneous medium are discussed.

We start from the wave equation for pressure $p_0(\mathbf{r}, t)$ in a nonabsorbing and nondispersive medium [8]

$$\nabla^2 p_0(\mathbf{r}, t) - \frac{1}{v_s^2}\frac{\partial^2 p_0(\mathbf{r}, t)}{\partial t^2} = -q(\mathbf{r}, t), \tag{3}$$

where $q(\mathbf{r}, t)$ is the source term and is nonzero only in R [the space enclosed by the detection surface Σ (Fig. 1)] and within the time period $[0, T_s]$. We have

$$p_0(\mathbf{r}, t) = \int_0^{T_s} dt_0 \int_R d\mathbf{r}_0 q(\mathbf{r}_0, t_0) g_+(\mathbf{r}, t|\mathbf{r}_0, t_0), \tag{4}$$

where $g_\pm(\mathbf{r}, t|\mathbf{r}_0, t_0) = \delta(t - t_0 \mp |\mathbf{r} - \mathbf{r}_0|/v_s)/(4\pi|\mathbf{r} - \mathbf{r}_0|)$ is a diverging (g_+) or converging (g_-) Green's function.

Time reversal of $p_0(\mathbf{r}, t)$ at time T_0 is defined as

$$p_r(\mathbf{r}, T_0) = p_0(\mathbf{r}, T_0), \qquad p_r'(\mathbf{r}, T_0) = -p_0'(\mathbf{r}, T_0), \tag{5}$$

where the prime represents the temporal derivative in this Letter, $p_r(\mathbf{r}, t)$ is the TR field of $p_0(\mathbf{r}, t)$, and T_0 is chosen to be large enough so that $p_0(\mathbf{r}, t) = 0$ for $\mathbf{r} \in R$, $t \geq T_0$. Then, $p_r(\mathbf{r}, t)$ can be uniquely determined by the initial conditions at T_0. The above definition of time reversal is analogous to the fact that a particle moves back along its trajectory if its velocity is reversed and its position is unchanged. According to this definition, we mean $p_r(\mathbf{r}, \hat{t})$ when we say time reversing a field back to time t, where a hat over a time variable t represents $2T_0 - t$.

In the case of a point source $\delta(\mathbf{r} - \mathbf{r}_0)\delta(t - t_0)$ in R, Eq. (5) becomes $g_r(\mathbf{r}, T_0|\mathbf{r}_0, t_0) = g_+(\mathbf{r}, T_0|\mathbf{r}_0, t_0)$, $g_r'(\mathbf{r}, T_0|\mathbf{r}_0, t_0) = -g_+'(\mathbf{r}, T_0|\mathbf{r}_0, t_0)$. It can easily be verified that the TR field

$$g_r(\mathbf{r}, t|\mathbf{r}_0, t_0) = g_-(\mathbf{r}, t|\mathbf{r}_0, \hat{t}_0) - g_+(\mathbf{r}, t|\mathbf{r}_0, \hat{t}_0), \qquad t \geq T_0, \tag{6}$$

because it satisfies both the homogeneous wave equation and the initial-value conditions shown above. This result is also obtained by Cassereau [3] and Porter [5]. Equation (6) shows that if we time reverse at T_0, the field of a point source which is located at $\mathbf{r}_0$ and excited at t_0, the TR field converges to $\mathbf{r}_0$ at time $\hat{t}_0$, and then diverges with an opposite amplitude. The diverging wave $g_+(\mathbf{r}, t|\mathbf{r}_0, \hat{t}_0)$, however, does not have a counterpart in the forward propagation. It exists because, unlike the forward propagation, there is no source inside Σ for $g_r(\mathbf{r}, t)$. The diverging wave with an opposite amplitude exactly cancels the source term related to the converging one.

In the case of an arbitrary source, similar results can be obtained after considering the linearity of the wave equation with respect to the source

$$p_r(\mathbf{r}, t) = \int_0^{T_s} dt_0 \int_R d\mathbf{r}_0 q(\mathbf{r}_0, t_0) g_r(\mathbf{r}, t|\mathbf{r}_0, t_0). \tag{7}$$

After substituting (6) into (7), using $g_-(\mathbf{r}, t|\mathbf{r}_0, t_0) = g_+(\mathbf{r}, -t|\mathbf{r}_0, -t_0)$, and variable transform, we have for $\mathbf{r}_d \in \Sigma$ (although it is valid for any $\mathbf{r}$)

$$p_r(\mathbf{r}_d, t) = p_0(\mathbf{r}_d, 2T_0 - t) + p_{\text{div}}(\mathbf{r}_d, t), \tag{8}$$

$$p_{\text{div}}(\mathbf{r}_d, t) = -\int_{2T_0 - T_s}^{2T_0} dt_0 \int_R d\mathbf{r}_0 q(\mathbf{r}_0, \hat{t}_0) g_+(\mathbf{r}_d, t|\mathbf{r}_0, t_0). \tag{9}$$

As in the case of a point source, the diverging component $p_{\text{div}}(\mathbf{r}_d, t)$ has no counterpart in the forward propagation and is, in general, not available from the experimental measurements of p_0 except in some special cases. Nevertheless, we show that $p_r(\mathbf{r}, t)$ before a specified time can be derived using only $p_0(\mathbf{r}_d, t)$.

Since there is no source for $p_r(\mathbf{r}, t)$ and $p_r(\mathbf{r}, T_0) = 0$ in R, $p_r(\mathbf{r}, t)$ in R can be expressed in terms of the field on Σ [9]:

$$p_r(\mathbf{r}, t) = -\int_{T_0}^{t^+} dt_0 \oint_\Sigma dS_d p_r(\mathbf{r}_d, t_0) \frac{\partial g_1(\mathbf{r}, t|\mathbf{r}_d, t_0)}{\partial n}, \tag{10}$$

where $\partial/\partial n$ is the derivative along the normal of Σ at $\mathbf{r}_d$ pointing away from the volume R, $g_1(\mathbf{r}, t|\mathbf{r}_0, t_0)$ with $\mathbf{r}, \mathbf{r}_0 \in (R \cup \Sigma)$ is Green's function subject to the homogeneous Dirichlet boundary condition on Σ [10], and t^+ is infinitesimally greater than t. Here, we show that $p_{ro}(\mathbf{r}, t)$, the contribution of $p_{\text{div}}(\mathbf{r}_d, t_0)$ to the right-hand side of (10), is zero before a specified time. After inserting (9) into (10), we have

$$p_{ro}(\mathbf{r}, t) = \int_{T_0}^{t^+} dt_0 \oint_\Sigma dS_d \int_{2T_0 - T_s}^{2T_0} dt_c \int_R d\mathbf{r}_c q(\mathbf{r}_c, \hat{t}_c) g_+(\mathbf{r}_d, t_0|\mathbf{r}_c, t_c) \frac{\partial g_1(\mathbf{r}, t|\mathbf{r}_d, t_0)}{\partial n}. \tag{11}$$

Considering $g_+(\mathbf{r}_d, t_0|\mathbf{r}_c, t_c) = 0$ when $t_0 < t_c + |\mathbf{r}_c - \mathbf{r}_d|/v_s$ and $g_1(\mathbf{r}, t|\mathbf{r}_d, t_0) = 0$ when $t < t_0 + |\mathbf{r} - \mathbf{r}_d|/v_s$, and assuming that $q(\mathbf{r}_c, t_c)$ is nonzero only within the period $[t_{c1}, t_{c2}]$, we conclude that $p_{ro}(\mathbf{r}, t) = 0$ if for any $\mathbf{r}_c \in R$ and $\mathbf{r}_d \in \Sigma$

$$t < 2T_0 - t_{c2} + |\mathbf{r}_d - \mathbf{r}_c|/v_s + |\mathbf{r} - \mathbf{r}_d|/v_s. \qquad (12)$$

Actually, $p_{ro}(\mathbf{r}, t)$ can be shown to be equivalent to the field induced by the reflection of the diverging field $p_{\mathrm{div}}(\mathbf{r}, t)$ by Σ. It contributes only to the late part of $p_r(\mathbf{r}, t)$. In many applications including tomography with diffracting sources and ultrasound therapy, we are interested only in the part of $p_r(\mathbf{r}, t)$ within the range defined by (12). For example, in our DT model, the heterogeneity at point $\mathbf{r}$ in Fig. 1 can be derived from $p_r(\mathbf{r}, \hat{t}_e(\mathbf{r}))$, as is shown in (17). Noticing $|t_e(\mathbf{r}) - t_e(\mathbf{r}_c)| \leq |\mathbf{r} - \mathbf{r}_c|/v_s$ and $t_{c1} = t_{c2} = t_e(\mathbf{r}_c)$, we find that (12) is minimally observed for any $\mathbf{r}_c \in R$ and $\mathbf{r}_d \in \Sigma$ to compute $p_r(\mathbf{r}, \hat{t}_e(\mathbf{r}))$ in DT. Similarly, we find that (12) can easily be met for other applications such as thermoacoustic tomography and ultrasound therapy. Therefore, $p_r(\mathbf{r}, t)$, within the range defined by (12), can be expressed as

$$p_r(\mathbf{r}, t) = -\int_{T_0}^{t^+} dt_0 \oint_{\Sigma} dS_d p_0(\mathbf{r}_d, \hat{t}_0) \frac{\partial g_1(\mathbf{r}, t|\mathbf{r}_d, t_0)}{\partial n}. \qquad (13)$$

Equation (13) shows that the TR field before a certain time in R is equivalent to the field [caused by the retransmission of $p_0(\mathbf{r}_d, t)$ from Σ in RTO] in a reflective cavity (formed by Σ) rather than in a free space. Therefore, the reflections from Σ also contribute to $p_r(\mathbf{r}, t)$. The reason is that the field transmitted in one position on Σ propagates to the other positions on Σ, and, consequently, the field in these positions changes. The reflections from Σ cancel the changes in these positions.

Next, we show that the reflections from Σ are negligible under certain conditions. The central concept is that $g_1(\mathbf{r}, t|\mathbf{r}_d, t_0)$ can be obtained in a model where the boundary Σ serves as a perfect mirror (with a phase shift of π after reflection), and a delta pulse source is launched at $\mathbf{r}_d$ and time t_0. Under the ray approach (geometrical optics approximation), $g_1(\mathbf{r}, t|\mathbf{r}_d, t_0)$ is the summation of the contributions from all the rays that go from $\mathbf{r}_d$ and arrive at $\mathbf{r}$ if the radii of Σ are much larger than the wavelength of the excitation pulse. As shown in Fig. 1, the first ray from $\mathbf{r}_d$ to $\mathbf{r}$ travels along the line connecting $\mathbf{r}_d$ and $\mathbf{r}$. The second ray is first reflected by the boundary at $\mathbf{r}_d$ and then goes to $\mathbf{r}$. Both of them arrive at $\mathbf{r}$ at time $t_0 + |\mathbf{r} - \mathbf{r}_d|/v_s$. The contribution of the first two rays to $\partial g_1/\partial n$ in (13) is $2\partial g_+/\partial n$. Then there are other rays (for example, the dashed line in Fig. 1) that are reflected at other points on the boundary such as A. In DT, it can be shown that when the to-be-reconstructed point $\mathbf{r}$ is near the center of Σ, and $l_{\mathrm{det}} > 2l_{\mathrm{obj}}$, where l_{det} is the average linear dimension of Σ and l_{obj} is the maximum linear dimension of the object, $p_r(\mathbf{r}, \hat{t}_e(\mathbf{r}))$ can be approximated well after replacing $\partial g_1/\partial n$ in (13) with $2\partial g_+/\partial n$ [11]

$$p_r(\mathbf{r}, t) \approx -2\int_{T_0}^{t^+} dt_0 \oint_{\Sigma} dS_d p_0(\mathbf{r}_d, \hat{t}_0) \frac{\partial g_+(\mathbf{r}, t|\mathbf{r}_d, t_0)}{\partial n}. \qquad (14)$$

Equation (14) shows that under certain conditions, time reversal can be approximated well by retransmission of the measured signals in RTO from the detection surface in a free space. Equation (14) also holds for applications other than DT when an appropriate l_{det} is chosen by using the demonstrated method for DT. Equation (14) can be transformed into

$$p_r(\mathbf{r}, t) \approx \frac{1}{2\pi} \oint_{\Sigma} dS_d \frac{\mathbf{n} \cdot (\mathbf{r}_d - \mathbf{r})}{|\mathbf{r} - \mathbf{r}_d|^2} \left[\frac{p_0(\mathbf{r}_d, t_{rd})}{|\mathbf{r} - \mathbf{r}_d|} - p_0'(\mathbf{r}_d, t_{rd})/v_s \right], \qquad (15)$$

where $t_{rd} = 2T_0 - t + |\mathbf{r} - \mathbf{r}_d|/v_s$. Equation (15) is in the form of the well-known delay-and-sum algorithm (backprojection to spheres) used in synthetic aperture imaging. Consequently, the physical meaning and the valid conditions of this widely used algorithm are revealed quantitatively for the first time from basic physics.

Now we discuss the reconstruction in DT. In the forward propagation, the secondary sources (the points of the objects) are not excited at the same time, since the incidence wave reaches different points at different times. Therefore, in the TR field, the diverging waves from some secondary sources mingle with the converging waves from other secondary sources according to (6). Nevertheless, we show that there is a strikingly simple relationship between the TR field and the heterogeneity under FBA. After combining (2), (6), and (7) and the application of inverse Fourier transform, the TR field of $\bar{\varphi}_n(\mathbf{r}, \omega)$ at time $\hat{t}_e(\mathbf{r})$ is

$$\varphi_{nr}(\mathbf{r}, \hat{t}_e(\mathbf{r})) = \int_R d\mathbf{r}_1 \gamma(\mathbf{r}_1) \times \int_{-\infty}^{\infty} dk \exp(-ik|\mathbf{r} - \mathbf{r}_s|) \bar{p}_t(\mathbf{r}_1, -\omega) \times [G_{\omega}^*(\mathbf{r}|\mathbf{r}_1) - G_{\omega}(\mathbf{r}|\mathbf{r}_1)], \qquad (16)$$

where * represents the complex conjugate. After applying FBA and some mathematical manipulations, we have

$$\gamma(\mathbf{r}) = 4 \frac{\partial[|\mathbf{r} - \mathbf{r}_s| \varphi_{nr}(\mathbf{r}, \hat{t}_e(\mathbf{r}))]}{\partial|\mathbf{r} - \mathbf{r}_s|}. \qquad (17)$$

Therefore, the reconstruction in DT can be implemented by first time reversing φ_n to obtain $\varphi_{nr}(\mathbf{r}, \hat{t}_e(\mathbf{r}))$ with (13) or (14), and then obtaining $\gamma(\mathbf{r})$ with (17).

A three-dimensional DT is numerically simulated (Fig. 2). The object is a sphere with a radius of 8 mm at the origin, and to validate FBA, $\gamma(\mathbf{r})$ is set to be 0.01 in the sphere and zero otherwise [12], and v_s is 1.5 km/s in the background. The illuminating source is at [0, 64, 0] mm. The 8192 detection positions are randomly

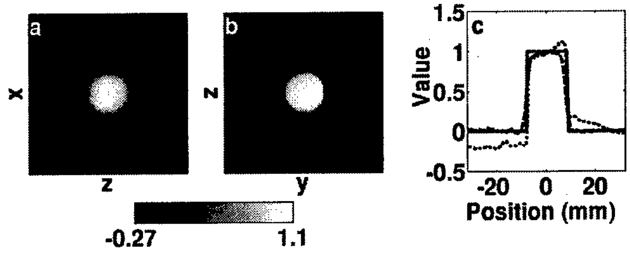

FIG. 2. (a) Reconstructed image section in DT along the $y = 0$ and (b) $x = 0$ planes. (c) The line graphs along the $z = 0$ (dotted line), $y = 0$ (dashed line) lines in (b) and the corresponding real value (solid line). The object values are normalized to 0.01.

distributed over an ellipsoid with three axes of [80, 64, 80] mm long and the center at the origin. The imaging space is a cube with a side length of 64 mm, centered at the origin, and mapped with a 128 by 128 by 128 mesh. In the forward problem, $\varphi_n(\mathbf{r}, t)$ is computed by the integration of the object value along a series of ellipsoids. The signals are within [0 1.5] MHz. In the inverse problem, we use (15) instead of the exact formula (13) to time reverse fields to save computation time. We swap the order of (17) and the integration in (15) to improve the computation accuracy. Figures 2(a) and 2(b) show that the shape and position of the object are reconstructed correctly. The line graphs in Fig. 2(c) show that the object is reconstructed quantitatively. There are some shadows from the object along the line (y axis) connecting the source and the object in Fig. 2(b). The shadows rotate when the position of the source changes. The shadows are probably caused by the limited bandwidth of the simulated signals. They can be eliminated if the illuminating source is placed in several positions and multiple sets of data are collected.

Our time-reversal methods are derived for waves in a homogeneous medium. The extension of most of them to a heterogeneous medium is straightforward. Equations (4)–(10) hold for a heterogeneous medium after Green's function is replaced by the corresponding one in a heterogeneous medium. In addition to replacing Green's function, v_s in (12) should be understood as the maximum of the acoustic speed in the medium to extend (11)–(13). Equation (14) can be extended after the minimum requirement for l_{det} is estimated. This estimation is more complex in a heterogeneous medium, since Green's function in a heterogeneous medium is usually a wave train rather than a delta pulse. To proceed from (14) to (15), we need to replace $|\mathbf{r} - \mathbf{r}_d|/v_s$ in (15) with $t_f(\mathbf{r}, \mathbf{r}_d)$, the flight time from $\mathbf{r}$ to $\mathbf{r}_d$, and assume that the heterogeneity changes only the flight time of a transient wave.

FBA is used in our discussion about DT. We realize that FBA does not hold for high frequencies. However, if we confine the frequency response range of the ultrasound transducer to the low-frequency range, FBA stands approximately. Alternatively, we can improve FBA by applying a distorted-wave Born approximation and time-reversal methods using Green's function in a heterogeneous medium. At last, it should be pointed out that our time-reversal methods can be easily applied to inverse diffraction, inverse source problems, and other tomographies using a diffracting source such as thermoacoustic tomography.

We are grateful to Minhua Xu for useful discussion about this study. This project was sponsored in part by U.S. Army Medical Research and Material Command Grant No. DAMD17-00-1-0455, National Institutes of Health Grant No. R01 EB000712, and Texas Higher Education Coordinating Board Grant No. ARP 000512-0063-2001.

---

*Email address: LWang@tamu.edu

[1] R. P. Porter, J. Acoust. Soc. Am. **80**, 1220 (1986); J. Thomas, P. Roux, and M. Fink, Phys. Rev. Lett. **72**, 637 (1994); J. H. Rose, in *Imaging of Complex Media with Acoustic and Seismic Waves*, edited by M. Fink, W. A. Kuperman, J. P. Montagner, and A. Tourin, Topics in Applied Physics Vol. 84 (Springer, Berlin, 2002), p. 97.
[2] M. Fink, IEEE Trans. Ultrason. Ferroelectr. Freq. Control **39**, 555 (1992).
[3] D. Cassereau and M. Fink, IEEE Trans. Ultrason. Ferroelectr. Freq. Control **39**, 579 (1992).
[4] A. Tourin, A. Derode, and M. Fink, Phys. Rev. Lett. **87**, 274301 (2001).
[5] R. P. Porter, Phys. Lett. **29A**, 19 (1969).
[6] E. Wolf, Opt. Commun. **1**, 153 (1969); A. J. Devaney, Ultrason. Imaging **4**, 336 (1982); T. Melamed, Y. Ehrlich, and E. Heyman, Inverse Probl. **12**, 977 (1996); S. J. Nortan and M. Linzer, IEEE Trans. Biomed. Eng. **BME-28**, 202 (1981); A. J. Devaney and G. Beylkin, Ultrason. Imaging **6**, 181 (1984).
[7] P. M. Morse and K. U. Ingard, *Theoretical Acoustics* (McGraw-Hill, New York, 1954).
[8] Our time-reversal methods can be extended to an absorbing medium by reversing the absorption coefficient.
[9] P. M. Morse and H. Feshbach, *Methods of Theoretic Physics* (McGraw-Hill, New York, 1953).
[10] An explicit expression of g_1, in the form of a series of eigenfunctions, can be found for the boundaries that fit with separable coordinates [9].
[11] First, after combining (13), (17), and the time-domain form of (2), we find that $g_1(\mathbf{r}, t|\mathbf{r}_d, t_0)$ only within $t < A_g$, where $A_g = t_0 + (|\mathbf{r} - \mathbf{r}_d| + 2l_{\text{obj}})/v_s$, is needed to compute $p_r(\mathbf{r}, \hat{t}_e(\mathbf{r}))$ using (13) for the DT application. Second, when $\mathbf{r}$ is near the center of Σ and $l_{\text{det}} > 2l_{\text{obj}}$, the difference in the flight times of the first two rays (arriving at $\mathbf{r}$ at time $t_0 + |\mathbf{r} - \mathbf{r}_d|/v_s$) and the other rays (such as ray *DAB*) is larger than $2l_{\text{obj}}/v_s$ in most cases, and, consequently, rays other than the first two make a contribution to $g_1(\mathbf{r}, t|\mathbf{r}_d, t_0)$ only when $t > A_g$, and to $p_r(\mathbf{r}, t)$ only when $t > \hat{t}_e(\mathbf{r})$.
[12] M. A. Fiddy, J. Phys. D **19**, 301 (1986).

730 OPTICS LETTERS / Vol. 29, No. 7 / April 1, 2004

Noninvasive photoacoustic angiography of animal brains *in vivo* with near-infrared light and an optical contrast agent

Xueding Wang and Geng Ku

Optical Imaging Laboratory, Department of Biomedical Engineering, Texas A&M University, College Station, Texas 77843-3120

Malgorzata A. Wegiel

Department of Chemistry and Biochemistry, Texas Tech University, Lubbock, Texas 79409-1061

Darryl J. Bornhop

Department of Chemistry, Vanderbilt University, Nashville, Tennessee 37235

George Stoica

Department of Pathobiology, Texas A&M University, College Station, Texas 77843-5547

Lihong V. Wang

Optical Imaging Laboratory, Department of Biomedical Engineering, Texas A&M University, College Station, Texas 77843-3120

Received August 21, 2003

Optical contrast agents have been widely applied to enhance the sensitivity and specificity of optical imaging with near-infrared (NIR) light. However, because of the overwhelming scattering of light in biological tissues, the spatial resolution of traditional optical imaging degrades drastically as the imaging depth increases. Here, for the first time to our knowledge, we present noninvasive photoacoustic angiography of animal brains *in vivo* with NIR light and an optical contrast agent. When indocyanine green polyethylene glycol, a novel absorption dye with prolonged clearance, is injected into the circulatory system of a rat, it obviously enhances the absorption contrast between the blood vessels and the background tissues. Because NIR light can penetrate deep into the brain tissues through the skin and skull, we are able to successfully reconstruct the vascular distribution in the rat brain from the photoacoustic signals. On the basis of differential optical absorption with and without contrast enhancement, a photoacoustic angiograph of a rat brain is acquired that matches the anatomical photograph well and exhibits high spatial resolution and a much-reduced background. This new technology demonstrates the potential for dynamic and molecular biomedical imaging. © 2004 Optical Society of America

OCIS codes: 170.5120, 170.3880, 170.0110, 170.1470.

The high sensitivity of optical imaging modalities aided by contrast agents parallels that of nuclear imaging and allows the visualization of organs such as the brain without the undesirable effect of ionizing radiation. Indocyanine dyes, with strong absorption in the near-infrared (NIR) spectra, are especially useful because NIR light has low absorption in biological tissues and consequently has relatively deep penetration. For example, indocyanine green (ICG), which has been approved by the Food and Drug Administration, in combination with NIR techniques, is employed widely in clinical applications such as cardiac output monitoring,[1] hepatic function study,[2] angiography in ophthalmology,[3] and tumor detection.[4] However, because of the strong scattering nature of biological tissues in NIR, pure optical imaging techniques, whether diffuse optical tomography, fluorescence imaging, or other microscopies, cannot provide high spatial resolution beyond the skin. The photoacoustic imaging technique, which has the merits of both light and ultrasound, has been proved to be a powerful tool for visualizing biological tissues with satisfactory sensitivity and spatial resolution.[5–10] In this study, distributions of NIR absorption in biological tissues that were modified by an optical contrast agent were imaged with the photoacoustic modality. With this technique we successfully achieved noninvasive photoacoustic angiography—mapping of the vasculature—in the cortex of rat brains *in vivo* for what appears to be the first time.

The setup for noninvasive photoacoustic angiography of rat brains is shown in Fig. 1(A). A tunable dye laser (ND6000, Continuum) pumped by a Nd:YAG laser (Brilliant B, Bigsky) was employed to provide laser pulses with a FWHM of 6.5 ns, a pulse repetition rate of 10 Hz, and a wavelength of 805 nm. The incident energy density of the laser beam was controlled to <2 mJ/cm^2 on the surface of the rat head, which induced a temperature rise in the brain vessels estimated to be <2.6 mK. An unfocused ultrasonic transducer (XMS-310, Panametrics) with a central frequency of 10.4 MHz, a bandwidth of 100% at -6 dB, and an

0146-9592/04/070730-03$15.00/0 © 2004 Optical Society of America

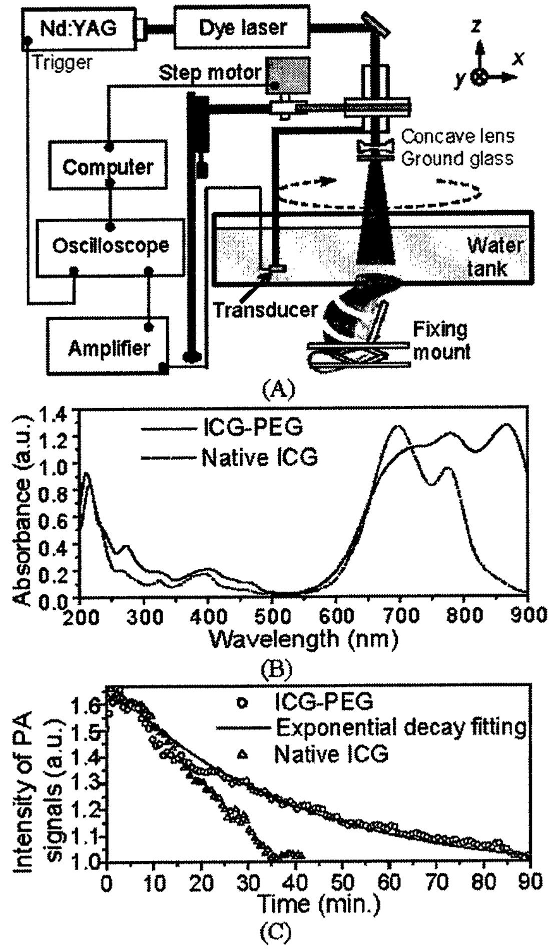

Fig. 1. (A) Schematic of noninvasive photoacoustic angiography in the rat brain, employing an optical contrast agent and a NIR laser. (B) Absorption spectra of ICG-PEG and native ICG. (C) Intensity of the photoacoustic signals from the blood vessels in the median fissure of the rat brain as a function of time after the intravascular injection of ICG-PEG (circles) or native ICG (triangles), which are normalized to the initial intensity of the photoacoustic signals before the injection. PA, photoacoustic.

active element of 2 mm in diameter was used to detect the photoacoustic signals. The transducer was driven by a computer-controlled step motor to scan around the cortex of the rat brain in the $x-y$ plane with a radius of 3 cm and a step size of 1.5°. The data acquisition time for one image was 23.5 min.

The rat was fixed by use of a homemade mount with its head protruding into the water tank through a hole in the bottom of the tank where a piece of clear polyethylene film between the water and the rat head sealed the hole. A thin layer of ultrasonic coupling gel was applied on the surface of the rat head. The photoacoustic signals detected by the transducer were received by an amplifier and then sent to an oscilloscope. Finally, a computer collected the digitized signals to reconstruct the distribution of optical absorption in the imaging plane through a modified backprojection algorithm.[11] Sprague Dawley rats (~150 g, Charles River Breeding Laboratories) were employed for the imaging experiments. Before imaging, the hair on each rat's head was removed with hair remover lotion. A dose of 87 mg/kg Ketamine plus 13 mg/kg Xylasine was administered intramuscularly to anesthetize the rats during the data acquisition.

The optical contrast agent was injected into the circulatory system of the rats through the tail vein. To prolong the circulation of ICG in blood, polyethylene glycol (PEG),[12] a polymer approved by the Food and Drug Administration with the structure $(\text{-CH}_2\text{CH}_2\text{O-})_n$, was adopted to stabilize the ICG. This PEG conjugate of ICG (ICG-PEG) with high optical absorption near the 805-nm wavelength [see Fig. 1(B)] was used as a contrast agent in photoacoustic tomography for the first time to our knowledge. The ICG-PEG in phosphate buffered saline (pH = 7.4; concentration = 3.2×10^{-4} M) was injected intravenously at a dosage of 0.25 ml/100 g body weight, which led to an estimated ICG concentration of $\sim 1 \times 10^{-5}$ M in the blood. With this ICG-PEG dosage and the applied laser energy density for this experiment, the magnitude of the photoacoustic signals received by the ultrasonic transducer was of the order of 10 μV. Considering the 60-μm resolution that has been achieved by this system (to be reported elsewhere), the number of molecules in the 60 μm × 60 μm × 60 μm resolvable volume is ~2 fmol, which represents an underestimate of the sensitivity of our imaging system.

By observing the changes in the intensity of the photoacoustic signals from the brain vessels, we studied the time-dependent variation of absorption in the brain blood attributable to the contrast agent [Fig. 1(C)]. The results represent the clearance profile of the dye from the circulatory system of the rat, where ICG-PEG shows an obviously slower clearance than the native ICG.

Photoacoustic angiographs of rat brains *in situ* based on either the intrinsic contrast or the ICG-PEG enhanced contrast were compared. The contrast between the large blood vessels and the background tissue was approximately 1.8:1 without the contrast agent. The contrast was enhanced to 2.8:1 by the ICG-PEG at the applied dosage.

ICG-PEG was applied to noninvasive photoacoustic angiography in the rat brain *in vivo* (Fig. 2). After the experiment, the rat recovered normally without noticeable health problems. Compared with the reference image in Fig. 2(A), the image in Fig. 2(B), obtained after the injection of ICG-PEG, represents a clearer map of the brain vascular branches that matches well with the photograph of the anatomy. Figure 2(A) was subtracted from the image with contrast enhancement in Fig. 2(B). The differential image in Fig. 2(C) depicts the distribution of differential optical absorption in the rat brain that is attributed to the injected contrast agent. This subtraction reduces the background and further enhances the contrast of blood vessels in rat brains. Some detailed brain vascular structures that cannot be visualized from the image in Fig. 2(B), such as the small vessel branches identified by the black arrows in the figure, were revealed by this differential image.

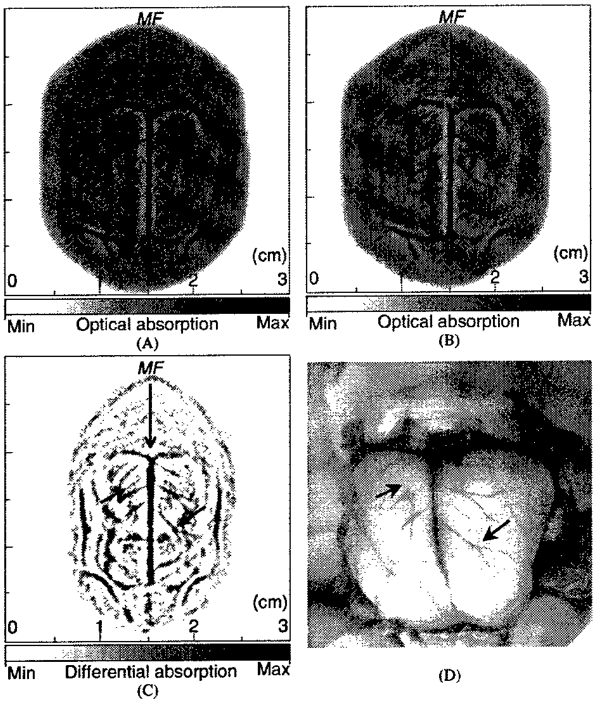

(A) (B) (C) (D)

Fig. 2. Noninvasive photoacoustic images of a rat brain *in vivo,* employing NIR light and an optical contrast agent (ICG-PEG). (A), (B) Photoacoustic images acquired before and after the injection of ICG-PEG, respectively, where the two gray scales are the same. MF, median fissure. (C) ICG-based angiograph of the rat brain (C = B − A). (D) Open-skull photograph of the rat brain obtained after the data acquisition for photoacoustic imaging.

More important, this experiment demonstrated the potential of photoacoustic tomography for dynamic and molecular imaging.

A circular scan of even an unfocused transducer was able to produce high-quality images of the cerebral cortex for the following reasons. Most large blood vessels are distributed in the brain cortex. The photoacoustic signals that originated from the strong optical absorption in the vasculature of the dorsal cerebral cortex were dominant. Conversely, the photoacoustic signals from the large vessels in the ventral brain were relatively small because of the attenuation of light in the brain. In addition, the aperture effect of the ultrasonic transducer provided some resolution along the z axis.

Images obtained with this setup represent a distribution of the averaged optical absorption during the data acquisition. In this case the applied contrast agent with a prolonged clearance time benefits the acquisition of imaging signals, especially when several images need to be acquired with the current imaging system after the intravascular injection. When an ultrasonic transducer array, instead of a single-element transducer, is adopted in the future, this technology will provide real-time and more accurate quantitative monitoring of the brain hemodynamics. Consequently, the clearance time will not need to be prolonged in that case. The *in vivo* dynamics of the exogenous dye can provide useful physiological information.

In summary, angiography in the rat brain yielding high contrast and high spatial resolution based on the photoacoustic imaging of exogenous contrast agents has been implemented noninvasively. This technique provides an accurate noninvasive monitoring method for fluid pathways in biological tissues, which makes it a powerful method for imaging vascular changes in tumors, delineating neovascularization, and studying global and regional hemodynamic activities in the brain. Since the contrast agent is expected to accumulate in neoplastic tissues or traumatized regions, this technique is promising for determining the margins of embedded tumors or bruises with a high degree of accuracy. More important, since contrast agents can be conjugated to bioactive peptides, proteins, antibodies, hormones, drugs, or other bioactive agents, this technique can be readily extended to molecular and functional imaging. For example, with high-frequency ultrasonic detection and tumor-targeted optical contrast agents, this technique offers promise for imaging pathologic processes at molecular and genetic levels. All these objectives can be accomplished by virtue of the high optical contrast and high ultrasonic resolution that this technique provides.

This study was sponsored in part by the National Institutes of Health, the Department of Defense, the National Science Foundation, and the Texas Advanced Research Program. L. Wang's e-mail address is LWang@tamu.edu.

References

1. Y.-L. He, H. Tanigami, H. Ueyama, T. Mashimo, and I. Yoshiya, Crit. Care Med. **26,** 1446 (1998).
2. J. Caesar, S. Shaldon, L. Chiandussi, L. Guevara, and S. Sherlock, Clin. Sci. **21,** 43 (1961).
3. B. F. Hochheim, Arch. Ophthalmol. **86,** 564 (1971).
4. M. M. Haglund, M. S. Berger, and D. W. Hochman, Neurosurgery **38,** 308 (1996).
5. C. G. A. Hoelen, F. F. M. de Mul, R. Pongers, and A. Dekker, Opt. Lett. **23,** 648 (1998).
6. R. A. Kruger, D. R. Reinecke, and G. A. Kruger, Med. Phys. **26,** 1832 (1999).
7. R. O. Esenaliev, A. A. Karabutov, and A. A. Oraevsky, IEEE J. Sel. Top. Quantum Electron. **5,** 981 (1999).
8. K. P. Köstli, D. Frauchiger, J. J. Niederhauser, G. Paltauf, H. P. Weber, and M. Frenz, IEEE J. Sel. Top. Quantum Electron. **7,** 918 (2001).
9. X. Wang, Y. Pang, G. Ku, X. Xie, G. Stoica, and L. V. Wang, Nat. Biotechnol. **21,** 803 (2003).
10. X. Wang, Y. Pang, G. Ku, G. Stoica, and L. V. Wang, Opt. Lett. **28,** 1739 (2003).
11. M. Xu and L. V. Wang, IEEE Trans. Med. Imaging **21,** 814 (2002).
12. S. Zalipsky, E. Brandeis, M. S. Newman, and M. C. Woodle, FEBS Lett. **353,** 71 (1994).

Reconstructions in limited-view thermoacoustic tomography

Yuan Xu and Lihong V. Wang[a)]
Optical Imaging Laboratory, Department of Biomedical Engineering, Texas A&M University, 3120 TAMU, College Station, Texas 77843-3120

Gaik Ambartsoumian and Peter Kuchment
Department of Mathematics, Texas A&M University, College Station, Texas 77843-3368

(Received 4 September 2003; revised 5 December 2003; accepted for publication 9 December 2003; published 11 March 2004)

The limited-view problem is studied for thermoacoustic tomography, which is also referred to as photoacoustic or optoacoustic tomography depending on the type of radiation for the induction of acoustic waves. We define a "detection region," within which all points have sufficient detection views. It is explained analytically and shown numerically that the boundaries of any objects inside this region can be recovered stably. Otherwise some sharp details become blurred. One can identify in advance the parts of the boundaries that will be affected if the detection view is insufficient. If the detector scans along a circle in a two-dimensional case, acquiring a sufficient view might require covering more than a π-, or less than a π-arc of the trajectory depending on the position of the object. Similar results hold in a three-dimensional case. In order to support our theoretical conclusions, three types of reconstruction methods are utilized: a filtered backprojection (FBP) approximate inversion, which is shown to work well for limited-view data, a local-tomography-type reconstruction that emphasizes sharp details (e.g., the boundaries of inclusions), and an iterative algebraic truncated conjugate gradient algorithm used in conjunction with FBP. Computations are conducted for both numerically simulated and experimental data. The reconstructions confirm our theoretical predictions. © *2004 American Association of Physicists in Medicine.*
[DOI: 10.1118/1.1644531]

Key words: thermoacoustic tomography, photoacoustic tomography, optoacoustic tomography, local tomography, limited view, incomplete data

I. INTRODUCTION

A correlation between the electromagnetic absorption of a biological tissue and its physiological and pathological features is reported.[1–4] To employ this contrast mechanism, thermoacoustic tomography (TAT), in which the thermoacoustic signals from a tissue sample are collected to map the distribution of the radiation absorption within the sample, has been developed to image biological tissue.[5–9] TAT, which is also referred to as photoacoustic or optoacoustic tomography (depending on the type of radiation used), combines good imaging resolution with good imaging contrast.

As it will be shown below, TAT signals can be represented in terms of a known circular radon transform. There exist explicit reconstruction formulas for this transform when data are collected along a line or a full circle in a two-dimensional (2-D) case and along a plane, sphere, or a cylinder in a three-dimensional (3-D) case.[10–15] In all these cases it is assumed that the imaged objects are located either on one side of the scanning line (plane), or inside the scanning circle (sphere, cylinder), without which assumption reconstruction is not always possible. The available inversion formulas employ either special-function expansions, or backprojection in the case of the linear or planar data-acquisition geometry.

Exact reconstruction algorithms for TAT based on series-expansion techniques are implemented in planar, spherical, and cylindrical configurations.[5–7,16] Following the line of Nortan,[17] an approximate modified backprojection algorithm has been developed from an exact 3-D model.[6] Other backprojection algorithms are also proposed.[8,18] In these algorithms for TAT, it is assumed that the thermoacoustic signals are detected in a full (panoramic) view. In other words, the detector moves along a whole circle in the 2-D case or sphere in the 3-D case. This means in particular that each point of the scanned object is visible from the detector's trajectory for 2π radians in the 2-D case or 4π steradians in the 3-D case. However, in many applications of TAT, the signals cannot be collected from all directions. For example, the solid angle of detection is at most 2π steradians for a breast. So, one faces here an incomplete data problem. Although one can show that theoretically an arbitrarily small scanning arc (i.e., the arc of a circle over which the detectors move) suffices for the uniqueness of recovery,[22] in practical implementations the limited-view problems usually lead to losing some parts of the high-frequency information and hence blurring of some sharp details.

In this paper, we present our results on the limited-view TAT. Although limited-view problems have been studied extensively in x-ray tomography,[19] diffraction tomography,[20] and reflectivity tomography,[21] to the best of our knowledge, no results on the limited-view TAT have been published. In the methods section, a formula for the forward problem is presented. In particular, it is shown that the TAT signals can be represented in terms of a known circular radon transform. This enables us to employ the known results that justify the theoretical possibility of reconstruction.[22] Then results by Quinto and Louis developed for sonar are applied to determine the "stably visible" parts of the objects in TAT.[23] In particular, a piece of the boundary of an object (i.e., interfaces between objects) can be stably reconstructed as soon as at any point on the boundary at least one of its two normal directions passes through a detector position. On an intuitive level, this is because an arbitrary interface can be considered as a combination of small flat interface segments, and each segment transmits acoustic waves identically in the two opposite directions perpendicular to the interface segment. This means that we need to collect signals at only one of the two directions to obtain information about the boundary segment. More complicated sharp details ("singularities") could be considered as well, which would entail using the notion of a wavefront of a function and other tools of microlocal analysis. However, among all possible singularities, tissue interfaces are of the most interest for TAT.

Exact reconstruction formulas for the limited-view TAT are not yet known. We derive an approximate filtered backprojection (FBP) algorithm that works well quantitatively. A version of this method that emphasizes singularities [a "local tomography" (LT) reconstruction] is also tested. The FBP results are then iteratively improved using a truncated conjugated gradient (TCG) method. Besides using numerical phantoms for calculations, we also conducted experimental measurements on physical phantoms and applied our reconstruction methods to the obtained data. The results of all these reconstructions confirm our theoretical predictions. These are addressed in the Sec. III.

II. METHODS

A. Formulas for the forward problem

We begin by presenting the forward problem for an acoustically homogeneous model. In the case of thermal confinement, the spectrum of the acoustic wave pressure $\overline{p}(\mathbf{r},k)$ at a detector position $\mathbf{r}$ is related to the spatial distribution of electromagnetic absorption $\varphi(\mathbf{r}')$,[5]

$$\overline{p}(\mathbf{r},k)=\frac{iv_s\beta I_0 k\overline{\eta}(k)}{4\pi C}\times\oint\varphi(\mathbf{r}')\frac{\exp(-ik|\mathbf{r}-\mathbf{r}'|/v_s)}{|\mathbf{r}-\mathbf{r}'|}d\mathbf{r}'. \quad (1)$$

Here k is the angular frequency with respect to t; v_s is the acoustic speed; C is the specific heat; β is the coefficient of volumetric thermal expansion; I_0 is a scaling factor proportional to the incident radiation intensity; $\varphi(\mathbf{r}')$ describes the to-be-reconstructed electromagnetic absorption property of the medium at $\mathbf{r}'$; and $\overline{p}(\mathbf{r},k)$ and $\overline{\eta}(k)$ are the temporal Fourier transforms of the pressure $p(\mathbf{r},t)$ and the shape of the irradiating pulse $\eta(t)$, respectively.

Defining $\overline{p_1}(\mathbf{r},k)=\overline{p}(\mathbf{r},k)/\overline{\eta}(k)$ and applying inverse Fourier transform, one obtains

$$p_1(\mathbf{r},t)=\frac{v_s\beta I_0}{4\pi C}\frac{\partial}{\partial t}\oint_{t=|\mathbf{r}-\mathbf{r}'|/v_s}\frac{\varphi(\mathbf{r}')}{|\mathbf{r}-\mathbf{r}'|}d\mathbf{r}', \quad (2)$$

where $p_1(\mathbf{r},t)$ is the deconvolution of $p(\mathbf{r},t)$ with respect to the profile of the electromagnetic pulse and can be interpreted as the detected pressure when the electromagnetic pulse is a delta (impulse) function. The physical meaning of this equation is that, in an acoustically homogeneous medium, the pressure p_1 at a spatial point $\mathbf{r}$ and time t is proportional to the time derivative of the integral of the absorbed electromagnetic energy over a spherical surface (a circle in the 2-D case) centered at $\mathbf{r}$ and with a radius of tv_s:

$$|\mathbf{r}-\mathbf{r}'|=tv_s. \quad (3)$$

2-D TAT is studied in our numerical simulations and experiments. It should be pointed out that 2-D TAT is valid for experimental configurations where thermoacoustic sources are approximately located within a thin slab or the ultrasonic transducers are cylindrically focused to select thermoacoustic sources from a thin slab.

B. Analysis of singularities in circular radon transform and limited-view TAT

1. Circular radon transform

It can be seen from Eq. (2) that $p_1(\mathbf{r},t)$ can be obtained from $\varphi(\mathbf{r}')$ after applying three linear operations: circular (spherical in 3-D) radon transform $\mathbf{R}$, multiplication by $1/t$, and differentiation $\mathbf{D}_t$ with respect to t. The circular radon transform defined as

$$\mathbf{R}\varphi(\mathbf{r},t)=\oint_{t=|\mathbf{r}-\mathbf{r}'|/v_s}\varphi(\mathbf{r}')d\mathbf{r}' \quad (4)$$

is similar to the conventional linear radon transform, except that the integration here is over a circle or a sphere rather than a line or a plane. In this paper, the set Σ of centers $\mathbf{r}$ of the circles (spheres) of integration coincides with the set of positions of the detector, and the set of radii (that are proportional to time t) is unrestricted. We call these circles (spheres) "projection curves" ("projection surfaces") and the set Σ the "scanning curve" (or "detector curve"). We assume that the source function $\varphi(\mathbf{r})$ is zero outside Σ and in a neighborhood of Σ. In other words, the scanned object is strictly inside the scanning detector trajectory Σ. In this case it is known that data collected from an arbitrarily small arc of the detector trajectory are theoretically sufficient for a complete reconstruction.[22] This result, however, neither provides reconstruction algorithms, nor guarantees that the reconstruction can be achieved in any practically stable manner. Indeed, it is well known that solving incomplete data problems usually leads to operations like Fourier filtrations with fast growing filters,[15] which implies high sensitivity to errors in data. This in turn requires cutting high frequencies and hence blurring the images. Sacrifices in high frequencies naturally lead to destroying sharp details (interfaces between different tissues) in the reconstruction. The question of what parts of

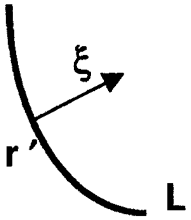

FIG. 1. Wavefront $WS(\varphi)$ of an image φ consisting of pairs $(\mathbf{r}',\xi)$, where point $\mathbf{r}'$ belongs to $\mathbf{L}$ (a jump interface in the image) and ξ is a nonzero vector normal to $\mathbf{L}$ at $\mathbf{r}'$.

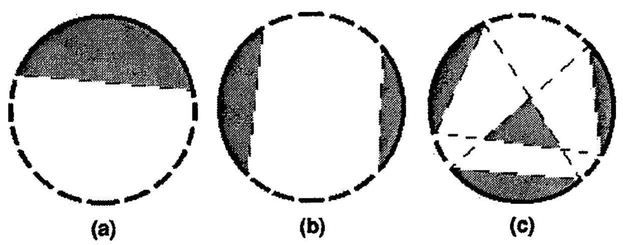

FIG. 2. (a) An illustration of the "detection regions" (shaded areas) of circular radon transform, when the detector moves along a single arc (solid) of a circle. (b) Two arcs. (c) Three arcs.

the singularities (i.e., sharp details) of the image can be stably reconstructed depending on the scanning geometry is addressed for the planar radon transform,[24] and for the circular one in connection with sonar.[23] Local tomography reconstructions also address similar issues.[25–28]

2. TAT

We would like to note that in Eq. (2) the presence of a temporal derivative in the TAT data (which is equivalent to a radial derivative after the circular radon transform) can only emphasize singularities and hence should not lead to additional blurring in comparison with the circular radon transform itself (this can be shown rigorously). In fact, as it will be seen later in this paper, this derivative is a natural part of the reconstruction procedure for the circular radon transform.

We will now apply to TAT the known results of integral geometry concerning singularity reconstruction.[23,24] The exact description would require the notions of microlocal analysis, in particular the one of a wavefront set of a function.[23,24] However, in tomographic problems, in particular in TAT, one is mostly interested in only one type of singularity: the jump of the imaged value φ across an interface (a curve in 2-D or a surface in 3-D). Assuming that φ is smooth except for a jump across a curve $\mathbf{L}$ in the plane (the 3-D situation is analogous with $\mathbf{L}$ being a surface), then the wavefront $WS(\varphi)$ of φ consists of pairs $(\mathbf{r}',\xi)$ where point $\mathbf{r}'$ belongs to $\mathbf{L}$ and ξ is a nonzero vector normal to $\mathbf{L}$ at $\mathbf{r}'$ as shown in Fig. 1.

Now Louis' results can be summarized as follows:[23] one can identify that a pair $(\mathbf{r}',\xi)$ belongs to the wavefront set of the image by looking at the singularities of the radon data if and only if among the circles (spheres) of integration ("projection curves") there exists at least one passing through the point $\mathbf{r}'$ and normal to ξ at this point. To put it differently, in TAT one can see without blurring only those parts of the interfaces that one can touch tangentially by circles (spheres) centered at detector positions. This means that one needs to have a detector located on the normal to $\mathbf{L}$ at $\mathbf{r}'$ in either direction.

What happens to other, "invisible" parts of the interfaces? We provide here a nontechnical explanation. One would need to recover these singularities from smooth parts of the measured data. This in turn means the involvement of operations like filtrations in the frequency domains with filters growing faster than any power. In order to avoid instabilities then, this clearly requires cutting those frequencies off, which causes blurring. The conclusion is that the "visible" parts of the interfaces should be possible to recover, while the others should blur independently of the reconstruction method used. A discussion of the related issues of stability of reconstruction would be too lengthy; one can find the relevant considerations in the literature.[29] In a nutshell, more stable tomographic problems allow one to estimate the error in the reconstruction (in a Sobolev norm) by the error in the data in a somewhat smoother norm. This, however, is impossible when the information about the wavefront is lost.

Let us make this geometry more explicit for our circular (spherical) trajectory of detectors. We pose the following question: Assume that only a part of the detector circle (sphere) is used for collecting data; at what locations then, all interfaces in the image will be completely recoverable? We will call the set of all such "good" locations the "detection region." For images outside this region, one needs to apply the tangent-circle test as described in the preceding two paragraphs to predict what parts of the boundaries will not be stably recoverable.

Assuming first that the detector moves along a single arc of the circle [Fig. 2(a)], then simple geometric consideration shows that the "detection region" is just the convex hull of this arc (i.e., the circular cap based on the arc). Here the "detection region" is shaded, and the arc of the circle where we do not position a detector is shown as a dotted line. Analogously, one can find the "detection region" (shaded) for two arcs [Fig. 2(b)]. The situation changes, however, for more complicated scanning trajectories. For instance, in the case of three arcs, one can have more than just circular caps in the "detection region" [Fig. 2(c)]. Here an additional triangular part of the "detection region" appears in the center. The situation can become even more complicated for spherical 3-D geometry. The general rule for finding the "detection region" is as follows: draw all lines such that both of their intersection points with the scanning circle (sphere) do not coincide with detector locations. These lines cover the "invisible" domain, so its complement forms the "detection region." Note that in the "invisible" domain some boundaries can still be recovered stably, while others blur away. Namely, the parts of the boundaries the normal lines to which pass through a detector position, and only those can be stably recoverable. The above conclusions are illustrated in Fig. 3, where the "invisible" parts of the object boundaries, i.e., the

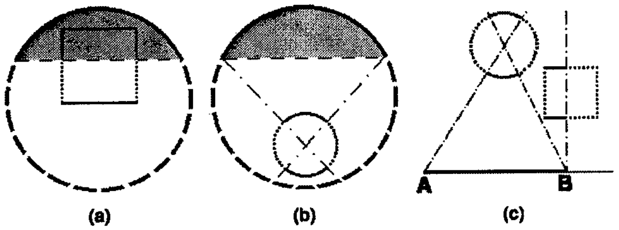

FIG. 3. (a) "Visible" (solid line) and "invisible" (dashed) boundaries of a square object, and the "detection regions" (shaded areas) when the detector moves along an arc (solid). (b) The same as (a) for a disk phantom. (c) The same as (a) except that the detector moves along the line segment AB and the objects are a square and a disk. The "visible" boundaries are expected to be recoverable stably, while the "invisible" boundaries should be blurred away.

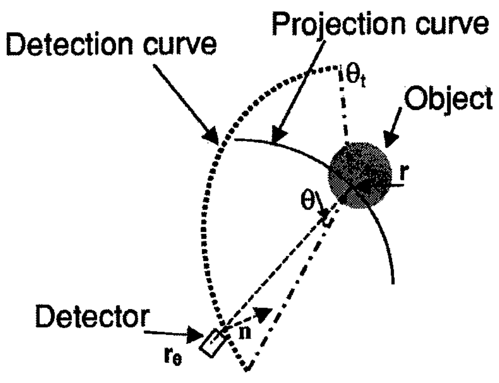

FIG. 4. A diagram to show the uniform rotation of θ in FBP in a circular radon transform or TAT. The dashed arrow represents the normal to the detection curve (dotted arc) at $\mathbf{r}_\theta$ and the dashed line is the normal to a projection arc centered at $\mathbf{r}_\theta$ and passing through a reconstructed point $\mathbf{r}$. θ_t is the detection view at $\mathbf{r}$, i.e., the angle subtended by the detection curve as viewed from $\mathbf{r}$.

ones to be blurred during the reconstructions, are shown with dotted lines. For instance, in Fig. 3(a) one has a cap "detection region" and a rectangular object that does not fit fully into it. Then one expects the dotted parts of the rectangle's boundary to be affected by blurring artifacts during the reconstruction. Figure 3(b) shows the expected reconstruction of a circular object located outside the "detection region." Let us remark that similar considerations apply to an arbitrary scanning geometry. For instance, Fig. 3(c) shows the parts (solid) of the boundaries of a circular and a square object that can be stably reconstructed from the detection on a segment AB.

C. Reconstruction methods

As it has already been mentioned before, exact inversion procedures are known for circular and spherical radon transforms in some special detection configurations.[10–15] However, for the circular trajectories of detectors only special-function-expansion methods are known, while formulas of the FBP type are available for the linear (planar) trajectories. Our approach is to use an approximate FBP formula, which happens to work well under most circumstances and can be improved in conjunction with post-processing by an iterative method. Namely, for objects not too close to the detectors, one can think of projection lines as close to straight lines, and hence the circular radon transform as being close to the standard radon transform. In this approach, the center $\mathbf{r}$ of the projection circle and its radius ρ (which is proportional to time) are analogs of the normal coordinates $(\hat{\theta},\varsigma)$ of a line $\mathbf{r}\cdot\hat{\theta}=\varsigma$ in the standard radon transform where $\hat{\theta}$ is a unit vector normal to the line. FBP inversion of the standard radon transform on the plane consists (up to a constant factor) in applying the first derivative with respect to ς, then Hilbert transform with respect to ς, and finally the backprojection operator, which averages over lines passing through a given point.[15] We implement a similar procedure in the circular radon transform. This amounts to a differentiation with respect to the radius, a Hilbert transform with respect to the radius, and then a circular backprojection, i.e., averaging over the circles passing through a given point. One should also make sure that during the backprojection the tangent lines (or the normal vectors) to the projection curves at the given point, for example, θ in Fig. 4, rather than the centers of the projection curves (which coincide with detector positions), rotate at a constant speed. Differentiation with respect to the radius is already contained in the TAT data, as shown in Eq. (2), so this step can be simplified in 2-D reconstructions (it is still required in a 3-D TAT). Based on this, we arrive in the Appendix at an approximate FBP reconstruction formula for the 2-D TAT,

$$\varphi(\mathbf{r})\approx\frac{C}{\beta I_0 v_s^2}\oint ds\frac{\mathbf{n}\cdot(\mathbf{r}-\mathbf{r}_\theta)}{|\mathbf{r}-\mathbf{r}_\theta|^2}\mathbf{H}(p_1(\mathbf{r}_\theta,|\mathbf{r}_\theta-\mathbf{r}|/v_s)\times|\mathbf{r}-\mathbf{r}_\theta|+p_2(\mathbf{r}_\theta,|\mathbf{r}_\theta-\mathbf{r}|/v_s)), \tag{5}$$

where $\mathbf{H}$ is a Hilbert transform; $p_2(\mathbf{r},t)=v_s\int_0^t p_1(\mathbf{r},t)dt$; $\mathbf{n}$ is the inward normal to the detection curve at $\mathbf{r}_\theta$; ds is the arc length differential; and the integration is along a complete detection curve (i.e., the one that runs around the objects). In the case of incomplete data, one just replaces the missing data with zeros (possibly gradually phasing off the existing data closely to the missing data region to reduce the artifacts caused by the missing data) and then applies the formula. Although this is not an exact inversion, one can show using microlocal analysis that it preserves all "visible" singularities (a conclusion supported by the numerical and experimental evidences presented below). If one is interested in singularities only (e.g., interfaces between different types of tissue), then one can drop the integral term $p_2(\mathbf{r}_\theta,|\mathbf{r}_\theta-\mathbf{r}|/v_s)$ in the last formula, since it corresponds to a pseudodifferential operator of a smaller order.

Let us also provide a local tomography formula for the 2-D TAT. In order to do this we replace the Hilbert transform by an additional time derivative. This then leads to the local tomography reconstruction:

$$\Lambda\varphi(\mathbf{r})=\frac{C}{\beta I_0 v_s^2}\oint ds\frac{\mathbf{n}\cdot(\mathbf{r}-\mathbf{r}_\theta)}{|\mathbf{r}-\mathbf{r}_\theta|^2}\left(\frac{\partial p_1}{\partial t}(\mathbf{r}_\theta,|\mathbf{r}_\theta-\mathbf{r}|/v_s)\times|\mathbf{r}-\mathbf{r}_\theta|+2v_s p_1(\mathbf{r}_\theta,|\mathbf{r}_\theta-\mathbf{r}|/v_s)\right). \tag{6}$$

As before, if one wants to recover singularities only, the term of a lower pseudo-differential order $2v_s p_1$ in this formula can be dropped.

One can apply a similar consideration to the 3-D TAT, which leads to the approximate FBP formula:

$$\varphi(\mathbf{r}) \approx -\frac{C}{2\pi\beta I_0 v_s^3} \oint dS \frac{\mathbf{n}\cdot(\mathbf{r}-\mathbf{r}_\theta)}{|\mathbf{r}-\mathbf{r}_\theta|^2} \times \left(\frac{\partial p_1(\mathbf{r}_\theta, |\mathbf{r}_\theta-\mathbf{r}|/v_s)}{\partial t} + \frac{2p_1(\mathbf{r}_\theta, |\mathbf{r}_\theta-\mathbf{r}|/v_s)v_s}{|\mathbf{r}_\theta-\mathbf{r}|} \right). \tag{7}$$

In the case of limited-angle detection, there is also the following possibly useful correction if one is interested in quantitative imaging. Here, we define a detection view θ_t (solid angle Ω_t for the 3-D case) at $\mathbf{r}$, which is the (solid) angle subtended by the detection curve (surface) when viewed from the reconstruction point $\mathbf{r}$ as shown in Fig. 4. Because of the incompleteness of data, the integral in the above equations runs over a portion of the detection curve (surface) only. One might want to compensate for that by multiplying the value of the reconstructed function at this point by a factor $2\pi/\theta_t$ ($4\pi/\Omega_t$ for the 3-D case). The factor appears when the backprojection operator is considered approximately as an averaging over the available projection curves passing through the reconstruction point $\mathbf{r}$. It should be noted that both θ_t and Ω_t depend on $\mathbf{r}$. The effectiveness of this compensation is shown below by our numerical simulation results of TAT.

There are three useful features of Eq. (5) and Eq. (7). First of all, they yield, as we intend to show in numerical simulations, acceptable quantitative results from limited-view data. Second, their computation complexity is much less than that for the iterative methods such as TCG, while they produce images of comparable quality. Finally, if an iterative method is necessary, our backprojection formula can serve as a good initial guess. This is also observed in our numerical simulations.

Although the above backprojection formula is shown to work well in numerical simulations, it is not exact. Nevertheless, one can show that it amounts to applying a pseudo-differential operator to the image φ (this is true if the data is gradually phased out near the areas of the missing data). Pseudo-differential operators are known not to shift locations of any singularities, including boundaries.[19,28,30] This means that although the backprojection formula might give imprecise values of φ, it will present the locations of the boundaries of all inclusions correctly.

Another reconstruction method is to apply an additional differentiation with respect to time (the radius) without applying a Hilbert transform, as shown in Eq. (6). This leads to a local tomography type formula.[25,28] The result of the procedure also produces an expression of the form $\Lambda\varphi$, where Λ is a pseudo-differential operator defined in Eq. (6). In this case, however, the operator has a positive order, which means that all the "visible" interfaces and other sharp details not only have correct locations, but also are emphasized. This effect is well known in image processing, where for instance the Laplace operator is sometimes used to emphasize the edges. One can also notice that our experimental data, due to the shape of the transducer's impulse response function and electromagnetic pulse shape, already carry a filtration that makes the reconstruction similar to the local one. Then, unless an appropriate deconvolution is applied to the data during pre-processing, the interfaces are accentuated in the reconstruction. The reader will notice this in our actual reconstructions from experimental data.

D. Numerical implementation

In the case of incomplete data discussed above, we complete it by concatenating with zeros (sometimes gradually smoothing the data to zero at the boundary in order to reduce the artifacts in the reconstruction). The FBP algorithm described above is first applied to the limited view data. Since the inversion formula we use is not exact even for complete data, we improve it by employing an iterative algebraic method for solving the discretized version of Eq. (2), starting with the FBP reconstruction as the initial guess. We adopt as such the TCG method for finding the least-squares solution of the discretized version of the problem. No preconditioner is used. We also employ local tomography procedure described above. We expect in all these methods to see the reconstructions that agree with the theoretical predictions stated in the previous section, i.e., sharp "visible" details with the "invisible" parts blurred.

III. RESULTS AND DISCUSSION

Our results consist of three parts: (1) inversion of simulated circular radon transform data to show the theoretical predictions about the "visible" and "invisible" boundaries, (2) reconstructions from simulated TAT data to test our reconstruction algorithms quantitatively, and (3) images based on experimental data collected from a physical phantom.

A. Numerical results for the limited-view circular radon transform

Figure 5 shows the inversion of the circular radon transform for different detection configurations and phantoms (shown in the first column from the left) to demonstrate our discussions on the "visible" and "invisible" boundaries. In the second column from the left, the detection curve is shown as the solid part of the outer circle, the "detection region" is shaded, and the "visible" (solid) and "invisible" (dashed) boundaries of the objects predicted by theory are shown. The inclusion represents the object to be imaged. The third and fourth columns from the left show the FBP reconstructions and the local tomography reconstructions, respectively. Notice the good agreement between the three columns on the right concerning reconstructions of the "visible" and "invisible" parts of the boundaries.

Figure 5(1a–1d) shows the results for a phantom containing a square inclusion. The data are collected from detectors located on the upper half-circle. Exactly the parts of the

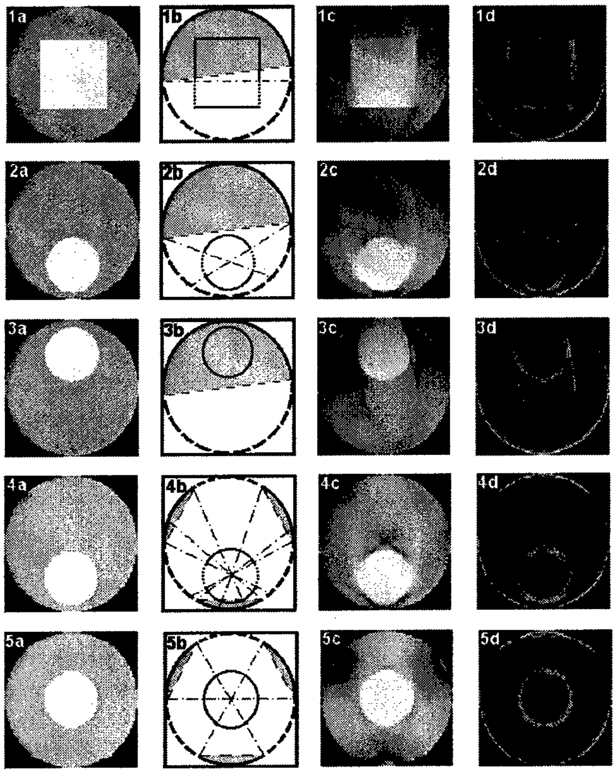

FIG. 5. (1a) A square phantom inside a circular detection curve in a circular radon transform. (1b) The diagram showing the detection curve (solid part of the outer circle), the "visible" (solid) and "invisible" (dashed) boundaries of the object predicted by theory, and the "detection region" (shaded). (1c) FBP reconstruction. (1d) Local tomography reconstruction, where the boundary is emphasized. (2a-2d) A disk phantom outside the "detection region." (3a-3d) A disk phantom inside the "detection region." (4a-4d) An off-center disk phantom and a detection curve consisting of three arcs. (5a-5d) A centered disk phantom and a detection curve consisting of three arcs.

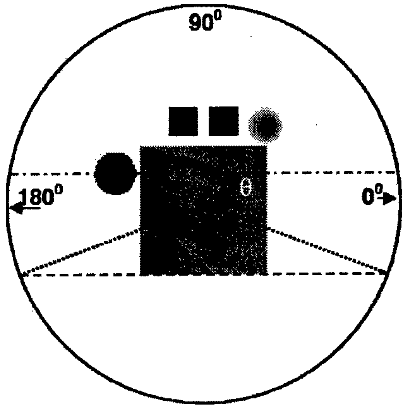

FIG. 6. A diagram of inclusions in TAT (used in Fig. 7). The value of the image $\varphi(\mathbf{r})$ is set to be 0.5 in the largest square and unity within other sharp inclusions and zero elsewhere. Inside the "soft" circular inclusion, this value drops linearly with the radius from unity at the center to zero at the interface.

boundary of the square predicted in this paper [see the dotted lines in Fig. 5(1b)] become blurred in Fig. 5(1c) and Fig. 5(1d).

Figure 5(2a–2d) and Fig. 5(3a–3d) show the reconstructions of circular inclusions from the data collected by the detector located along the upper half-circle. In Fig. 5(2a–2d), the phantom is completely outside the "detection region," which leads to blurring of its right and left boundaries in accordance with the theory. In Fig. 5(3a–3d), however, the boundaries of the disk are recovered sharply, since the inclusion is in the "detection region." Notice here some deterioration of the image near the detector circle. This can be attributed to the fact that near the detector circle, linear, and circular radon transform become noticeably different, and so the quality of our approximate formulas diminishes. This problem can be dealt with in two ways: one can make sure that the detectors do not approach the imaged objects too closely (this will be enforced in our further numerical simulations and experiments), or to improve the reconstruction quality by post-processing with an iterative algebraic reconstruction method.

Other limited-view reconstructions from the circular radon data are shown in Fig. 5(4a–4d) and Fig. 5(5a–5d), where there are three arcs of detection, 60 degrees each, with 60 degrees intervals between them. An off-center and a centered circular inclusion are reconstructed in Fig. 5(4a–4d) and Fig. 5(5a–5d), respectively. The results agree well with the theory: some parts of the boundary of the off-center disk are blurred; namely, those where the normals do not pass through any detector positions. However, the in-center disk is reconstructed sharply, in spite of the fact that it does not fit into the "detection region." The reason is that in this case every normal to the boundary of the inclusion passes through a detector.

B. Reconstruction from simulated limited-view TAT data

A numerical phantom that contains four sharp and one soft inclusions is shown in Fig. 6. Among the sharp ones we have one large and two small squares and one disk. The object value, which represents the electromagnetic energy deposition, is set to be 0.5 within the largest square and unity within other sharp inclusions and zero elsewhere. Inside the "soft" circular inclusion, this value drops linearly with the radius from unity at the center to zero at the interface in order to simulate a gradual interface. The imaged field of 154 mm by 154 mm is mapped with a 128×128 mesh. The detection circle has a radius of 133 mm and is centered at the center of the picture. We scan 200 steps in all the simulations. The gray scale and the scale bar of the images are shown below the images in Fig. 7. The top row of reconstructions employs the local tomography formula that emphasizes the boundaries. The next one uses the FBP formula, and the lowest one shows the improvements achieved by running the algebraic reconstruction method (TCG) starting with the FBP as an initial guess.

The left column uses only the data collected from the $\pi/2$ detection arc in the first quadrant. None of the phantom inclusions fits into the "detection region." One can see that all parts of the inclusion boundaries the normals to which do not intersect the detector arc are blurred (even in the local to-

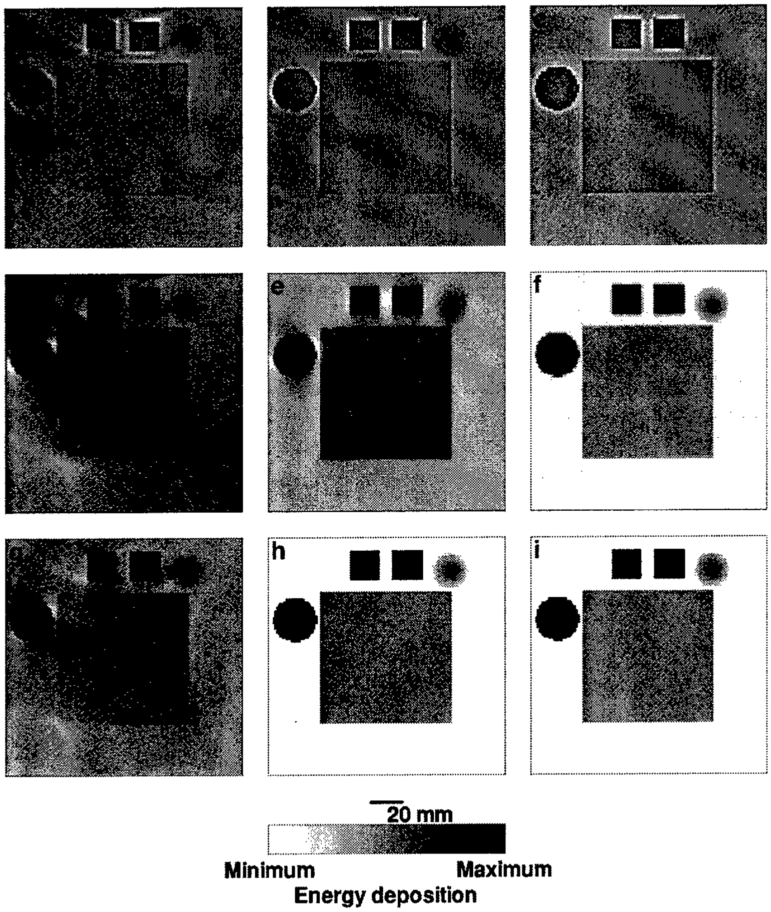

FIG. 7. Images reconstructed from simulated TAT data corresponding to the phantom in Fig. 6. The three columns correspond from the left to the right to detection angles of 90 degrees (from 0° to 90°), 217 degrees (from $-19°$ to 198° as shown by the angle θ in Fig. 6), and 360 degrees, respectively. The three rows correspond from top to bottom to the local tomographic reconstruction, FBP, and FBP with the consecutive TCG, respectively. The values of (minimum, maximum) of the gray scale for (a)–(i) are $(-0.8081, 1.0000)$, $(-0.8302, 1.0000)$, $(-0.7515, 1.0000)$, $(-2.0745, 1.7899)$, $(-0.6385, 1.0723)$, $(-0.1030, 1.0349)$, $(-0.9284, 1.2859)$, $(-0.0326, 1.0030)$, and $(-0.0149, 1.0021)$, respectively. The maxima of the local reconstructions are normalized to unity.

mography reconstruction). Other parts of the boundaries are sharp. This is in perfect agreement with our theoretical prediction. The soft inclusion is not significantly affected by the artifacts.

The middle column employs the data collected from the detector arc of approximately 217 degrees (the angle θ in Fig. 6), whose chord coincides with the bottom side of the large square inclusion. In this case all inclusions are in the "detection region," and hence all the boundaries are reconstructed sharply. The third column represents the full data reconstruction. Notice that the quality of the final reconstructions in the last two columns is the same.

Figures 8(a) and 8(b) show the reconstructed image $\varphi(\mathbf{r})$ along the dashed–dotted line in Fig. 6 using the FBP [Figs. 7(d)–7(f)] and TCG reconstructions [Figs. 7(g)–7(i)], respectively. The exact value is also shown for comparison. It can be found in Fig. 8(a) that the results of FBP are in good agreement with the real value for the case of 217-degree and 360-degree detection, where all objects are in the "detection region." Iteration improves the results further as shown in Fig. 8(b). Even for the case of a 90-degree detection curve, the profile of the objects is reconstructed. Comparing (a) and (b), one can find that the significant overshoot and undershoot in FBP can be considerably reduced by TCG iterations (we remind the reader that FBP is only an approximation rather than the implementation of an exact formula).

C. Dependence of reconstruction on scanned angular range

Figure 9 shows the relative error of each reconstruction as a function of the scanned angular range with respect to the center of the scan. We study the mean reconstruction values in the hard sphere, the central square, and the background. The errors of reconstruction are normalized to the corresponding real values in the cases of the hard sphere and the central square and to the real value of the hard sphere in the

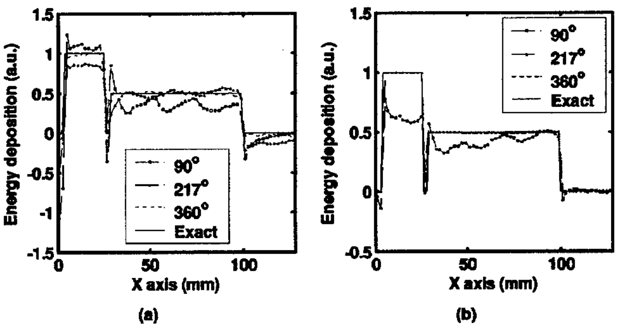

FIG. 8. (a) The graphs of FBP reconstructions shown in Figs. 7(d)–7(f) and the corresponding exact value along the dashed–dotted line in Fig. 6. (b) The graphs corresponding to TCG reconstructions, Figs. 7(d)–7(f), along the same line as in (a).

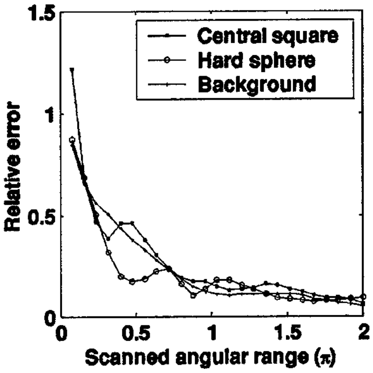

FIG. 9. The dependence of the relative errors of the mean values in the hard sphere (circle markers), the central square (square markers), and the background (asterisks) on the scanned angular range.

case of the background (because its real value is zero). When the scanned angular range is less than π, the errors decrease sharply with the increasing scanned angular range. On the other hand, when the scanned angular range is larger than π, the errors change much more slowly as the scanned angular range increases. The results agree with our theoretical conclusions. However, there are some fluctuations added to the trends of the curves. By comparing the three curves in Fig. 9, we find that these fluctuations depend strongly on the location of the object with respect to the detection curve. A more extensive study is needed to understand these fluctuations. There are some residual errors even in the full-view detection in Fig. 9. This is because we use an approximate backprojection algorithm, which is widely employed in experiments due to its better computation efficiency and stability when compared to the more accurate iteration algorithms.

D. Experimental results

The experimental setup is described in our previous paper and will not be repeated here.[6] The sample and the polar coordinate system describing the scanning orbit are shown in Fig. 10(a). The sample consists of a muscle cylinder of 4 mm in diameter and 5 mm in length embedded in a chunk of pork fat of 1.2 cm in radius r_f. There is a 10-mm fat layer below the muscle and another 7-mm one above it. An electromagnetic pulse is delivered to the sample from below (i.e., from behind the picture plane). With a scanning radius of $r_d = 7.1$ cm, thermoacoustic data are collected around the sample over a 2π angular span with 161 steps. As it is mentioned above, the electromagnetic pulse profile and the impulse response function of the ultrasonic transducer impose a filter on the thermoacoustic signals. We attempted to correct this effect using deconvolution but found that the resulted images were distorted, due to the lack of precise knowledge of the filter. Therefore, we do not use deconvolution in the reconstruction. This leads, as is explained above, to somewhat emphasized interfaces.

Figures 10(b)–10(d) show the reconstructed images using FBP with three sets of data. In the first of them, we choose the data collected along a circular detector arc of 92 degrees located at the top of the picture and almost symmetric with respect to its vertical axes. One sees that the left and right boundaries of the muscle cylinder and of the pork chunk are blurred away, since their normal lines do not touch the detector arc, while the rest of the boundary is sharp. The next figure shows reconstruction obtained with the data collected from a 202-degree arc [which is about $180+2*a\sin(r_f/r_d)$ obtained in the same way as θ in Fig. 6], when the whole phantom fits into the detection region. All boundaries are sharp now. Finally, the last figure shows the reconstruction with the full-view data.

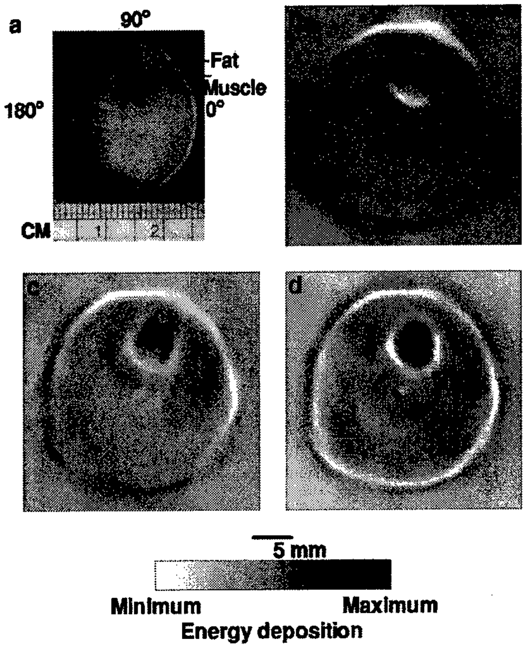

FIG. 10. (a) A photograph of the experimental sample. (b)–(d) TAT reconstructions using detection arcs of 92 degrees [from 50° to 142° in (a)], 202 degrees (from −18° to 184°), and 360 degrees, respectively. The blurred parts of the boundaries in (b) due to the limited view agree with the theoretical predictions. In (c) all the boundaries are resolved, since the object fits into the "detection region."

Notice that although no local reconstruction algorithms are applied, the boundaries are somewhat emphasized. The reason for this is the presence in the data of the impulse response function of the ultrasonic transducer, which has an effect similar to the application of an additional derivative with respect to the radius of the circle of integration. The presence of such a derivative emphasizes high frequencies and makes the reconstruction similar to a version of a local tomography algorithm.

E. Discussion

As mentioned above, although circular scanning is used in both our numerical and experimental studies, our conclusions can be applied to other configurations as well. In TAT with a planar configuration,[18,31–33] detections are implemented on a part of a line or a plane where the scanning view is quite limited; consequently, artifacts and interface blurring appear in the reconstructed images. In fact, in planar and linear scanning geometries one can never have an object immersed entirely into the "detection region" because the normal lines to any interfaces that are orthogonal to the detector plane (line) never pass through a detector. As a consequence, those parts of the interfaces will be blurred in any kind of reconstruction. For a sufficiently large view, these parts will be small, but theoretically will never disappear. For example, 2-D planar detection is utilized to image artificial blood vessels;[18] the scanning view is about 2.18 steradians. Therefore, it is not surprising that only the interfaces more-or-less parallel to the plane of detection are well imaged. Linear scanning detection is used to image a 2-D phantom.[32] Because the view of the linear scsanning[32] is much larger than that of planar scanning,[18] the interfaces are recovered much more completely. However, due to a limited view, artifacts and interface blurring similar to those demonstrated in our numerical and experimental studies still appear in the images.[32]

By comparing Figs. 7 and 10, we observe that the quality of images reconstructed from incomplete data when an object is in the detection region, is comparable with those from the full-view data. Scanning a smaller range has the advantages of reducing the scanning time or the size of the acoustic transducer array. It should be pointed out that this advantage usually exists in the case when both the sample and medium are relatively acoustically homogeneous. When strong wavefront distortion caused by acoustic heterogeneities occurs, it might be beneficial to collect the signal from all directions.

IV. CONCLUSIONS

It is explained theoretically what parts of the image can be stably recovered in the limited-view TAT. Analytic and algebraic reconstruction methods are developed and applied to numerical phantoms and experimental data. Both numerical and experimental results agree perfectly with the theoretical conclusions. The results can be applied practically to quantitative reconstructions with incomplete data, as well as to designing efficient scanning geometries in TAT and interpreting the obtained images.

ACKNOWLEDGMENTS

The work of the first two authors was sponsored in part by the U.S. Army Medical Research and Material Command Grant No. DAMD17-00-1-0455, the National Institutes of Health Grant No. R01 EB000712, and the Texas Higher Education Coordinating Board Grant No. ARP 000512-0063-2001. The work of the last two authors was sponsored in part by the NSF Grants No. DMS-9971674 and No. DMS-0296150.

APPENDIX: DERIVATION OF EQ. (5):

Equation (2) can be rewritten as

$$p_1(\mathbf{r},t)=\frac{\beta I_0}{4\pi C}\mathbf{D}_t\frac{\mathbf{R}\varphi}{t}. \tag{A1}$$

We define $p_2(\mathbf{r},t)=v_s\int_0^t p_1(\mathbf{r},t)dt$. Then we have

$$\frac{4\pi C t p_2(\mathbf{r},t)}{\beta I_0 v_s}=\mathbf{R}\varphi. \tag{A2}$$

If the detector is not very close to the objects, we can approximate the circular radon transform by the standard radon transform. The forward and inverse formulas for the standard radon transform are[15]

$$m(\varsigma,\theta)=\int_{r\cdot\theta=\varsigma} f(\mathbf{r})d\mathbf{r}, \tag{A3}$$

and

$$f(\mathbf{r})=\frac{1}{4\pi}\int_0^{2\pi} d\theta\mathbf{H}\frac{\partial m(\mathbf{r}\cdot\theta,\theta)}{\partial\varsigma}, \tag{A4}$$

where **H** is the Hilbert transform. Although the circular radon transform is different, one can write down an approximate inversion formula modeled after Eq. (A4). By combining an analog of Eq. (A4) with Eq. (A2), one obtains an approximate formula,

$$\varphi(\mathbf{r})\approx\frac{C}{\beta I_0 v_s^2}\int_0^{2\pi} d\theta\mathbf{H}(p_1(\mathbf{r}_\theta,|\mathbf{r}_\theta-\mathbf{r}|/v_s)|\mathbf{r}_\theta-\mathbf{r}| + p_2(\mathbf{r}_\theta,|\mathbf{r}_\theta-\mathbf{r}|)), \tag{A5}$$

where θ is defined as in Fig. 4. According to Fig. 4, we have the relation

$$d\theta=ds\frac{\mathbf{n}\cdot(\mathbf{r}-\mathbf{r}_\theta)}{|\mathbf{r}-\mathbf{r}_\theta|^2}, \tag{A6}$$

where **n** is the inward normal to the detection curve at $\mathbf{r}_\theta$ and ds is the arc length differential of the detection curve. After substituting this identity into Eq. (A5) we obtain Eq. (5). Equation (7) can be derived in a similar way.

[a] Author to whom correspondence should be addressed. Telephone: 979-847-9040; fax: 979-845-4450; electronic mail: LWang@tamu.edu; URL: http://oilab.tamu.edu

[1] W. Joines, R. Jirtle, M. Rafal, and D. Schaeffer, "Microwave power absorption differences between normal and malignant tissue," Int. J. Radiat. Oncol.-Biol. Phys. **6**, 681–687 (1980).

[2] S. Chaudhary, R. Mishra, A. Swarup, and J. Thomas, "Dielectric properties of normal human breast tissues at radiowave and microwave frequencies," Indian J. Biochem. Biophys. **21**, 76–79 (1984).

[3] W. Joines, Y. Zhang, C. Li, and R. Jirtle, "The measured electrical properties of normal and malignant human tissues from 50–900 MHz," Med. Phys. **21**, 547–550 (1994).

[4] W. F. Cheong, S. A. Prahl, and A. J. Welch, "A review of the optical properties of biological tissues," IEEE J. Quantum Electron. **26**, 2166–2185 (1990).

[5] Y. Xu, D. Feng, and L.-H. V. Wang, "Exact frequency-domain reconstruction for thermoacoustic tomography: I. Planar geometry," IEEE Trans. Med. Imaging **21**, 823–828 (2002).

[6] M. Xu and L.-H. V. Wang, "Time-domain reconstruction for thermoacoustic tomography in a spherical geometry," IEEE Trans. Med. Imaging **21**, 814–822 (2002).

[7] Y. Xu, M. Xu, and L.-H. V. Wang, "Exact frequency-domain reconstruction for thermoacoustic tomography: II. Cylindrical geometry," IEEE Trans. Med. Imaging **21**, 829–833 (2002).

[8] R. A. Kruger, P. Liu, Y. R. Fang, and C. R. Appledorn, "Photoacoustic ultrasound (PAUS)—reconstruction tomography," Med. Phys. **22**, 1605–1609 (1995).

[9] C. G. A. Hoelen, F. F. M. Mul, R. Pongers, and A. Dekker, "Three-dimensional photoacoustic imaging of blood vessels in tissue," Opt. Lett. **23**, 648–650 (1998).

[10] J. A. Fawcett, "Inversion of *n*-dimensional spherical averages," SIAM (Soc. Ind. Appl. Math.) J. Appl. Math. **45**, 336–341 (1985).

[11] L.-E. Andersson, "On the determination of a function from spherical averages," SIAM (Soc. Ind. Appl. Math.) J. Math. Anal. **19**, 214–232 (1988).

[12] S. Nilsson, "Application of fast backprojection techniques for some inverse problems of integral geometry," Linköping Studies in Science and Technology, Dissertation 499, Department of Mathematics, Linköping University, Linköping, Sweden, 1997.

[13] A. Denisjuk, "Integral geometry on the family of semi-spheres," Fract. Calc. Appl. Anal. **2**, 31–46 (1999).

[14] V. P. Palamodov, "Reconstruction from limited data of arc means," J. Fourier Anal. Appl. **6**, 25–42 (2000).

[15] F. Natterer and F. Wuebbeling, *Mathematical Methods in Image Reconstruction* (SIAM, Philadelphia, PA, 2001), Sect. 2.5.3.

[16] K. P. Köstli, M. Frenz, H. Bebie, and H. P. Weber, "Temporal backward projection of optoacoustic pressure transients using Fourier transform methods," Phys. Med. Biol. **46**, 1863–1872 (2001).

[17] S. J. Nortan and M. Linzer, "Ultrasonic reflectivity imaging in three dimensions: exact inverse scattering solution for plane, cylindrical and spherical aperture," IEEE Trans. Biomed. Eng. **BME-28**, 202–220 (1981).

[18] C. G. A. Hoelen and F. F. M. Mul, "Image reconstruction for photoacoustic scanning of tissue structures," Appl. Opt. **39**, 5872–5883 (2001).

[19] A. H. Delaney and Y. Bresler, "Globally convergent edge-preserving regularized reconstruction: an application to limited-angle tomography," IEEE Trans. Image Process. 7, 204–221 (1998).

[20] X. Pan and M. Anastasio, "Minimum-scan filtered backpropagation algorithms in diffraction tomography," J. Opt. Soc. Am. **16**, 2896–2903 (1999).

[21] X. Pan, Y. Zou, and M. Anastasio, "Data redundancy and reduced-scan reconstruction in reflectivity tomography," IEEE Trans. Image Process. **12**, 784–795 (2003).

[22] M. L. Agranovsky and E. T. Quinto, "Injectivity sets for the radon transform over circles and complete systems of radial functions," J. Funct. Anal. **139**, 383–413 (1996).

[23] A. K. Louis and E. T. Quinto, "Local tomographic methods in sonar," in *Surveys on Solution Methods for Inverse Problems* (Springer-Verlag, Vienna, 2000), pp. 147–154.

[24] E. T. Quinto, "Singularities of the x-ray transform and limited data tomography in R^2 and R^3," SIAM J. Math. Anal. **24**, 1215–1225 (1993).

[25] A. Faridani, E. L. Ritman, and K. T. Smith, "Local tomography," SIAM (Soc. Ind. Appl. Math.) J. Appl. Math. **52**, 459–484 (1992).

[26] A. Faridani, E. L. Ritman, and K. T. Smith, "Local tomography. Examples of local tomography," SIAM (Soc. Ind. Appl. Math.) J. Appl. Math. **52**, 1193–1198 (1992).

[27] A. Faridani, D. V. Finch, E. L. Ritman, and K. Smith, "Local tomography II," SIAM (Soc. Ind. Appl. Math.) J. Appl. Math. **57**, 1095–1127 (1997).

[28] P. Kuchment, K. Lancaster, L. Mogilevskaya, and M. Mogilevsky, "On local tomography," Inverse Probl. **11**, 571–589 (1995).

[29] V. Isakov, *Inverse Problems for Partial Differential Equations*, Applied Mathematical Science (Springer-Verlag, Berlin, 1998), Vol. 127.

[30] G. Beylkin, "The inversion problem and applications of the generalized radon transform," Commun. Pure Appl. Math. **37**, 579–599 (1984).

[31] G. Ku and L.-H. V. Wang, "Scanning microwave-induced thermoacoustic tomography: signal, resolution, and contrast," Med. Phys. **28**, 4–10 (2001).

[32] D. Feng, Y. Xu, G. Ku, and L.-H. V. Wang, "Microwave-induced thermoacoustic tomography: reconstruction by synthetic aperture," Med. Phys. **28**, 2427–2431 (2001).

[33] C. G. A. Hoelen, R. Pongers, G. Hamhuis, F. F. M. Mul, and J. Greve, "Photoacoustic blood cell detection and imaging of blood vessels in phantom tissue," SPIE **3196**, 142–153 (1998).